Politecnico di Torino

ScuDo
Scuola di Dottorato ~ Doctoral School
WHAT YOU ARE, TAKES YOU FAR

Doctoral Dissertation
Doctoral Program in Aerospace Engineering (36^{th}cycle)

Heat Transfer in Non-isothermal Particle-laden Turbulent Flows

Theoretical and numerical analysis

By

Hamid Reza Zandi Pour

******

Supervisor(s):
Prof. Michele Iovieno

Doctoral Examination Committee:
Prof. Carlo Massimo Casciola, University of Rome La Sapienza, Carlomassimo.Casciola@uniroma1.it (Referee)
Prof. Alessandra Sabina Lanotte, CNR NANOTEC, alessandrasabina.lanotte@cnr.it (Referee)
Prof. Luca Brandt, KTH Royal Institute of Technology, luca@mech.kth.se
Prof. Antonella Abbá, Politecnico di Milano, antonella.abba@polimi.it
Prof. Paolo Gualtieri, University of Rome La Sapienza, paolo.gualtieri@uniroma1.it

Politecnico di Torino
2024

Declaration

I hereby declare that, the contents and organization of this dissertation constitute my own original work and does not compromise in any way the rights of third parties, including those relating to the security of personal data.

Hamid Reza Zandi Pour
2024

* This dissertation is presented in partial fulfillment of the requirements for **Ph.D. degree** in the Graduate School of Politecnico di Torino (ScuDo).

I would like to dedicate this thesis to my beloved wife, Zahra Kashi.

Acknowledgements

I would like to acknowledge my supervisor, Professor Michele Iovieno, for giving me the opportunity to conduct my PhD degree under his supervision, and for his patience and spectacular mentorship. I would like to thank him for teaching me how to tackle a problem and maintain a research within the very challenging subject and the last unsolved problem in the classical mechanics, turbulence. I would like to express my ultimate gratitude to him for all the time he spent to exceptionally and professionally guide me during my PhD degree journey, and for every single precious scientific point I have learned from him. I also would like to acknowledge Professor Perry L. Johnson for accepting me as his visiting scholar and for his professional guidance and exceptional advice during the last months of my degree. I am so appreciative of him for his strong support, scientific advice and consideration despite all the difficulties with working online in different time zones. My ultimate gratitude also goes for my former mentor, Professor Carlo Massimo Casciola, the one who firstly introduced the turbulence world to me and encouraged me to pursue my enthusiasm in discovering more insights within this very challenging area of research, and for teaching me to love turbulence. I would like to acknowledge my devoted and beloved wife, Zahra Kashi, because without her I would have been unable to accomplish the PhD degree. I would like to thank her not only for supporting me in fulfillment of my academic career, but also for supporting me in all aspects of our challenging journey of life that we started and we have been going through, together. Besides, I would like to offer a very special gratitude to Professor Marco Gherlone, the coordinator of my degree, for all the support and facilitation during my entire career at Politecnico di Torino. HPCPoliTo, CINECA and EuroHPC are also acknowledged for providing the required computational resources and technical support during my research activity. Finally, I would like to thank all the staff member of DIMEAS, ScuDo, and administration of Politecnico di Torino as well as my all dear friends that have been supportive to me during this period of time.

Abstract

The main focus of this thesis is to study the heat transfer in non-isothermal turbulent particle-laden flows. Numerical and theoretical tools are used to better understand this non-trivial multi physics and multi-scale problem. Several aspects of such complex problem have been observed in order to discover, formulate and quantify the role of inertial heavy particles in heat transfer within a turbulent unbounded shearless flow. For this reason, a basic flow configuration has been considered to mimic a small part of the real-world physical domain e.g. a small portion of warm cloud in atmosphere. Numerical results have been obtained from the direct numerical simulations (DNSs) within the valid range of point-particle (PP) Eulerian-Lagrangian (EL) approach. In the first part, the theoretical background is introduced which consists of the governing equations for the carrier flow and discrete phase. In the second part, the numerical method and the limits and assumptions which have been used throughout this study, are discussed. In addition, statistics of temperature and heat flux computed by DNS are provided and discussed at different flow conditions in terms of flow parameters. Two main sets of numerical results are provided and evaluated in order to cover a wide range of physical problem in which the research objective can be addressed by varying the carrier flow Taylor micro-scale Reynolds number (from 37 to 124) and particle Stokes number (from 0.1 to 6) and thermal stokes number (from 0.1 to 10). The effect of particle inertial, thermal inertial, carrier flow Taylor microscale Reynolds number, particle thermal back-reactions in collisionless and collisional regimes are evaluated and discussed at a fixed particle volume fraction, particle-to-fluid density ratio and fluid Prandtl number. A novel decomposition is also proposed to reveal the mechanisms behind the modification of temperature statistical moments and velocity-temperature correlation in terms of fluid velocity and temperature correlation and particle acceleration and temperature time derivative statistics. In the third section, we use kinetic theory to formulate a kinetic-based probabilistic framework to describe the non-isothermal particle-laden

turbulent flow. This approach allows us to derive macroscopic field equations for the discrete phase by utilizing the single-particle probability density function (pdf). The transport equation of this pdf is also derived to investigate the dynamical and thermal behavior of inertial particle in the phase space by looking at the unclosed statistical moment within the pdf evolution equation. Most important moment, particle temperature time derivative conditional on particle position, velocity, and temperature is selected to be investigated at different time and position using the data obtained by DNSs. The self-similar evolution of the pdf in the phase space will be also discussed in this part. In the fourth part, a comprehensive self-similarity analysis for fluid and particle mean temperature fields in differential and integral forms is performed and the theoretical findings are validated with the numerical results. Finally, in the last part, a new theory for detecting the thermal caustics in turbulent non-isothermal flows laden with particles, is proposed. This theory can be used to determine the flow condition at which particle temperature gradient field has a finite-time singularity.

Contents

List of Figures

List of Tables

Chapter 1

Introduction

1.1 Background

Particle-laden turbulent flows which involve multi-scale interplay between suspended inertial particles (or bubbles or droplets) and fluid turbulent fields, are present and play a vital role in many natural and industrial processes. Understanding such flow regimes is essential for designing more efficient and greener energy conversion systems [1, 2], for removing more plastic particles from the oceans [3], for improving air quality [4] and for better understanding the could physics [5–8]. Meanwhile, in single-phase non-isothermal turbulent flows, transport of fluid temperature that can be advected and diffused both passively and actively by the fluid turbulent velocity field, per se, is a complex problem and it has been under investigation for decades. For instance, in [9] the very complex problem of passive dispersion of fluid temperature field by turbulent motion has been investigated and revealed insightful information about the universal intermittent behavior due to the formation of ramp-cliff structures of the temperature field and consequently the onset of large temperature gradients on small-scale due to turbulent motion. Further studies have been done on the fluid temperature transport by turbulence to better understand the underlying physics and report the characteristics of the anomalous scaling behavior of passive scalar field [10, 11]. Presence of inertial particles make the situation more sophisticated and simultaneous fluid-particle dynamical and thermal interaction has not been fully understood even in simple flow configurations. Although passive scalar and particle transport in turbulent flows, has been studied since the pioneering work of Taylor

[12] and Kraichnan [13], the problem which involves the full dynamical and thermal interaction of inertial particle with turbulent fields are quite a new topic and there have been a few works in the past decades. One can find some of the best literature reviews addressing the recent theoretical, numerical and experimental analyses of particle-laden turbulent flows in [14–19].

In non-isothermal particle-laden turbulent flows, the existence of a very complex thermal and dynamical interplay calls for understanding of many local and non-local phenomena and mechanisms that affect the physics of the flow. Some of the most significant ones are turbulence-induced thermophoresis, turbophoresis, clustering, preferential concentration, sweep-stick mechanisms, scattering, caustics, thermal caustics and preferential sampling. Moreover, in the presence of turbulent mixing, multiscale interaction between mixing dynamics and turbulent flow influences the overall heat, mass and momentum transport in the flow domain. Furthermore, in two-way coupling regimes, in which particles are able to alter the turbulence characteristics through their feedback, another level of complexity arises. In a generic non-isothermal turbulent flow laden with inertial heavy particles, like the case of this study, suspended particles can carry enthalpy through the mixing layer, and interact dynamically and thermally with the turbulent fields and mixing at the same time according to their inertia and thermal inertia. Direct measurements of particle-laden flow, especially when thermal interaction between fluid and particles has to be considered, are very complex and difficult. Therefore, most of experimental works have used PIV (particle image velocimetry) and PTV (particle tracking velocimetry) in order to collect bulk statistics of fluid particles and suspended particles. For instance, near-wall interaction of particles in wall-bounded flows has been investigated recently by [20, 21], while Lewis et al. [22] carried out a gas-particle turbulent flow experimentally by using a method called two-colour laser induced fluorescence (LIF) in order to obtain the statistics of fluid temperature in a flow laden with particles and subject to a high radiative flux, and Banko et al. [23] have investigated the effect of particle preferential concentration on fluid temperature statistics through changing the absorption of radiative heat flux in turbulent square duct flow. In general, there exist a few experimental works on the heat transfer in particle-laden turbulent flow. In most of existing experimental works, bulk property and fluid temperature statistics are reported. A priori statistical approaches to these flows, mostly based on the stochastic theory, can also return important insight under certain ad hoc assumptions. For instance, kinetic theory is used to derive the single particle or fluid -particle pdf

transport equation, and proposing two-phase Eulerian-Eulerian macroscopic field equations along with some closure models [24–26].

Therefore, performing high fidelity numerical simulations, e.g. DNS, can fill the gap and gives detailed temperature statistics of both phases to better understand the thermal transport in a turbulent flow seeded by inertial particles. The availability of high performance computing (HPC), and the development of parallel algorithms and architectures, have provided researchers with a very powerful computing means for performing simulation-assisted analysis of turbulence. Many studies on particle-laden flows in non-isothermal systems have focused on wall-bounded flows. Zonta et al. [27] simulated a channel flow when the inertial particles are present and the Prandtl number and volume fraction are fixed, observing an enhancement in heat transfer for small particles and a reduction for very large ones. Kuerten et al. [28] found that inertial particles with a high specific heat capacity enhance the heat transfer in a channel flow through the preferential concentration in near-wall region, a phenomenon which is known as turbophoresis, and quantified particles contribution to the overall mean Nusselt number. They found that the increase in particle velocity-temperature correlation in wall-normal direction especially in two-way coupling regime when the turbophoresis is higher than the one-way coupling regime. Nakhaei et al. [29], investigated the effect of very large inertial particle with quite a high volume fraction on heat transfer in a non-isothermal channel flow and found that inertial particles tend to reduce the convective turbulent heat flux resulting in a reduction in the overall heat transfer with respect to unseeded flow. This overall reduction has been explained as due to the increase in the exchanged heat between carrier flow and the suspended particles and the less-efficient fluid-particle heat transfer in near wall region, which decreases the velocity fluctuation by turbopheresis. In their numerical experiments, the volume fraction and the ratio of thermal Stokes-to-Stokes number and particle density were kept constant. Lessani et al. [30] found that heat transfer from the solid wall increases proportionally with with the thermal Stokes number when the mass loading and particle Stokes number are fixed. The results also indicated the reduction in convective turbulent Nusselt number with increase in particle thermal Stokes number at fixed volume fraction and particle Stokes number.

Other works have numerically studied the heat transfer modulation by the presence of inertial particles in homogeneous isotropic turbulent flows, the fundamental archetype of most theoretical studies on turbulence. Pouransari et al. [2, 31], investi-

gated particle-to-fluid heat transfer in a homogeneous and isotropic turbulent flow with a non constant density at low Mach number. They found a strong dependence of particle-to-fluid heat transfer on Stokes number and particle spatial distribution, and weak dependence on flow Reynolds number and particle-to-fluid heat capacity ratio. By using DNS data, they develop a small-scale phenomenological model which is able to capture the effect of clustering on heat transfer and introduced a timescale for particle modulation of fluid temperature in two-way coupling regime. More recently, Carbone et al. [32] carried out a comprehensive study on multiscale fluid-particle thermal interaction in isotropic turbulence. They showed how fluid temperature variance monotonically decreases with particle thermal relaxation time and that, while the probability density function of the fluid temperature gradient scales with its variance, the probability density function of particle temperature time derivative does not scale in a self-similar manner but shows multi-fractality at small-scales. Their results suggest that the alignment of particle velocity and local fluid temperature gradient plays a significant role in the clustering on the fluid temperature fronts. Moreover, they showed how fluid temperature increments, a measure of fluid temperature fluctuations, are monotonically suppressed by particle thermal feedback as particle inertia increases, and provided a statistical analysis to characterize the particle thermal caustics and non-local thermal behaviour of particles. They explained how particle temperature increments in the dissipation range show a multifractal behaviour. This analysis has been extended by Saito et al. [33] who also used a Langevin equation to model the fluctuations of fluid temperature seen by particles. These results are consistent with the analysis by Béc et al. [11], who quantitatively and qualitatively showed the significance of fluid temperature fronts at different particle inertia and thermal inertia ranges. That work discussed how inertial particles tend to preferentially sample the advected scalars, concentrating in the regions of high scalar gradients, and experiencing strong temperature fluctuations along their Lagrangian trajectory due to the intermittency of the turbulent flow which advects the passive scalar field. Moreover, [11] reported two different power-laws of the variance of particle temperature time derivative at low and high particle thermal inertia ranges.

The variance of particle temperature time derivative was used as a measure for assessment of inter-phase and inter-scale heat transport, which increases with the particle inertia. Following the works by Carbone et al. [32] and Bec et al.[11], most recently, Li et al. [34] performed an analysis on the effect of gravity on temperature

statistics in a homogeneous and isotropic turbulent flow laden with inertial particles. They reported the the effect of gravity on the preferential concentration, formation of temperature gradients fronts, and multi-scale heat transfer in one-way coupling regime at different range of particle inertia and thermal inertia. They showed how particle preferential concentration and fluid temperature gradients are correlated and they highlighted the non-local effect for larger particles, i.e. the path-history effect on the heat transfer and clustering. They reported that gravity weakens the non-local effect for higher-inertia particles by changing the way that particle sample fluid velocity gradient history along their trajectories, leading to an enhanced aggregation of particles in the direction of gravity. Moreover, they showed how gravity increases the particle heat transfer at different range of inertia and thermal inertia by comparing the statistics with the case of zero gravity. Although these works have analyzed in detail the multiscale fluid-particle thermal interactions, they have only considered a situation in which both fluid temperature and velocity fields are isotropic, statistically homogeneous and steady. Nonetheless, the existing literature features limited research on this topic when the temperature field is inhomogeneous and statistically unsteady, as in the presence of a developing mixing layer.

1.2 Objective

The main objective of this work is to quantify the role of dynamical and thermal behaviors of suspended particles in heat transfer in a shearless unbounded turbulent flow. The Eulerian-Lagrangian point-particle direct numerical simulations are employed in order to obtain the statistics of both phases which can describe the fluid-particle thermal and mechanical interactions. The simplest thermally inhomogeneous flow generated by a temperature step between two homothermal regions is considered within which the fluid temperature field is passively advected and diffused by an incompressible homogeneous and isotropic turbulent velocity field. As a result of such temperature discontinuity, an inter-turbulent thermal mixing occurs between two identical velocity fields leading to the genesis and the evolution of a temporally-growing thermal mixing layer at the interface of two homothermal regions. Additionally, the flow is seeded by small monodisperse spherical particles, with the aim of analyzing the impact of inertial particles on the heat transfer process taking place between the two regions. The quantification is conducted for a wide

range of Stokes numbers and thermal Stokes numbers in one-and two-way coupling regimes at different Taylor microscale Reynolds number in both collisional and collisionless at a fixed particle volume fraction, particle-to-fluid density ratio and Prandtl number. A large set of direct numerical simulations are performed mimicking different flow conditions by altering the relevant particle and turbulence control parameters, i.e. Taylor Reynolds number, particle Stokes number, and thermal Stokes number. Two main set of simulations are carried out to cover the physical space of the problem to address the research objective. In the first set, the ratio between thermal Stokes number to Stokes number is kept constant while in the second set, these two numbers can independently take the values within the limit of the numerical approach. The main goal of this part is to describe and characterize the impact of particle inertia and thermal inertia on the turbulent heat flux in the inhomogeneous direction at different particle inertia and thermal inertia ranges. Moreover, fluid-particle dynamical and thermal interactions are investigated for a case that their thermal inertia and inertia are not proportional and can independently vary. Relative particle-to-fluid velocity-temperature correlation is presented to analyze the overall impact of particles in contributing to heat transfer process in mixing layer. This relative heat flux ration reveals the particle contribution to the global heat transfer specifically at the center of flow domain at which the mixing is maximum. The results show how particles enhance the global heat transfer with respect to unseeded flow at different particle inertia and thermal inertia and for different turbulent characteristics. In addition to the numerical observations which form the main structure of this work, we aim to use the valuable DNS date to develop some new theoretical analyses on the heat transfer in particle-laden turbulent flows. Accordingly, a comprehensive self-similarity analysis both in differential form and integral form is carried out to find the self-similar and quasi self-similar solutions for particle and fluid mean temperature fields. Moreover, to analyze the particle complex dynamical and thermal behavior in phase space and physical space, kinetic theory and statistical physics fundamentals, have been adopted to derive a single particle pdf transport equation similar to the derivation of Boltzmann equation in statistical mechanics for a system of particles. Thanks to this probabilistic description, we can explore the other aspects of the physical problem by computing the mesosccopic information, which are unclosed terms within the kinetic pdf transport equation. The kinetic pdf method also gives us an analytical tool to derive macroscopic field equations for disperse particles which can be used in self-similarity analysis. Furthermore, the

particle field equations are employed to proposed a novel theory to formulate the onset of thermal caustics. Analogous to the caustics in particle velocity field, thermal caustics can occur when particle velocity gradient tensor has finite-time singularity and this effect enters into the particle temperature gradient field. This theory is used to analyze the thermal caustics via the dynamics of particle temperature gradient vector which is coupled with particle velocity gradient tensor field, by determining the particle inertia and thermal inertia ranges in which the evolution can be smooth or explosive.

1.3 Outline

The physical model of the problem we tackle is described in chapter 2, including the governing equations of carrier flow and particles, numerical method, and simulation setup. In chapter 3, the simulation results of two main sets of numerical simulations, fixed and variable thermal Stokes number to Stokes number ratio, are provided and discussed. The fluid and particle statistics are reported in terms of a various range of simulated Stokes number and thermal Stokes number at different Taylor microscale Reynolds numbers for one-and two-way coupling regimes both with and without considering inter-particle collisions. In chapter 4 the kinetic pdf method is adopted to derive the evolution equation for the single particle pdf subject to turbulent temperature and velocity fields. This pdf is also used to obtain the field-like macroscopic equations for disperse particles. Particle mean temperature field equation is then employed as well as fluid mean temperature equation to perform a self-similarity analysis in chapter 5 in both differential and integral form. Finally, in chapter 6 a novel theory is proposed to formulate the formation of thermal caustics in non-isothermal particle-laden turbulent flows. It is shown how the dynamics of particle temperature gradient vector can have the finite-time singularity leading to an explosive evolution as a results of the singular values of particle velocity gradient tensor, particle velocity field and particle number density field. Furthermore, the ranges of particle inertia and thermal inertia at which finite-time blowup occurs in particle temperature gradient evolution is identified and discussed in this chapter. It should be noted that some parts of the results in the chapter 3 have been already published and some other parts are still under consideration for publication. Some parts of the investigation which is dedicated to collisionless regime, have been

published in [35, 36]. Some of the results in the collisional regimes have been published in [37–40]. Parts of the study on the particle thermal Stokes and Stokes number such that they are not proportional and they can change independently, heave been published in [41].

Chapter 2

Heat transfer in particle-laden turbulent flows: Theory

2.1 Introduction

The objective of this chapter is to provide the theoretical foundations needed for analysis of and the thermal inertial influences of the inertial heavy particles on the heat transport phenomenon between two homogeneous and isotropic turbulent zones with uniform temperature. To address this goal, a basic and simple flow configuration is assumed to computationally represent the physics of the flow of interest leading to a simplification in required equations. Since this problem has intrinsically a very complex nature, most significant flow parameters have been chosen to characterize the flow, keeping the others constant during the numerical observation. For instance, parametrization of the turbulent carrier flow is done only through the dimensionless number, Taylor microscale Reynolds number, while particle thermal and inertial behavior is investigated through thermal Stokes number and Stokes number. However, other parameters such as Prandtl number, particle volume fraction and particle-to-fluid density ratio can also be taken as control parameters of the simulation, but throughout this work they are kept constant, assuming that particle are heavy enough with respect to fluid, suspension is dilute and momentum diffusion to thermal diffusion remains constant in the fluid flow resulting in constant Prandtl number. To perform such analysis we need to derive the governing equations of continuous and discrete phases. Such equations for carrier flow in Eulerian frame are presented

in section 2.2 , and particle Lagrangian equations are provided in 2.3. As regrades the fluid governing equations, the turbulence theory is used to derive the relevant statistical representation of the fluid fields in turbulent condition. However, the equations mostly derived for a generic case, at the end of the derivations, the final version of the equations under the assumptions of the present study, e.g. homogeneity and isotropy in velocity field, will be presented. The limitation and the scope of each equation is also discussed separately for the continues and discrete phases. In 2.4 additional discussion is presented on the particle interaction forces and appropriate conditions for this study is identified accordingly. The formulation of inter-phase exchange of energy between carrier flow and inertial particles under the assumptions of this work, is discussed and provided in section 2.5. By deriving and analyzing these governing equations, this chapter establishes a foundation for a more profound understanding of heat transport mechanisms in turbulent flows with inertial particles, paving the way for further theoretical and computational investigations.

2.2 Governing equations of continuous phase

As it is customary in the context of turbulence theory, to obtain equations for mean and fluctuating temperature fields using well-known Reynolds decomposition allowing further analytical and numerical analysis of flow statistics which is the main aim of this work. Accordingly, the simplest flow condition is assumed for a fluid velocity field which is statistically stationary, homogeneous and isotropic. Fluid flows including single- or multi-phase flows are commonly in a turbulent condition. Any generic turbulent flow intrinsically behaves in a a random manner across a wide spectrum of scales. In this investigation, where no solid wall is present, the basic flow configuration is chosen such that to represent a forced homogeneous and isotropic (FHIT) velocity field. This setting is quite a general scenario to address fundamental aspect of turbulence and it is very useful to develop theoretical aspect of turbulence and its interaction with other physical phenomena, such as particle suspension which is the scope of this work. Especially in this representation, the small scale turbulence in the dissipative range is well-resolved, and the interaction with particle dispersion or inter-scale energy flux with or without particle can be effectively studied. In the cubic or parallelepiped flow domain, periodic boundary conditions can be easily imposed onto velocity field at any side, however; in case

of parallepiped for passive scalar other treatment is needed which will be discussed later in detail. In the velocity field, there is no mean flow component, and due to the homogeneity in all direction turbulent shear stress term in the momentum equation. In this case, the fluid flow is called shear-less turbulent free flow regime, indicating that there is no shear and no solid wall to confine the flow. Moreover, due to the isotropy, statistical distribution and property of the velocity fluctuations in all directions are identical. In this section, We derive the required evolution equations for carrier flow which are used in this work. First, we derive the generic form of field equations assuming that the fluid is Newtonian and incompressible in subsection 2.2.1. In addition to the fluid velocity and temperature fields, the generic transport equations for the gradients of velocity and temperature are provided and discussed. Subsequently in subsection 2.2.2 turbulence theory is utilize in order to derive the fluid transport equations in turbulent flow. At the end of each derivation, the ad hoc assumptions of this work including isotropy and homogeneity will be applied to obtain the equations for the numerical analysis according to the scope of this study.

2.2.1 Fluid field equations

The starting point is to introduce the continuity equation and momentum conservation equation for a Newtonian and incompressible fluid. This set of field equations are indeed the Navier-Stokes equations and are given by

$$\frac{\partial u_i}{\partial x_i} = 0, \tag{2.1}$$

$$\frac{\partial u_i}{\partial t} + u_j \frac{\partial u_i}{\partial x_j} = -\frac{1}{\rho_0}\frac{\partial p}{\partial x_i} + \nu \frac{\partial^2 u_i}{\partial x_j \partial x_j} + f_{u,i}, \tag{2.2}$$

where ρ_0 denotes constant fluid density, ν is the fluid kinematic viscosity and $\boldsymbol{f}_u$ is an external body force. Fluid pressure, and velocity fields are denoted respectively by $\boldsymbol{u}(t,\boldsymbol{x})$ and $p(t,\boldsymbol{x})$. We can also derive the momentum equation by using the definition of vorticity field $\boldsymbol{\omega}(t,\boldsymbol{x}) = \nabla \times \boldsymbol{u}(t,\boldsymbol{x})$ and also can replace the convective term in the equation by using the identity $\boldsymbol{u}\cdot\nabla\boldsymbol{u} = \boldsymbol{\omega}\times\boldsymbol{u} + 1/2\nabla(\boldsymbol{u}\cdot\boldsymbol{u})$ and introduce a new pressure field (i.e. total pressure $P = p + 1/2\nabla(\boldsymbol{u}\cdot\boldsymbol{u})$) to recast the equation in rotation form. This new pressure field which is also called the Bernoulli pressure includes the thermodynamic pressure and so-called dynamic pressure or hydrodynamic contribution to the pressure field due to the fluid kinetic energy. Consequently,

the incompressible Navier Stokes equation in rotational form reads

$$\nabla \cdot \boldsymbol{u} = 0, \tag{2.3}$$

$$\frac{\partial \boldsymbol{u}}{\partial t} - \boldsymbol{u} \times \boldsymbol{\omega} = -\frac{1}{\rho_0}\nabla P + \nu \nabla^2 \boldsymbol{u} + \boldsymbol{f}_u. \tag{2.4}$$

Moreover, fluid temperature field with no bulk heat sources or sinks is considered. However, the only bulk source or sink term is C_T which is the particle back reactions on fluid temperature and it will be defined in detail later on. In order to derive the fluid temperature equation we need to start with the evolution equation of fluid entalphy

$$\frac{\partial h}{\partial t} + u_j \frac{\partial h}{\partial x_j} = A_{ij}\Sigma_{ij} + \frac{\mathrm{D}p}{\mathrm{D}t} - \frac{\partial q_{H,i}}{\partial x_i} + C_h, \tag{2.5}$$

where $A_{ij} = \partial_j u_i$ denotes fluid velocity gradient tensor which can be decomposed into two symmetric and anti-symmetric parts $A_{ij} = S_{ij} + \Omega_{ij}$. The symmetric part is strain-rate tensor $S_{ij} = (1/2)(A_{ij} + A_{ji})$ while anti-symmetric part is rotation-rate tensor $\Omega_{ij} = (1/2)(A_{ij} - A_{ji})$. The strain-rate tensor indicate the deformation rate of a local fluid parcel due to the stretching/compression and is used to define the local dissipation rate $\varepsilon = 2\nu S_{ij}S_{ij}$. Meanwhile, rotation-rate tensor determines the vorticity pseudovector field $\omega_i = -2\varepsilon_{ijk}\Omega_{jk}$, via $\Omega_{ij} = -(1/2)(\varepsilon_{ijk}\omega_k)$. The local enstrophy, can be also derive from this relation as $\omega^2 = -2\Omega_{ij}\Omega_{ij}$. The enstrophy and dissipation rate are proportional to the invariant of the strain-rate tensor and rotation-rate tensor and their dynamics can be understood by looking of the evolution of these quantities which both inherit the information from the velocity gradient tensor. Therefore, we specifically derive the evolution equation for the velocity gradient tensor and the derivation of equations for enstrophy and dissipation rate are not presented separately in this study. In addition to velocity gradient tensor which exists in the enthalpy equation in the term that indicates the energy loss due to the viscous forces, there exist $\Sigma_{ij} = 2\mu S_{ij} - 2/3(A_{kk}\delta_{ij})$ which denotes viscous stress tensor in terms of its symmetric part S_{ij} and trace of the velocity gradient tensor A_{kk}. Due to the incompressiblity, this term is zero. From the incompressibility assumption and also by assuming the carrier flow as a calorically perfect gas with heat capacity c_{p0} at constant pressure, and using ideal gas equation of state ($p = \rho_0 RT$), we can access the thermodynamic pressure and derive the fluid temperature field $T(t,\boldsymbol{x})$ equation from energy conservation equation ($h = \rho_0 c_{p0} T$). We can neglect the term

$\mathrm{D}p/\mathrm{D}t$ and the viscous work in the entalphy equation and by using the Fourier's law and substituting the heat flux with $q_{H,i} = -\lambda \partial_i T$, where λ is the fluid thermal conductivity coefficient, we can write the fluid temperature equation

$$\frac{\partial T}{\partial t} + u_j \frac{\partial T}{\partial x_j} = \kappa \frac{\partial^2 T}{\partial x_j \partial x_j} + \frac{1}{\rho_0 c_{p0}} C_T, \tag{2.6}$$

where κ denotes the fluid thermal diffusivity. We have derived the fluid momentum and temperature fields under certain conditions that have been explained. We continue with the derivation of evolution equation of velocity gradient tensor A_{ij} and temperature gradient vector G_j. To do that we need to take the gradient from both sides of fluid momentum and temperature equations. First we proceed with taking the gradient of the fluid momentum equation (2.2) which leads to

$$\frac{\partial}{\partial t}\left(\frac{\partial u_i}{\partial x_j}\right) + \frac{\partial u_k}{\partial x_j}\frac{\partial u_i}{\partial x_k} + u_k \frac{\partial^2 u_i}{\partial x_j \partial x_k} = -\frac{1}{\rho_0}\frac{\partial^2 p}{\partial x_j \partial x_i} + \nu \frac{\partial}{\partial x_j}\left(\frac{\partial^2 u_i}{\partial x_k \partial x_k}\right) + \frac{\partial f_{u,i}}{\partial x_j}. \tag{2.7}$$

If we define $F_{u,ij} = \partial f_{u,i}/\partial x_j$, and introduce the definition of velocity gradient tensor $A_{ij} = \partial_j u_i$ into the equation (2.7), we get

$$\frac{\partial A_{ij}}{\partial t} + u_k \frac{\partial A_{ij}}{\partial x_k} = -A_{ik}A_{kj} - \frac{1}{\rho_0}\frac{\partial^2 p}{\partial x_i \partial x_j} + \nu \frac{\partial^2 A_{ij}}{\partial x_k \partial x_k} + F_{u,ij}. \tag{2.8}$$

The dynamics of velocity gradient tensor in turbulent flows has been under investigations since the pioneering works of Meneveau et al. [42], by other researchers in order to develop turbulence theory and improving the existing turbulence models. For instance, Carbone et al. in and Johnson et al. in [43]. have extensively studied velocity gradient tensor and developed models for the terms in the gradient velocity tensor transport equation. Most crucial term in the equation is called pressure Hessian, ($H_{ij} = \partial_i \partial_j p$) has been under investigation by Johnson et ql. and Carbone et al. , to better understand the dynamics of the velocity gradient tensor and to develop sub-grid scale models for large eddy simulation (LES). In analogy to the fluid momentum equation, we have this additional term which make the dynamics more complicated. The non-linear term $A_{ik}A_{kj}$ is called velocity gradient tensor self-amplification and it is a local term while pressure Hessian is a non-local term relating the pressure field to the velocity gradient tensor. The trace of pressure

Hessian is also produce another non-local effect through the deviatoric part of the pressure Hessian, and on the other side, the deviatoric part of local self-amplification term adds another local effect through isotropic pressure effect. In general, pressure Hessian term H_{ij} and viscous Laplacian term $\nu\partial_k\partial_k A_{ij}$ which indeed are non-local terms and cannot be expressed in terms of local values of velocity gradient tensor, are not closed from Lagrangian point of view, in the equation (2.8) and require closure models. On the other hand, the closed non-linear term $A_{ik}A_{kj}$ and the isotropic part of the pressure encode interesting dynamics of the turbulent flow such as stretching and tilting of vorticity field $\omega_i = \varepsilon_{ijk}A_{kj}$, and strain-rate tensor [44, 43]. As it has been shown earlier, this quantity is related to the small-scale turbulence and dissipation rate and enstrophy can be studied and better understood through its symmetric and anti-symmetric components. This implied that vortical structure of turbulence are connected to the dynamics of such quantity. More importantly the non-linearity of the advective term in the Navier-Stokes equation which is the origin of term $-\boldsymbol{A}^2$, can be assessed and analyzed in order to reveal more insights. On the other hand, non-locality of the velocity field in the incompressible flow regime, due to the coupling between momentum and continuity equation through pressure field, can be characterized in terms of velocity gradient tensor. In this case, pressure field can be obtained as the solution of a Poisson equation. If we derive the evolution equation for trace of velocity gradient tensor, i.e. A_{ii}, by taking gradient with respect to index i from the momentum equation (2.2), we have

$$\frac{\partial}{\partial t}\left(\frac{\partial u_i}{\partial x_i}\right)+\frac{\partial u_k}{\partial x_i}\frac{\partial u_i}{\partial x_k}+u_k\frac{\partial^2 u_i}{\partial x_i\partial x_k}=-\frac{1}{\rho_0}\frac{\partial^2 p}{\partial x_i\partial x_i}+\nu\frac{\partial}{\partial x_i}\left(\frac{\partial^2 u_i}{\partial x_k\partial x_k}\right)+\frac{\partial f_{u,i}}{\partial x_i}. \quad (2.9)$$

From continuity equation equation (2.1) we know that $\partial_i u_i = 0$, then the trace of the momentum equation reduces to

$$\frac{1}{\rho_0}\frac{\partial^2 p}{\partial x_i\partial x_i} = -A_{ki}A_{ik}+F_{u,ii}. \quad (2.10)$$

Equation (2.10) is the pressure Poisson equation which is indeed the trace of the pressure Hessian term in the velocity gradient equation (2.8) and is expressed in terms of local velocity gradient and the trace of the trace of the external force gradient tensor, $F_{u,ii}$. As it can been in the equation (2.10) the non-locality of the pressure is related to the non-linearity of the velocity gradient tensor, which is an obvious

indication of the complexity of the dynamics of the velocity gradient tensor. In order to derive the evolution equation of temperature gradient vector we need to take the spatial derivative from the temperature field equation (2.6) which returns

$$\frac{\partial}{\partial t}(\frac{\partial T}{\partial x_j})+u_k\frac{\partial}{\partial x_j}(\frac{\partial T}{\partial x_k})+\frac{\partial u_k}{\partial x_j}\frac{\partial T}{\partial x_k}=\kappa\frac{\partial}{\partial x_j}(\frac{\partial^2 T}{\partial x_k\partial x_k})+\frac{1}{\rho_0 c_{p0}}\frac{\partial C_T}{\partial x_j}.$$

By defining the fluid temperature gradient vector $G_j=\partial T/\partial x_j$ and substituting this new variable in the temperature gradient budget equation, and after some manipulations we have

$$\frac{\partial G_j}{\partial t}+u_k\frac{\partial G_j}{\partial x_k}=\kappa\frac{\partial^2 G_j}{\partial x_k\partial x_k}-G_kA_{kj}+\frac{1}{\rho_0 c_{p0}}\frac{\partial C_T}{\partial x_j}. \tag{2.11}$$

Recently, several models for the Lagrangian evolution of velocity gradient tensor in turbulent flows have been proposed. Some of these proposed models have been derived directly from Navier-Stokes equations, some others from the phenomenological relations. For example, Johnson et al. in [44] derived and proposed a stochastic model for growth of intermittency resulting from the velocity gradient self-stretching and rotation. The proposed model is able to predict the topology of the velocity gradient tensor, e.g. the vorticity alignment with strain-rate tensor eigenframes. They used a physically motivated closure on the recent deformation of Gaussian fields (RDGF) approach for computing the conditional averages of the pressure Hessian and viscous Laplacian [44]. Xhang et al. in [45] have used the same approach to propose a similar Lagrangian model for passive scalar gradient vector in isotropic turbulent flow. The modified model proposed by them showed a good agreement with DNS data in reproducing of scalar gradient vector production rate and alignment of the gradient vector G_k with the eigenvectors of strain-rate tensor S_{kj} in the equation (2.11). The crucial term in the scalar gradient vector evolution equation is the local term $-G_kA_{kj}$ which is highly influenced by the alignment of scalar gradient vector and the symmetric part of the velocity gradient tensor, i.e. the strain-rate tensor. There is no non-local pressure Hessian term like the velocity gradient tensor evolution equation for scalar gradients. Consequently, there is no mechanisms like pressure Hessian to regulate the scalar gradient vector self-amplification due to the G_kA_{kj}, causing the magnitude of scalar gradient $||\boldsymbol{G}||^2$ to grow when $G_kA_{kj}G_j<0$ [45]. Another difference in scalar gradient vector equation with the velocity gradient tensor equation is that there is no non-linear term and the term $-G_kA_{kj}$ which is

originated in the linear advection of the scalar by the fluid velocity field, in the scalar transport equation and this remains also linear to the velocity gradient, in the equation (2.11). However, linearity does not reduce the complexity of the dynamics. The crucial problem to understand the dynamics of the scalar gradient is to close the diffusion by proposing a proper closure model and investigating the dynamics of the linear part through the eigenframes of the strain-rate tensor. This means that to better understand the dynamics of the G_j, the dynamics of A_{kj} should also be captured. In other words, these two equations are coupled and to study the scalar gradient and develop the Lagrangian model, both quantities must be analyzed.

The velocity gradient tensor equation (2.8) and temperature gradient vector equation (2.11) can be also expressed in terms of their invariant. In case of velocity gradient tensor, the mathematical object that represent this physical quantity, as it has been introduced earlier, is a second-order tensor, A_{ij}. We mathematically use a solenoidal vector field, for representing incompressible fluid velocity field which is the case of this study indeed, in order to satisfy the continuity equation. From the linear algebra, we know that in this case the trace of velocity gradient tensor must be zero, due to the divergence-free nature of the velocity field. Accordingly, the trace of velocity gradient is equal to the trace of its symmetric part, i.e. the strain-rate tensor. The trace of S_{ij} can be also written as the sum of its three real eigenvalues, yielding the following equations for incompressible flow

$$\delta_{ij}A_{ji} = \delta_{ij}(S_{ji} + \Omega_{ji}) = \delta_{ij}S_{ji} = A_{ii} = \lambda_1 + \lambda_2 + \lambda_3 = 0. \tag{2.12}$$

The principal coordinates are characterized by these unequal three real eigenvalues which are orthogonal. The order of these eigenvalues of strain-rate tensor is such that $\lambda_1 > \lambda_2 > \lambda_3$. Then, we can deduce that the first eigenvalue must be positive ($\lambda_1 > 0$), the third one should be negative ($\lambda_3 < 0$), and the second one can either be positive or negative. The physical interpretation of this mathematical conclusion, is that λ_1 indicates the principal directions of maximum fluid extension rate, λ_2 shows the principal directions of the fluid maximum compression rate, and λ_2 is a priori the principal direction that the fluid deformation rate can be extensive or compressing. The intermediate eigenvalue of strain-rate tensor, λ_2 in many turbulent flows is shown to be positive due to the universal properties of micro-scale turbulence [46]. It has been found that in assumed universal behavior of micro-scale turbulence, the vorticity field aligned with the intermediate direction, while tends to misalign with

the compressive direction and remains quite indifferent to the extensive direction [47].

Meanwhile, the antisymmetric part of velocity gradient tensor, the rotation-rate tensor determines the magnitude and direction of the rotation-rate of a fluid parcel. Meneveau showed in [42] that for a three-dimensional incompressible fluid velocity field, a total five invariant are required for fully characterization of the velocity gradient tensor, i.e. a traceless second-order tensor with eight independent elements. These five intrinsic, orientation-invariant scalar are needed to specify the orientation of a frame in a three-dimensional space and can be two independent eigenvalues of strain-rate tensor and three vorticity components in the strain-rate tensor eigenframe or any appropriately defined tensor contractions. Commonly, the following five scalar invariats are considered as in [42]

$$\begin{aligned} Q &= -\frac{1}{2}A_{ik}A_{ki} = \frac{1}{4}\omega_i\omega_i - \frac{1}{2}S_{ij}S_{ji}, \\ R &= -\frac{1}{3}A_{ij}A_{jk}A_{ki} = -\frac{1}{3}S_{ij}S_{jk}S_{ki} - \frac{1}{4}\omega_i S_{ij}\omega_j, \\ Q_S &= -\frac{1}{2}S_{ij}S_{ji}, \\ R_S &= -\frac{1}{3}S_{ij}S_{jk}S_{ki}, \\ V^2 &= S_{ik}S_{ij}\omega_j\omega_k. \end{aligned} \tag{2.13}$$

However, for velocity gradient tensor, in most cases, the three principal scalar invariants are used.

$$\begin{aligned} I_1 &= \mathrm{tr}(\boldsymbol{A}) = \lambda_1 + \lambda_2 + \lambda_3, \\ I_2 &= \frac{1}{2}[(\mathrm{tr}(\boldsymbol{A}))^2 - (\mathrm{tr}(\boldsymbol{A}^2)] = \lambda_1\lambda_2 + \lambda_1\lambda_3 + \lambda_2\lambda_3, \\ I_3 &= \frac{1}{6}(\mathrm{tr}(\boldsymbol{A}))^3 - \frac{1}{2}[\mathrm{tr}(\boldsymbol{A})(\mathrm{tr}(\boldsymbol{A}^2)] + \frac{1}{3}(\mathrm{tr}(\boldsymbol{A}^3) = \det(\boldsymbol{A}) = \lambda_1\lambda_2\lambda_3. \end{aligned} \tag{2.14}$$

Due to the incompressibility ($\mathrm{tr}(\boldsymbol{A}) = 0$), the first principal invariant is zero, the second and third principal invariants of the characteristic equation of velocity gradient tensor, in terms of four different invariants can be used as it is shown respectively as Q and R in the equation (2.13). Q is an indication of balance between the enstrophy and strain-rate tensor magnitude, while R shows the balance between the dissipation rate production (strain-rate self-amplification) and enstrophy production (vortex

stretching/compressing). Note that a point in the commonly used so-called QR space can reveal the encoded information about the dynamics of the velocity gradient tensor [43]. On the other hand, for the temperature gradient vector, from a mathematical standpoint, we know that there only exists one invariant for a vector, which is its magnitude. Therefore, the magnitude of temperature gradient vector, $||\boldsymbol{G}||^2$ is consider the scalar invariant to study the dynamics of the temperature gradient vector. In order to further our knowledge of the behavior of temperature gradient tensor in turbulent flows, it is necessary to investigate the evolution of an enstrophy-like quantity, which can be interpreted as the temperature dissipation rate. It will be shown and discussed in the next chapter, how temperature variance is generated at large-scale by the mean scalar gradient, and how it is dissipated by the temperature gradient vector variance at small-scale. Because mean velocity and scalar have a minimal effect on the production of temperature variance dissipation which is proportional to the temperature gradient vector variance [47]. In a generic form, the transport equation for the magnitude (squared) of the fluid velocity gradient $||\boldsymbol{G}||^2$ can be derived by multiplying the equation (2.11) by $\boldsymbol{G}$ resulting in

$$\frac{\partial(G_iG_i/2)}{\partial t}+u_j\frac{\partial(G_iG_i/2)}{\partial x_j}=-G_iS_{ij}G_j+\kappa\frac{\partial^2(G_iG_i/2)}{\partial x_j\partial x_j}-\kappa(\frac{\partial G_i}{\partial x_j}\frac{\partial G_i}{\partial x_j}). \quad (2.15)$$

Equation (2.15) is very similar to the enstrophy equation and the term $-G_iS_{ij}G_j$ is playing the same role as vortex stretching term in the ensrophy equation. Thus, the alignment of the temperature gradient vector with the eigenframe of the strain-rate tensor determines the production or destruction of the $(G_iG_i/2)$. Paul et al. in [47] have shown that this term contribute the most in the production of the temperature gradient vector magnitude (or variance in turbulent flow) [47]. Similar to the enstrophy, we can express the temperature gradient vector in terms of strain-rate tensor eigenvector basis. Eigencontribution to temperature gradient production is given by

$$-G_iS_{ij}G_j=-||\boldsymbol{G}||^2\lambda_k\cos\,(\boldsymbol{G},\boldsymbol{e}_k), \quad (2.16)$$

where $\boldsymbol{e}_k$ denote the $k-th$ principal eigenvector of the strain-rate tensor $\boldsymbol{S}$, indicating the direction along which the strain is aligned. λ_k denote the eigenvalues of strain-rate tensor $\boldsymbol{S}$ associated with the $k-th$ principal eigenvector. $\cos\,(\boldsymbol{G},\boldsymbol{e}_k)$ represents the cosine of the angle between the temperature gradient $\boldsymbol{G}$ and the $k-th$ principal eigenvector $\boldsymbol{e}_k$. In turbulent flows, $-G_iS_{ij}G_j>0$ is considered as a universal behavior

of small-scale passive scalar turbulence. Similarly, we also have $\lambda_2 > 0$ on average, in many turbulent regimes. It has been observed that fluctuating temperature gradient field, G_i' aligns with λ_3, i.e. the compressive principal strain, while it is normal to the intermediate λ_2. It also aligns with the λ_1, the extensive principal strain in 45°. As reported and confirmed in many studies, the production of $\langle G_i G_i \rangle$ occurs due to the λ_3. Further discussion and details as regards the stretching/tilting of the temperature gradient vector and its alignment with eigenvectors of the strain-rate tensor can be found in [47].

2.2.2 Fluid field equations in turbulent flow

Many natural and industrial flow regimes are turbulent and unlike the laminar flows, fluid motion is chaotic and the fluid velocity exhibits random fluctuations at each point in the flow domain. This means that the analytical solution does not exist and statistical analysis is required to understand and gain insights into the random dynamical nature of such a flow regime. In turbulent flows, fluid properties are usually transported and mixed more efficiently, however; kinetic energy is dissipated at small-scale through the turbulence cascade of turbulent kinetic energy. Turbulence is a stochastic, unsteady, random, irreversible and disordered phenomenon, which changes their proprieties over time. The randomness makes turbulence more complex than the laminar flows in the same flow configuration, and calls for more complex statistical description. In addition, in turbulent flows experimental analysis, repeatability cannot be achieved like the laminar regime due to the high sensitivity of the flow to the initial conditions. Consequently, the only assessment of the turbulent flows can be done through the statistics of the flow both obtained from experiments or numerical analysis. In general, turbulent flows consist of eddies of different sizes. Large eddies transfer their energy and break up into smaller eddies, and dissipate energy at small-scale. Accordingly, turbulent motion of fluid is a multi-scale phenomenon taking place over a wide range of spatiotemporal scales, and local fluid field variables undergo significant fluctuations. In this study, that we use an Eulerian-Lagrangian point-particle DNS, we need to solve all the relevant time and spatial scales of the turbulent fields i Eulerian grids. Therefore, a set of appropriate fluid field equations which describe properly the dynamics of the carrier flow should be derived first for the numerical analysis. In the previous section, we derived the fluid velocity and temperature as well as the evolution equations for

their gradient fields under the incomressibility condition of the velocity field and passive advection of the temperature field. In this part, under the same conditions, we employ the common statistical approach to derive the evolution equation of fluid turbulent field variables, such as velocity, temperature and etc. For this reason, the generic Reynolds decomposition is used. The fluid velocity field $\boldsymbol{u}(t,\boldsymbol{x},\omega)$ at time t and position $\boldsymbol{x}$ for a specific realization ω can be decomposed into a mean component and a fluctuating component as follows

$$\boldsymbol{u}(t,\boldsymbol{x},\omega) = \langle \boldsymbol{u} \rangle(t,\boldsymbol{x}) + \boldsymbol{u}'(t,\boldsymbol{x},\omega). \tag{2.17}$$

Here, $\langle \boldsymbol{u} \rangle(t,\boldsymbol{x})$ represents the ensemble average of the velocity field over all possible flow realizations ω, where $\omega \in \Omega$ is a specific realization in the sample space Ω. The sample space Ω contains all possible realizations of the random velocity field of the fluid. The term $\boldsymbol{u}'(t,\boldsymbol{x},\omega)$ denotes the fluctuating component of the velocity field relative to the mean. To connect the ensemble averages with time averages, we invoke the property of ergodicity. Ergodicity allows us to replace ensemble averages with time averages for sufficiently long observation periods, assuming the process is ergodic. For an ergodic process, the ensemble average of any fluid field (e.g., velocity or temperature) is equivalent to its time average. Mathematically, ergodicity is expressed as

$$\langle u_i \rangle(t,\boldsymbol{x}) = \lim_{N\to\infty} \frac{1}{N} \sum_{n=1}^{N} {u_i}^n(t,\boldsymbol{x}) = \lim_{\tau\to\infty} \frac{1}{\tau} \int_0^{\tau} u_i(t,\boldsymbol{x},\omega)\mathrm{d}t = \overline{u_i}(t,\boldsymbol{x}), \tag{2.18}$$

where N is the total number of realizations of the fluid in the sample space Ω, and τ is the duration of the sampling interval. Both N and τ are assumed to be sufficiently large. This means that the time average $\overline{u_i}(t,\boldsymbol{x})$ over a single realization is representative of the ensemble average $\langle u_i \rangle(t,\boldsymbol{x})$ over many realizations. This assumption is common in turbulence and statistical mechanics when dealing with large, complex systems. The ergodic property states that for ergodic systems, the time average of the quantity of interest is equal to the ensemble average of that quantity. To compute the average of any quantity in a turbulent flow, we must know the probability density function (pdf) of each event. Since turbulence is a stochastic process, the pdf of the velocity field varies with time, reflecting the random nature of the flow. The velocity field in a turbulent regime is therefore a random field, capable of taking on a range of values during different realizations. The

underlying stochastic process governing these random fluctuations is described by the Navier-Stokes equations. Note that even if the Navier-Stokes equations per se are deterministic, their solutions can exhibit chaotic behavior, leading to the stochastic nature of the velocity field in turbulent flow regimes. If the pdf of the velocity field remains constant over time, we are able to compute the mean velocity. However, in general the pdf can evolve over time making the analysis of turbulent flows more complex, for instance in statistically unsteady flows. In some cases, the pdf of velocity can change over time at a given point in space. Nonetheless, in a generic way, the ensemble average of the velocity field $\boldsymbol{u}(t,\boldsymbol{x},\omega)$ is given by

$$\langle \boldsymbol{u} \rangle (t,\boldsymbol{x}) = \int \mathrm{d}\omega f(\omega) \boldsymbol{u}(t,\boldsymbol{x},\omega), \tag{2.19}$$

where $\boldsymbol{u}(t,\boldsymbol{x},\omega)$ represents the velocity field for a particular realization ω. $f(\omega)$ is pdf for a given realization ω in the sample space Ω. The integral is taken over all possible realizations ω, weighted by their pdf. This formulation allows us to compute the expected value (ensemble average) of the velocity field, considering the stochastic nature of turbulence. The pdf $f(\omega)$ is central to the statistical description of turbulence, and understanding its evolution over time is key to analyzing turbulent flows. if the pdf is assumed to be time-independent, the statistical analysis is simplified and it allows for the derivation of governing equations for a statistically steady turbulent flow regime whose pdf at each point remains constant with time. If the pdf evolves in time, other pdf-based approaches, like Direct Simulation Monte Carlo (DSMC) may be needed to tackle the problem. Since we need the pdf to take the ensemble average of random velocity field. Employing the typical kinetic method which is used in statistical physics, we can define the pdf of the velocity field $f(t,\boldsymbol{u})$ at time t and phase space point $\overline{\boldsymbol{u}}$ as

$$f(t,\overline{\boldsymbol{u}}) = \langle \delta[\overline{\boldsymbol{u}} - \boldsymbol{u}(t,\boldsymbol{x},\omega)] \rangle = \int \mathrm{d}\omega f(\omega) \delta[\overline{\boldsymbol{u}} - \boldsymbol{u}(t,\boldsymbol{x},\omega)], \tag{2.20}$$

where $\boldsymbol{u}(t,\boldsymbol{x},\omega)$ is the velocity field for a particular realization ω. $\delta(\cdot)$ is the Dirac delta function, which ensures that the pdf $f(t,\boldsymbol{u})$ is centered around the value $\boldsymbol{u}(t,\boldsymbol{x},\omega)$ for each realization. By using this approach time evolution equation for pdf can be obtained as

$$\frac{\partial f(t,\overline{\boldsymbol{u}})}{\partial t} = \frac{\langle \delta[\overline{\boldsymbol{u}} - \boldsymbol{u}(t,\boldsymbol{x},\omega)] \rangle}{\partial t}. \tag{2.21}$$

This equation expresses how the pdf evolves over time, reflecting the stochastic nature of the turbulent flow. In practice, this can lead to more complex equations like the Fokker-Planck equation, which governs the evolution of the pdf in turbulent systems. Fokker-Planck equation, can describe how pdf evolves over time under the influence of drift and diffusion terms. The DSMC can solve the equation numerically. However, DSMC may not be the most common method for turbulence analysis in fluid dynamics, especially in fully developed turbulence where the flow is generally dense and not rarefied. Instead, DSMC is more relevant for kinetic theory of gases where rarefaction effects are significant. For turbulent flows where the pdf evolves over time, alternative methods such as Large Eddy Simulation (LES) or Direct Numerical Simulation (DNS) are often employed. These methods handle the complexity of turbulence by resolving different scales or using models to approximate unresolved scales. The reason is that Kinetic method used in statistical physics often involves averaging over less complex interactions and spatial arrangements, making it easier to achieve a meaningful description of the system's macroscopic properties from the system's microscopic states. On the contrary, turbulence deals with a wide range of spatial scales, from large eddies to small, dissipative structures. Therefore, averaging over these scales, may not be able to capture the essential physics at larger scales without losing important details of finer-scales. Moreover, the nonlinear interactions between different scales in turbulence complicate the coarse-graining process. These interactions can lead to complex dependencies that are difficult to capture with simple ensemble averaging techniques. Moreover, the turbulent velocity at each point in space is influenced by other spatial points, leading to non-local interactions. For instance, the spatial correlation of fluid turbulent velocity field $\boldsymbol{u}(t,\boldsymbol{x})$ is given by

$$R_u(\boldsymbol{x},\boldsymbol{x}+\boldsymbol{r}) = \langle \boldsymbol{u}(t,\boldsymbol{x}) \cdot \boldsymbol{u}(t,\boldsymbol{x}+\boldsymbol{r}) \rangle, \tag{2.22}$$

where $\boldsymbol{x}$ and $\boldsymbol{x}+\boldsymbol{r}$ are spatial points separated by a separation vector $\boldsymbol{r}$. This correlation function describes how the turbulent velocity at one point in space is correlated with the velocity at another point separated by $\boldsymbol{r}$. The temporal correlation function for the velocity field is also given by

$$R_u(\tau) = \langle \boldsymbol{u}(t,\boldsymbol{x}) \cdot \boldsymbol{u}(t+\tau,\boldsymbol{x}) \rangle, \tag{2.23}$$

where τ is the time difference. This temporal correlation function describes how the turbulent velocity at a given point in space is correlated with the velocity at the same spatial point but at a different time. In addition, to fully understand the turbulent velocity field, one would need to track the time evolution of the flow field at all points in space, which is often impractical. The degrees of freedom in turbulent flow are vast, as turbulence involves a wide range of interacting scales and complex patterns. The high dimensionality and complexity of the turbulent field make it challenging to use the same kinetic method used in statistical physics or in studying other stochastic processes. In the simplest case, which velocity field is modeled as homogeneous and isotropic field, spatial correlation becomes a function of separation vector due to the homogeneity $R_u(\boldsymbol{x},\boldsymbol{x}+\boldsymbol{r}) = R_u(\boldsymbol{r})$ and finally a function of the magnitude of separation vector not on its direction due to the isotropy ($R_u(\boldsymbol{x},\boldsymbol{x}+\boldsymbol{r}) = R_u(||\boldsymbol{r}||)$). This means that the correlation between velocities at two points in space depends only on their relative separation, not their absolute location in homogeneous flows. If the pdf is time-independent and the flow is statistically stationary, the flow statistics and pdf of the velocity remain constant in time. Thus, we can introduce the mean and fluctuating velocity fields as

$$\langle \boldsymbol{u} \rangle(t,\boldsymbol{x}) = \int \mathrm{d}\omega f(\omega)\boldsymbol{u}(t,\boldsymbol{x},\omega), \tag{2.24}$$

$$\langle \boldsymbol{u}'(t,\boldsymbol{x},\omega) \rangle = \int \mathrm{d}\omega f(\omega)\Big[\boldsymbol{u}(t,\boldsymbol{x},\omega) - \langle \boldsymbol{u} \rangle(t,\boldsymbol{x})\Big] = \int \mathrm{d}\omega f(\omega)\boldsymbol{u}'(t,\boldsymbol{x},\omega) = 0, \tag{2.25}$$

which leads to the Reynolds decomposition in a generic form for the fluid velocity field

$$\boldsymbol{u}(t,\boldsymbol{x}) = \langle \boldsymbol{u} \rangle(t,\boldsymbol{x}) + \boldsymbol{u}'(t,\boldsymbol{x}). \tag{2.26}$$

Note that in equation (2.26) the fluctuating part $\boldsymbol{u}'(t,\boldsymbol{x})$ represents the deviation from the mean and inherently depends on the specific realization ω. In this case, the decomposition is independent of the specific details of the pdf of the realizations ω. In this study, we use DNS to solve all spatiotemporal scales of the fluid turbulent fields, the Reynolds decomposition, i.e. equation (2.26) is utilized to derive the fluid turbulent fields. It should be noted that the properties of the Reynolds decomposition impose no effect on averaging due to differentiation, integration, constant multiplication, addition and subtraction. Nevertheless, multiplication has effects due

to non-linearity character in the governing equations. Product of two fluctuating variables is usually non-zero because of the existing correlation they are statistically dependent variable unless the correlation between them goes zero. Now we can proceed to derive the fluid field equations in a turbulent flow regime. At first, the equations are presented for a generic flow condition, in which an incompressible velocity field advects a passive scalar along with laden particles. It is assumed that a source term in the temperature equation exists which represents the particle thermal feedback. This term, $C_T(t,\boldsymbol{x})$, will be defined properly in the next section 2.3. At the end of the derivation of the relevant equations, the homogeneity and isotropic conditions of the velocity field as well as the conditions of the temperature field will be imposed to derive the equations under the assumptions for this study. By using Reynolds decomposition for fluid velocity and temperature fields we can write the fluid field equations in two separate parts, mean flow field and fluctuating field. The fluid decomposed fields are denoted by

$$\begin{aligned} u_i &= \langle u_i \rangle + u_i', \\ p &= \langle p \rangle + p', \\ T &= \langle T \rangle + T', \\ C_T &= \langle C_T \rangle + C_T', \\ A_{ij} &= \langle A_{ij} \rangle + A_{ij}', \\ G_j &= \langle G_j \rangle + G_j', \end{aligned} \tag{2.27}$$

where the operator $\langle \cdot \rangle$ stands for ensemble averaging, over all possible realizations of fluid fields in a turbulent flow motion. Ensemble averaging enables us to calculate not just the mean but also higher-order statistical moments of various quantities in turbulent flows. However, by their very definition, the first moments of the fluctuating components are zero. This means that the average of these fluctuations is always zero, so we have $\langle u_i' \rangle = \langle T' \rangle = \langle C_T' \rangle = \langle A_{ij}' \rangle = \langle G_j' \rangle = 0$.

Beyond the mean velocity field, another crucial measure is the root mean square (rms) of the velocity fluctuations, which serves as an indicator of turbulence intensity. This rms value reflects how much the velocity fluctuates around the mean velocity and is given by $u_{rms} = \sqrt{\langle u_i'^2 \rangle}$, where u_i' represents the $i-th$ component of the fluctuating velocity. In isotropic flows, the rms value simplifies to $u_{rms} = \sqrt{\langle u_1'^2 \rangle}$, assuming that the velocity fluctuations in the x_1 direction are the same as those

in the other directions (x_2 and x_3). For homogeneous and isotropic turbulence, the turbulent kinetic energy E_k is given by $E_k = (3/2)u_{rms}^2$. In our case, the flow regime is unbounded, and the velocity field is statistically homogeneous in all directions. This means that the spatial gradients of the mean statistical quantities are zero in every direction, as the flow properties remain unchanged under translations of the coordinate system. Additionally, due to isotropy, the statistical moments are invariant under translation, rotation, and reflection, resulting in equal values across all directions: $\langle {u_1}'^2 \rangle = \langle {u_2}'^2 \rangle = \langle {u_3}'^2 \rangle$. Consequently, in the absence of any preferred direction or bulk motion, the mean velocity field is zero in all directions: $\langle u_1 \rangle = \langle u_2 \rangle = \langle u_3 \rangle = 0$. The flow is also shear-free, which implies that the cross-terms of the Reynolds stress tensor vanish, i.e., $\langle u_i' u_j' \rangle = 0$ for $i \neq j$. This condition reflects the absence of shear in the flow, indicating that the velocity fluctuations in different directions are uncorrelated on average, leading to no momentum transfer between different coordinate directions. The shear-free condition typically arises because of the absence of velocity gradients, which can result in the cross-terms being zero or negligible. Moreover, under the assumption of homogeneity, the spatial gradients of the Reynolds stresses are also zero, such that $\partial_j \langle u_i' u_j' \rangle = 0$ for $i \neq j$.

Note that isotropy implies homogeneity. Under the conditions of homogeneity and isotropy, the behavior of the flow is assumed to be universal at small scales, as described by Kolmogorov's hypothesis (K41 theory). According to this hypothesis, small-scale turbulent eddies have a universal form determined solely by the mean dissipation rate of turbulent kinetic energy, ε, and the kinematic viscosity, ν. Through dimensional analysis, this leads to the Kolmogorov time scale $\tau_\eta = (\nu/\varepsilon)^{1/2}$ and the Kolmogorov length scale $\eta = (\nu^3/\varepsilon)^{1/4}$. In this range, the relevant dimensionless number is the Taylor microscale Reynolds number, which represents the ratio between the timescales of large and small eddies. It is given by $\mathrm{Re}_\lambda = \tau/\tau_\eta$, where $\tau = \ell/u_{rms} = u_{rms}^2/\varepsilon$ is the large-eddy turnover time, and $\ell = E_k^{-3/2}/\varepsilon$ is the integral length scale of the flow. However, the Taylor microscale Reynolds number can also be expressed in terms of the Taylor length scale λ and the turbulent kinetic energy E_k

$$\mathrm{Re}_\lambda = \frac{u_{rms}\lambda}{\nu} = \frac{2E_k}{\sqrt{5/3\nu\varepsilon}}. \tag{2.28}$$

In our case, the fluid temperature field exhibits homogeneity in the x_1 and x_2 directions. This implies that the partial derivatives of the mean temperature and the

heat fluxes with respect to these directions are zero $\partial_1\langle u_1'T'\rangle = \partial_2\langle u_2'T'\rangle = 0$ and $\partial_1\langle T\rangle = \partial_2\langle T\rangle = 0$. The next chapter will discuss this in greater detail. The mean temperature gradient is imposed along the x_3 direction, which is the direction of inhomogeneity in our flow domain. Due to the homogeneity in the x_1 and x_2 directions, the average heat fluxes in these directions are also zero ($\langle u_1'T'\rangle = \langle u_2'T'\rangle = 0$). However, in the x x_3 direction, where the temperature field is inhomogeneous, the turbulent heat flux component is non-zero ($\partial_3\langle u_3'T'\rangle \neq 0$). Additionally, the gradient of the heat flux component in the x_3 direction is also non-zero, as indicated by ($\partial_3\langle u_3'T'\rangle \neq 0$). This non-zero gradient is evident in both the fluctuating and mean temperature field equations, with ($\partial_3\langle T\rangle \neq 0$) reflecting the imposed mean scalar gradient in the x_3 direction.

To derive the governing equations for turbulent flow, we first introduce the decomposed field variables into the equations presented in section 2.2.1. We begin with the momentum equation, where we replace the velocity field with its mean and fluctuating components. For this derivation, we assume that the external forcing term is a zero-mean linear deterministic force, which will be defined in chapter 3.3

$$\frac{\partial(\langle u_i\rangle + u_i')}{\partial t} + (\langle u_i\rangle + u_i')\frac{\partial(\langle u_i\rangle + u_i')}{\partial x_j} = -\frac{1}{\rho_0}\frac{(\langle p\rangle + p')}{\partial x_i} + \nu\frac{\partial(\langle u_i\rangle + u_i')}{\partial x_j \partial x_j} + f_{u,i}'. \tag{2.29}$$

By averaging both sides of equation (2.29), we can derive the equation for the mean velocity

$$\frac{\partial\langle u_i\rangle}{\partial t} + \langle u_j\rangle\frac{\partial\langle u_i\rangle}{\partial x_j} = -\frac{1}{\rho_0}\frac{\partial\langle p\rangle}{\partial x_i} + \nu\frac{\partial^2\langle u_i\rangle}{\partial x_j\partial x_j} - \frac{\partial\langle u_i'u_j'\rangle}{\partial x_j}. \tag{2.30}$$

By subtracting equation (2.30) from equation (2.29), we obtain the fluctuating velocity field as

$$\frac{\partial u_i'}{\partial t} + \langle u_j\rangle\frac{\partial u_i'}{\partial x_j} = -\frac{1}{\rho_0}\frac{\partial p'}{\partial x_i} + \nu\frac{\partial^2 u_i'}{\partial x_j\partial x_j} - u_j'\frac{\partial\langle u_i\rangle}{\partial x_j} - u_j'\frac{\partial u_i'}{\partial x_j} + f_{u,i}'. \tag{2.31}$$

By applying the assumptions of homogeneity and isotropy to the velocity field, the mean flow field equation (2.30) can be disregarded, and the mean fluctuating

equation (2.31) simplifies to the following form

$$\frac{\partial u_i'}{\partial t} + u_j' \frac{\partial u_i'}{\partial x_j} = -\frac{1}{\rho_0}\frac{\partial p'}{\partial x_i} + \nu \frac{\partial^2 u_i'}{\partial x_j \partial x_j} + f_{u,i}'. \tag{2.32}$$

The equation (2.32) is the one we solve in our study using DNS. Additionally, the equation (2.8) which describes the evolution of the velocity gradient tensor A_{ij}, can be decomposed as

$$\frac{\partial(\langle A_{ij}\rangle + A_{ij}')}{\partial t} + (\langle u_k\rangle + u_k')\frac{\partial(\langle A_{ij}\rangle + A_{ij}')}{\partial x_k} = -(\langle A_{ik}\rangle + A_{ik}')(\langle A_{kj}\rangle + A_{kj}') \\ -\frac{1}{\rho_0}\frac{\partial^2(\langle p\rangle + p'))}{\partial x_i \partial x_j} + \nu \frac{\partial^2(\langle A_{ij}\rangle + A_{ij}')}{\partial x_k \partial x_k} + F_{u,ij}'. \tag{2.33}$$

We can take average from both sides of the equation (2.33) to derive the mean velocity gradient tensor transport equation as

$$\frac{\partial \langle A_{ij}\rangle}{\partial t} + \langle u_k\rangle \frac{\partial \langle A_{ij}\rangle}{\partial x_k} = -\langle A_{ik}\rangle\langle A_{kj}\rangle - \langle A_{ik}' A_{kj}'\rangle - \frac{1}{\rho_0}\frac{\partial^2\langle p\rangle}{\partial x_i \partial x_j} + \nu \frac{\partial^2 \langle A_{ij}\rangle}{\partial x_k \partial x_k}. \tag{2.34}$$

The equation (2.34) gives the transport of the mean velocity gradient tensor in an incompressible turbulent flow. The equations shows how the mean field is advected and diffused by turbulence. Mean pressure Hessian quantifies the non-local effects on the evolution through the mean pressure gradient interaction. It shows how the spatial variations in the mean pressure field affect the mean velocity gradients Diffusion term reveals how the mean velocity gradients are smoothed out due to the effects of viscosity. Self-amplification terms, also captures the production or destruction due to the interaction of mean and fluctuating components of velocity gradient tensor. Term $-\langle A_{ik}' A_{kj}'\rangle$ explains how fluctuations in the velocity field contribute to the changes in the mean velocity gradient tensor. This term reflects the interaction between the fluctuating velocity gradients and the mean velocity gradients, indicating how turbulence modifies the mean field. $-\langle A_{ik}\rangle\langle A_{kj}\rangle$ reflects the stretching and tilting of the mean velocity gradient tensor due to interactions with itself. It shows how the mean velocity gradients affect each other through the velocity gradient tensor. In a homogeneous and isotropic turbulence domain with periodic boundary conditions, the mean flow quantities such as $\langle u_i\rangle$ and $\langle A_{ij}\rangle$ are zero. Consequently, there is no mean pressure gradient or external forces, which results in $\langle f_{u,i}\rangle = \langle p\rangle = 0$. The mean velocity gradient tensor equation, under these conditions, simplifies to show

that the mean terms balance out to zero. However, the fluctuating velocity gradient tensor A'_{ij} introduces non-zero correlations, such as $\langle A'_{ik}A'_{kj}\rangle$, which are crucial for capturing the turbulent dynamics and dissipation. These fluctuating terms are non-zero and represent the turbulent interactions and energy dissipation mechanisms that are not directly accounted for by the mean equations. Therefore, while the mean gradient terms balance to zero, the fluctuating field correlations like $\langle A'_{ik}A'_{kj}\rangle$ are essential for understanding the full turbulence behavior and energy dissipation.

Accordingly, we need to derive the fluctuating velocity gradient field. For this reason, we subtract the mean equation (2.34) from the full equation (2.33) to obtain the fluctuation field.

$$\frac{\partial A'_{ij}}{\partial t} + u'_k\frac{\partial A'_{ij}}{\partial x_k} = -\langle A_{ik}\rangle A'_{kj} - A'_{ik}\langle A_{kj}\rangle - \langle u_k\rangle\frac{\partial\langle A_{ij}\rangle}{\partial x_k} - \langle u_k\rangle\frac{\partial A'_{ij}}{\partial x_k} - u'_k\frac{\partial\langle A_{ij}\rangle}{\partial x_k}$$
$$-\frac{1}{\rho_0}\frac{\partial^2 p'}{\partial x_i\partial x_j} + \nu\frac{\partial^2 A'_{ij}}{\partial x_k\partial x_k} + F'_{u,ij}. \tag{2.35}$$

In the equation (2.35) terms $-\langle A_{ik}\rangle A'_{kj}$ and $-A'_{ik}\langle A_{kj}\rangle$ describe the interaction between the fluctuating velocity gradients and the mean velocity gradients. They show how the mean velocity gradients stretch or deform the fluctuations, and vice versa. The pressure Hessian term represents the contribution from the fluctuating pressure field to the evolution of the fluctuating velocity gradients. It accounts for how fluctuations in pressure contribute to changes in the velocity gradient tensor. In our case, where $\langle u_k\rangle = \langle A_{ij}\rangle = 0$ the equation (2.35) simplifies to

$$\frac{\partial A'_{ij}}{\partial t} + u'_k\frac{\partial A'_{ij}}{\partial x_k} = -\frac{1}{\rho_0}\frac{\partial^2 p'}{\partial x_i\partial x_j} + \nu\frac{\partial^2 A'_{ij}}{\partial x_k\partial x_k} + F'_{u,ij}. \tag{2.36}$$

Now we can use the equation (2.36) to derive its higher order statistical moments or its correlations with other fluctuating fields, if needed. Note that this equation which specified for homogeneous and isotropic turbulence with periodic boundary conditions. In this case, diffusion will generally act to damp and smooth the fluctuating velocity gradient tensor, the pressure gradient term and external forcing can have more complex effects depending on their specific nature. In particular, the pressure gradient term generally acts to modify the distribution and magnitude of the fluctuating velocity gradient tensor. It does not necessarily smooth or damp the

fluctuations in the same way as viscosity. Instead, it can create or modify structures in the turbulent field by influencing how pressure variations affect the velocity gradients. The pressure gradient can either enhance or suppress fluctuations depending on the nature of the pressure field and its spatial variation. On the other hand, Viscous diffusion smooths and damps the fluctuations. It acts to reduce the magnitude of the fluctuations by spreading them out over a larger area, leading to a decrease in the intensity of the velocity gradient tensor fluctuations. This term counteracts the accumulation of high-gradient regions and helps to dissipate the turbulent fluctuations over time. By applying the same procedure to the fluid temperature field, the temperature can be expressed in terms of mean and fluctuating components as follows

$$\frac{\partial\langle T\rangle}{\partial t}+\frac{\partial T'}{\partial t}+\frac{\partial[(\langle u_j\rangle+u_j')(\langle T\rangle+T')]}{\partial x_j}=\kappa\frac{\partial^2(\langle T\rangle+T')}{\partial x_j\partial x_j}+\frac{1}{\rho_0 c_{p0}}[\langle C_T\rangle+C_T'].\tag{2.37}$$

To derive the mean temperature field equation, we need to average both sides of equation (2.37). After averaging, the mean temperature field is obtained as

$$\frac{\partial\langle T\rangle}{\partial t}+\frac{\partial(\langle u_j\rangle\langle T\rangle)}{\partial x_j}=\kappa\frac{\partial^2\langle T\rangle}{\partial x_j\partial x_j}-\frac{\partial\langle u_j'T'\rangle}{\partial x_j}+\frac{1}{\rho_0 c_{p0}}\langle C_T\rangle.\tag{2.38}$$

To derive the time evolution equation for the turbulent fluid temperature field, we can subtract the mean temperature equation (2.38) from equation (2.32). After performing this subtraction, we obtain the fluctuating temperature field as follows

$$\frac{\partial T'}{\partial t}+\frac{\partial(u_j'T')}{\partial x_j}=\kappa\frac{\partial^2 T'}{\partial x_j\partial x_j}-\frac{\partial(\langle u_j\rangle T')}{\partial x_j}-\frac{\partial(u_j'\langle T\rangle)}{\partial x_j}+\frac{1}{\rho_0 c_{p0}}C_T'.\tag{2.39}$$

We can apply the assumptions of statistical homogeneity, isotropy, and incompressibility of the velocity field to both the mean and fluctuating temperature fields to derive the simplified equations for our flow configuration as follows

$$\frac{\partial\langle T\rangle}{\partial t}=\kappa\frac{\partial^2\langle T\rangle}{\partial x_j\partial x_j}-\frac{\partial\langle u_j'T'\rangle}{\partial x_j}+\frac{1}{\rho_0 c_{p0}}\langle C_T\rangle,\tag{2.40}$$

$$\frac{\partial T'}{\partial t}+u_j'\frac{\partial T'}{\partial x_j}=\kappa\frac{\partial^2 T'}{\partial x_j\partial x_j}-u_j'\frac{\partial\langle T\rangle}{\partial x_j}+\frac{1}{\rho_0 c_{p0}}C_T'.\tag{2.41}$$

Note that $\langle u_j' T \rangle = \partial_j \langle T \rangle = 0$ for $j = 1,2$ in our flow regime. To derive the evolution equation for the fluid temperature variance, we need to multiply both sides of equation (2.39) by T'. Using the identity

$$T' \cdot \nabla^2 T' = \Big[\nabla^2 (T'^2/2) - (\nabla T' \nabla T') \Big],$$

we obtain

$$\frac{\partial (T'^2/2)}{\partial t} + \frac{\partial (u_j' T'^2/2)}{\partial x_j} = \kappa \Big[\frac{\partial^2 (T'^2/2)}{\partial x_j \partial x_j} - (\frac{\partial T'}{\partial x_j} \frac{\partial T'}{\partial x_j}) \Big] - \frac{\partial [\langle u_j \rangle (T'^2/2)]}{\partial x_j}$$
$$- T' \frac{\partial (u_j' \langle T \rangle)}{\partial x_j} + \frac{1}{\rho_0 c_{p0}} (T' C_T'). \tag{2.42}$$

Averaging equation (2.42) yields a general transport equation for the temperature variance, given by

$$\frac{\partial \langle T'^2/2 \rangle}{\partial t} + \frac{\partial \langle u_j' T'^2/2 \rangle}{\partial x_j} = \kappa \Big[\frac{\partial^2 \langle T'^2/2 \rangle}{\partial x_j \partial x_j} - \langle \frac{\partial T'}{\partial x_j} \frac{\partial T'}{\partial x_j} \rangle \Big] - \frac{\partial (\langle u_j \rangle \langle T'^2/2 \rangle)}{\partial x_j}$$
$$- \langle u_j' T' \rangle \frac{\partial \langle T \rangle}{\partial x_j} + \frac{1}{\rho_0 c_{p0}} \langle T' C_T' \rangle. \tag{2.43}$$

The equation (2.43) shows the transport equation of the fluid temperature variance in a turbulent flow. Temperature variance quantifies the magnitude of deviations of the instantaneous temperature from its mean value. A higher variance indicates larger fluctuations or deviations from the average temperature. Additionally, temperature variance reflects the intensity of mixing and fluctuations within the fluid. High variance typically corresponds to strong turbulent mixing and thermal activity. In the turbulent mixing layer, high temperature variance can indicate zones where thermal gradients are strong and mixing is occurring. As any turbulent transport equation, it indicates how the temperature variance is advected by turbulence and is diffused by thermal diffusion process. Moreover, we can see the dissipation of the variance as well as the production terms, due to the mean temperature gradient and turbulent heat flux interaction. The effect of particle thermal feedback can also be seed in $\langle T' C_T' \rangle$. In our flow, which a strong mean gradient in direction x_3 exists, theoretically we expect an increase in temperature variance in this direction. This strong mean temperature gradient can increase the temperature variance through enhanced mixing and stirring. The transport equation for the turbulent heat flux can be derived by

multiplying the fluctuating temperature equation (2.42) by u_i'. Applying the identity

$$\boldsymbol{u'} \cdot \nabla^2 T' = \nabla \cdot \Big[\boldsymbol{u'} \cdot \nabla T' + T' \cdot \nabla \boldsymbol{u'} \Big] - \nabla \boldsymbol{u'} \nabla T',$$

we obtain

$$\begin{aligned} &\frac{\partial (u_i' T')}{\partial t} + \frac{\partial (u_i' u_j' T')}{\partial x_j} = \frac{\partial}{\partial x_j} \Big[\kappa u_i' \frac{\partial T'}{\partial x_j} + \nu T' \frac{\partial u_i'}{\partial x_j} \Big] - (\nu + \kappa) [\frac{\partial u_i'}{\partial x_j} \frac{\partial T'}{\partial x_j}] \\ &- \frac{\partial (u_i' \langle u_j \rangle T')}{\partial x_j} - \frac{\partial (u_i' u_j' \langle T \rangle)}{\partial x_j} + \frac{1}{\rho_0 c_{p0}} (u_i' C_T'). \end{aligned} \tag{2.44}$$

Averaging both sides of the equation (2.44) yields

$$\begin{aligned} &\frac{\partial \langle u_i' T' \rangle}{\partial t} + \frac{\partial \langle u_i' u_j' T' \rangle}{\partial x_j} = \frac{\partial}{\partial x_j} \Big[\kappa \langle u_i' \frac{\partial T'}{\partial x_j} \rangle + \nu \langle T' \frac{\partial u_i'}{\partial x_j} \rangle \Big] - (\nu + \kappa) \langle \frac{\partial u_i'}{\partial x_j} \frac{\partial T'}{\partial x_j} \rangle \\ &- \langle u_j \rangle \frac{\partial \langle u_i' T' \rangle}{\partial x_j} - \langle u_i' u_j' \rangle \frac{\partial \langle T \rangle}{\partial x_j} + \frac{1}{\rho_0 c_{p0}} \langle u_i' C_T' \rangle. \end{aligned} \tag{2.45}$$

Transport equation for turbulent heat flux is derived in equation (2.45). The heat flux can be advected by turbulent flow and diffuses by both thermal and viscous diffusion. Both thermal diffusivity and viscosity can also contribute to the dissipation of turbulent heat flux through the interaction between temperature gradients and velocity gradients. It accounts for how turbulence causes heat flux to decay due to the combined effects of viscosity and thermal diffusion.. The equation indicate the effect of particle thermal feedback and shows how mean temperature gradient can generate heat flux through interaction with turbulence. Another important fluid field of interest for this study is the temperature variance flux. The transport equation for this quantity can be derived similarly to the turbulent heat flux. Specifically, we multiply the temperature variance equation (2.42) by the fluctuating velocity field u_i' and use the identity

$$\boldsymbol{u'} \cdot \nabla^2 (T'^2/2) = \nabla \cdot \Big[\boldsymbol{u'} \cdot \nabla (T'^2/2) + (T'^2/2) \cdot \nabla \boldsymbol{u'} \Big] - \nabla \boldsymbol{u'} \nabla (T'^2/2),$$

resulting in

$$\frac{\partial(u_i'T'^2/2)}{\partial t}+\frac{\partial(u_i'u_j'T'^2/2)}{\partial x_j}=\frac{\partial}{\partial x_j}\Big[\kappa u_i'\frac{\partial(T'^2/2)}{\partial x_j}+\nu(T'^2/2)\frac{\partial u_i'}{\partial x_j}\Big]$$
$$-(\nu+\kappa)\Big[\frac{\partial(T'^2/2)}{\partial x_j}\frac{\partial u_i'}{\partial x_j})\Big]-\kappa\Big[u_i'\frac{\partial T'}{\partial x_j}\frac{\partial T'}{\partial x_j}\Big]-\langle u_j\rangle\frac{\partial[u_i'(T'^2/2)]}{\partial x_j}$$
$$-u_i'u_j'T'\frac{\partial\langle T\rangle}{\partial x_j}+\frac{1}{\rho_0 c_{p0}}(u_i'T'C_T'). \tag{2.46}$$

Averaging all terms over the ensemble yields the transport equation for the temperature variance flux

$$\frac{\partial\langle u_i'T'^2/2\rangle}{\partial t}+\frac{\partial\langle u_i'u_j'T'^2/2\rangle}{\partial x_j}=\frac{\partial}{\partial x_j}\Big[\kappa\langle u_i'\frac{\partial(T'^2/2)}{\partial x_j}\rangle+\nu\langle(T'^2/2)\frac{\partial u_i'}{\partial x_j}\rangle\Big]$$
$$-(\nu+\kappa)\langle\frac{\partial(T'^2/2)}{\partial x_j}\frac{\partial u_i'}{\partial x_j}\rangle-\kappa\langle u_i'\frac{\partial T'}{\partial x_j}\frac{\partial T'}{\partial x_j}\rangle-\langle u_j\rangle\frac{\partial\langle u_i'(T'^2/2)\rangle}{\partial x_j}$$
$$-\langle u_i'u_j'T'\rangle\frac{\partial\langle T\rangle}{\partial x_j}+\frac{1}{\rho_0 c_{p0}}\langle u_i'T'C_T'\rangle. \tag{2.47}$$

The flux of temperature variance is transported by turbulence in space and time according to the transport equation (2.47). This equation describes the complex interplay between turbulence, temperature gradients, and particle thermal feedback mechanisms in determining the behavior of temperature variance in turbulent flows. Similar to the turbulent heat flux and temperature variance, there is a production term due to the mean temperature gradient and its interaction with turbulence. Understanding the behaviour of this quantity can help us to gain insight into the turbulent transport of the variance, especially in the mixing layer where different scales of turbulent are interacting and transporting the thermal energy. Meanwhile, the particle feedback term in the equation indicate how particles can change the flux of the variance by interacting with turbulent heat flux. The assumptions of incompressibility, homogeneity, and isotropy of the fluid velocity field simplify the derived transport equations for temperature variance, heat flux, and variance flux to the following

forms

$$\frac{\partial\langle T'^2/2\rangle}{\partial t}+\frac{\partial\langle u_j'T'^2/2\rangle}{\partial x_j}=\kappa\Big[\frac{\partial^2\langle T'^2/2\rangle}{\partial x_j\partial x_j}-\langle\frac{\partial T'}{\partial x_j}\frac{\partial T'}{\partial x_j}\rangle\Big]-\langle u_j'T'\rangle\frac{\partial\langle T\rangle}{\partial x_j}$$
$$+\frac{1}{\rho_0 c_{p0}}\langle T'C_T'\rangle, \tag{2.48}$$

$$\frac{\partial\langle u_i'T'\rangle}{\partial t}+\frac{\partial\langle u_i'u_j'T'\rangle}{\partial x_j}=\frac{\partial}{\partial x_j}\left[\kappa\langle u_i'\frac{\partial T'}{\partial x_j}\rangle+\nu\langle T'\frac{\partial u_i'}{\partial x_j}\rangle\right]-(\nu+\kappa)\langle\frac{\partial u_i'}{\partial x_j}\frac{\partial T'}{\partial x_j}\rangle$$
$$-\langle u_i'u_j'\rangle\frac{\partial\langle T\rangle}{\partial x_j}+\frac{1}{\rho_0 c_{p0}}\langle u_i'C_T'\rangle, \tag{2.49}$$

$$\frac{\partial\langle u_i'T'^2/2\rangle}{\partial t}+\frac{\partial\langle u_i'u_j'T'^2/2\rangle}{\partial x_j}=\frac{\partial}{\partial x_j}\Big[\kappa\langle u_i'\frac{\partial(T'^2/2)}{\partial x_j}\rangle+\nu\langle(T'^2/2)\frac{\partial u_i'}{\partial x_j}\rangle\Big]$$
$$-(\nu+\kappa)\langle\frac{\partial(T'^2/2)}{\partial x_j}\frac{\partial u_i'}{\partial x_j}\rangle-\kappa\langle u_i'\frac{\partial T'}{\partial x_j}\frac{\partial T'}{\partial x_j}\rangle-\langle u_i'u_j'T'\rangle\frac{\partial\langle T\rangle}{\partial x_j}+\frac{1}{\rho_0 c_{p0}}\langle u_i'T'C_T'\rangle, \tag{2.50}$$

where $\langle u_3'u_j'\rangle=(1/3)\langle u_j'^2\rangle\delta_{3j}$ which is zero for $j\neq 3$ and for $j=3$ is equal to $\langle u_3'^2\rangle$ due to the isotropy. Moreover, we have only turbulent flux in x_3 direction resulting in $\langle u_i'T\rangle=\partial_i\langle T\rangle=0$ for $i=1,2$. The next step involves deriving the evolution equation for the temperature gradient vector in turbulent flows. To accomplish this, we first use the decomposed quantities introduced in (2.27) and express the equation in terms of both the mean and fluctuating fields, similar to the approach taken for other fluid fields. As with the fluid velocity field, we initially disregard the mean component of the velocity gradient tensor ($\langle u_i\rangle=\langle A_{ij}\rangle=0$). We will first derive the generic form of the equations and then apply the assumptions of incompressibility, homogeneity, and isotropy. The temperature gradient vector equation (2.11) after decomposition is as follows

$$\frac{\partial(\langle G_k\rangle+G_k')}{\partial t}+\frac{\partial[(\langle u_j\rangle+u_j')(\langle G_k\rangle+G_k')]}{\partial x_j}=\kappa\frac{\partial^2(\langle G_k\rangle+G_k')}{\partial x_j\partial x_j}-(\langle G_j\rangle+G_j')A_{jk}'$$
$$+\frac{1}{\rho_0 c_{p0}}\frac{\partial(\langle C_T\rangle+C_T')}{\partial x_k}. \tag{2.51}$$

After ensemble averaging of the equation (2.51), the mean temperature gradient transport equation is obtained

$$\frac{\partial \langle G_k \rangle}{\partial t} + \frac{\partial (\langle u_j \rangle \langle G_k \rangle)}{\partial x_j} = \kappa \frac{\partial^2 \langle G_k \rangle}{\partial x_j \partial x_j} - \langle G'_j A'_{jk} \rangle - \frac{\partial \langle u'_j G'_k \rangle}{\partial x_j} + \frac{1}{\rho_0 c_{p0}} \frac{\partial \langle C_T \rangle}{\partial x_k}. \quad (2.52)$$

If we subtract the mean temperature gradient equation (2.52) from the instantaneous temperature gradient equation (2.51) we can have the fluctuating temperature gradient equation such that

$$\begin{aligned} &\frac{\partial G'_k}{\partial t} + \frac{\partial (u'_j G'_k)}{\partial x_j} = \kappa \frac{\partial^2 G'_k}{\partial x_j \partial x_j} - G'_j A'_{jk} - \langle G_j \rangle A'_{jk} \\ &- \frac{\partial (\langle u_j \rangle G'_k)}{\partial x_j} - \frac{\partial (u'_j \langle G_k \rangle)}{\partial x_j} + \frac{1}{\rho_0 c_{p0}} \frac{\partial C'_T}{\partial x_k}. \end{aligned} \quad (2.53)$$

In our homogeneous and isotropic velocity field and applying the incompressibility, the mean and fluctuation equations for temperature gradient vector read

$$\frac{\partial \langle G_k \rangle}{\partial t} = \kappa \frac{\partial^2 \langle G_k \rangle}{\partial x_j \partial x_j} - \langle G'_j A'_{jk} \rangle - \frac{\partial \langle u'_j G'_k \rangle}{\partial x_j} + \frac{1}{\rho_0 c_{p0}} \frac{\partial \langle C_T \rangle}{\partial x_k}, \quad (2.54)$$

$$\frac{\partial G'_k}{\partial t} + u'_j \frac{\partial G'_k}{\partial x_j} = \kappa \frac{\partial^2 G'_k}{\partial x_j \partial x_j} - G'_j A'_{jk} - \langle G_j \rangle A'_{jk} - u'_j \frac{\partial \langle G_k \rangle}{\partial x_j} + \frac{1}{\rho_0 c_{p0}} \frac{\partial C'_T}{\partial x_k}. \quad (2.55)$$

In the mean temperature gradient transport equation ((2.54)), the mean temperature gradient $\langle G_k \rangle$ is advected by turbulence and diffused by thermal diffusivity. The production or destruction term $-\langle G'_j A'_{jk} \rangle$ captures the interaction between the fluid temperature gradient fluctuations and the components of the velocity gradient tensor. This term describes how turbulence influences the mean temperature gradient through these interactions. Depending on the alignment of the temperature gradient with the principal eigenvectors of the strain-rate tensor, this term can either generate or destroy the mean temperature gradient. The velocity gradient tensor stretches and tilts $\langle G_k \rangle$ during the evolution. The divergence of the turbulent flux of the temperature gradient $\partial_j \langle u'_j G'_k \rangle$ accounts for the transport of the temperature gradient by turbulent velocity fluctuations u'_j. The gradient of the thermal feedback term $\left(1\rho_0 c_{p0}\right) \partial_k \langle C_T \rangle$ captures the effect of particle-fluid thermal coupling on the temperature gradient and its transport. Meanwhile, In the fluctuating temperature gradient equation ((2.55)), the evolution of the fluctuating temperature gradient G'_k

is driven by several key processes. The term $u'_j \partial_j G'_k$ represents the advection of temperature gradient fluctuations by the turbulent velocity fluctuations. The diffusion term $\kappa \partial_j^2 G'_k$ accounts for the spreading of these fluctuations due to thermal diffusivity. The interaction terms $-G'_j A'_{jk}$ and $-\langle G_j \rangle A'_{jk}$ describe the influence of the fluctuating and mean velocity gradient tensors on the temperature gradient fluctuations. The first term, $-G'_j A'_{jk}$, reflects the direct interaction between temperature gradient fluctuations and the turbulent velocity field, while $-\langle G_j \rangle A'_{jk}$ represents how the mean temperature gradient influences the evolution of fluctuations. Together, these terms indicate that the velocity field can stretch, rotate, and align the temperature gradient fluctuations, potentially leading to either amplification or suppression of these fluctuations. Additionally, the term $-u'_j \partial_j \langle G_k \rangle$ captures the effect of the turbulent advection of the mean temperature gradient on the fluctuating component, linking the mean and fluctuating fields. Finally, the fluctuating thermal feedback term $\left(1\rho_0 c_{p0}\right) \partial_k C'_T$ describes the effect of particle-fluid thermal coupling on the temperature gradient fluctuations, which is particularly important in the presence of inertial particles. Analyzing equations ((2.54)) and ((2.55)) allows us to study how inertial particles, turbulence, and thermal gradients interact and evolve over time, particularly in the context of a thermal mixing layer. For obtaining temperature gradient variance balance equation , we can multiply the temperature gradient fluctuating equation (2.53) by G'_k, and by using the identity

$$G'_k \partial_j^2 G'_k = \partial^2 (G'_k G'_k/2) - \partial_j G'_k \partial_j G'_k,$$

we have

$$\frac{\partial (G'_k G'_k/2)}{\partial t} + \frac{\partial [u'_j (G'_k G'_k/2)]}{\partial x_j} = \kappa [\frac{\partial^2 (G'_k G'_k/2)}{\partial x_j \partial x_j} - \frac{\partial G'_k}{\partial x_j} \frac{\partial G'_k}{\partial x_j}] - G'_j A'_{jk} G'_k$$
$$- \langle G_j \rangle A'_{jk} G'_k - \frac{\partial [\langle u_j \rangle (G'_k G'_k/2)]}{\partial x_j} - u'_j G'_k \frac{\partial \langle G_k \rangle}{\partial x_j} + \frac{1}{\rho_0 c_{p0}} G'_k \frac{\partial C'_T}{\partial x_k}. \tag{2.56}$$

We can now take ensemble average from both sides of the equations

$$\frac{\partial \langle G'_k G'_k/2 \rangle}{\partial t} + \frac{\partial \langle u'_j (G'_k G'_k/2) \rangle}{\partial x_j} = \kappa [\langle \frac{\partial^2 (G'_k G'_k/2)}{\partial x_j \partial x_j} \rangle - \langle \frac{\partial G'_k}{\partial x_j} \frac{\partial G'_k}{\partial x_j} \rangle] - \langle G'_j A'_{jk} G'_k \rangle$$
$$- \langle G_j \rangle \langle A'_{jk} G'_k \rangle - \frac{\partial [\langle u_j \rangle \langle G'_k G'_k/2 \rangle]}{\partial x_j} - \langle u'_j G'_k \rangle \frac{\partial \langle G_k \rangle}{\partial x_j} + \frac{1}{\rho_0 c_{p0}} \langle G'_k \frac{\partial C'_T}{\partial x_k} \rangle. \tag{2.57}$$

The equation (2.57) describes the transport of the variance of the turbulent temperature gradient. This quantity is crucial because it affects the dissipation of the temperature fluctuation variance, as represented in equation (2.43). Understanding this variance helps identify regions where temperature gradients are high but temperature fluctuations are low, which is important in the study of particle-laden flows, particularly for low-inertia particles that tend to move towards regions of higher $G'_k G'_k/2$ i.e. higher temperature dissipation zones [11]. In two-way thermal coupling regime, the complex interactions between particle thermal feedback and turbulence can be better understood and modeld by the term $(1\rho_0 c_{p0})\langle G'_k \partial_k C'_T \rangle$. This term captures how the thermal feedback from particles is correlated with the temperature gradient fluctuations. Moreover, the interaction of the variance of the temperature gradient is significantly influenced by how the velocity gradient components interact with both fluctuating and mean temperature gradients. The stretching and tilting of the fluctuating temperature gradient, which depend on the alignment between G'_k and the principal eigenvector of the symmetric part of A'_{jk}, can either amplify or dampen $\langle G'_k G'_k/2 \rangle$. Additionally, the term term $-\langle G_j \rangle \langle A'_{jk} G'_k \rangle$ indicates that in the presence of a strong mean gradient (such as in the x_3 direction in our case), the dynamics of $\langle G'_k G'_k/2 \rangle$ can be influenced through interactions with the fluctuating temperature gradient stretching/tilting term $\langle A'_{jk} G'_k \rangle$. The gradient of the mean temperature gradient also contributes to the production of this quantity by interacting with the turbulent transport of G'_k.

To derive the evolution equation for temperature gradient flux it is required to multiply the fluctuating temperature gradient equation by fluctuating velocity u'_i, and by using the identity

$$u'_i \partial_j^2 G'_k = \partial_j (u'_i \partial_j G'_k + G'_k \partial_j u'_i) - (\partial_j G'_k \partial_j u'_i),$$

we have

$$\frac{\partial (u'_i G'_k)}{\partial t} + \frac{\partial (u'_i u'_j G'_k)}{\partial x_j} = \frac{\partial}{\partial x_j}[\kappa u'_i \frac{\partial G'_k}{\partial x_j} + \nu G'_k \frac{\partial u'_i}{\partial x_j}] - (\kappa + \nu)[\frac{\partial G'_k}{\partial x_j} \frac{\partial u'_i}{\partial x_j}] - u'_i G'_j A'_{jk}$$
$$- u'_i \langle G_j \rangle A'_{jk} - \frac{\partial (u'_i \langle u_j \rangle G'_k)}{\partial x_j} - u'_i u'_j \frac{\partial \langle G_k \rangle}{\partial x_j} + \frac{1}{\rho_0 c_{p0}} u'_i \frac{\partial C'_T}{\partial x_k}. \tag{2.58}$$

By taking average of this equation we can derive the transport equation for temperature gradient flux

$$\frac{\partial\langle u_i'G_k'\rangle}{\partial t}+\frac{\partial\langle u_i'u_j'G_k'\rangle}{\partial x_j}=\langle\frac{\partial}{\partial x_j}[\kappa u_i'\frac{\partial G_k'}{\partial x_j}]\rangle+\langle\frac{\partial}{\partial x_j}[\nu G_k'\frac{\partial u_i'}{\partial x_j}]\rangle-(\kappa+\nu)\langle\frac{\partial G_k'}{\partial x_j}\frac{\partial u_i'}{\partial x_j}\rangle$$
$$-\langle u_i'G_j'A_{jk}'\rangle-\langle G_j\rangle\langle A_{jk}'u_i'\rangle-\frac{\partial(\langle u_i'G_k'\rangle\langle u_j\rangle)}{\partial x_j}-\langle u_i'u_j'\rangle\frac{\partial\langle G_k\rangle}{\partial x_j}+\frac{1}{\rho_0 c_{p0}}\langle u_i'\frac{\partial C_T'}{\partial x_k}\rangle. \tag{2.59}$$

The equation (2.59) governs the transport of the turbulent flux of the temperature gradient $\langle u_i'G_k'\rangle$. This flux represents how turbulent fluctuations in the velocity field transport temperature gradient fluctuations across the flow. Like the other transported quantity, $\langle u_i'G_k'\rangle$ is advected by turbulent velocity and diffused by thermal diffusivity and viscous effect . Similarly each term in the equation plays a specific role in describing this transport. Diffusion terms reflect how the spreading of temperature gradients and velocity fluctuations contributes to the overall flux. There is a dissipation term in the equation from the effect of thermal diffusion and molecular viscous diffusion. The term $-\langle u_i'G_j'A_{jk}'\rangle$ reveals the effect of the fluctuating velocity gradient tensor on the turbulent flux of the temperature gradient. Interaction of the velocity fluctuations with the stretching/tilting of the fluctuating temperature gradient can be seen in this term. Moreover, this equation indicates the significance of the mean temperature gradient in the dynamics of the mean gradient flux. The last term also shows the effect of particle thermal back-recreation on the turbulent flux of the temperature gradient. The equation for temperature gradient variance flux is given by multiplying the equation of temperature gradient variance (2.56) by fluctuating velocity u_i' and by the use of identity

$$u_i'\partial_j^2(G_k'G_k'/2)=\partial_j[(u_i'\partial_j(G_k'G_k'/2)+(G_k'G_k'/2)\partial_j u_i')]-(\partial_j(G_k'G_k'/2)\partial_j u_i'),$$

leading to

$$\frac{\partial(u_i'G_k'G_k'/2)}{\partial t}+\frac{\partial[u_i'u_j'(G_k'G_k'/2)]}{\partial x_j}=\frac{\partial}{\partial x_j}[\kappa u_i'\frac{\partial(G_k'G_k'/2)}{\partial x_j}+\nu(G_k'G_k'/2)\frac{\partial u_i'}{\partial x_j}]$$
$$-(\nu+\kappa)[\frac{\partial(G_k'G_k'/2)}{\partial x_j}\frac{\partial u_i'}{\partial x_j}]-\kappa[u_i'\frac{\partial G_k'}{\partial x_j}\frac{\partial G_k'}{\partial x_j}]-u_i'G_j'A_{jk}'G_k'$$
$$-u_i'\langle G_j\rangle A_{jk}'G_k'-\frac{\partial[u_i'\langle u_j\rangle(G_k'G_k'/2)]}{\partial x_j}$$
$$-u_i'u_j'G_k'\frac{\partial\langle G_k\rangle}{\partial x_j}+\frac{1}{\rho_0 c_{p0}}u_i'G_k'\frac{\partial C_T'}{\partial x_k}. \tag{2.60}$$

Consequently, the transport equation of temperature gradient flux by averaging the equation (2.60) is obtained as

$$\frac{\partial\langle u_i'G_k'G_k'/2\rangle}{\partial t}+\frac{\partial\langle u_i'u_j'(G_k'G_k'/2)\rangle}{\partial x_j}=\langle\frac{\partial}{\partial x_j}[\kappa u_i'\frac{\partial(G_k'G_k'/2)}{\partial x_j}]\rangle+\langle\frac{\partial}{\partial x_j}[\nu(G_k'G_k'/2)\frac{\partial u_i'}{\partial x_j}]\rangle$$
$$-(\nu+\kappa)\langle\frac{\partial(G_k'G_k'/2)}{\partial x_j}\frac{\partial u_i'}{\partial x_j}\rangle-\langle u_i'G_j'A_{jk}'G_k'\rangle-\langle G_j\rangle\langle A_{jk}'G_k'u_i'\rangle$$
$$-\kappa\langle u_i'\frac{\partial G_k'}{\partial x_j}\frac{\partial G_k'}{\partial x_j}\rangle-\frac{\partial[\langle u_j\rangle\langle u_i'(G_k'G_k'/2)\rangle]}{\partial x_j}-\langle u_i'u_j'G_k'\rangle\frac{\partial\langle G_k\rangle}{\partial x_j}+\frac{1}{\rho_0 c_{p0}}\langle u_i'G_k'\frac{\partial C_T'}{\partial x_k}\rangle. \tag{2.61}$$

At this stage, we can incorporate the assumptions of incompressibility, homogeneity, and isotropy of the velocity field to express the transport equations for temperature gradient variance, flux, and variance flux in accordance with the study's assumptions

as

$$\frac{\partial\langle G'_k G'_k/2\rangle}{\partial t}+\frac{\partial\langle u'_j\left(G'_k G'_k/2\right)\rangle}{\partial x_j}=\kappa\left[\langle\frac{\partial^2\left(G'_k G'_k/2\right)}{\partial x_j\partial x_j}\rangle-\langle\frac{\partial G'_k}{\partial x_j}\frac{\partial G'_k}{\partial x_j}\rangle\right]$$
$$-\langle G'_j A'_{jk}G'_k\rangle-\langle G_j\rangle\langle A'_{jk}G'_k\rangle-\langle u'_j G'_k\rangle\frac{\partial\langle G_k\rangle}{\partial x_j}+\frac{1}{\rho_0 c_{p0}}\langle G'_k\frac{\partial C'_T}{\partial x_k}\rangle, \tag{2.62}$$

$$\frac{\partial\langle u'_i G'_k\rangle}{\partial t}+\frac{\partial\langle u'_i u'_j G'_k\rangle}{\partial x_j}=\langle\frac{\partial}{\partial x_j}\left[\kappa u'_i\frac{\partial G'_k}{\partial x_j}\right]\rangle+\langle\frac{\partial}{\partial x_j}\left[\nu G'_k A'_{ij}\right]\rangle-(\kappa+\nu)\langle\frac{\partial G'_k}{\partial x_j}A'_{ij}\rangle$$
$$-\langle u'_i G'_j A'_{jk}\rangle-\langle G_j\rangle\langle A'_{jk}u'_i\rangle-\langle u'_i u'_j\rangle\frac{\partial\langle G_k\rangle}{\partial x_j}+\frac{1}{\rho_0 c_{p0}}\langle u'_i\frac{\partial C'_T}{\partial x_k}\rangle, \tag{2.63}$$

$$\frac{\partial\langle u'_i G'_k G'_k/2\rangle}{\partial t}+\frac{\partial\langle u'_i u'_j\left(G'_k G'_k/2\right)\rangle}{\partial x_j}=\langle\frac{\partial}{\partial x_j}\left[\kappa u'_i\frac{\partial\left(G'_k G'_k/2\right)}{\partial x_j}\right]\rangle$$
$$+\langle\frac{\partial}{\partial x_j}\left[\nu\left(G'_k G'_k/2\right)A'_{ij}\right]\rangle-(\nu+\kappa)\langle\frac{\partial\left(G'_k G'_k/2\right)}{\partial x_j}A'_{ij}\rangle-\langle u'_i G'_j A'_{jk}G'_k\rangle$$
$$-\langle G_j\rangle\langle A'_{jk}G'_k u'_i\rangle-\kappa\langle u'_i\frac{\partial G'_k}{\partial x_j}\frac{\partial G'_k}{\partial x_j}\rangle-\langle u'_i u'_j G'_k\rangle\frac{\partial\langle G_k\rangle}{\partial x_j}+\frac{1}{\rho_0 c_{p0}}\langle u'_i G'_k\frac{\partial C'_T}{\partial x_k}\rangle. \tag{2.64}$$

We know that in our flow domain $\langle G_k\rangle=0$ for $k=1,2$. Indeed, the temperature fronts, introduced in [11] and identified as a very significant parameters in local and non-local heat transfer between particles and fluid, can be determined by studying the equation (2.62)-(2.64). Since the fluid velocity gradient tensor, highly influence the thermal field and heat transfer, as we have seen its interaction with several quantities, it is worth deriving the relevant transport equation describing its dynamics. To derive the budget equation for the variance of the velocity gradient tensor, $A'_{ik}A'_{ki}$, multiply equation (2.36) by A'_{ki} resulting in

$$\frac{\partial A'_{ik}A'_{ki}}{\partial t}+\frac{\partial u'_j A'_{ik}A'_{ki}}{\partial x_j}=-A'_{ki}A'_{ij}A'_{jk}-A'_{ki}\frac{1}{\rho_0}\frac{\partial^2 p'}{\partial x_k\partial x_i}+\nu A'_{ki}\frac{\partial^2 A'_{ik}}{\partial x_j\partial x_j}+A'_{ki}F'_{u,ik}. \tag{2.65}$$

By applying the identity $A'_{ki}\partial_j^2 A_{ik} = \partial_j \left[A'_{ki}\partial_j A'_{ik} - A'_{ki}\partial_j A'_{ik}\right] - \partial_j A'_{ki}\partial_j A'_{ik}$ and averaging both sides of equation (2.65), we obtain

$$\frac{\partial \langle A'_{ik}A'_{ki}\rangle}{\partial t} + \frac{\partial \langle u'_j A'_{ik}A'_{ki}\rangle}{\partial x_j} = -\langle A'_{ij}A'_{jk}A'_{ki}\rangle - \frac{1}{\rho_0}\langle A'_{ki}\frac{\partial^2 p'}{\partial x_k \partial x_i}\rangle$$
$$+ \nu\langle \frac{\partial}{\partial x_j}\left[A'_{ki}\frac{\partial A'_{ik}}{\partial x_j}\right]\rangle + \nu\langle \frac{\partial}{\partial x_j}\left[A'_{ik}\frac{\partial A'_{ki}}{\partial x_j}\right]\rangle - 2\nu\langle \frac{\partial A'_{ik}}{\partial x_j}\frac{\partial A'_{ki}}{\partial x_j}\rangle + \langle A'_{ki}F'_{u,ik}\rangle. \quad (2.66)$$

The equation (2.66) provides the transport equation for $\langle A'_{ik}A'_{ki}\rangle$. In fact, this correlation represents the product of the components of the velocity gradient tensor, contracted over the indices i and k. It gives a measure of the interplay between different components of the velocity gradient tensor. This quantity can provide insight into certain nonlinear effects and interactions within the turbulence. In turbulent flows, the interaction of velocity gradients with thermal fields leads to enhanced mixing of temperature. provides a measure of how the velocity gradients stretch and tilt the fluid elements in different directions. It captures the interaction between different components of the velocity gradient tensor. In turbulence theory, analysis of magnitude squared of velocity gradient tensor is also wildly use to understand the energy dissipation and the stretching of fluid elements. Therefore, it is worth deriving the transport equation for the magnitude of fluid velocity gradient tensor, by multiplying the equation (2.8) by A'_{ki} and performing ensemble averaging, resulting in

$$\frac{\partial \langle A'_{ik}A'_{ik}/2\rangle}{\partial t} + \frac{\partial \langle u'_j \left(A'_{ik}A'_{ik}/2\right)\rangle}{\partial x_j} = -\langle A'_{ij}A'_{jk}A'_{ki}\rangle - \frac{1}{\rho_0}\langle A'_{ik}\frac{\partial^2 p'}{\partial x_k \partial x_i}\rangle$$
$$+ \nu\langle \frac{\partial}{\partial x_j}\left[\frac{\partial \left(A'_{ik}A'_{ik}/2\right)}{\partial x_j}\right]\rangle - \nu\langle \frac{\partial A'_{ik}}{\partial x_j}\frac{\partial A'_{ik}}{\partial x_j}\rangle + \langle A'_{ki}F'_{u,ik}\rangle. \quad (2.67)$$

The equation (2.67) describes the transport of the magnitude of the velocity gradient tensor in a turbulent flow. This magnitude squared reveals how much the velocity field is changing in different directions. The first term on the right hand side, $-\langle A'_{ij}A'_{jk}A'_{ki}\rangle$ represents the self-amplification of of velocity gradient tensor. It reflects how the interactions between different components of the velocity gradient tensor can lead to an increase in the magnitude of the tensor, thus amplifying turbulence. The correlation with pressure Hessian term describes the interaction between the velocity gradient tensor and the pressure gradient. In fact, it captures the effect

of pressure fluctuations on the kinetic energy associated with the velocity gradients, contributing to energy redistribution in the flow. Diffusion term is responsible for Spreading of associated energy with velocity gradient due to the viscosity. Moreover, the dissipation term quantifies how the strain-rate tensor, the symmetric part of the velocity gradient, converts the kinetic energy into thermal energy, through removing energy from the turbulent motion. The last term quantifies the impact and interaction of the external forcing gradient on the velocity gradient magnitude. We are also interested in deriving the evolution equation for the term $A'_{ik}G'_k$, which appears in the transport equations for the variance of the velocity gradient tensor. This term can be interpreted as the flux of the temperature gradient vector G_k carried by the velocity gradient tensor A_{ik}. Therefore, we need to multiply the velocity gradient tensor equation (2.65) by G'_k, leading to

$$\frac{\partial\left(A'_{ik}G'_k\right)}{\partial t}+\frac{\partial\left(u'_jA_{ik}G'_k\right)}{\partial x_j}=-\left(A'_{ij}A'_{jk}G'_k\right)-\frac{1}{\rho_0}G'_k\frac{\partial^2p'}{\partial x_k\partial x_i}+\nu\frac{\partial^2A'_{ik}}{\partial x_j\partial x_j}G'_k+\left(F'_{u,ik}G'_k\right). \tag{2.68}$$

Using the relation

$$\partial_j^2A_{ik}G'_k=\partial_j\left[\partial_jA'_{ik}G'_k-A'_{ik}\partial_jG'_k\right]-\partial_jA'_{ik}\partial_jG'_k,$$

and averaging both sides of the equation (2.68), we obtain

$$\begin{aligned}&\frac{\partial\langle A'_{ik}G'_k\rangle}{\partial t}+\frac{\partial\langle u'_jA_{ik}G'_k\rangle}{\partial x_j}=-\langle A'_{ij}A'_{jk}G'_k\rangle-\frac{1}{\rho_0}\langle G'_k\frac{\partial^2p'}{\partial x_k\partial x_i}\rangle\\&+\langle\frac{\partial}{\partial x_j}\left[\kappa A'_{ik}\frac{\partial G'_k}{\partial x_j}\right]\rangle+\langle\frac{\partial}{\partial x_j}\left[\nu\frac{\partial A'_{ik}}{\partial x_j}G'_k\right]\rangle-(\nu+\kappa)\langle\frac{\partial A'_{ik}}{\partial x_j}\frac{\partial G'_k}{\partial x_j}\rangle+\langle F'_{u,ik}G'_k\rangle.\end{aligned} \tag{2.69}$$

Equation (2.69) shows the dynamics of correlation of fluid velocity gradient and temperature gradient. The first term on the right hand side, $-\langle A'_{ij}A'_{jk}G'_k\rangle$ reflects the production or destruction of the correlation between A'_{ik} and G'_k due to the interaction between the components of the velocity gradient tensor. It indicates how the stretching or tilting of the fluid velocity gradient tensor impacts the temperature gradient. If the velocity gradients cause a change in G'_k, it affects the correlation negatively or positively. Therefore, we can see that the alignment between the

temperature gradient and eigenvectors of the fluid strain-rate tensor plays a crucial role in the production or destruction of $\langle A'_{ik}G'_k\rangle$. Moreover, the pressure gradient correlation with temperature gradient shows how fluctuations in pressure and their gradients interact with the temperature gradient to influence the correlation $\langle A'_{ik}G'_k\rangle$. Moreover, Dissipation term indicates how energy associated with the fluctuations in the temperature gradient and the velocity gradient tensor is dissipated through viscous and thermal processes. Meanwhile, thermal and viscous diffusion captures the effect of thermal diffusivity and momentum diffusivity of the evolution of the correlation $\langle A'_{ik}G'_k\rangle$. Finally, the correlation between temperature gradient and external forcing gradient tensor represents how external forces applied to the fluid affect the correlation $\langle A'_{ik}G'_k\rangle$.

To derive the budget equation for the quantity $\langle T'A'_{ik}\rangle$, we multiply the transport equation for the fluid velocity gradient tensor by T' and we get

$$\frac{\partial\left(T'A'_{ik}\right)}{\partial t}+\frac{\partial u'_j\left(T'A'_{ik}\right)}{\partial x_j}=-\left(T'A'_{ij}A'_{jk}\right)-\frac{1}{\rho_0}T'\frac{\partial^2 p'}{\partial x_k\partial x_i}+\nu T'\frac{\partial^2 A'_{ik}}{\partial x_j\partial x_j}+\left(T'F'_{u,ik}\right). \tag{2.70}$$

Given the relation

$$T'\partial_j^2 A_{ik}=\partial_j\left[T'\partial_j A'_{ik}-A'_{ik}\partial_j T'\right]-\partial_j A'_{ik}\partial_j T',$$

and after averaging of all terms, the equation has the following form

$$\begin{aligned}\frac{\partial\langle T'A'_{ik}\rangle}{\partial t}+\frac{\partial\langle u'_jT'A'_{ik}\rangle}{\partial x_j}&=-\langle T'A'_{ij}A'_{jk}\rangle+\langle\frac{\partial}{\partial x_j}\left(\nu T'\frac{\partial A'_{ik}}{\partial x_j}\right)\rangle+\langle\frac{\partial}{\partial x_j}\left(\kappa A'_{ik}G'_j\right)\rangle\\&-(\nu+\kappa)\langle\frac{\partial A'_{ik}}{\partial x_j}G'_j\rangle-\frac{1}{\rho_0}\langle T'\frac{\partial^2 p'}{\partial x_k\partial x_i}\rangle+\langle T'F'_{u,ik}\rangle.\end{aligned} \tag{2.71}$$

The equation (2.71) represents the time evolution of the average the correlation between fluid temperature and velocity gradient tensor. It captures how the fluctuations in temperature combined with the local deformation of the flow change as time progresses. The advection term accounts for the movement of temperature fluctuations and their effect on the velocity gradient tensor across space due to the velocity fluctuations. On the right hand side $-\langle T'A'_{ij}A'_{jk}\rangle$ is a production or

destruction term due to the interaction between the temperature fluctuations and velocity gradient self-amplifications. Depending on the non-linear self-amplification of the velocity gradient tensor, this term can contribute or remove $\langle T'A'_{ik}\rangle$. The term $-(1/\rho_0)\langle T'\partial_k^2 p'\rangle$ captures the coupling between the temperature fluctuations and pressure gradient. It captures how the fluctuations in pressure, through their gradient, influence the correlation of temperature fluctuations and velocity gradient tensor components. Moreover, term $\langle T'F'_{u,ik}\rangle$ indicates how temperature fluctuations interact with the gradient of external forcing. The other terms quantify the thermal and viscose diffusion and dissipation of $\langle T'A'_{ik}\rangle$. While the diffusion terms show how temperature gradients combined with the velocity gradient tensor diffuse through the flow, the dissipation term shows how the energy associated with the temperature and velocity gradient gradients fluctuations is dissipated through these processes.

If we define the heat flux gradient tensor by $\Phi_{ik} = \partial_k(u'_i T')$ the budget equation for this tensor can be derived by taking spatial derivative of both sides of the evolution equation of fluid heat flux (2.45), and having

$$\frac{\partial}{\partial x_k}\left[\frac{\partial(u'_i T')}{\partial t} + u'_j\frac{\partial(u'_i T')}{\partial x_j}\right] = \frac{\partial}{\partial x_k}\left[\frac{\partial}{\partial x_j}\left(\kappa u'_i G'_j + \nu T' A'_{ij}\right) - (\nu+\kappa)\left(A'_{ij}G'_j\right)\right.$$
$$\left. -\frac{\partial(u'_i\langle u_j\rangle T')}{\partial x_j} - u'_i u'_j\frac{\partial\langle T\rangle}{\partial x_j} + \frac{1}{\rho_0 c_{p0}}(u'_i C'_T)\right]. \tag{2.72}$$

For the simplicity, the operation of all spatial derivatives in the equation (2.72) is done term by term, and conveniently we aim to expressed them in terms of fluid

temperature and velocity fields and their corresponding gradients as follows

$$
\begin{aligned}
&\frac{\partial}{\partial x_k}\left[\frac{\partial(u_i'T')}{\partial t}\right]=\frac{\partial}{\partial t}\left[\frac{\partial(u_i'T')}{\partial x_k}\right]=\frac{\partial}{\partial t}\left[u_i'G_k'+T'A_{ik}'\right]=\frac{\partial\Phi_{ik}}{\partial t},\\
&\frac{\partial}{\partial x_k}\left[u_j'\frac{\partial(u_i'T')}{\partial x_j}\right]=A_{jk}'\frac{\partial(u_i'T')}{\partial x_j}+u_j'\frac{\partial^2(u_i'T')}{\partial x_k\partial x_j}=\Phi_{ij}A_{jk}'+u_j'\frac{\partial\Phi_{ik}}{\partial x_j},\\
&\frac{\partial}{\partial x_k}\left[\frac{\partial}{\partial x_j}\left[\kappa u_i'G_j'\right]\right]=\kappa\frac{\partial}{\partial x_k}\left[u_i'\frac{\partial G_j'}{\partial x_j}+A_{ij}'G_j'\right]=\kappa\left[A_{ik}'\frac{\partial G_j'}{\partial x_j}+u_i'\frac{\partial^2G_j'}{\partial x_k\partial x_j}+\frac{\partial A_{ij}'}{\partial x_k}G_j'+A_{ij}'\frac{\partial G_j'}{\partial x_k}\right],\\
&\frac{\partial}{\partial x_k}\left[\frac{\partial}{\partial x_j}\left[\nu T'A_{ij}'\right]\right]=\nu\frac{\partial}{\partial x_k}\left[A_{ij}'G_j'+T'\frac{\partial A_{ij}'}{\partial x_j}\right]=\nu\left[\frac{\partial A_{ij}'}{\partial x_k}G_j'+A_{ij}'\frac{\partial G_j'}{\partial x_k}+G_k'\frac{\partial A_{ij}'}{\partial x_j}+T'\frac{\partial^2A_{ij}'}{\partial x_k\partial x_j}\right],\\
&\frac{\partial}{\partial x_k}\left[-(\nu+\kappa)\left(A_{ij}'G_j'\right)\right]=-(\nu+\kappa)\left[\frac{\partial A_{ij}'}{\partial x_k}G_j'+A_{ij}'\frac{\partial G_j'}{\partial x_k}\right],\\
&\frac{\partial}{\partial x_k}\left[-\langle u_j\rangle\frac{\partial(u_i'T')}{\partial x_j}\right]=-\left[\langle A_{jk}\rangle\frac{\partial(u_i'T')}{\partial x_j}+\langle u_j\rangle\frac{\partial^2(u_i'T')}{\partial x_kx_j}\right],\\
&\frac{\partial}{\partial x_k}\left[-u_i'u_j'\langle G_j\rangle\right]=-\left[\frac{\partial(u_i'u_j')}{\partial x_k}\langle G_j\rangle+(u_i'u_j')\frac{\partial\langle G_j\rangle}{\partial x_k}\right],\\
&\frac{\partial}{\partial x_k}\left[\frac{1}{\rho_0c_{p0}}(u_i'C_T')\right]=\frac{1}{\rho_0c_{p0}}\left[A_{ik}'C_T'+u_i'\frac{\partial C_T'}{\partial x_k}\right].
\end{aligned}
\tag{2.73}
$$

Assuming that $\langle u_j\rangle=\langle A_{jk}\rangle=\partial_k\langle u_i'u_j'\rangle=0$ for the homogeneous and isotropic turbulence, the terms derived in (2.73) can be introduced in the evolution equation for the turbulent heat flux gradient tensor (2.72). Then, after averaging the transport equation of turbulent heat flux gradient tensor is simplified to

$$
\begin{aligned}
\frac{\partial\Phi_{ik}}{\partial t}+\frac{\partial\langle u_j'\Phi_{ik}\rangle}{\partial x_j}&=\langle\frac{\partial}{\partial x_j}\left[\kappa u_i'\frac{\partial G_j'}{\partial x_k}\right]\rangle+\langle\frac{\partial}{\partial x_j}\left[\nu T'\frac{\partial A_{ij}'}{\partial x_k}\right]\rangle\\
&+\kappa\left[\langle A_{ik}'\frac{\partial G_j'}{\partial x_j}\rangle-\langle A_{ij}'\frac{\partial G_j'}{\partial x_k}\rangle\right]\\
&+\nu\left[\langle\frac{\partial A_{ik}'}{\partial x_j}G_k'\rangle-\langle\frac{\partial A_{ij}'}{\partial x_k}G_j'\rangle\right]\\
&-\langle u_i'u_j'\rangle\frac{\partial\langle G_j\rangle}{\partial x_k}-\langle\Phi_{ij}A_{jk}'\rangle+\frac{1}{\rho_0c_{p0}}\left[\langle A_{ik}'C_T'\rangle+\langle u_i'\frac{\partial C_T'}{\partial x_k}\rangle\right].
\end{aligned}
\tag{2.74}
$$

Note that $\langle G_j \rangle = 0$ for $j = 1,2$. The terms in the equation (2.74) shed light on the complex nature of heat transfer within our flow domain, particularly when considering two-way thermal coupling with particles, in a case where feedback term C_T' exists. Specifically, in the x_3 direction, there are two key production terms: one arising from the mean temperature gradient and the other from the interaction between the turbulent heat flux gradient tensor and the fluid velocity gradient tensor. This equation helps elucidate the mechanisms driving thermal energy transport, especially in scenarios where particle inertia and thermal inertia play significant roles in coupling with local fluid fields. Numerical results can provide deeper insights into the dynamics of this quantity, which is crucial for understanding the complex heat transfer processes in this flow regime. It is also evident that the alignment of the turbulent heat flux gradient tensor with the eigenvectors of the fluid strain-rate tensor has a substantial impact on both the dynamics of the heat flux gradient tensor and overall heat transfer in the x_3 direction. This theoretical framework can be further validated through numerical simulations in future studies, which will explore the contributions of each term to the heat transfer process in the examined flow regime. It should be noted that while the numerical results in the following chapter will utilize some of the quantities whose transport equations are derived here e.g. fluctuation velocity, mean and fluctuation temperature, temperature variance, turbulent heat flux and flux of temperature variance , others will be addressed in subsequent future works. However, in the last chapter, the transport equation derived for fluid velocity gradient and temperature gradient will be used to develop the theoretical analysis of particle thermal caustics in non-isothermal particle-laden flows.

2.3 Governing equations of discrete phase

2.3.1 Particle dynamics

In order to describe the dynamics of N_p suspended particle in a fluid flow, we need to use Lagrangian equation of motion of each individual particle. Each particle is released within the carrier flow and is tracked by its Lagrangian position of its center of mass along its trajectory. This position can be computed instantaneously by following Lagrangian equation which is called particle trajectory or Lagrangian

kinematic equation

$$\frac{\mathrm{d}\mathbf{X_p(t)}}{\mathrm{d}t} = \mathbf{V_p(t)}, \tag{2.75}$$

where $\mathbf{X_p}$ is the position of $p-th$ spherical particle within the fluid medium which indeed represents a material point with radius R, density ρ_p and mass m_p and $\mathbf{V_p}$ is the velocity of this assumed rigid sphere. Note that this trajectory is different from the surrounding fluid particle trajectory which is described in Eulerian grid by field description as provided in the previous section. For passive particle or inertialess tracer $\boldsymbol{V}_p = \boldsymbol{u}(t,\boldsymbol{X}_p(t))$, where $\boldsymbol{u}(t,\boldsymbol{X}_p(t))$ is the carrier fluid velocity field sampled at particle position. On the other hand, inertial particles satisfy the following Lagrangian equation (i.e. Newton's second law of motion)

$$m_p \frac{\mathrm{d}\boldsymbol{V}_p(t)}{\mathrm{d}t} = \sum \boldsymbol{F}_p, \tag{2.76}$$

where the term $\boldsymbol{F}_p$ in the right-hand side of the equation consists of all forces acting on the particle. The dynamics of a rigid spherical particle suspended in a fluid are characterized, in a generic form, by an equation historically known as the Basset-Boussinesq-Oseen (BBO) equation. This equation provides a comprehensive framework to account for all the forces acting on the center of mass of the particle, including drag, added mass, and the Basset history force. The origins of the BBO equation can be dated back to Stokes' law, formulated by George Gabriel Stokes in 1851, which describes the drag force experienced by a spherical object moving through a viscous fluid [48]. This foundational work laid the groundwork for understanding the drag component of the forces acting on a particle in a fluid. In 1877, Joseph Boussinesq introduced the concept of added mass, which accounts for the additional inertia experienced by a particle due to the acceleration of the surrounding fluid. This was a significant step towards a more complete understanding of the dynamics of particles in fluids [49]. Alfred Barnard Basset made a further crucial contribution in 1888 by introducing the history or memory term in the equation. This term, now known as the Basset force, accounts for the unsteady viscous effects experienced by a particle due to its past accelerations in the fluid. Basset's work was published in his treatise on hydrodynamics [50]. Later, Carl Wilhelm Oseen contributed to the understanding of viscous drag in 1927 by linearizing the Navier-

Stokes equations around a moving body, refining the drag component in the equation. Oseen's work helped to complete the formulation of what is now known as the BBO equation [51]. The BBO equation is crucial for understanding the behavior of small spherical particles in fluid flows, particularly when the particle's inertia cannot be neglected. However, while the BBO equation is foundational, it is less frequently used in modern applications without modification due to its complexity and the challenges in accounting for certain practical effects. In many modern applications, an advanced and practically-oriented version of the BBO equation, known as the Maxey-Riley-Gatignol (MRG) equation, is commonly used. The theoretical foundation of almost all point-particle Eulerian-Lagrangian approaches is based on this equation. The MRG equation was proposed by Maxey and Riley [52] , and independently by Gatignol [53] in 1983. Both the BBO and MRG equations describe the motion of a spherical particle suspended in a viscous fluid, but with a key difference: the Faxén correction in the MRG formulation. The Faxén correction, which includes terms such as the Laplacian of the fluid velocity seen by the particle (denoted as $\nabla^2 \boldsymbol{u}(t, \boldsymbol{X}_p)$), accounts for the effects of the particle's finite size in a non-uniform fluid flow. This modification is crucial in ensuring that the MRG equation accurately represents the influence of the surrounding fluid's velocity field, particularly when the particle's size is not negligible compared to the flow's characteristic length scales. The Faxén correction is essential in capturing the effects of the viscous forces on the particle, which are significant in many practical scenarios involving fluid-particle interactions. The MRG equation strictly holds only for a small rigid sphere suspended in a nonuniform unsteady flow. Furthermore, it is only valid for point particle assumption implying that particle radius R must be smaller than the carrier flow characteristic length scale, which is Kolmogorov length scale (i.e. $\eta = (\nu^3/\varepsilon)^{1/4}$) in the turbulent flow. Another important constraint to this equation is the particle Reynolds number that must be very small. Particle Reynolds number is defined by

$$\mathrm{Re}_p = \frac{2R|\boldsymbol{u}(t, \boldsymbol{X}_p) - \boldsymbol{V}_p|}{\nu}. \tag{2.77}$$

Note that in general, for finite-size particles, like particles comparable to or larger than the Kolmogorov length scale, the MRG equation's applicability is limited, and additional corrections or alternative models are needed to account for size effects. Although the MRG equation is valid for low particle Reynolds number, but it can

take into account the effects of finite particle size through the Faxén correction terms which is a function of Re_p [53]. Homann and Béc [54] showed that the effect of these correction terms is significant for larger particles, but negligible if the particle diameter is equal to the Kolmogorov size or smaller. In the valid range, for small point-like particles, the MRG equation is given by

$$m_p \frac{\mathrm{d}\boldsymbol{V}_p(t)}{\mathrm{d}t} = \boldsymbol{F}_{SD} + \boldsymbol{F}_B + \boldsymbol{F}_{PG} + \boldsymbol{F}_{AM} + \boldsymbol{F}_{BH}. \tag{2.78}$$

The terms on the right hand side denote respectively the Stokes drag force, the buoyancy force, the force by undisturbed velocity field or pressure gradient force, the added mass force, and the Basset history force. In addition to the forces given in the above equation of motion of particle, in several cases also the lift force is taken into account which is not the case of our study. The explicit expression for each force term in the equation must be provided. We start with he buoyancy force which reads

$$\boldsymbol{F}_B = (m_p - m_0)\boldsymbol{g}, \tag{2.79}$$

where $\boldsymbol{g}$ is the gravitational acceleration and m_0 stands for fluid mass that occupies the same volume of particle ($m_0 = 4/3\pi R^3 \rho_0$). Under the point-particle assumption in Stoksian regime ($\mathrm{Re}_p \ll 1$), and without considering finite-size effect ($R/\eta \ll 1$) and Faxén correction, for a tiny rigid sphere the Stokes drag force reads

$$\boldsymbol{F}_{SD} = 6\pi R\mu(\boldsymbol{u}(t,\boldsymbol{X}_p) - \boldsymbol{V}_p), \tag{2.80}$$

where μ is the fluid dynamic viscosity. However, many empirical correlations have been developed to provide more accurate expression for Stokes drag acting on spherical particles. In a generic form we expressed the drag force F_D in terms of a generic drag coefficient C_D which can take into account both linear and the non-linear forces

$$\boldsymbol{F}_D = \frac{1}{2} C_D \rho_0 \pi R^2 (\boldsymbol{u}(t,\boldsymbol{X}_p) - \boldsymbol{V}_p)|\boldsymbol{u}(t,\boldsymbol{X}_p) - \boldsymbol{V}_p|. \tag{2.81}$$

For instance, this coefficient for a light particle dragged by a viscous fluid as a function of particle Reynolds number is proposed by Schiller and Naumann [55] as

$$C_D = \frac{24}{\mathrm{Re}_p}(1 + 0.15\mathrm{Re}_p^{0.687}). \tag{2.82}$$

In our study, the linear model is used under which the non-linear correction is not needed due to the very low Re_p. The drag force in the particle momentum equation indeed represents the friction exerted by fluid viscosity on the particle surface. In the case of a rigid sphere falling through a quiescent fluid, viscous effects and buoyancy forces reach an equilibrium, leading to the well-known Stokes solution for the settling velocity. The rigid sphere asymptotically reaches its terminal velocity in air or settling velocity in a liquid, which is expressed by

$$\boldsymbol{V}_{p,T} = \frac{2}{9} g R^2 \frac{\rho_p - \rho_0}{\mu}, \tag{2.83}$$

where the Stokes force is $\boldsymbol{F}_{SD} = 6\mu\pi R\boldsymbol{V}_{p,T}$, and g denotes the gravitational acceleration. The next term considered is the force due to the undisturbed velocity field, often referred to as the pressure gradient force. This force represents the effect on a hypothetical sphere of fluid, with the same volume as the particle, due to the changes in the undisturbed flow field. It is given by

$$\boldsymbol{F}_{PG} = m_0 \frac{\mathrm{D}\boldsymbol{u}(t, \boldsymbol{X}_p)}{\mathrm{D}t}, \tag{2.84}$$

where m_0 is the mass of the fluid displaced by the particle, and the material derivative is evaluated at the particle's position $\boldsymbol{X}_p$. This material derivative captures both the temporal change in the fluid velocity and the spatial change as the particle moves through the flow. The material derivative $\mathrm{D}/\mathrm{D}t$ represents the rate of change of the fluid velocity experienced by the particle and is expressed as

$$\frac{\mathrm{D}(\cdot)}{\mathrm{D}t} = \frac{\partial(\cdot)}{\partial t} + \boldsymbol{u} \cdot \frac{\partial(\cdot)}{\partial \boldsymbol{x}}, \tag{2.85}$$

where $\partial_t(\cdot)$ is the local time derivative and $\boldsymbol{u} \cdot \nabla(\cdot)$ accounts for the spatial variation as the particle moves with the fluid velocity $\boldsymbol{u}$. In contrast, the total time derivative of a quantity $(\cdot)$ for the particle is given by

$$\frac{\mathrm{d}(\cdot)}{\mathrm{d}t} = \frac{\partial(\cdot)}{\partial t} + \boldsymbol{V}_p \cdot \frac{\partial(\cdot)}{\partial \boldsymbol{x}}. \tag{2.86}$$

The relationship between the material derivative and the total time derivative is

$$\frac{\mathrm{D}(\cdot)}{\mathrm{D}t} = \frac{\mathrm{d}(\cdot)}{\mathrm{d}t} - \boldsymbol{W}_p \cdot \frac{\partial(\cdot)}{\partial \boldsymbol{x}}, \tag{2.87}$$

where $\boldsymbol{W}_p = (\boldsymbol{V}_p - \boldsymbol{u}(t, \boldsymbol{X}_p))$ represents the relative velocity of the particle with respect to the surrounding fluid. Initially, the pressure gradient force was not included in the derivation of the particle equation of motion. However, Maxey and Riley [52] demonstrated that both pressure gradient and viscous forces are significant under certain flow conditions. Meanwhile, if we neglect the finite-size effects, the added mass force is expressed by

$$\boldsymbol{F}_{AM} = \frac{1}{2} m_0 \left(\frac{\mathrm{D}\boldsymbol{u}(t, \boldsymbol{X}_p)}{\mathrm{D}t} - \frac{\mathrm{d}\boldsymbol{V}_p(t)}{\mathrm{d}t} \right). \tag{2.88}$$

Note that the first term between the parentheses has the same shape as the pressure gradient force, while the second term has the same shape as the particle acceleration. The added mass actually is the effect of fluid displacement by the motion of particles. To model this dynamic effect, an additional mass, which moves with the particle, is considered. For a rigid particle in a fluid, this added mass is found to be half of the mass of the displaced fluid. This accounts for the additional inertia that the particle effectively acquires due to its interaction with the surrounding fluid. Finally, the last term in generic equation of motion of particle is the Basset history force, which is defined by

$$\boldsymbol{F}_{BH} = 6R^2 \rho_0 \sqrt{\pi \nu} \int_0^t \frac{1}{\sqrt{t-\tau}} \frac{\mathrm{d}}{\mathrm{d}\tau} [\boldsymbol{u}(t, \boldsymbol{X}_p(t)) - \boldsymbol{V}_p(t)] \mathrm{d}\tau. \tag{2.89}$$

This term accounts for the unsteady viscous effects, such as the transient regime of the boundary layer around the spherical particle. It is computationally demanding due to the integral over the particle's time history, and as such, it is often neglected in practical applications [19]. The Basset force represents the accumulated effect of the fluid's viscous response to the particle's motion over time. Initially proposed by Boussinesq in 1885 [56] and further developed by Basset in 1888 [50], this force is expressed as an integral that includes the history of the particle's interaction with the surrounding fluid. Its integral form incorporates the influence of past fluid velocities and accelerations, reflecting the cumulative nature of viscous effects on the particle. For light particles, especially neutrally buoyant particles such as bubbles suspended in a denser liquid where the particle density is much lower than the fluid density ($\rho_p/\rho_0 < 100$), the Basset history force cannot be neglected. In such cases, this term must be included along with other significant forces to accurately describe the particle's motion. However, in scenarios where the particle density is much

greater than the fluid density ($\rho_p \gg \rho_0$), as in our problem, the Basset history force is excluded due to its negligible effect compared to other forces. In general, for small and heavy particles, it has been observed that the pressure gradient force, added mass force, and Basset history force are relatively small and often negligible compared to the drag force [57] In certain flow configurations, additional forces may need to be considered in the particle momentum equation. For instance, if inter-particle interactions, either short-range or long-range, adhesive forces, Brownian effects are significant, these forces, along with other relevant ones, should be incorporated into the model. In section 2.4 we will discuss some of these interaction forces, and the conditions on which additional interaction forces become considerable will be identified. Additionally, lift force can be an important consideration in some flow regimes. There are generally two mechanisms for lift force acting on a particle. The first is the Saffman lift force (or shear-induced lift), which arises from the shear in the fluid velocity. This mechanism is due to the asymmetric advection of the vorticity generated by the surrounding flow shear at the particle's surface, resulting in a force perpendicular to the relative motion between the fluid and the particle. This force, derived by Saffman [58] and later extended by Legendre and Magnaudet [59] for drops of arbitrary viscosity, decreases rapidly with increasing Reynolds number in low Reynolds number linear shear flow. The second mechanism is the Lighthill-Auton lift, which arises from the secondary velocity field induced by stream-wise non-zero vorticity. This shear-induced lift force, described by Lighthill [60] and Auton [61], has the same direction as the Saffman lift force. The slip-rotation lift force or Magnus force is another important type of lift force, resulting from the rotation of the particle. This force, first explored by Rubinow and Keller [62], acts perpendicular to both the relative velocity and the rotation axis of the particle. The lift force acting on a particle can be generally expressed as

$$\boldsymbol{F}_L = m_0 C_L(\boldsymbol{u}(t,\boldsymbol{X}_p) - \boldsymbol{V}_p) \times \boldsymbol{\omega}, \tag{2.90}$$

where ω denotes the vorticity of the disturbed flow or the particle's rotational velocity and C_L is the lift coefficient, which must be defined based on the specific problem and flow conditions. In this expression, m_0 is the mass of the fluid displaced by the particle. The term $(\boldsymbol{u}(t,\boldsymbol{X}_p) - \boldsymbol{V}_p)$ represents the relative velocity between the fluid and the particle, and $\boldsymbol{\omega}$ captures the effect of the vorticity or rotational component. The lift force is perpendicular to both the relative velocity and the vorticity vector, making it crucial for accurately modeling particle behavior in complex flows. For

example, in the context of the Saffman lift force, the lift coefficient C_L depends on the particle's Reynolds number Re_p and the shear rate Sr_p of the surrounding fluid. The shear rate Sr_p is defined as

$$\mathrm{Sr}_p = \frac{R|\partial V_{p,i}/\partial x_j|}{|u_i - V_{p,i}|}, \tag{2.91}$$

where R is the particle radius, $V_{p,i}$ is the $i-th$ component of the particle velocity, u_i is the $i-th$ component of the fluid velocity, and $\partial V_{p,i}/\partial x_j$ represents the rate of change of the particle velocity with respect to the spatial coordinates. The lift force, in light particle suspensions, can be significant due to this shear-induced effect. However, for the purposes of this analysis, we focus on the forces that are most relevant given the conditions. Specifically, we consider the linear Stokes drag as the only force affecting the particle dynamics. All other forces, including the Saffman lift force and others, are neglected in the following analysis. The MRG equation describes the motion of a spherical particle suspended in a fluid, accounting for various forces acting on the particle. Given that the mass of a monodispersed spherical particle is $m_p = 4/3\pi R^3$, where ρ_p is the particle density and R is the radius, we can express the MRG equation in terms of particle acceleration as follows

$$\begin{aligned}\frac{\mathrm{d}\boldsymbol{V}_p}{\mathrm{d}t} = \frac{\boldsymbol{u}(t,\boldsymbol{X}_p) - \boldsymbol{V}_p}{\tau_v} + (1 - \frac{\rho_0}{\rho_p})\boldsymbol{g} + \frac{\rho_0}{\rho_p}\frac{\mathrm{D}\boldsymbol{u}(t,\boldsymbol{X}_p)}{\mathrm{D}t} + \frac{1}{2}\frac{\rho_0}{\rho_p}(\frac{\mathrm{D}\boldsymbol{u}(t,\boldsymbol{X}_p)}{\mathrm{D}t} - \frac{\mathrm{d}\boldsymbol{V}_p}{\mathrm{d}t}) \\ \sqrt{\frac{9}{2\pi}\frac{\rho_0}{\rho_p}\frac{1}{\tau_v}}\int_0^t \frac{1}{\sqrt{t-\tau}}\frac{\mathrm{d}}{\mathrm{d}\tau}[\boldsymbol{u}(t,\boldsymbol{X}_p(t)) - \boldsymbol{V}_p(t)]\mathrm{d}\tau,\end{aligned} \tag{2.92}$$

where τ_v is the particle momentum or dynamical response time and it is given by

$$\tau_v = \frac{2}{9}\frac{\rho_p}{\rho_0}\frac{R^2}{\nu}, \tag{2.93}$$

where ν is the kinematic viscosity of the fluid. The equation (2.92) incorporates the key forces acting on a spherical particle in a fluid, including drag, buoyancy, pressure gradient, added mass, and history effects. Particle response time τ_v provides us a tool to measure the particle inertia by a timescale that shows how particles with different inertia respond to the carrier flow excitation. The MRG equation can be dimensionless by introducing the reference time, length and velocity scales, t_0, L_0 and $\boldsymbol{u}_0$. Thus, the dimensionless variables can be defined by

$$t^* = \frac{t}{t_0}, \quad \boldsymbol{X}_p^* = \frac{\boldsymbol{X}_p}{L_0}, \quad \boldsymbol{V}_p^* = \frac{\boldsymbol{V}_p}{\boldsymbol{u}_0}, \quad \boldsymbol{u}^* = \frac{\boldsymbol{u}}{\boldsymbol{u}_0}, \quad \rho^* = \frac{\rho_p}{\rho_0} \tag{2.94}$$

Consequently, the dimensionless MRG equation after transformation becomes

$$\frac{\mathrm{d}\boldsymbol{V}_p^*}{\mathrm{d}t^*} = \frac{\boldsymbol{u}^*(t^*,\boldsymbol{X}_p^*) - \boldsymbol{V}_p^*}{\mathrm{St}} + \frac{1-\rho^*}{\mathrm{Fr}}\boldsymbol{e}_g + \rho^* \frac{\mathrm{D}\boldsymbol{u}^*(t^*,\boldsymbol{X}_p^*)}{\mathrm{D}t^*} + \frac{1}{2}\rho^*\left(\frac{\mathrm{D}\boldsymbol{u}^*(t^*,\boldsymbol{X}_p^*)}{\mathrm{D}t^*} - \frac{\mathrm{d}\boldsymbol{V}_p^*}{\mathrm{d}t^*}\right)$$
$$\sqrt{\frac{9}{2\pi}\frac{\rho^*}{\mathrm{St}}}\int_0^{t^*} \frac{1}{\sqrt{t^*-\tau^*}}\frac{\mathrm{d}}{\mathrm{d}\tau^*}[\boldsymbol{u}^*(t^*,\boldsymbol{X}_p(t)^*) - \boldsymbol{V}_p(t)^*]\mathrm{d}\tau, \tag{2.95}$$

where ρ^* is the fluid-to-particle density ratio, and $\boldsymbol{e}_g$ is the unit vector in the direction of gravitational acceleration. St is Stokes number, denoting the ratio of the particle response time to the reference time scale t_0, and Fr is the Froude number, representing the ratio of inertial forces to gravitational forces. These dimensionless numbers are defined by

$$\mathrm{St} = \frac{\tau_v}{t_0} \tag{2.96}$$

$$\mathrm{Fr} = \frac{\boldsymbol{V}_0/t_0}{g} = \frac{\boldsymbol{V}_0^2}{gL_0} \tag{2.97}$$

This dimensionless formulation captures the essential dynamics of the particle in a non-dimensional framework, making it easier to compare different scenarios and analyze the relative importance of various forces acting on the particle. In turbulent flow, which is the context of this study, the Stokes number can be defined in terms of the small-scale turbulence timescale, specifically the Kolmogorov timescale $\tau_\eta = (\nu/\varepsilon)^{1/2}$. This dimensionless number, known as the small-scale Stokes number, is given by

$$\mathrm{St}_\eta = \frac{\tau_v}{\tau_\eta} \tag{2.98}$$

For non-buoyant heavy inertial particles, where $\rho_p/\rho_0 \gg 1$ and $R \ll \eta$ with $\eta = (\nu^3/\varepsilon)^{1/4}$ representing the Kolmogorov length scale, the dimensional equation

simplifies to

$$\frac{\mathrm{d}\boldsymbol{V}_p}{\mathrm{d}t} = \frac{\boldsymbol{u}(t,\boldsymbol{X}_p) - \boldsymbol{V}_p}{\tau_v}. \tag{2.99}$$

This simplified equation, (2.99), which describes the dynamics of inertial particles suspended in a turbulent flow, is utilized in this study.

2.3.2 Particle thermodynamics

In this section, we derive the governing equation for particle thermal behavior in the Lagrangian frame. Analogous to the particle momentum equation, we use the particle's total energy or enthalpy evolution equation to derive the particle temperature evolution equation. Consequently, any change in particle enthalpy must be accounted for in this equation. In our study, the particle exchanges heat with the surrounding fluid solely through convection. For a solid particle model, where the particle's mass remains constant throughout the process, latent heat is not included in the enthalpy equation. However, in other scenarios, additional heat transfer mechanisms (such as radiative heat transfer) or heat sources/sinks (such as vaporization enthalpy) may be incorporated into the enthalpy equation. Moreover, conductive heat transfer within the particle is neglected due to the small particle radius. For particles of size ($\sim \mathcal{O}(10^{-6})m$), the Biot number, defined as $\mathrm{Bi} = hR/\lambda_p \ll 0.1$, (where h, is much less than 0.1 (where h is the convective heat transfer coefficient, λ_p is the particle thermal conductivity, and R is the particle radius). Neglecting conduction is justified under the assumption of a finite heat capacity (lumped-capacitance model) because convection is significantly more effective than conduction in this size range. Thus, for such particles, where heat is exchanged only through convection with the carrier flow, the particle enthalpy equation simplifies to a Newton-like equation that describes sensible enthalpy.

$$\frac{\mathrm{d}h_p(t)}{\mathrm{d}t} = 2\mathrm{Nu}\pi R\lambda\,(T(t,\boldsymbol{X}_p) - \Theta_p(t)), \tag{2.100}$$

where λ is the fluid thermal conductivity, and $(T(t,\boldsymbol{X}_p)$ is the fluid temperature viewed by particle and Θ_p is the temperature of $p-th$ spherical particle. The Nu denotes the Nusselt number and can be obtained from an empirical correlation which is known as Ranz-Marshall correlation [63]. The Nu is indeed a correction for the

finite-size effect and is given by

$$\mathrm{Nu} = 2 + 0.6(\mathrm{Re}_p)^{1/2}(\mathrm{Pr})^{1/3}. \tag{2.101}$$

In our study since the particle Reynolds number is very small we only use the first part of the correlation, i.e. $\mathrm{Nu} = 2$. If c_{pp} is the particle isobaric heat capacity, particle enthalpy can be written in terms of particle temperature

$$h_p(t) = m_p c_{pp} \Theta_p(t). \tag{2.102}$$

By substituting the enthalpy in the equation we derive the Lagrangian evolution equation of particle temperature. The particle temperature time derivative is given by:

$$\frac{\mathrm{d}\Theta_p(t)}{\mathrm{d}t} = \frac{3\lambda}{\rho_p c_{pp} R^2}(T(t,\boldsymbol{X}_p) - \Theta_p(t)). \tag{2.103}$$

Similar to the particle momentum equation, we can express the particle temperature time derivative equation in terms of particle thermal response time, defined as

$$\tau_\vartheta = \frac{1}{3}\frac{\rho_p c_{pp}}{\rho_0 c_{p0}}\frac{R^2}{\kappa}. \tag{2.104}$$

Consequently, the particle temperature evolution equation in dimensional form reads

$$\frac{\mathrm{d}\Theta_p(t)}{\mathrm{d}t} = \frac{(T(t,\boldsymbol{X}_p) - \Theta_p(t))}{\tau_\vartheta}. \tag{2.105}$$

Just as the momentum response time τ_v measures how quickly a particle responds to changes in the local carrier flow velocity, the thermal response time τ_ϑ indicates the time required for a particle to adjust to the local carrier flow temperature. For a given particle-to-fluid density ratio, τ_ϑ depends on the particle size and the ratio of the particle's heat capacity to that of the fluid. Larger particles, or those with a higher heat capacity ratio, exhibit longer response times due to their higher thermal inertia. In our study, we explore a wide range of thermal inertia values alongside different particle inertia to investigate the complex heat transfer mechanisms in non-isothermal particle-laden turbulent flows. The validity of the derived equations is contingent upon the conditions where the particle is much smaller than the Kolmogorov length

scale. Under these conditions, finite-size effects are negligible, and the disturbances to the local fluid temperature field caused by the particles are not considered. Thus, both Eulerian and Lagrangian equations use undisturbed quantities in this study. Although actual temperature fields would account for both disturbed and undisturbed components, this assumption is justified within the point particle framework [32]. The statistical moments of the temperature field gradient, including both disturbed and undisturbed fields, have been analyzed by Carbone et al. [32]. In the point particle regime, where there is a significant scale separation between the particle radius and the Kolmogorov microscale, an analytical solution for the temperature field can be derived.

Carbone et al. [32] also addressed the validity of the assumption that particle perturbations can be neglected in the point particle model. They demonstrated that the margin of error introduced by this assumption is at most about 15% even for large particles with $\mathrm{St} = 3$. This supports our decision to disregard particle-induced disturbances in the fluid temperature field. In addition to neglecting the particle-induced disturbances in the fluid temperature field, we assume that the inter-phase exchange of thermal energy between the continuous and discrete phases occurs primarily through diffusion, with a characteristic timescale of R^2/κ, where R is the particle radius and κ is the thermal diffusivity of the fluid. This assumption is consistent with the one applied to the momentum equation in the Stokesian regime, where the dominant force on the particle is the Stokes drag. In other words, the inter-phase momentum transfer at the particle surface can be adequately modeled using Stokes drag [52]. Moreover, the diffusive timescale of heat transfer for a point particle in a turbulent field must be smaller than the Kolmogorov timescale. Therefore, we can assume that the inter-phase heat transfer takes place through a quasi-steady process, allowing us to use Newton's law of cooling to characterize the heat transfer process. Similar to the particle momentum equation, equation 2.105 can be non-dimensionalized by introducing the reference time t_0, length L_0, velocity $\boldsymbol{u}_0$ and temperature T_0 scales. Thus, the dimensionless particle temperature time derivative is given by

$$\frac{\mathrm{d}\Theta_p^*(t^*)}{\mathrm{d}t^*} = \frac{(T^*(t^*, \boldsymbol{X}_p^*) - \Theta_p^*(t^*))}{\mathrm{St}_\vartheta}, \tag{2.106}$$

where St_ϑ is the particle thermal Stokes number and is defined by

$$\mathrm{St}_\vartheta = \frac{\tau_\vartheta}{t_0} \tag{2.107}$$

In a turbulent flow regime, the relevant time scale is typically the small-scale time scale, known as the Kolmogorov time scale τ_η. Accordingly, the small-scale thermal Stokes number is defined as

$$\mathrm{St}_\vartheta = \frac{\tau_\vartheta}{\tau_\eta}. \tag{2.108}$$

2.4 Particle interaction forces and Brownian motion effect

In this part we discuss the generic interaction forces that may present in particle momentum equation on some conditions. We present the particle equation of motion in the more general form of the Basset-Boussinesq-Oseen (BBO) equation, as introduced in in 2.3.1. This generic form can also be applied to non-spherical particles, although the forces in the BBO equation are originally derived for spherical particles and require modification for non-spherical cases. However, for non-spherical particles, the BBO equation requires modifications or alternative models like those based on slender body theory may be necessary [64]. Let us start with recalling the Lagrangian trajectory of a generic particle $p-th$, i.e. $\mathrm{d}\boldsymbol{X}_p(t)/\mathrm{d}t = \boldsymbol{V}_p(t)$. The momentum equation for this generic-shaped particle with mass m_p is given by

$$m_p \frac{\mathrm{d}\boldsymbol{V}_p(t)}{\mathrm{d}t} = \boldsymbol{F}_{INT} + \boldsymbol{F}_{EXT} + \boldsymbol{F}_{BROW} \tag{2.109}$$

where $\boldsymbol{F}_{INT}$ denotes the interaction forces exerted on particle including fluid long-range, and short-range, particle-particle and particle-wall interactions. As shown in the 2.3.1 in a viscous flow, the fluid long-range hydrodynamic forces include the drag, lift, Basset history, pressure gradient, and added mass forces that according to the size of the particle and its density ratio to the fluid these terms can be taken into account or disregarded from the equation (2.109). In addition, the short-range hydrodynamic force include lubrication force and other hydrodynamic forces like

drag and lift. Lubrication force is active when a thin-layer of fluid between two particle forms due to the short distance between particles. In this situation, particles can change their momentum through this thin layer. This mechanisms can also exists in wall-bounded flows acting between particle and a wall, arising from the pressure distribution in the thin fluid film between them. The height of this gap and the roughness of the surface of the particles can determine the magnitude of this force. Other hydrodynamic short-range forces excluding the lubrication force, can occur between multiple particles, modifying the drag and lift forces experienced by each particle. Note that the transition between short-range and long-range forces is gradual, and the relative importance of each type depends on the particle Reynolds number, particle spacing, and fluid properties. The concept of "short-range" and "long-range" interaction is often relative and can vary depending on the specific problem and the length scales involved. Consider two spherical particles approaching each other in a fluid. At large distances, the long-range hydrodynamic forces (drag, lift) dominate. As the particles get closer, the lubrication forces become increasingly important. The exact point at which one force becomes dominant over the other depends on the particle size, fluid viscosity, and relative velocity.

Another interaction force, is the inter-particle collision term which could have two different types. If the contact is significant, the friction force at contact must be added to the equation. Moreover, the head-on or oblique inter-particle collisions can be effective depending on the particle and carrier flow regimes, especially for a denser suspension. Both elastic and inelastic collision can occur and change the momentum of each particle through this effect. Note that in wall-bounded flows, the particle-wall interaction can be seen as a collision between a particle with another particle with the infinite radius. In some cases, the contact mechanics is used to model and investigate the cohesive and frictional collisions of particles with one another or solid walls. $\boldsymbol{F}_{EXT}$ denotes any external forces acting on any individual particle, e.g. the buoyancy force due to the gravitational force or electric field.

The last term $\boldsymbol{F}_{BROW}$ is the Brownian effect due to the microscopic fluctuations of the particle suspended in a fluid or fluid flow. While Brownian motion is often neglected in solving the equations for the fluid at the macroscopic scale, it becomes important for very small particles (e.g., in aerosol or colloidal suspensions). Although there is no universally accepted criterion for considering this term, it is recommended for tiny particles of the order of a few microns or less. Suspended particles with this

size or less are called colloidal in a generic sense, while larger particles are usually considered inertial particles[65].

The key factor like the Basset-Boussinesq-Oseen equation or . Maxey-Riley-Gatignol, is the size of particle which can determine which forces are present in the equation (2.109) under the assumptions we made in this study. Let us start with term $\boldsymbol{F}_{BROW}$, the Brownian force term due to the effect of the microscopic thermal noise. As it has been mentioned before this work is more focused on the inertial spherical particles with the size of less than Kolmogorov, and of the order of more than $10\mu m$. Thus, the Brownian effect due to the fluctuation-dissipation nature of the problem at microscale, is neglected in our study. On the other hand, particle-to-fluid density ratio is of order 1000, and the correction needed for light particles are disregarded. Since as discussed in 2.3.1 Particle-to-fluid density ratio can affect the significance of certain forces, such as added mass. The fluid flow is also in the Stokes regime and therefore, the only present force acts on particle is the Stokes drag, representing the only long-range hydrodynamic interaction force in the equation (2.109). Moreover, another contribution $\boldsymbol{F}_{INT}$ is due to the particle collision with one another or wall. Since our flow is unbounded, then there is no wall interaction accordingly. The inter-particle collision exists in parts of study since we aim to explore the role of this forces in heat transfer, even if the volume fraction of our study implies the dilute suspension. Moreover, short-range interaction of particle through fluid medium, i.e. lubrication force, is not considered at the volume fraction of our study. As regards the $\boldsymbol{F}_{EXT}$, there is no external field influences the particles and the particles are non-buoyant in our case and particles have no electrical charge either.

2.5 Particle feedback

In the previous sections, the governing equations for both the continuous (fluid) and discrete (particle) phases have been derived based on the assumptions pertinent to this study. These equations describe the momentum and energy transport for both the carrier fluid and the suspended particles. However, to fully capture the dynamics in a two-way coupling regime, it is essential to also model the feedback of the particles on the fluid velocity and temperature fields. In particulate flows, the interaction between the particles and the fluid can be characterized by different coupling regimes. According to the well-known classification proposed by Elghobashi in [66], these

regimes, one-way and two-way coupling, can be distinguished based on the volume fraction of the particles, φ, which is a critical parameter in determining the nature of particle-fluid interactions. The volume fraction φ is defined as the ratio of the volume occupied by the particles to the total volume of the system:

$$\varphi = \frac{N_p \mathscr{V}_p}{\mathscr{V}}, \tag{2.110}$$

where $\mathscr{V}_p$ is the volume of $p-th$ spherical particle, $\mathscr{V}$ is a generalized volume element of the fluid-particle system and N_p is the total number of spherical inertial particles within the volume element $\mathscr{V}$. Since in our point particle Eulerian-Lagrangian approach, we solve the governing equations in an Eulerian grid, the best choice for this volume element is the grid or cell volume. In the two-way coupling regime, it is crucial to incorporate the feedback effects of particles into the governing equations for the fluid. This involves adding source terms to the fluid momentum and energy equations that account for the cumulative impact of the particles drag force and thermal interactions. These source terms are typically derived based on the particle number density, their relative velocity with respect to the fluid, and the thermal gradients between the particles and the surrounding fluid. Elgobashi identified the one-way coupling for $\varphi < 10^{-6}$, while $\varphi > 10^{-6}$ up to a certain limit ($\varphi \approx 10^{-4}$ or 10^{-3}), falls into two-way coupling regime. However, recent investigations by Petersen et al. in [67] have approximately confirmed this classification, though it applies specifically to gas-solid flow regimes. In contrast, for solid-liquid two-phase flows, the critical volume fraction for transitioning to two-way coupling appears to be higher, around $\varphi > 10^{-4}$, because no modulation has been found below this range [68, 69, 15]. Determining an exact threshold for this transition remains challenging due to the complex nature of turbulence modulation by suspended particles. Our study focuses primarily on heat transfer and thermal effects. For this purpose, all numerical observations are conducted at a fixed volume fraction on the order of 10_{-4}. To evaluate the effect of particle back-reaction on the fluid's temperature field, we consider only thermal coupling between the phases. The momentum equation, however, remains in the one-way coupling regime throughout all case studies Carbone et al. in [32] found that the impact of momentum coupling is minimal in the thermal analysis of particle suspensions in turbulent flows. Therefore, to better understand the effects of thermal coupling on heat transfer, we conducted simulations using both one-way and two-way coupling regimes at a fixed volume fraction. This approach

allows us to explore how particle thermal feedback might enhance or diminish heat transfer compared to a one-way coupled flow. In Section 2.2, we introduced the particle thermal feedback, denoted as C_T. This term represents the thermal feedback from spherical particles per unit volume and unit time, and is given by

$$C_T(t,\boldsymbol{x}) = \frac{4}{3}\pi R^3 \rho_p c_{pp} \sum_{p=1}^{N_p} \frac{\mathrm{d}\Theta_p(t)}{\mathrm{d}t} \delta[\boldsymbol{x} - \boldsymbol{X}_p(t)], \tag{2.111}$$

where $\delta(\cdot)$ is the Dirac delta function centered on the particle position. In the point-particle approach, the feedback is effectively the projection of the particle back-reaction onto the grid points, which can be modeled by a superposition of $\delta(\cdot)$ functions. The inter-phase heat exchange between the fluid and particles in two-way coupling differs significantly from the one-way coupling scenario. In one-way coupling, energy flows from the fluid to the particle through mechanisms like convection, but the particle enthalpy content does not affect the fluid enthalpy. In contrast, in a two-way thermally coupled case, particles act as thermal sinks at their positions, with their feedback being incorporated into the fluid energy equation. This feedback term captures the thermal energy extracted by the particles, directly influencing the fluid temperature field. The numerical implementation of particle thermal feedback will be discussed in detail in next chapter.

2.6 Conclusion

In this chapter, we have established the theoretical foundation needed for investigating heat transfer in non-isothermal particle-laden flows. We derived and discussed the governing equations for both the continuous phase (the carrier fluid) and the discrete phase (the suspended particles), providing a robust framework for analyzing the dynamics and thermodynamics of both phases and their dynamical and thermal interactions. We also addressed the limitations and scope of these equations, outlining the assumptions made to our specific case study. Additionally, we performed a statistical analysis to derive the transport equations for fluid statistical moments in turbulent flows. Since we investigate the energy exchange between the carrier fluid and the inertial particles, in both one- and two-way coupling regimes, we also need a model for the particle thermal feedback on fluid temperature field. Thus, the expression which captures the particle thermal feedback is also developed and discussed.

While the derivation of statistically averaged transport equations for quantities such as turbulent heat flux and temperature variance was conducted under general flow conditions, we have marked the specific equations required for our problem by discussing the most relevant statistical quantities to the present study. Although some of these derived and discussed equations are utilized in the numerical analysis in the subsequent chapter, others are left for the future work to be numerically evaluated. It should be noted that he theoretical framework and generic equations presented in this chapter are not only applicable to the specific configuration of our study but also provide a foundation for analyzing more complex flow regimes different from our flow configuration.

Chapter 3

Heat transfer in particle-laden turbulent flows: Numerical method and results

3.1 Introduction

The basic flow configuration, which encapsulates the core physical problem of this study, i.e. heat transfer in non-isothermal particle-laden turbulent flows, is profoundly described in section 3.2, where the governing equations are presented in their non-dimensional form. In section 3.3, the numerical method utilized for conducting direct numerical simulations and solving numerically these governing equations is elaborated upon, providing a clear roadmap of the computational approach employed in this study. Moving forward to section 3.4, the results from the various set of simulations are meticulously presented and critically examined. This section is central to this present work as it directly addresses the primary objective of the study, which is to quantify the inertial and thermal effects of particles on heat transfer and the thermal field. This is achieved through the analysis of one-point and one-time statistical moments and correlations up to the second order. Furthermore, the study address the impact of key parameters, such as particle thermal feedback, inter-particle collisions, the Taylor microscale Reynolds number of the carrier flow, as well as the particle thermal Stokes number and Stokes number. Each of these factors is

considered and analyzed, contributing to a comprehensive understanding of their roles in the complex interplay between particles and turbulent fields.

3.2 Physical problem

This work aims to to investigate the heat transfer between two zones with different uniform temperatures, T_1 and $T_2 < T_1$, which are subjected to a homogeneous and isotropic turbulent velocity field. Therefore, the governing equations are numerically solved in a parallelepiped computational domain, with Cartesian coordinates (x_1, x_2, x_3). The dimensional carrier fluid field equations in Eulerian coordinate reads

$$\nabla \cdot \boldsymbol{u} = 0, \tag{3.1}$$

$$\frac{\partial \boldsymbol{u}}{\partial t} + \boldsymbol{u} \cdot \nabla \boldsymbol{u} = -\frac{1}{\rho_0} \nabla p + \nu \nabla^2 \boldsymbol{u} + \boldsymbol{f}_u, \tag{3.2}$$

$$\frac{\partial T}{\partial t} + \boldsymbol{u} \cdot \nabla T = \kappa \nabla^2 T + \frac{1}{\rho_0 c_{p0}} C_T. \tag{3.3}$$

Moreover, the entire domain is seeded uniformly by inertial spheres mimicking suspended particle whose velocity and temperature are initialized with the same fluid fields. Numerical scheme is discussed in detail in the section 3.3. Briefly speaking, each particle individually is tracked along its Lagrangian trajectory within the Eulerian grid by using Lagrangian Particle Tracking (LPT) technique. In this method each individual particle in the ensemble within the grid cell is modeled as a point-like, impenetrable, and undeformable rigid computational sphere.The employed Lagrangian governing equations for particles are

$$\frac{\mathrm{d}}{\mathrm{d}t} \begin{Bmatrix} \boldsymbol{X}_p(t) \\ \boldsymbol{V}_p(t) \\ \Theta_p(t) \end{Bmatrix} = \begin{bmatrix} 0 & 1 & 0 \\ 0 & -1/\tau_v & 0 \\ 0 & 0 & -1/\tau_\vartheta \end{bmatrix} \begin{Bmatrix} \boldsymbol{X}_p(t) \\ \boldsymbol{V}_p(t) \\ \Theta_p(t) \end{Bmatrix} + \begin{bmatrix} 0 \\ (1/\tau_v)\boldsymbol{u}(t, \boldsymbol{X}_p) \\ (1/\tau_\vartheta) T(t, \boldsymbol{X}_p) \end{bmatrix} \tag{3.4}$$

The dimension of this simple computational domain is defined by $x_1 \in [0, L_1]$, $x_2 \in [0, L_1]$ and $x_3 \in [-L_3/2, L_3/2]$, where L_1 is the domain length in directions x_1

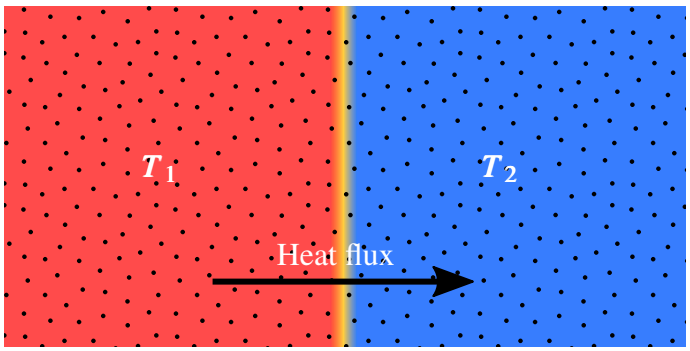

Fig. 3.1 Schematic of the parallelepiped computational domain

and x_2, and L_3 is the length in direction x_3. Two dimensions are set as $L_3 = 2L_1$ to avoid constraining the process, which ideally occurs in an infinite domain, through the computational domain extent. The temperature distribution is initialized by setting the temperature equal to T_1 in the half-domain where $x_3 < 0$ and to T_2 in the half-domain where $x_3 > 0$. The schematic representation of the computational domain can be seen in figure 3.1

3.2.1 Adimensionalization of governing equations

The governing equations ((3.1)-(2.111)) are solved in dimensionless form, normalizing them by using the size of the domain in the homogeneous direction, $L_1^* = L_1/(2\pi)$, as reference length, a reference velocity $U = (4\varepsilon L_1^*)^{1/3}$ deduced from the imposed mean kinetic energy dissipation rate ε through the body force $\boldsymbol{f}_u$ (see [32]), and the temperature difference $T_1 - T_2$. The dimensionless quantities can be computed as follows

$$\begin{aligned} \tilde{\boldsymbol{x}} = \boldsymbol{x}/L_1^*, \qquad \tilde{t} = tU/L_1^*, \qquad \tilde{\boldsymbol{u}} = \boldsymbol{u}_i/U, \\ \tilde{p} = (p - p_0)/(\rho U^2), \qquad \tilde{T}_* = T_*/(T_1 - T_2), \\ \tilde{X}_p = \boldsymbol{X}_p/L_1, \qquad \tilde{V}_p = \boldsymbol{V}_p/U, \qquad \tilde{\Theta}_p^* = \Theta_p^*/(T_1 - T_2). \end{aligned} \tag{3.5}$$

In the dimensionless form, the flow is governed by the Reynolds number $\mathrm{Re} = UL_1^*/\nu$, the Prandtl number $\mathrm{Pr} = \nu/\kappa$, and the particle-to-fluid heat capacity ratio $\varphi_\vartheta = \varphi(\rho_p c_{pp})/(\rho_0 c_{p0})$, where φ is the particle volume fraction, while particle dynamics is described by the Stokes numbers, which represent the ratio between their

relaxation times and the flow timescales. Given the arbitrariness of the length scale L_1^*, the flow is more conveniently and usually described by the Taylor microscale Reynolds number $\mathrm{Re}_\lambda = u'\lambda/\nu$, where λ is the Taylor microscale (u' is the root mean square velocity and $\lambda = u'/\sqrt{\langle||\nabla \boldsymbol{u}||^2\rangle}$ is the Taylor microscale), while the Kolmogorov timescale $\tau_\eta = (\nu/\varepsilon)^{1/2}$, which is the smallest timescale of the flow and characterizes the small scale velocity fluctuations of the fluid phase, will be used as reference timescale to normalize instead of the large-scale time of the adimensionalization. Thus, the Stokes number $\mathrm{St} = \tau_v/\tau_\eta$ and the thermal Stokes number $\mathrm{St}_\vartheta = \tau_\vartheta/\tau_\eta$ are used to describe the particle dynamical and thermal behaviour. By using the normalization defined in (3.5), having chosen $L_3 = 2L_1$, the dimensionless form of the governing equations ((3.1)-(3.3)) for the carrier flow is

$$\frac{\partial \tilde{u}_i}{\partial \tilde{x}_i} = 0, \tag{3.6}$$

$$\frac{\partial \tilde{u}_i}{\partial \tilde{t}} + \tilde{u}_j \frac{\partial \tilde{u}_i}{\partial \tilde{x}_j} = -\frac{\partial \tilde{p}}{\partial \tilde{x}_i} + \frac{1}{\mathrm{Re}} \frac{\partial^2 \tilde{u}_i}{\partial \tilde{x}_j \partial \tilde{x}_j} + \tilde{f}_{u,i}, \tag{3.7}$$

$$\frac{\partial \tilde{T}_*}{\partial \tilde{t}} + \tilde{u}_j \frac{\partial \tilde{T}_*}{\partial \tilde{x}_j} = -\frac{1}{2\pi}\tilde{u}_3 + \frac{1}{\mathrm{RePr}} \frac{\partial^2 \tilde{T}_*}{\partial \tilde{x}_j \partial \tilde{x}_j} + \tilde{C}_T, \tag{3.8}$$

where $\mathrm{Re} = (4\varepsilon L^4)^{1/3}/\nu$ is the Reynolds number, $\mathrm{Pr} = \kappa/\nu$ is the Prandtl number. This equations are solved in a $(0,2\pi)\times(0,2\pi)\times(-2\pi,2\pi)$ domain with periodic boundary conditions on $\tilde{u}_i$, $\tilde{p}$, $\tilde{T}_*$. Equation (4.1) becomes, in dimensionless form,

$$\frac{\mathrm{d}}{\mathrm{d}t}\begin{Bmatrix} \tilde{X}_{p,i}(\tilde{t}) \\ \tilde{V}_{p,i}(\tilde{t}) \\ \tilde{\Theta}^*_p(\tilde{t}) \end{Bmatrix} = \begin{bmatrix} 0 & 1 & 0 \\ 0 & -1/\tilde{\tau}_v & 0 \\ 0 & -\frac{1}{2\pi}\delta_{i3} & -1/\tilde{\tau}_\vartheta \end{bmatrix} \begin{Bmatrix} \tilde{X}_{p,i}(t) \\ \tilde{V}_{p,i}(t) \\ \tilde{\Theta}^*_p(t) \end{Bmatrix} + \begin{bmatrix} 0 \\ (1/\tilde{\tau}_v)\boldsymbol{u}(\tilde{t},\tilde{\boldsymbol{X}}_p) \\ (1/\tilde{\tau}_\vartheta)\tilde{T}_*(\tilde{t},\tilde{\boldsymbol{X}}_p) \end{bmatrix} \tag{3.9}$$

where the dimensionless particle relaxation times are given by

$$\tilde{\tau}_v = \mathrm{St}\frac{\tau_\eta U}{L_1^*} = \mathrm{St}\frac{2}{\mathrm{Re}^{1/2}}, \tag{3.10}$$

$$\tilde{\tau}_\vartheta = \mathrm{St}_\vartheta \frac{\tau_\eta U}{L_1^*} = \mathrm{St}_\vartheta \frac{2}{\mathrm{Re}^{1/2}}. \tag{3.11}$$

Finally, the dimensionless particle feedback term $\tilde{C}_T$ can be expressed as

$$\tilde{C}_T = \varphi_\vartheta \frac{16\pi^3}{N_p} \sum_{p=1}^{N_p} \frac{\tilde{T}_*(\tilde{t},\tilde{\boldsymbol{x}}) - \tilde{\Theta}^*_p(\tilde{t})}{\tilde{\tau}_\vartheta} \tilde{\delta}(\tilde{\boldsymbol{x}} - \tilde{\boldsymbol{X}}_p), \tag{3.12}$$

where φ_ϑ is the particle-to-fluid heat capacity ratio. A deterministic body force $\tilde{\boldsymbol{f}}$, linear function of the velocity, is used in equation (3.7) to keep the velocity field statistically steady by injecting energy in a single wavenumber $\tilde{k}_f$ (see also [32, 36] for further details about the forcing). In dimensionless form its representation in the Fourier space is given by

$$\hat{\tilde{\boldsymbol{f}}}(\tilde{t},\tilde{\boldsymbol{\kappa}}) = \frac{1}{4}\frac{\hat{\tilde{\boldsymbol{u}}}(\tilde{t},\tilde{\boldsymbol{\kappa}})}{\sum_{||\tilde{\boldsymbol{\kappa}}||=\tilde{\kappa}_f}\left|\left|\hat{\tilde{\boldsymbol{u}}}(\tilde{t},\tilde{\boldsymbol{\kappa}})\right|\right|^2}\tilde{\delta}(||\tilde{\boldsymbol{\kappa}}|| - \kappa_f). \tag{3.13}$$

The dimensionless formulation of the physical model of this section is the one actually discretized by the numerical code.

3.3 Numerical Method

Single-phase turbulent flow, per se, represents a multiscale and complex problem, often regarded as one of the last unsolved challenges in classical mechanics. The inherent complexity of this phenomenon is significantly heightened when a discrete phase, such as point-mass particle, is introduced into the already chaotic turbulent fields. The dual challenge of addressing both the turbulent flow and the interactions with a dispersed phase necessitates the use of advanced numerical simulations. In particular, when these simulations are performed with high fidelity, such as Direct Numerical Simulation (DNS), they require the resolution of all relevant spatiotemporal scales, including the smallest scales of turbulence. This demand places an immense burden on computational resources, requiring the use of massively parallel high-performance computing architectures and highly efficient algorithms. Although the application of DNS remains constrained to low to moderate Reynolds number flows due to these computational demands, it still serves as an invaluable tool in cases involving the interplay between particles and turbulent flow. In such cases, DNS can provide the detailed data necessary to deepen our understanding of this complex and non-trivial phenomenon. From a theoretical perspective, the Maxey-Riley-Gatignol (MRG) equation continues to be a focal point in the study of particle-laden turbulent flow, remaining an active and interesting subject in the literature. Despite its longstanding presence and the considerable interest it has generated, significant theoretical progress towards finding an analytical solution has yet to be achieved. This ongoing challenge underscores the relevance of our

work, in which we aim to establish a foundation for formulating the thermal and dynamical performance of heavy suspended inertial particles in turbulent flows, using the insights gained from DNS results. To accomplish this, the spatial discretization in our simulations is performed using the Fourier-Galërkin Pseudo-spectral method. This method constructs the solution as a finite Fourier series, enabling precise representation of the flow field while leveraging the efficiency of spectral methods. This approach not only ensures high accuracy in the numerical solution but also aligns with the demanding requirements of DNS, allowing us to capture the complex interactions between turbulence and dispersed particles with the necessary level of detail.

Time integration is carried out for both the carrier flow equations ((3.1)-(3.3)) and the particle equations (4.1) using a second-order exponential integrator, which ensures accuracy and stability over the course of the simulations. For the interaction between the particles and the fluid, B-spline reversed interpolation (NUFFT forward) is employed for the back reaction or feedback from particles to the fluid, while B-spline interpolation (NUFFT backward) is utilized to determine the fluid velocity and temperature at the particle positions. These interpolation techniques are essential for accurately capturing the exchange of momentum and energy between the fluid and particles, and they are explained in detail in [70]. The fluid flow is driven by a deterministic linear forcing applied in Fourier space, which maintains the desired turbulence characteristics over time. In addition, forward and inverse Fourier transforms are used to transition between real space and complex (Fourier) space, allowing efficient handling of the spectral data. The resolution of the simulation is directly tied to the number of Fourier modes considered, with a higher number of modes leading to finer resolution and more accurate representation of the turbulent structures. The evolution of particle trajectories, velocities, and temperatures is computed at each time step by discretizing the corresponding governing equations. The Eulerian carrier flow field variables, such as fluid velocity and temperature, are computed at the nodes of a structured grid. However, since particles can be randomly distributed anywhere within the computational domain, a B-spline interpolation was necessary to compute the forces exerted by the fluid on the particles and to capture the back reactions of particles on the continuous fluid fields. This interpolation ensures that the interaction between the discrete and continuous phases is accurately represented, maintaining the integrity of the simulation results.

In spectral methods, computations are typically performed in real space but are transformed into spectral space through a series of Fourier transforms. This approach has earned significant interest in the field of computational fluid dynamics because, in Fourier space, the spatial derivatives in the Navier-Stokes equations are eliminated, leaving only temporal derivatives in the transformed equations. This transformation simplifies the handling of differential operators and can lead to more efficient computations. However, the challenge arises with the nonlinear terms, particularly the convective term in the fluid momentum equation. In Fourier space, this term manifests as a convolution integral, which is computationally expensive and impractical to evaluate directly. To overcome this, an inverse Fourier transform is employed, allowing the nonlinear term to be computed in real space. This practice gives rise to the term pseudospectral method, as it combines spectral and real-space computations. In pseudospectral methods, the flow fields are evaluated on a fixed Eulerian grid, which must be structured, Cartesian, and uniformly spaced to take full advantage of the Fast Fourier Transform (FFT) algorithm. This grid structure is essential for efficiently managing the computational demands of the spectral method. Parallel to the typical particle Lagrangian tracking algorithms, the Lagrangian equations for each individual particle are integrated along its path, taking into account the dynamics of the particle as it interacts with the surrounding flow. However, effective inter-phase coupling, between the discrete particles and the continuous fluid phase, requires a method that is both accurate and specialized, differing from those used solely for fluid or particle solvers. In a one-way coupling regime, where the particles do not affect the fluid flow but are influenced by it, the forcing terms in the particle momentum and energy equations must be computed by interpolating fluid properties (such as velocity and temperature) at the particle position within the Eulerian grid cells. Conversely, when feedback from particles onto the fluid flow is considered (as in two-way coupling), this effect must be accurately projected back from the particle position onto the Eulerian grid points. Direct interpolation from the grid to the particle position is computationally straightforward, with several interpolation methods available in the literature varying in accuracy, such as linear or B-spline interpolation schemes. The feedback computation, however, is more challenging, with fewer effective methods available. One commonly used technique is the Particle-In-Cell (PIC) method, which is a low-order scheme employed to project the influence of the particle phase back onto the Eulerian grid. The smoothness of the resulting projected fields is heavily influenced by the particle number density.

However, this low-order method has notable drawbacks. Due to the use of low-order polynomials, the accuracy of Lagrangian particle statistics can be compromised, as discussed by Hinsberg et al. in [71]. Furthermore, Carbone et al. demonstrated in [32] that Eulerian statistics can also be degraded when low-order methods are employed. Additionally, low-order schemes can introduce numerical instabilities, leading to a reduction in the overall accuracy and reliability of the simulation results.

In general, low-order methods can significantly reduce the overall accuracy of numerical simulations, particularly in complex flows involving particle interactions. However, B-spline interpolation has proven to be a robust and reliable method for one-way coupling flows, where the influence of the particles on the fluid is negligible. As demonstrated by Carbone et al. in [70], this method was effectively introduced and implemented in a pseudo-spectral code. In this study, we employ a forward NUFFT to compute particle feedback at the Eulerian grid points, while B-spline interpolation is conducted via a backward NUFFT. The foundation of this method lies in the convolution theorem for Fourier transforms. The approach involves convolving the particle phase data with a prescribed basis function, followed by a FFT. Due to the inherent symmetry between the backward and forward transformations, the non-local convolution operation, initially computed in physical space, is effectively canceled out in Fourier space. This symmetry not only simplifies the computational process but also ensures that the interpolation scheme meets all necessary consistency constraints, allowing for the efficient implementation of high-order interpolations. The accuracy and reliability of this method have been rigorously examined and documented by Carbone et al. in [70, 32]. Their work demonstrates that the NUFFT method accurately represents the particle phase in Fourier space and provides a detailed spectral characterization of the particle statistics. This capability is crucial for high-fidelity simulations where precise representation of both the fluid and particle phases is essential for capturing the complex interactions and dynamics within the flow.

Alternatively to low-order methods for feedback modeling, Gaussian kernels have been employed to regularize the impulsive forces exerted by particles, as demonstrated in [72]. This technique, often referred to as regularization functions in the literature, addresses the issue of computational instabilities. However, the choice of regularization scale can introduce high-frequency damping into the simulation, which may affect the accuracy of the results. To mitigate this scale dependence, the Steady Stokeslet approach has been proposed [73]. Although this method effectively

cancels the scale dependence, it presents significant challenges in parallelized simulations, as each particle can influence a large portion of the surrounding domain, leading to considerable computational overhead. More recently, a more affordable and efficient method has been introduced by Gualtieri et al. in [74] for calculating particle back-reaction on a Cartesian grid. This approach utilizes the closed solution of an unsteady Stokes flow around a small rigid spherical particle and analytically isolates the singular part of the Stokes flow surrounding each particle. The isolated singular component is then reintroduced into the flow after a predefined regularization time. This method, known as the Exact Regularized Point Particle (ERPP) approach, ensures accurate conservation of mass, momentum, and energy. However, the algorithm requires computing the analytical solution for unsteady Stokes flow at the previous time step for each time step, which adds computational complexity. In this study, we employ NUFFT approach, which is implemented in three distinct steps. First, a convolution of the field is performed in physical space using a basis function to regularize the field. Next, the regularized field is transformed into Fourier space. Finally, a deconvolution operation is carried out in Fourier space to retrieve the desired results. The accuracy of this method is influenced by the choice of the basis function used for the convolution and by the smoothness of the field. Within the point-particle approach, where particles are modeled as material points, the particle feedback is represented by a superposition of Dirac delta functions centered on the particles. Due to its superior performance compared to other available methods, the B-spline polynomial basis was selected by Carbone et al. as the basis function for this approach [32]. The B-spline interpolation not only ensures higher accuracy but also enhances the smoothness of the interpolated fields, making it an optimal choice for capturing the complex interactions between particles and the carrier flow.

Carbone et al. in [70, 75] assessed the accuracy of the NUFFT in DNS by examining how the order of the B-spline basis influences the spectral representation of the coupling terms. A quantitative assessment of convergence is achieved by comparing the spectra of the coupling terms calculated using B-splines of varying orders. In DNS using NUFFT with B-spline basis, a significant issue arises from the self-interaction of particles. This self-interaction occurs when particles interact with themselves, leading to an artificial and infinite accumulation of spectral energy, particularly at large wavenumbers. This problem is amplified for particles with high inertia $(\mathrm{St} > 1)$, where the lack of correlation between particle pairs induces a dominant κ^2 trend in the spectrum. κ^2 trend refers to the scaling of the spectral

energy associated with these high-inertia particles increasing with the square of the wavenumber. This typically means that more energy is concentrated in the higher wavenumbers (smaller scales), which can be a signature of strong particle self-interaction or other similar phenomena. This trend distorts the spectral energy distribution, making it challenging to accurately represent the underlying physical processes. Carbone et al. addresses this issue by carefully distinguishing between the full distribution C, which accounts for the variable density of particles, and the equivalent field a, which is the smooth field that the particles interpolate. The expression for the equivalent field a involves several approximations, notably neglecting variations of the field on the scale of Δx. When the number of particles in a given box B is sufficiently large, symmetry causes the odd derivative contributions to vanish, while even derivatives significantly impact the representation of the equivalent field. The curvature of the field a at a point x provides the most substantial contribution, ensuring a more accurate and regularized spectral energy representation, effectively mitigating the self-interaction problem. More detail can be found in [70, 75]. The delta function is highly localized in physical space and can be challenging to represent numerically on a discrete grid, especially in Fourier space where its Fourier transform is constant. To ensure an accurate representation of particle feedback in Fourier space, we employ smoothing or regularization techniques that approximate the delta function more effectively on a discrete grid. In our study, the impact of self-interaction artifacts is further minimized due to the nature of the dilute suspension, where particles are sparsely distributed, making self-interaction less likely.

In physical models in literature for capturing the particle feedback, is mostly a delta function. Delta function in fact represents the interaction in a highly localized manner. In general, this method does not involve any form of regularization, leading to challenges in accurately representing the particle feedback, especially when considering the spectral energy at large wavenumbers. Regularization, however, plays a critical role in smoothing out these interactions by filtering out the high-frequency components that contribute to the artificial spectral energy caused by particles self-interaction. In the NUFFT approach, as we use in this study, B-splines are used to model the particle feedback. Thus, the regularization is achieved by transforming the smooth field a into spectral space via a FFT, leading to the mitigation of the high wavenumber artifacts. In contrast, in ERPP method by Gualtieri et al., the unsteady Stokes equation for each particle, analytically solves for the particle interaction without the need for empirical regularization techniques. This method

provides an exact representation of the particle feedback by solving the Stokes equation directly, capturing the precise dynamics of each particle interaction with the fluid. While this approach is more computationally intensive, it eliminates the need for artificial regularization and provides a more accurate solution in scenarios where precise fluid-particle interactions are critical [74]. Overall, the choice between these approaches depends on the balance between computational efficiency and the need for accuracy in representing particle feedback. NUFFT method with B-spline basis and regularization via FFT provides a practical solution for large-scale simulations, while ERPP approach is suited for cases requiring exact solutions at the expense of higher computational cost.

If any fluid field variable, such as fluid velocity or temperature, is known at a finite number of discrete points M in physical space, we can perform a discrete FFT algorithm. These quantities can be expressed as finite Fourier series:

$$\boldsymbol{u}(t,\boldsymbol{x}) = \sum_{k} e^{i\boldsymbol{k}\cdot\boldsymbol{x}} \hat{\boldsymbol{u}}(t,\boldsymbol{k}) \tag{3.14}$$

$$T(t,\boldsymbol{x}) = \sum_{k} e^{i\boldsymbol{k}\cdot\boldsymbol{x}} \hat{T}(t,\boldsymbol{k}) \tag{3.15}$$

where $\boldsymbol{k}$ is the wavenumber vector, and $\hat{\boldsymbol{u}}(t,\boldsymbol{k})$ and $\hat{T}(t,\boldsymbol{k})$ are the Fourier coefficients of the velocity and temperature fields in Fourier space, respectively. To perform the Fourier transform, all Fourier coefficients must be known. However, since it is impossible to compute an infinite number of Fourier coefficients, we assume that the Fourier coefficients are limited to a finite number N , such that $\hat{\boldsymbol{u}}(t,\boldsymbol{k}) = \hat{T}(t,\boldsymbol{k}) = 0$ for $\|\boldsymbol{k}\| > N/2$. This assumption is justified by the concept of exponential convergence, which ensures that the truncated Fourier series can still accurately represent the variable of interest in Fourier space. The computational complexity of the FFT algorithm in this approach is of the order $N \log N$, making it highly efficient for large datasets. For any discrete Fourier transform, the length of the Fourier transform N is determined by the number of function values M in physical space, such that $N = M$. As a result, we obtain a truncated Fourier series, leading to an interpolating polynomial of order N, as opposed to the infinite-order polynomial that would be expected in theory. In standard FFT applications, if it is required that $N > M$, the output of the FFT algorithm is padded with zeros for values of $k > M$. Conversely, if $N < M$, the output is truncated, or chopped, to match the desired length. This truncation or padding is an essential part of working with discrete

data in Fourier space, allowing us to manage the balance between computational feasibility and the accuracy of the spectral representation of fluid field variables.

By setting $L_1 = 2\pi$, we effectively define both the length of the computational domain in the homogeneous direction and the periodicity of the functions under consideration. This choice simplifies the Fourier series expansion as it ensures that the coefficient $(1/NL_1)^3 = (1/2\pi/L_1)^3$, which appears in the series, will cancel out. In this context, the wavenumber $\boldsymbol{k}$ is expressed as

$$\boldsymbol{k} = k_0\boldsymbol{n} = k_0(n_1\boldsymbol{e}_1 + n_2\boldsymbol{e}_2 + n_3\boldsymbol{e}_3), \tag{3.16}$$

where $k_0 = 2\pi/L_1$ represents the fundamental or zero wavenumber, and n_i are integers satisfying $1 - N/2 < n_i < N/2$. Here, N denotes the total number of Fourier modes considered in each direction, which also dictates the grid resolution Δx in the physical space. The general Fourier mode, a product of individual modes in the directions 1, 2, and 3, can be written as

$$e^{i\boldsymbol{k}\cdot\boldsymbol{x}} = e^{ik_0n_1x_1}e^{ik_0n_2x_2}e^{ik_0n_3x_3}. \tag{3.17}$$

From the magnitude of the wavenumber vector $||\boldsymbol{k}||$, we can determine its direction $\boldsymbol{e} = \boldsymbol{k}/||\boldsymbol{k}||$, where $||\boldsymbol{k}|| = \sqrt{k_1^2 + k_2^2 + k_3^2} = k$. The grid spacing Δx is inversely related to the maximum wavenumber k_{max} and is given by

$$\Delta x = \frac{L_1}{N} = \frac{\pi}{k_{max}}, \tag{3.18}$$

where $k_{max} = Nk_0/L_1 = \pi N/L_1$. The Fourier transforms between physical space and Fourier space are computed using the Fast Fourier Transform (FFT) algorithm. Given the finite number of modes considered, it is crucial to apply appropriate dealiasing techniques to mitigate aliasing errors and ensure the accuracy of the simulation.

To derive the governing equations in Fourier space, we first apply the Fourier transform to all field variables in the equations. This process is relatively straightforward for linear terms. However, applying the Fourier transform to the nonlinear terms, such as those appearing in the convective term of the momentum equation, presents a more complex challenge. We begin by focusing on the convective term in the momentum equation. Taking the Fourier transform of this term, we then consider the spatial derivatives in physical space. This results in the following equation in

Fourier space

$$\frac{\partial \hat{u}_j(t,\boldsymbol{k})}{\partial t} + \hat{G}_j(t,\boldsymbol{k}) = -ik_j\hat{p}(t,\boldsymbol{k}) - \frac{1}{\mathrm{Re}}k^2\hat{u}_j(t,\boldsymbol{k}), \tag{3.19}$$

where $\hat{G}_j$ is defined as $\hat{G}_j = (k_j k_k/k^2)\hat{G}_k$. By using this relationship, the projection tensor $P_{jk}(\boldsymbol{k})$ is introduced, defined as $P_{jk} = [\delta_{jk} - (k_j k_k/k^2)]$. This allows us to express $\hat{G}_j$ in terms of the projection tensor: $\hat{G}_j = P_{jk}\hat{G}_k$. This projection is critical for ensuring that the terms are projected onto a plane perpendicular to the wavenumber vector $\boldsymbol{k}$. From the continuity equation for incompressible flow, we know that $k_j\hat{u}_j = 0$. Multiplying the transformed momentum equation (3.19) by k_j, we derive the transformed Poisson equation for pressure in Fourier space. This equation expresses the pressure term in terms of the convective term

$$k^2\hat{p}(t,\boldsymbol{k}) = ik_j\hat{G}_j(t,\boldsymbol{k}), \tag{3.20}$$

This equation provides the necessary relation between pressure and the convective term in the transformed Navier-Stokes equations.

By substituting the pressure Fourier coefficient into the transformed momentum equation (3.19), we can derive the equation in terms of the projection operator P_{jk} and the velocity Fourier coefficient. This results in

$$\frac{\partial \hat{u}_j(t,\boldsymbol{k})}{\partial t} = -\frac{1}{\mathrm{Re}}k^2\hat{u}_j(t,\boldsymbol{k}) - P_{jk}\hat{G}_k(t,\boldsymbol{k}). \tag{3.21}$$

In our case, where there is an external forcing term, the non-dimensional fluid governing equations in Fourier space are given by

$$k_j\hat{u}_j = 0, \tag{3.22}$$

$$\frac{\partial \hat{u}_j}{\partial t} + ik_k\widehat{u_k u_j} = -ik_j\hat{p} - \frac{1}{\mathrm{Re}}k^2\hat{u}_j + \hat{f}_{u,j}, \tag{3.23}$$

$$\frac{\partial \hat{T}_j}{\partial t} + ik_k\widehat{u_k T_j} = -\frac{1}{\mathrm{RePr}}k^2\hat{T}_j + \hat{C}_T. \tag{3.24}$$

In our study, the velocity field is considered as a forced homogeneous and isotropic field, which means that it is uniformly distributed and statistically similar in all directions, and it is influenced by an external forcing term. On the other hand, the temperature field is treated as a time-evolving passive scalar, which implies that it

does not influence the flow dynamics but responds to the changes in the flow field. To address this setup, the Fourier coefficient of the external body force, $\hat{f}_{u,j}$, can be obtained by analyzing the transport equation for turbulent kinetic energy. In the case where the forcing term is a linear function of the velocity field, specifically $\hat{f}_{u,j} = \alpha \hat{u}_i(t,\boldsymbol{k})$ and $\forall \alpha \in \mathbb{R}$, the linear deterministic forcing term can be expressed as

$$\hat{f}_{u,i}(t,\boldsymbol{k}) = \varepsilon \frac{\hat{u}_i(t,\boldsymbol{k})}{\sum_{||\boldsymbol{\kappa}||=\kappa_f} ||\hat{u}_i(t,\boldsymbol{k})||^2} \delta(||\boldsymbol{k}|| - k_f), \tag{3.25}$$

where ε denotes the energy dissipation imposed by the forcing term, and k_f is the specific wavenumber at which forcing is applied. The delta function $\delta(||\boldsymbol{k}|| - k_f)$ ensures that the forcing is active only at the wavenumber k_f, while $\hat{f}_{u,j}(t,\boldsymbol{k})$ is zero for other wavenumbers. To discretize the spatial domain of the fluid phase equations, we use a fully dealiased pseudospectral method, which is implemented with the 3/2-rule to avoid aliasing errors [76]. This method ensures that the spatial domain is accurately represented by a finite set of Fourier modes. The interpolation of fluid velocity and temperature at particle positions, as well as the computation of particle thermal feedback, is conducted using a modern numerical method [70, 75]. This method employs inverse and forward non-uniform fast Fourier transforms (NUFFT) combined with a fourth-order B-spline basis to achieve high accuracy in representing the particle phase. Given that the forcing term dictates the mean dissipation rate ε under statistically steady conditions, the Kolmogorov microscale η can be determined in advance. This scale is essential for understanding the turbulence dynamics. Additionally, the integral scale of the flow is controlled by the forced wavenumber k_f, which directly influences the energy distribution across different scales in the flow. By knowing these scales, we can better analyze and interpret the interplay between turbulence and particle dynamics, thermodynamics and overall heat transfer processes.

3.3.1 Simulation setup and flow parameters

As explained in the previous section, we solve the carrier flow governing equations ((3.1)–(3.3)) using a Fourier-Galërkin method. In this approach, periodic boundary conditions are applied to each face of the computational domain, which assumes a statistically homogeneous turbulent flow. However, special treatment is required for

the fluid temperature field in the inhomogeneous direction. The initial temperature difference between two homothermal regions leads to the formation of a time-evolving mixing layer across the separating plane. This mixing layer thickens over time due to the combined effects of diffusion and convection. In such a case, it is expected that two highly intermittent sublayers will develop, bounding a well-mixed central region of the mixing layer between the two temperature regions [77]. Moreover, to avoid numerical issues arising from the discontinuity between the two homothermal halves of the computational domain (located at $x_3 = 0$), the initial temperature profile is smoothly initialized using a hyperbolic tangent function, similar to the approach described in [8] and [77]. The initial temperature $T(0,\boldsymbol{x})$ is given by

$$T(0,\boldsymbol{x}) = T_1 + \frac{T_2 - T_1}{2}\left[1 + \tanh\left(a\frac{x_3 - L_3/2}{L_3/2}\right)\right], \tag{3.26}$$

where a is a parameter controlling the smoothness of the transition. To avoid the Gibbs phenomenon during the discrete Fourier transform operation, the coefficient a must be chosen to ensure that the smoothing transition spans over a length of a few grid spacing Δx. On the other hand, the particle velocity and temperature fields are initialized based on the carrier fluid fields at the particle positions. For temperature, this initialization assumes that particles have been in the two uniform temperature regions long enough to achieve thermal equilibrium with the surrounding carrier flow. This approach ensures that the particles start with temperature conditions that are consistent with the initial distribution in the fluid, avoiding any spurious effects due to initial misalignment of the particle and fluid temperature fields. Thus, to simulate a single temperature mixing layer in a consistent way, we decompose the temperature field into a steady mean linear field and a residual fluctuating part as follows

$$T(t,\boldsymbol{x}) = \frac{T_1 + T_2}{2} + \frac{T_2 - T_1}{L_3}x_3 + T_*(t,\boldsymbol{x}), \tag{3.27}$$

where the origin is taken at the center of the domain, allowing periodic boundary conditions to be applied to the residual part T_*. The same decomposition is applied to the particle temperature

$$\Theta_p(t) = \frac{T_1 + T_2}{2} + \frac{T_2 - T_1}{L_3}x_3 + \Theta_p^*(t). \tag{3.28}$$

The initial fluid velocity field is derived from a dedicated simulation of homogeneous and isotropic turbulence, carried out until a statistically steady state is achieved. A large-scale, low-wavenumber forcing, which is a linear function of the current velocity, is applied as described in [32]. To maintain consistency with the physics of the two-phase flow and the boundary conditions of the fluid phase, any particle that exits the computational domain is reintroduced on the opposite side with the same velocity and residual temperature Θ_p^*. This approach ensures that no spurious values are introduced in the inhomogeneous direction x_3, as the temperature Θ_p^* of the particles entering and exiting the domain has the same probability density function. The modified fluid and particle temperatures, using this decomposition, can be expressed as:

$$\partial_t T_* + \boldsymbol{u} \cdot \nabla T_* = -\frac{T_2 - T_1}{L_3} u_3 + \kappa \nabla^2 T_* + \frac{1}{\rho_0 c_{p0}} C_T, \tag{3.29}$$

$$\frac{\mathrm{d}\Theta_p^*}{\mathrm{d}t} = \frac{T_*(t, \boldsymbol{x}_p) - \Theta_p^*}{\tau_\vartheta} - \frac{T_2 - T_1}{L_3} V_{p,3}. \tag{3.30}$$

Numerical simulations are carried out by solving the non-dimensional governing equations for both the continuous fluid phase and the discrete particle phase. In the simulation, the carrier flow is governed by the relevant dimensionless numbers: the Reynolds number Re, which represents the ratio of inertial forces to viscous forces, and the Prandtl number $\mathrm{Pr} = \nu/\kappa$, which indicates the ratio of momentum diffusivity to thermal diffusivity. Non-buoyant heavy inertial particles are characterized by two dimensionless numbers: the Stokes number and the thermal Stokes number. The Stokes number, $\mathrm{St} = \tau_v/\tau_\eta$, represents the particle momentum response time τ_v relative to the small-scale turbulence time scale, known as the Kolmogorov time scale $\tau_\eta = (\nu/\varepsilon)^{1/2}$. The thermal Stokes number, $\mathrm{St}_\vartheta = \tau_\vartheta/\tau_\eta$, compares the particle thermal response time to the Kolmogorov time scale. The ratio between these two numbers specifies the particle-to-fluid heat capacity ratio. Other parameters that characterize different flow regimes include the particle volume fraction φ, the particle thermal mass fraction φ_ϑ, and the particle-to-fluid density ratio ρ_p/ρ_0.

A large number of flow parameters is required for a comprehensive set of simulations to cover the entire parameter space, which implies considerable computational resources. Due to limitations in computational resources and the vast degrees of freedom of the problem, considering all relevant parameters is impractical. Therefore, we must fix some of the parameters. The selection of the most important parameters

is essential, especially when thermal two-way coupling is considered. In such cases, each combination of St and St_ϑ must be simulated separately, which is computationally demanding. Additionally, investigating the effect of inter-particle collisions increases computational time due to the time-consuming nature of collision detection algorithms. Consequently, in the present study, we restrict our focus to heat transfer at low to moderate Reynolds numbers. Specifically, we simulate only four Taylor microscale Reynolds numbers $\mathrm{Re}_\lambda = u'\lambda/\nu = 2E_k/\sqrt{5/3\nu\varepsilon}$, where $u' \equiv \sqrt{2E_k/3}$ is the root mean square of fluid velocity fluctuations, $\tau \equiv \ell/u'$ is the large-eddy turnover time, and E_k is the turbulent kinetic energy. In the first set of simulations, where $\mathrm{St}_\vartheta/\mathrm{St}$ is kept constant, we simulate different Taylor microscale Reynolds numbers Re_λ ranging from 37 to 124. The extension to higher Reynolds numbers, at which a fully developed inertial range exists, is left for future exploration. In all simulations, grid spacing Δx is determined by considering only active Fourier modes after dealiasing. However, since the mixing of a scalar through a sharp scalar interface is mainly driven by the large scales of the flow [32], and the largest eddies are considered the most important in thermal coupling [11], these Reynolds numbers should be high enough to quantify heat transfer between the two homogeneous regions in a developed turbulent flow. Flows at different Reynolds numbers have been obtained by varying the grid resolution and by modulating the wave number κ_f at which the forcing is applied. The main parameters of the simulations are listed in Table 3.1. To allow the temperature mixing layer to develop without being confined by the domain, an aspect ratio of 2 to 3 for the domain has been used. Specifically, the dimensionless domain is 2π in directions x_1 and x_2, but 4π or 6π in direction x_3. Consequently, the parallelepiped domain has been discretized with $128^2 \times 384$ grid points at $\mathrm{Re}_\lambda = 37$ and with $256^2 \times 512$ grid points at higher Reynolds numbers, maintaining the same resolution in all directions. Because the code is dealiased using the 3/2 rule, the maximum simulated wavenumber is $N/2$ and not $N/3$, where N is the nominal number of points in x_1 and x_2 directions. Consistently, all non-linear convective terms, as well as fluid interpolation at particle positions and particle thermal back-reactions on the temperature field, are computed on a 3/2 times finer grid. Thus, a $192^2 \times 576$ grid is used at $\mathrm{Re}_\lambda = 37$ and a $384^2 \times 768$ grid is used at higher Reynolds numbers. With the resolution set such that $\Delta x/\eta \simeq 1.6$, where Δx is the mesh spacing in physical space (or $\Delta x/\eta \simeq 1.1$ if considering the 3/2-rule finer grid), the method allows accurate interpolation in physical space and a precise spectral representation of thermal feedback (see [70] for error evaluation), as discussed in

detail previously. In all simulated flows in this study, to avoid complexity, some of the carrier flow and particle parameters are kept constant. Specifically, the Prandtl number on the fluid side, and the particle volume fraction and particle-to-fluid density ratio on the particle side, are held constant. For the first set of simulations, in the collisionless regime, the carrier flow and particle parameters are reported in Tables 3.1 and 3.2. For the collisional regime, to quantify the effect of particle collisions, simulations are performed with the same settings, but the Re_λ for collisional regimes ranges from 56 to 124. In the second set of simulations, with $\mathrm{St}_\vartheta/\mathrm{St} \neq \mathrm{Const.}$, only one Re_λ, 56, is simulated due to the large range of particle parameters. However, the comparison between one-way and two-way coupling is provided for all cases to evaluate the effect of particle thermal feedback.

Table 3.1 Dimensionless flow parameters of carrier phase flow fields for $\mathrm{St}_\vartheta/\mathrm{St} = \mathit{Const}$.

Simulation		**I**	**II**	**III**	**IV**
Taylor microscale Reynolds number	Re_λ	37	56	86	124
Prandtl number	Pr	0.71	0.71	0.71	0.71
mean turbulent kinetic energy dissipation rate	ε	0.25	0.25	0.25	0.25
Forced wavenumber	k_f	3	5	$\sqrt{6}$	$\sqrt{3}$
Kolmogorov length scale	η	0.041	0.0153	0.0153	0.0153
Kolmogorov time scale	τ_η	0.188	0.098	0.098	0.098
Taylor microscale	λ	0.51	0.226	0.29	0.35
Integral length scale	ℓ	0.72	0.40	0.74	0.94
Root mean square of velocity fluctuations	u'	0.64	0.59	0.71	0.85
Resolution	$\Delta x/\eta$	1.2	1.6	1.6	1.6
Grid size (after dealiasing)	$N_1 = N_2$	128	256	256	256
	N_3	384	512	512	512

The particles seeding the flow are monodisperse, meaning they have identical physical properties, same radius, density, and specific heat, resulting in the same relaxation times for all particles. Particle inertia is characterized by the Stokes number, $\mathrm{St} = \tau_v/\tau_\eta$, while particle thermal inertia is described by the thermal Stokes number, $\mathrm{St}_\vartheta = \tau_\vartheta/\tau_\eta$. The ratio $\mathrm{St}_\vartheta/\mathrm{St} = (3/2)(c_{pp}/c_{p0})\mathrm{Pr}$ represents the relationship between momentum and thermal relaxation times and depends solely on the thermal properties of the carrier fluid and particles. For air, this ratio ranges

between 0.5 and 1 for metallic particles and soot, about 2 for organic materials like wood or oils, slightly above 2 for ice particles, and around 4.43 for pure water droplets. In our simulations, we cover a wide range of Stokes numbers, from 0.1 to 3, while keeping $\mathrm{St}_\vartheta/\mathrm{St}$ fixed at 0.5 and 4.43, with a Prandtl number of 0.71. This approach allows us to explore a representative parameter range for particles in air. Relevant particle parameters are summarized in Table 3.2. We use a particle volume fraction of $\varphi = 4 \times 10^{-4}$ in all simulations. This value is sufficient to ensure that two-way momentum coupling between particles and the fluid is significant but low enough to neglect particle collisions and interactions, which become notable at volumes greater than 10^{-3}. Two-way coupling is appropriate for this volume fraction [78], but we also considered one-way coupling scenarios. Without collisions, particles behave independently, making one-way coupling feasible. The high volume fraction provides a larger statistical sample but does not represent actual particle concentrations. In the collisional regime, however, the number of particles is crucial. Therefore, simulations in this regime are conducted with enough particles to accurately capture collision effects on flow statistics, particularly heat flux.

Table 3.2 Particle parameters in dimensionless code units for one-way and two-way coupling regimes.

Particle volume fraction	φ	4×10^{-4} (two-way coupling)
Density ratio	ρ_p/ρ_0	10^3
Stokes number ratio	$\mathrm{St}_\vartheta/\mathrm{St}$	0.5 ; 1 ; 2 ; 3 ; 4 ; 4.43 (one-way coupling)
		4.43 (two-way coupling)
Stokes number	St	0.1 ; 0.2 ; 0.3 ; 0.5 ; 0.7 ; 0.8 ; 0.9 ; 1 ; 1.2 ; 1.5 ; 2 ; 2.5 ; 3

In the first part of the study, both particle thermal inertia and particle inertia are considered together as dependent parameters in the numerical analysis. As shown in Table 3.1, results from simulations covering four different Taylor microscale Reynolds numbers, Re_λ, are discussed. To analyze the effects of particle thermal inertia independently of particle inertia, we should treat momentum and thermal relaxation times as separate parameters. This approach contrasts with previous studies where these parameters are typically proportional, allowing us to isolate and examine each effect individually. For simplicity and to focus on particle inertia, we perform simulations at a single Reynolds number, equal to 56, thereby reducing the number of variables. Our main goal in this part is to clarify and characterize how

particle inertia and thermal inertia affect turbulent heat flux, while also investigating the behavior of particles under various limiting conditions.

Table 3.3 Flow parameters for $\mathrm{St}_\vartheta/\mathrm{St} \neq \text{Const.}$

Taylor Reynolds number	Re_λ	56
Taylor microscale	λ	0.226
Integral length scale	ℓ	0.40
R.M.S of velocity fluctuations	u'	0.59
Forced wavenumber	k_f	5
Prandtl number	Pr	0.71
mean TKE dissipation rate	ε	0.25
Kolmogorov length scale	η	0.0153
Kolmogorov time scale	τ_η	0.098
Particle volume fraction	φ	4×10^{-4}
Density ratio	ρ_p/ρ_0	10^3
Thermal Stokes number	St_ϑ	0.1 ; 0.2 ; 0.3 ; 0.5 ; 0.7; 1 ; 1.2 ; 1.5 ; 2 ; 3 ; 4 ; 5 ; 6 ; 7 ; 8 ; 9 ; 10
Stokes number	St	0.2 ; 0.3 ; 0.5 ; 0.7 ; 0.8; 0.9 ; 1 ; 1.2 ; 1.5 ; 2 ; 2.5 ; 3

In our simulated flow configuration, the velocity field is homogeneous and isotropic, while the temperature field exhibits inhomogeneity in the x_3 direction. Consequently, we average Eulerian fluid mean values over (x_1, x_2) planes. For particle Eulerian averages, we consider only those particles whose positions in the x_3 direction fall within the range $x_3 - \Delta x$ to $x_3 + \Delta x$, where Δx represents the grid spacing in physical space. Given that the temperature field is time-dependent, we cannot perform a temporal average of temperature statistics directly. Nevertheless, since some statistical ratios remain constant over time, we can compute temporal averages of these ratios. To enhance the reliability and accuracy of our results, each simulation has been repeated at least three times using different, uncorrelated initial velocity fields to expand the statistical ensemble. This approach is sufficient for obtaining accurate first- and second-order single-point statistics. However, exploring higher-order moments and two-point statistics would require an even larger ensemble.

3.3.2 Inter-particle collision model

In simulations involving particle collisions, we must account for elastic binary collisions in conjunction with the governing equations for both the fluid and particle phases. This requires modeling discrete collision events within the computational domain. The objective of this section is to investigate the effects of inter-phase collisions on heat transfer between two homothermal regions, as well as on the temperature statistics of both the fluid and particles. From a theoretical perspective, in the collisional regime, the particle momentum equation should incorporate short-range and long-range hydrodynamic forces in addition to contact forces. In our simulations, which operate in the two-way coupling regime, the primary significant force acting on the particles is the long-range hydrodynamic force. This force varies based on flow conditions, particle size, and density, as discussed earlier. For a more comprehensive approach to modeling colliding particles in both unbounded and wall-bounded flows, the particle momentum equation, incorporating contact and short-range hydrodynamic forces, can be expressed as:

$$m_p \frac{\mathrm{d}\boldsymbol{V}_p(t)}{\mathrm{d}t} = \boldsymbol{F}_{FPL} + \boldsymbol{F}_{FPS} + \boldsymbol{F}_C \tag{3.31}$$

$\boldsymbol{F}_{FPS}$ denote the short-range hydrodynamic forces, including lubrication, lift and drag forces have been previously addressed in chapter 2. The term $\boldsymbol{F}_{FPL}$ represents all long-range hydrodynamic forces acting on particle p from the surrounding fluid flow. This includes various forces such as drag force, lift force, buoyancy force, pressure gradient force, added mass force, and Basset history force. Specifically, $\boldsymbol{F}_{FPL}$ can be expressed as

$$\boldsymbol{F}_{FPL} = \boldsymbol{F}_D + \boldsymbol{F}_L + \boldsymbol{F}_B + \boldsymbol{F}_{PG} + \boldsymbol{F}_{AM} + \boldsymbol{F}_{BH} \tag{3.32}$$

where each term represents the respective force contributions. The particle contact or interaction force $\boldsymbol{F}_C$ accounts for all existing interactions with other particles and solid walls. It can be written as

$$\begin{aligned} \boldsymbol{F}_C &= \sum_p \boldsymbol{F}_{pq} + \sum_w \boldsymbol{F}_{pw} \\ &= \sum_p \left(\boldsymbol{F}^n_{pq} + \boldsymbol{F}^t_{pq} + \boldsymbol{F}^a_{pq}\right) + \sum_w \left(\boldsymbol{F}^n_{pw} + \boldsymbol{F}^t_{pw} + \boldsymbol{F}^a_{pw}\right), \end{aligned} \tag{3.33}$$

where $\boldsymbol{F}^n_{pq}$ and $\boldsymbol{F}^t_{pq}$ denote the normal and tangential interaction forces exerted on particle p by another particle q, respectively. These forces are crucial for capturing the complex dynamics of particle-laden flows, particularly in regimes where particle collisions and frictional interactions are significant. Normal force is essential for capturing collision dynamics between particles. It represents the force exerted perpendicular to the contact surface, influencing how particles bounce off each other or deform upon impact. Meanwhile, tangential force resists relative sliding between particles and is crucial for understanding frictional interactions during collisions. It determines how particles drag against each other, affecting their relative motion and energy dissipation. The term $\boldsymbol{F}^a_{pq}$ represents the adhesive forces arising from surface interactions, such as van der Waals forces, which are important at small scales or in materials prone to sticking. Similarly, $\boldsymbol{F}^n_{pw}$ and $\boldsymbol{F}^t_{pw}$ represent the normal and tangential forces between particle p and a solid wall, a common scenario in wall-bounded flows. The term $\boldsymbol{F}^a_{pw}$ accounts for adhesive interactions between particles and the wall, influencing the flow characteristics, especially in confined geometries where particles may adhere to the wall. This comprehensive formulation of $\boldsymbol{F}_C$ integrates all relevant interaction forces, offering a robust framework for analyzing particle behavior in complex flows, including those with significant wall effects and inter-particle adhesive interactions.

In the absence of a viscous fluid, dry inter-particle collisions occur between two spherical particles with initial impact velocities $\boldsymbol{V}_p$ and $\boldsymbol{V}_q$, and rebound velocities $\boldsymbol{V}^*_p$ and $\boldsymbol{V}^*_q$. These collisions can be categorized based on the angle of incidence: a head-on collision, where the angle is zero, and an oblique collision, where the incidence and rebound angles differ from zero. For head-on collisions, kinetic energy is dissipated solely due to contact mechanics. The dry restitution coefficient quantifies this energy loss, defined as the ratio of the relative impact velocity to the relative rebound velocity. By analyzing these angles and velocities in both normal and tangential directions, we can characterize the collision dynamics. Hertzian contact theory is commonly used to model and compute the normal component of the collision velocity and force. In particle-laden flows, where spherical particles interact with a surrounding fluid, collisions are categorized as wet collisions. As discussed in chapter 2, when the particle volume fraction increases, the flow transitions to a dense suspension, requiring a four-way coupling regime. In this scenario, three types of collisions may occur: long-range hydrodynamic interactions, short-range hydrodynamic interactions, and particle-particle contact forces. When particles or

particles and walls are separated by a small gap, the problem is treated as a lubrication case using the Stokes regime, where surface roughness becomes significant. Here, particles interact via a thin fluid layer, sometimes modeled as a three-way coupling regime. Complexities arise in particle-particle contact forces when collisions are neither perfectly elastic nor inelastic. Adhesive collisions involve modeling adhesion or plasticity for normal forces, and static and dynamic friction for tangential forces. This is a challenging task both mathematically and computationally. Contact theory is applicable to both particle-particle and wall-particle interactions. In wall interactions, the wall is treated as a spherical particle with an infinite radius, as detailed by Costa et al. [79].

In our simulation setup, we are dealing with an unbounded flow where wall interactions are not present. Additionally, we assume that inter-particle collisions are perfectly elastic, meaning the restitution coefficient is set to 1. Given the small size of the spherical particles, collisions are non-cohesive, and no friction forces between particles are considered. Furthermore, due to the very low particle volume fraction, lubrication effects, such as thin-layer contact forces, do not play a role in this collisional flow regime. Since there is no heat transfer during impact events, the collisions do not influence the particle temperature equation. Collision detection in particle simulations can be approached using different algorithms depending on the method employed. In the Discrete Element Method (DEM), collisions are detected by checking the overlap between spherical particles [80]. A standard approach involves a geometric check, where the distance between the centers of two particles is compared to their diameters. DEM typically employs spatial partitioning techniques such as grids or neighbor lists to efficiently detect potential collisions and resolve them [81]. This method is well-suited for simulations with a large number of particles due to its simplicity and efficiency in handling granular flow dynamics. In contrast, Molecular Dynamics (MD) simulations model particle interactions based on pair potentials, detecting collisions when particles come within a specified cutoff radius [82]. Forces between particles are computed using potential functions, such as Lennard-Jones or Coulombic potentials [83]. MD simulations often use techniques like the Verlet list or cell list to efficiently handle interactions, focusing on precise force calculations and time integration. While both DEM and MD involve particle interactions and collision handling, they differ in their computational approaches and objectives. DEM focuses on the mechanics of granular flows and collision dynamics with spatial partitioning for efficiency, making it suitable for larger-scale

simulations with less emphasis on detailed force calculations [81]. MD, on the other hand, is employed for detailed, atomic-scale simulations, emphasizing accurate force computations and precise time integration [82]. Our model uses a first-order particle trajectory reconstruction approach for collision detection. This method is straightforward and effective for simulations where particles move with constant velocity between time steps. By calculating the potential collision distance at each time step, the model efficiently detects collisions and updates particle velocities based on momentum and energy conservation principles, as outlined by [84]. This approach combines the geometric simplicity of DEM with the trajectory-based collision detection often found in MD simulations, providing a practical solution for simulating particle-laden flows. For simulating the collisional regime, our model considers inter-particle collisions occurring when the distance between the centers of two spherical particles equals their diameter. To incorporate these collisions into the numerical simulation, we perform a first-order particle trajectory reconstruction at each time step. A collision between the $p-$th and $q-$th particles within a time step $t \in [t_n, t_{n+1})$ is detected when the following condition is met:

$$\left\| (1-\tilde{t})(\boldsymbol{X}_p(t_n) - \boldsymbol{X}_q(t_n)) + \tilde{t}(\boldsymbol{X}_p(t_{n+1}) - \boldsymbol{X}_q(t_{n+1})) \right\| = 2R, \tag{3.34}$$

where $\tilde{t} = t - t_n/\Delta t$ is the normalized time within the interval $[0,1)$. The collision detection formula given by Equation (3.34) calculates the distance between two particles at any point in time t during the time step. This distance is compared to twice the particle radius R to determine if a collision has occurred. If the calculated distance equals $2R$, a collision is detected. Upon detecting a collision, the model updates the positions and velocities of the colliding particles based on the principles of momentum and energy conservation. The particles then continue with their post-collision velocities for the remainder of the time step, as detailed in [84]. However, direct collision detection is computationally intensive, with a complexity scaling as $\mathcal{O}(N_p^2)$ due to the need to check all pairs of particles. This becomes impractical for simulations with a large number of particles N_p. To address this challenge, our approach employs a spatial partitioning strategy to improve computational efficiency. Specifically, we use a method akin to the linked-cell or cell-linked list approach. In this method, the simulation domain is divided into a grid of smaller boxes or cells. Each cell contains a list of particles located within its boundaries. Collision checks are then restricted to particles within the same cell and, optionally, neighboring cells. This reduces the number of particle pairs that need to be examined, thus lowering the

number of collision checks from $\mathcal{O}(N_p^2)$ to approximately $\mathcal{O}(N_p)$ per box, depending on the particle density and box size. To further manage computational load and avoid the limitations imposed by box boundaries, we implement a technique where the boxes are periodically shifted. This shifting ensures that particles near the boundaries are not excluded from collision checks due to being on the edge of a box. After shifting the boxes, the collision detection algorithm is rerun to account for the new particle positions and maintain accuracy [84]. This spatial partitioning approach is consistent with common practices in both DEM and MD simulations, where spatial grids or cells are used to limit the number of particle pairs considered for interactions. By leveraging these techniques, our model efficiently manages the computational demands of collision detection in particle-laden flows, aligning with the principles of both DEM and MD while optimizing performance for large-scale simulations. The cell-index method proposed by Onishi et al. in [84] involves dividing the simulation domain into a grid of smaller cells. Each particle is assigned to a specific cell based on its position. The key idea is that a particle can only collide with particles in the same or neighboring cells, which drastically reduces the number of particle pairs that need to be checked for potential collisions. The cell-index method, like the linked-cell method, is focused on reducing the computational burden of collision detection in particle simulations by leveraging spatial partitioning. Both methods are particularly valuable in simulations involving a large number of particles, such as those used in DEM or MD simulations. The primary difference between the cell-index and linked-cell methods lies in implementation details and the specific strategies used to manage particles within cells. However, both share the common goal of improving computational efficiency through spatial partitioning [84]. To derive the collision detection formula, we start by defining the positions of particles p and q at time t, by $\boldsymbol{X}_p(t)$ and $\boldsymbol{X}_q(t)$. For a time step Δt, the position at any intermediate time t can be interpolated linearly such that

$$\boldsymbol{X}_p(t) = \boldsymbol{X}_p(t_n) + \frac{t - t_n}{\Delta t}(\boldsymbol{X}_p(t_{n+1}) - \boldsymbol{X}_p(t_n)) \tag{3.35}$$

$$\boldsymbol{X}_q(t) = \boldsymbol{X}_q(t_n) + \frac{t - t_n}{\Delta t}(\boldsymbol{X}_q(t_{n+1}) - \boldsymbol{X}_q(t_n)) \tag{3.36}$$

Let $\tilde{t} = (t - t_n)/\Delta t$. Thus, the positions can be rewritten as

$$\boldsymbol{X}_p(t) = \boldsymbol{X}_p(t_n) + \tilde{t}(\boldsymbol{X}_p(t_{n+1}) - \boldsymbol{X}_p(t_n)) \tag{3.37}$$

$$\boldsymbol{X}_q(t) = \boldsymbol{X}_q(t_n) + \tilde{t}(\boldsymbol{X}_q(t_{n+1}) - \boldsymbol{X}_q(t_n)) \tag{3.38}$$

Now we can compute the relative position (center-to-center distance) vector between the particles at time t as

$$\boldsymbol{X}_p(t) - \boldsymbol{X}_q(t) = (\boldsymbol{X}_p(t_n) - \boldsymbol{X}_q(t_n)) + \tilde{t}((\boldsymbol{X}_p(t_{n+1}) - \boldsymbol{X}_p(t_n)) - (\boldsymbol{X}_q(t_{n+1}) - \boldsymbol{X}_q(t_n))) \tag{3.39}$$

To detect a collision, the magnitude of this relative position vector must equal the diameter of the particles, $2R$:

$$\left\| (1-\tilde{t})(\boldsymbol{X}_p(t_n) - \boldsymbol{X}_q(t_n)) + \tilde{t}(\boldsymbol{X}_p(t_{n+1}) - \boldsymbol{X}_q(t_{n+1})) \right\| = 2R \tag{3.40}$$

3.4 Results and discussion

In this section, we begin by analyzing and discussing the numerical data obtained from a comprehensive set of direct numerical simulations with dimensionless parameters previously outlined in Section 3.3.1. To maintain clarity in our numerical experiment of the dynamical and thermal behavior of inertial particles in non-isothermal turbulent flows, we focus on the most relevant and significant flow parameters. Specifically, the carrier flow is characterized by the Taylor microscale Reynolds number, while other flow parameters, such as the Prandtl number and mean kinetic energy dissipation rate, are held constant. The Taylor microscale Reynolds number in our simulations ranges from 37 to 124, providing sufficient data to gather the necessary statistics before reaching saturation in the computational domain. Regarding particle parameters, the volume fraction is maintained at y 4×10^{-4} for all numerical simulations, ensuring that we remain within the dilute suspension regime. Additionally, the particle-to-fluid density ratio is kept constant at around 10^3, simulating the behavior of water droplets suspended in air. The numerical simulations differ primarily by two dimensionless numbers: the thermal Stokes number and the Stokes number. The ratio between these two numbers determines the two major classes of simulations discussed in Subsections 3.4.1 and 3.4.2. In Subsection 3.4.1, the

ratio between the thermal Stokes number and the Stokes number is held constant equal to 4.43. Meanwhile, in subsection 3.4.2, these parameters are allowed to vary independently. In both cases, we utilize a broad range of Stokes numbers and thermal Stokes numbers to ensure a comprehensive analysis of the suspended inertial particle behavior under various conditions. This allows us to explore the impact of different inertia and thermal inertia of particles suspended in a turbulent flow. By varying these parameters, we can better understand how they influence the thermal dynamics and overall behavior of the particles, providing valuable insights into the complex interactions at play in non-isothermal particle-laden turbulent flows. The impact of inter-particle collisions is also analyzed only in subsection 3.4.1. Given that the effect of collisions at the simulated volume fraction is minimal, we omit the consideration of collisional effects in the subsequent simulations discussed in Subsection 3.4.2.

3.4.1 Fixed thermal Stokes to Stokes number ratio

In this part, we present and discuss the results from our direct numerical simulations, focusing on cases where the ratio between the particle thermal response time and the momentum response time is constant. Initially, we examine how particle inertia influences fluid temperature statistics and the velocity-temperature correlation in a one-way coupling regime. This analysis provides insight into the impact of particle inertia on the thermal mixing dynamics of the fluid. Next, we extend our discussion to two-way coupling scenarios to explore the role of particle thermal feedback in overall heat flux and the temperature one-point statistical moments. This investigation helps us understand how interactions between the particles and the fluid affect the overall heat transfer within the turbulent flow. The final part of subsection 3.4.1 is dedicated to analyzing the collisional regime, which differs from the previously discussed collisionless scenarios due to the presence of inter-particle elastic collisions. Here, we aim to quantify the effects of particle-particle collisions on turbulent heat flux, maintaining the same flow configuration and simulation parameters as in the collisionless regime. Additionally, we present results on the conditional temperature difference at collision events and the computed collision frequency to further elucidate the influence of collisions on the overall heat transfer.

One-Way Coupling

We begin our discussion by analyzing the results from simulations conducted in a collisionless regime with a fixed ratio $\tau_\vartheta/\tau_v = 4.43$. The primary goal is to quantify how particle inertia and the Taylor microscale Reynolds number of the carrier flow affect turbulent heat flux in both one-way and two-way thermal coupling regimes. To achieve this, we present the results separately for each regime, enabling us to observe the individual effects of particle inertia, turbulent flow motion, and particle thermal feedback. In our setup, the flow domain is initially divided by an interface separating two homothermal zones with uniform temperatures. This interface evolves due to turbulent eddies, creating a mixing region characterized by high temperature variance. In this mixing zone, particles are exposed to varying temperature fronts, even if the fluid temperature field remains unaffected by the particles in the one-way thermal coupling regime. Figure 3.2 illustrates the temperature field and particle temperatures for $\mathrm{St}_\vartheta/\mathrm{St} = 4.43$ at three different Stokes numbers: 0.2, 1, and 2. The visualization captures the clustering behavior of particles, which is less pronounced for particles with lower inertia and becomes most evident at $\mathrm{St} = 1$. Particles, transported by turbulent eddies, spread along with the fluid temperature gradients created by the interface separation. Consequently, they encounter varying temperature fronts in the thermal mixing zone, resulting in heating or cooling depending on their inertia, thermal response, and initial temperature. To quantify the width of the thermal mixing layer where the thermal mixing processes occur at the interface between two regions, we use the fluid mean temperature distribution shown in Figure 3.3a. This characteristic lengthscale, referred to as the temporal mixing layer thickness $\delta(t)$, can be defined as

$$\delta(t) = \frac{T_1 - T_2}{\max\{|\partial\langle T\rangle/\partial x_3|\}}, \tag{3.41}$$

where $\langle T\rangle$ represents the fluid mean temperature, which varies from T_1 to T_2. This definition provides a length scale for measuring the thickness of the time-evolving thermal mixing layer based on the relevant temperature gradient. It is analogous to the vorticity thickness in thin shear flows, differing from the definition used in shearless mixing studies (e.g., [77]). However, it offers the advantage of being independent of the shape of the mean temperature profile and avoids arbitrary boundary definitions for the thermal mixing layer. In cases where the mean temperature evolves self-similarly, as demonstrated and discussed analytically in detail in chapter 5, this

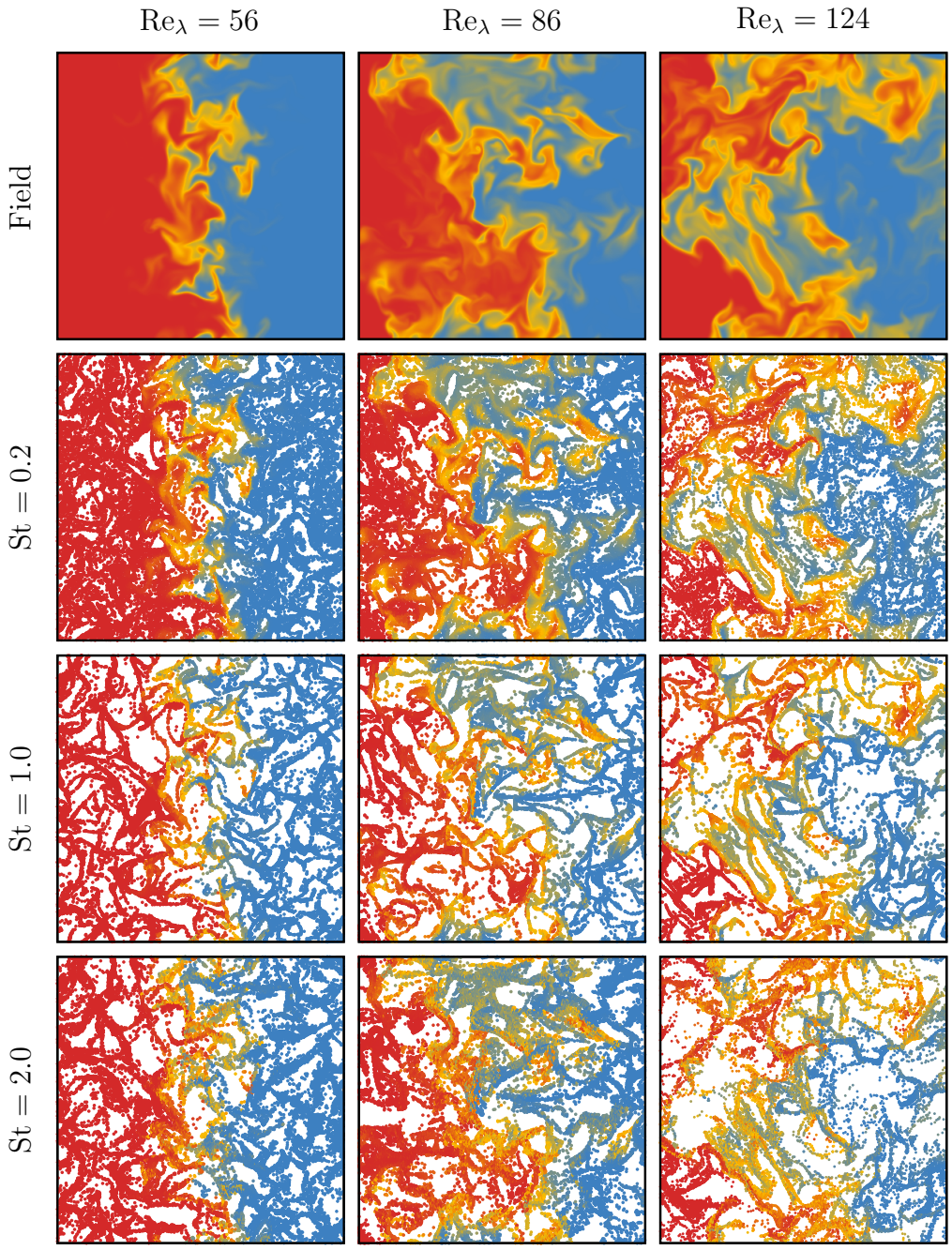

Fig. 3.2 Snapshot of the non-dimensional fluid temperature at dimensionless time $t/\tau = 3$ in a (x_1, x_3) plane, perpendicular to the initial temperature gradient, in the center of the computational domain (a $2\pi \times 2\pi$ square in dimensionless units) in the one-way coupling regime. The top panels illustrate the carrier flow temperature, while each subsequent row indicate the particle temperature in the vicinity of such a plane for three different Stokes numbers at $\tau_\vartheta/\tau_\nu = 4.43$. In order to have a similar number of particles in the visualization, the thermal mixing layer thickness, in which the particles are depicted, increases with the Stokes number. Note that the size of particles is out of scale. The red colour corresponds to the maximum temperature in the domain, and the blue colour to the lowest.

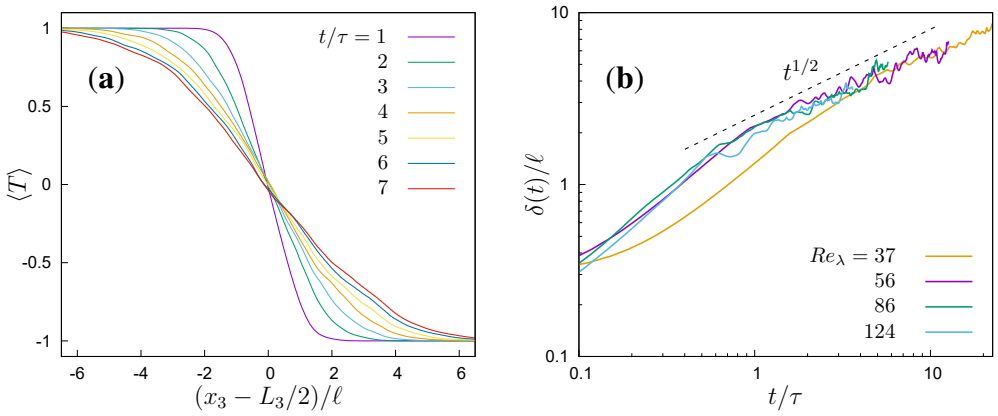

Fig. 3.3 One-way coupling. (**a**) Time evolution of the dimensionless mean fluid temperature at $\mathrm{Re}_\lambda = 56$; (**b**) Growth of the mixing layer thickness at different Re_λ (both panels at $\tau_\vartheta/\tau_v = 4.43$).

definition aligns with any alternative definitions, as they will yield the same time evolution results. After a brief initial transient period, approximately one or two eddy turnover time $\tau = \ell/u'$, self-similarity is observed. The length of this initial transient is nearly independent of Reynolds number but shows weak dependence on the initial temperature profile. For instance, in the simulation with $\mathrm{Re}_\lambda = 37$, where the coarser resolution (refer to Table 3.1) results in a smoothed temperature step (Equation (3.26)), this dependency is noted. Following this initial transient, the mixing layer thickness exhibits a diffusive growth $\delta \sim t^{1/2}$. More precisely, in dimensionless terms, it scales as $(\delta/\ell) \sim (t/\tau)^{1/2}$, indicating the dominant influence of large-scale turbulent eddies (Figure 3.3b). This behavior is consistent with previous observations of shearless mixing spreading in decaying turbulent flows (e.g., [77]).

After the initial transient phase, during which velocity-temperature correlations form and particles cluster according to their inertia, a self-similar stage of evolution is observed. In this stage, all single-point statistics of the carrier fluid and suspended particles collapse when properly rescaled. Specifically, the distance from the center of the domain (initial temperature discontinuity) is scaled by δ, and the amplitude of higher moments and velocity-temperature correlations is scaled with powers of $1/\delta$. As shown in [77], a high-variance region develops at the center of the flow domain. The temperature variance distribution also exhibits a self-similar stage of evolution when positions are normalized by δ and values are normalized by t^{-1}. Temperature fluctuations arise from the interaction between the two regions with different temperatures but tend to decay as the mean temperature gradient, which

drives the fluctuations, decreases. Figure 3.4 illustrates the variance of fluid and particle temperatures. Panel (a) shows variance for different $\mathrm{St}_\vartheta/\mathrm{St}$ ratios at a fixed Reynolds number, $\mathrm{Re}_\lambda = 56$, while panel (b) presents variance for different Reynolds numbers with a constant $\mathrm{St}_\vartheta/\mathrm{St}$ ratio of 4.43.

Although the mean temperature of particles at a given x_3 position is nearly identical to the flow temperature across all Stokes numbers (with variations smaller than the measurement uncertainty), particle inertia tends to increase the temperature variance (Figure 3.4). This is due to the larger relaxation time of the particles, allowing them to retain their temperature for longer durations. In our simulations, since St_ϑ and St are not independent, particles with higher inertia also exhibit higher thermal inertia. Consequently, as $\mathrm{St} \to 0$, the temperatures of fluid and particles converge, and their variances become similar. The particle temperature variance increases with the Stokes number when $\mathrm{St}_\vartheta/\mathrm{St}$ exceeds 2, while remaining around one at lower $\mathrm{St}_\vartheta/\mathrm{St}$ ratios (Figure 3.4a). This effect diminishes as the Reynolds number increases (Figure 3.4b). This trend can be attributed to the dominance of large-scale motions in forming the temperature mixing layer. The ratio of particle relaxation time to eddy turnover time, $\tau_\vartheta/\tau = (\tau_\eta/\tau)\mathrm{St}_\vartheta$, decreases with increasing Reynolds number, leading to reduced particle relaxation relative to the flow timescale. According to Zaichik et al. [26], the increased variance of particle temperature compared to fluid temperature variance is characteristic of flows with a mean temperature gradient. This is because the particulate phase lacks a dissipation mechanism, unlike the carrier flow phase. In contrast, homogeneous turbulence with a uniform mean temperature produces the opposite effect: $\langle\Theta_p'^2\rangle/\langle T'^2\rangle$ decreases with increasing particle inertia [85, 26].

However, the most important single-point statistics are the correlations between temperature and velocity fluctuations because they are proportional to the heat transfer between the two flow regions at different temperature, whose quantification is our main aim. Figure 3.5 shows the time evolution of this correlation for both phases in one-way coupling at $\mathrm{Re}_\lambda = 56$ and different particle Stokes numbers. As it can be seen the correlation reduces with time in a self-similar manner for all particle Stokes number and the fluid. Figure 3.6 shows an example of the spatial distribution of the fluid and particle temperature–velocity correlation at $\mathrm{Re}_\lambda = 56$ and different St. The maximum of the correlation decreases with time as $t^{-1/2}$, i.e., like the inverse of δ, due to the thickening of the temperature layer which reduces the amplitude of temperature fluctuations. An increase of particle inertia leads to

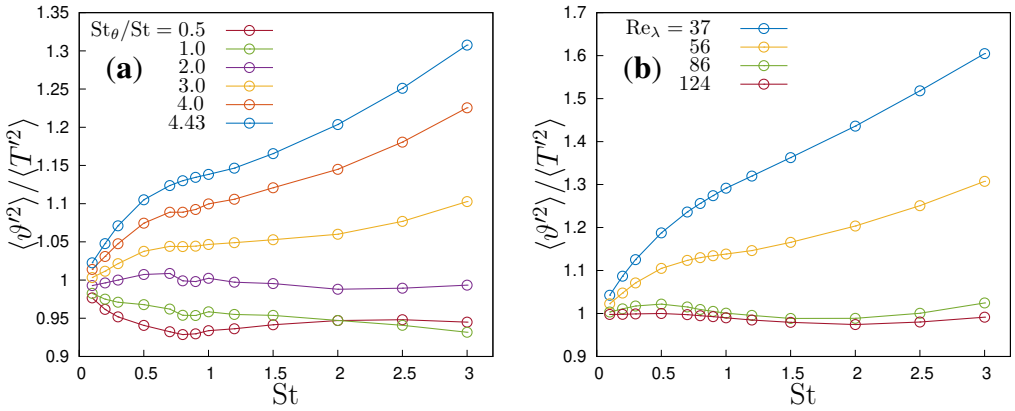

Fig. 3.4 Particle temperature variance to fluid temperature variance ratio against Stokes number in one-way coupling simulations for (**a**) different thermal Stokes number to Stokes number ratios $\mathrm{St}_\vartheta/\mathrm{St}$, and (**b**) different Taylor microscale Reynolds numbers Re_λ at $\mathrm{St}_\vartheta/\mathrm{St} = 4.43$.

an increase of particle velocity–temperature correlation up to about $\mathrm{St} \sim 1$ and then a decrease for higher St at the same time and Reynolds number. This translates into a different modulation of the heat transfer. The heat flux (actually, the flux of enthalpy) $\dot{q}$ in the direction of the temperature inhomogeneity x_3 can be decomposed into the contribution of thermal diffusion, convection by fluid velocity, and transport associated with the particle motion. All these contributions are maximum in the centre of the domain (i.e., at the position of the initial temperature step), and, in the self-similar stage, reduce in time as $t^{-1/2}$ while the mixing layer grows and the driving mean temperature gradient reduces. Inertial particles can carry large temperature differences at long distances; therefore, they can give a significant contribution to the heat transfer. To quantify the effect of each parameter on heat transfer, we use the Nusselt number, Nu. The Nusselt number is defined as the ratio of convective heat transfer to conductive heat transfer by thermal diffusion in a static, non-moving system. In the context of our flow configuration, we use the mixing thickness δ as the length scale, since it is the only dynamically significant length scale for heat transfer. During the self-similar stage of mixing evolution, the Nusselt number Nu remains constant. This constancy arises because δt captures the relevant length scale for the evolving mixing layer. To derive the Nusselt number Nu, we apply standard dimensional analysis to the system of equations ((3.6))–((3.9)) and ((3.12)). In our case, the convective heat transfer is characterized by the turbulent mixing and transport of heat, while the conductive heat transfer is governed by

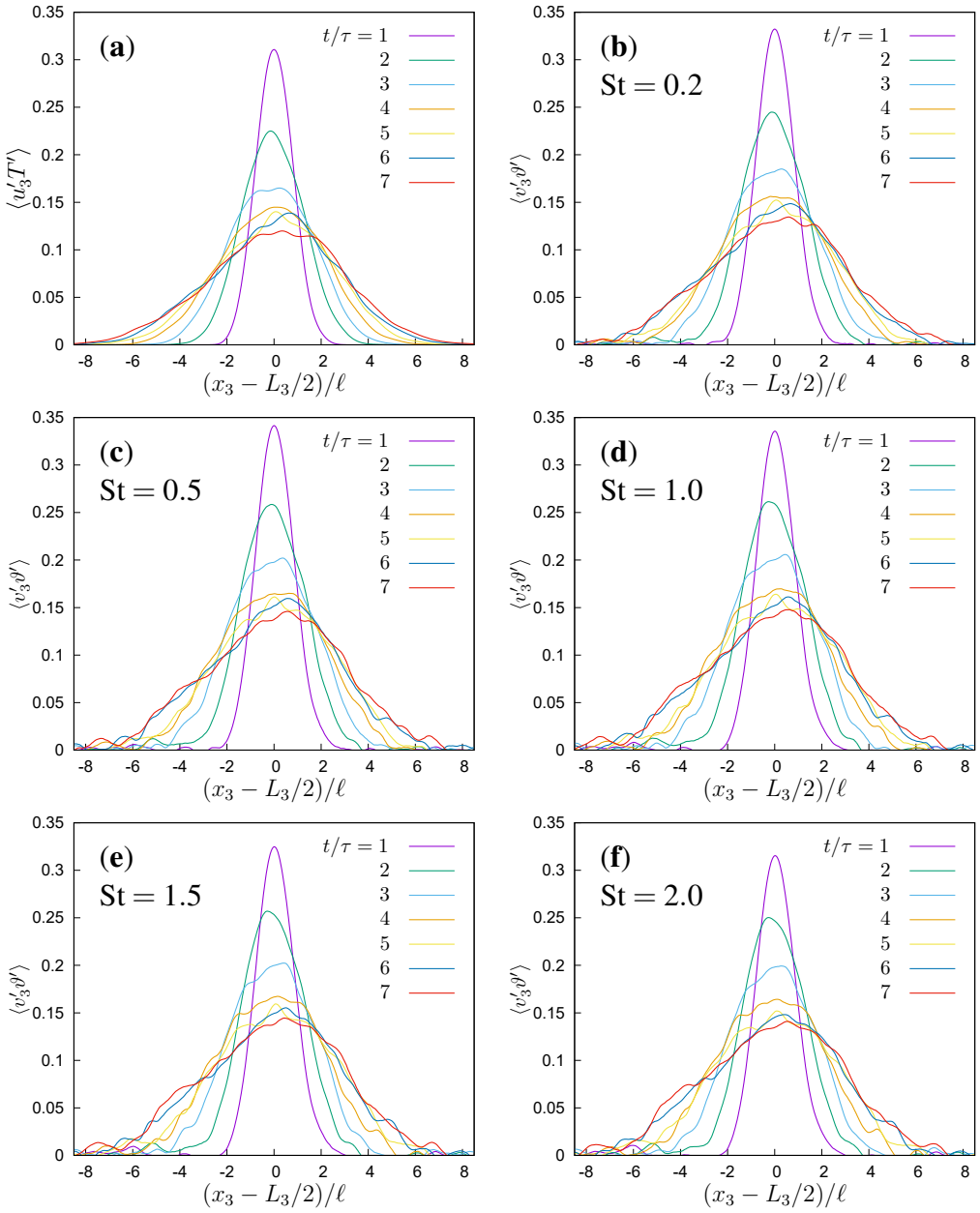

Fig. 3.5 One-way coupling simulations at $\mathrm{Re}_\lambda = 56$ and $\mathrm{St}_\vartheta/\mathrm{St} = 4.43$. Time evolution of (**a**) the fluid velocity and temperature correlation and the particle velocity and temperature correlation for (**b**) $\mathrm{St} = 0.2$, (**c**) $\mathrm{St} = 0.5$, (**d**) $\mathrm{St} = 1.0$, (**e**) $\mathrm{St} = 1.5$ and (**f**) $\mathrm{St} = 2.0$.

thermal diffusion. By analyzing the ratios of these quantities, we can assess the efficiency of heat transfer within the turbulent flow and understand the influence of different parameters on the heat transfer process. Thus, from dimensional analysis

Nusselt number in our fluid-particle system can be expressed as

$$\mathrm{Nu} = \mathrm{Nu}(\mathrm{Re}, \mathrm{Pr}, \varphi_\vartheta, \mathrm{St}, \mathrm{St}_\vartheta), \tag{3.42}$$

where Re is the Reynolds number, $\mathrm{Pr} = \nu/\kappa$ the Prandtl number, St and St_ϑ the Stokes and thermal Stokes number, and φ_ϑ is the ratio between particle heat capacity and fluid heat capacity. As observed above, the heat flux per unit surface and unit time is given by the sum of heat flux due to diffusion, convection, and particle motions, $\dot{q} = \dot{q}_d + \dot{q}_c + \dot{q}_p$, where, from Equations ((3.6))–((3.9)),

$$\dot{q}_d = -\lambda \frac{\partial \langle T \rangle}{\partial x_3}, \tag{3.43}$$

$$\dot{q}_c = \rho_0 c_{p0} \langle u_3' T' \rangle, \tag{3.44}$$

$$\dot{q}_p = \varphi \rho_p c_{pp} \langle V_{p,3}' \Theta_p' \rangle. \tag{3.45}$$

Therefore, the Nusselt number can be written as

$$\mathrm{Nu} = 1 + \mathrm{Nu}_c + \mathrm{Nu}_p, \tag{3.46}$$

where Nu_c and Nu_p are the convective and particle contributions, given by

$$\mathrm{Nu}_c = \mathrm{RePr} \frac{-\langle \tilde{u'}_3 \tilde{T}' \rangle}{\partial \langle \tilde{T} \rangle / \partial \tilde{x}_3}, \tag{3.47}$$

$$\mathrm{Nu}_p = \varphi \mathrm{RePr} \frac{\rho_p c_{pp}}{\rho_0 c_{p0}} \frac{-\langle \tilde{V'}_{p,3} \tilde{\Theta'}_p \rangle}{\partial \langle \tilde{T} \rangle / \partial \tilde{x}_3} = \varphi_\vartheta \mathrm{RePr} \frac{-\langle \tilde{V'}_{p,3} \tilde{\Theta'}_p \rangle}{\partial \langle \tilde{T} \rangle / \partial \tilde{x}_3}, \tag{3.48}$$

where the tilde indicates dimensionless variables.

The ratio $\mathrm{Nu}_p/\mathrm{Nu}_c$ serves as a key indicator of the enhancement in heat transfer due to the presence of particles. In the one-way coupling regime, where the carrier fluid temperature remains unaffected by the particles, the convective heat flux is solely influenced by the fluid properties and underlying turbulence. Consequently, the Nusselt number for the carrier fluid, Nu_c, is a function of the Reynolds number (Re) and the Prandtl number (Pr), such that $\mathrm{Nu}_c = \mathrm{Nu}_c(\mathrm{Re}, \mathrm{Pr})$. In this regime, only the particle Nusselt number Nu_p is influenced by particle inertia and thermal inertia. For particles in the collisionless one-way coupling regime, their velocity and temperature are determined by the carrier flow and their respective relaxation times, τ_v and τ_ϑ. Since particles do not interact with each other either directly through

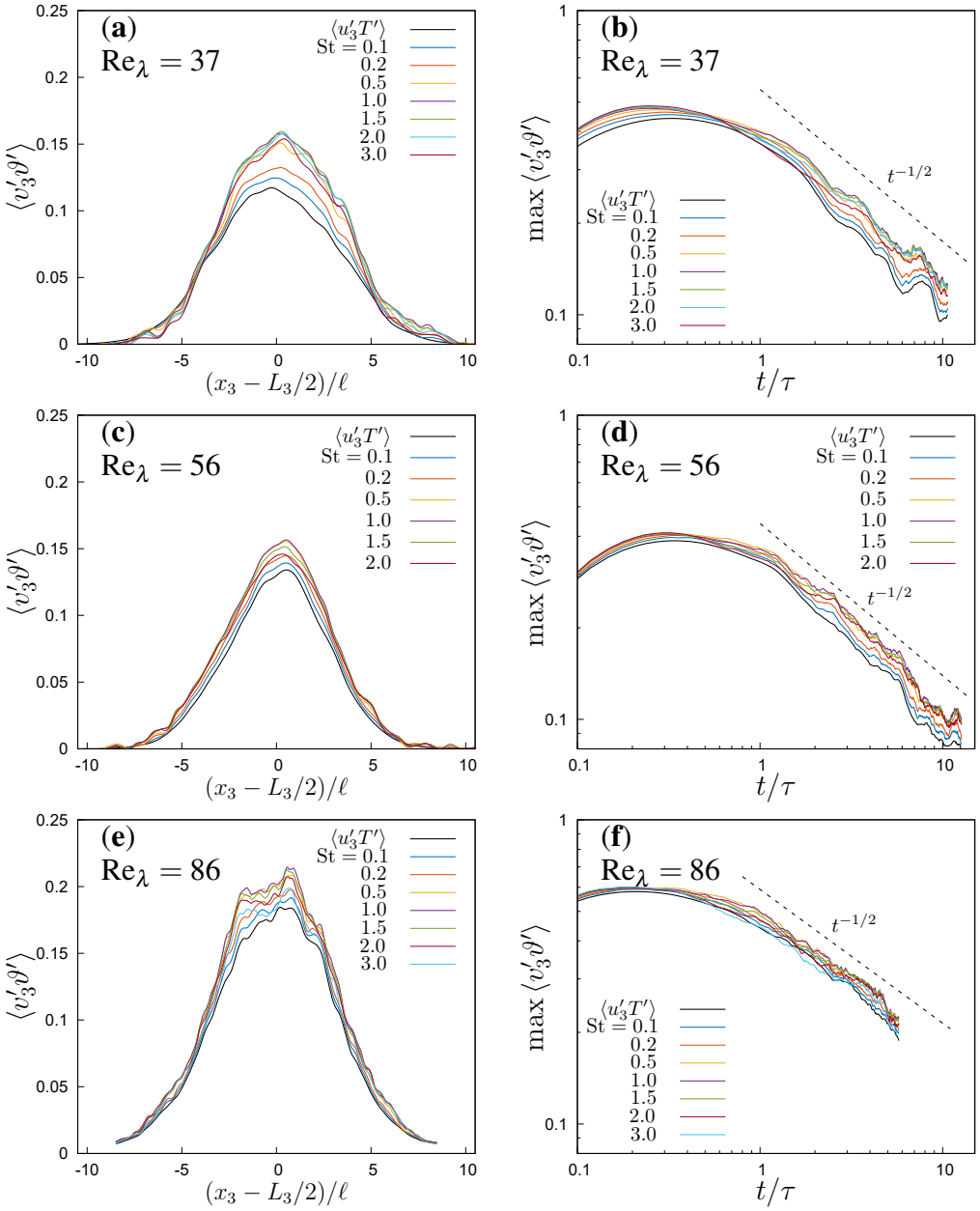

Fig. 3.6 Spatial distribution of (**a**) velocity and temperature correlation at $t/\tau = 6$ and $\mathrm{Re}_\lambda = 56$ and the maximum heat flux of carrier flow field for (**b**) $\mathrm{Re}_\lambda = 37$, (**c**) $\mathrm{Re}_\lambda = 56$ and (**d**) $\mathrm{Re}_\lambda = 86$ (all for different Stokes number in one-way coupling simulations at $\mathrm{St}_\vartheta/\mathrm{St} = 4.43$).

collisions or indirectly via the carrier fluid, the correlation $\langle v'_{p,3}\Theta'_p \rangle$ is influenced

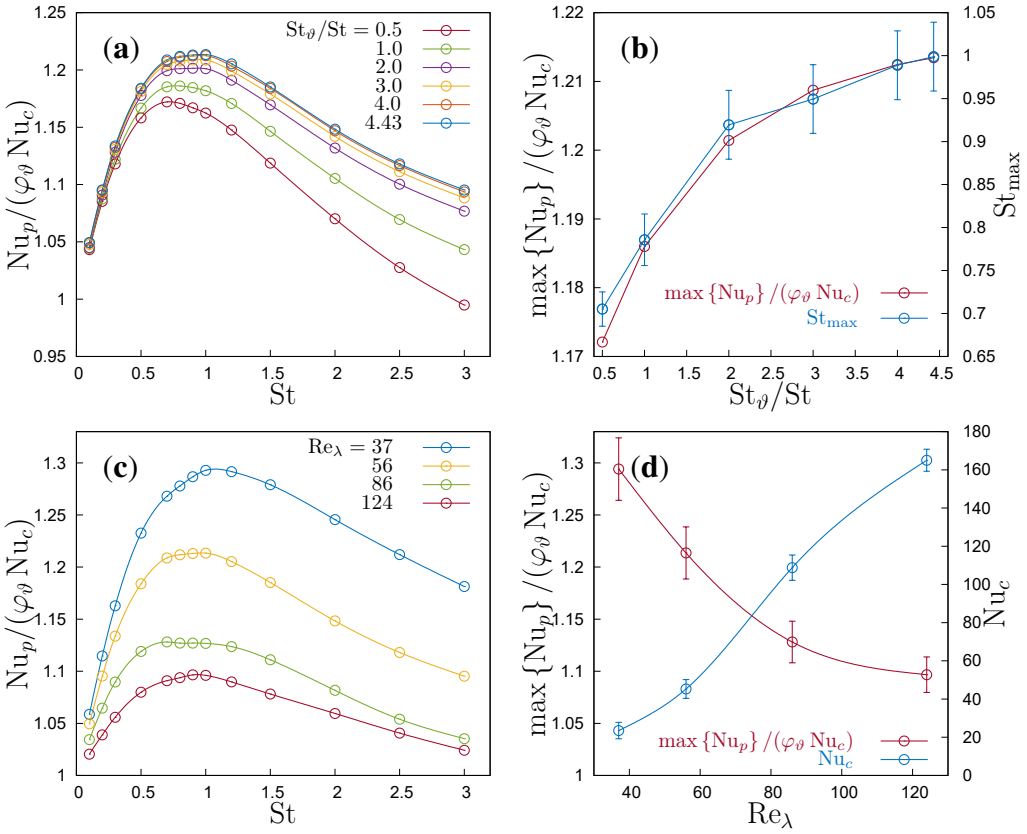

Fig. 3.7 One-way coupling regime. (**a**) Particle contribution to the Nusselt number, Nu_p as a function of the Stokes number at $\mathrm{Re}_\lambda = 56$; Nu_c is the fluid convection contribution to the Nusselt Number, φ_ϑ is the particle-to-fluid heat capacity ratio. (**b**) Maximum particle Nusselt number and the corresponding Stokes number as function of Stokes number to thermal Stokes number ratio at $\mathrm{Re}_\lambda = 56$. (**c**) Particle motion contribution to the Nusselt number, Nu_p as a function of the Stokes number and Reynolds number at $\mathrm{St}_\vartheta/\mathrm{St} = 4.43$. (**d**) Variation of convective Nusselt number in terms of Taylor Reynolds number Re_λ at $\mathrm{St}_\vartheta/\mathrm{St} = 4.43$.

solely by the fluid-to-particle interactions. As a result, the ratio

$$\frac{\langle \tilde{V}'_{p,3}\tilde{\Theta}'_p\rangle}{\langle \partial T/\partial x_3\rangle}$$

in equation (3.48) depends on Re, Pr, the particle inertia and thermal inertia. Therefore, Nu_p can be expressed as a linear function of φ_ϑ, the ratio of particle heat capacity to fluid heat capacity:

$$\mathrm{Nu}_p = \varphi_\vartheta \mathrm{RePr} f(\mathrm{Re}, \mathrm{Pr}, \mathrm{St}, \mathrm{St}_\vartheta).$$

The presence of a self-similar stage implies that the Nusselt number is independent of time, as all fluxes exhibit the same temporal evolution. The heat flux between the two homothermal regions is evaluated at the central plane of the domain, which is where the mean temperature gradient of the carrier fluid is maximal. Figure 3.7a illustrates the contribution of particle motion to the Nusselt number as a function of the Stokes number in the one-way coupling regime, for various ratios of the thermal Stokes number to the Stokes number at a fixed Reynolds number ($\mathrm{Re}_\lambda = 56$). Figure 3.7c displays the particle contribution to the Nusselt number across different Reynolds numbers, but for a constant ratio of thermal Stokes number to Stokes number ($\mathrm{St}_\vartheta/\mathrm{St} = 4.43$).

As the Stokes number approaches zero, particles behave as passive tracers and, with the thermal Stokes number also approaching zero, they tend to reach thermal equilibrium with the local carrier fluid. Consequently, in this limit, the Nusselt number for particles, Nu_p, approaches $\varphi_\vartheta \mathrm{Nu}_c$. The heat flux reaches a maximum when the Stokes number is near one, corresponding to the point of maximum particle clustering. However, within the ranges of $\mathrm{St}_\vartheta/\mathrm{St}$ investigated, this maximum is not observed precisely at $\mathrm{St} = 1$, but rather at a smaller Stokes number. This optimal Stokes number increases with $\mathrm{St}_\vartheta/\mathrm{St}$, starting from around 0.6 when $\mathrm{St}_\vartheta/\mathrm{St} = 0.5$ and approaching nearly 1 when $\mathrm{St}_\vartheta/\mathrm{St} = 4.43$, as illustrated in Figure 3.7b for simulations at $\mathrm{Re}_\lambda = 56$. This trend is consistent across all Reynolds numbers, suggesting that the maximum heat transfer due to particles is achieved at $\mathrm{St} = 1$ only in the asymptotic limit where $\mathrm{St}_\vartheta/\mathrm{St} \to \infty$. The maximum heat flux increases monotonically with the $\mathrm{St}_\vartheta/\mathrm{St}$ ratio, indicating that particles with high thermal capacities can significantly enhance heat flux. However, the particle-to-fluid heat capacity ratio, φ_ϑ, can be on the order of 10^{-1} even for small sub-Kolmogorov particles in dilute suspensions. Thus, particles can significantly increase overall heat flux, even within the one-way coupling regime. It is evident that heat transfer enhancement due to particles is more strongly influenced by the Stokes number, St, than by the thermal Stokes number, St_ϑ, as shown by the data in Figure 3.7a and 3.7c. Specifically, within the range of particle-to-fluid thermal capacity ratios examined, the maximum particle Nusselt number varies by about 5% for a given Reynolds number. For $\mathrm{St} \gtrsim 1$, particle velocity dynamics become increasingly nonlocal, reducing clustering and, consequently, the heat flux. Although an asymptotic limit for $\mathrm{St} \to \infty$ cannot be inferred from the range of Stokes numbers investigated, in such a limit, particle dynamics would become uncorrelated with the carrier fluid

dynamics. Therefore, the heat transport would approach a diffusive limit, leading to $\mathrm{Nu}_p/(\varphi_\vartheta \mathrm{Nu}_c) \to 1$. This behavior is consistent with the present simulations. The rate at which this limit is approached appears to depend on the $\mathrm{St}_\vartheta/\mathrm{St}$ ratio and is significantly slower for higher values of $\mathrm{St}_\vartheta/\mathrm{St}$. However, since our simulations consider a collisionless particle-laden flow, this asymptotic limit cannot be fully reproduced by current simulations.

It should be noted that, unlike the Rayleigh–Bénard problem analyzed by Park et al. [86],the preferential concentration and clustering affect the overall heat transfer not only in the two-way thermal coupling regime but also in the one-way coupling regime, even in the absence of any thermal modulation of the carrier flow by particles. Although the ratio $\mathrm{Nu}_p/\mathrm{Nu}_c$ decreases with increasing Reynolds number, the particle contribution to heat transfer actually increases because Nu_c itself grows with Re_λ. Our results suggest that $\mathrm{Nu}_p \to \varphi_\vartheta \mathrm{Nu}_c$ as $\mathrm{Re}_\lambda \to \infty$, regardless of the Stokes number. The dependence of the convective Nusselt number on the Reynolds number is illustrated in Figure 3.7d. However, as the Reynolds number increases, the particle Nusselt number grows at a slower rate compared to the convective Nusselt number, resulting in a reduced ratio $\mathrm{Nu}_p/\mathrm{Nu}_c$ (see Figures 3.7c and 3.7d). By fitting the data shown in Figure 3.7d, one can infer that the maximum particle Nusselt number scales as

$$\max_{\mathrm{St}}\{\mathrm{Nu}_p\} \sim \varphi_\vartheta \mathrm{Nu}_c \left(1 + a\,\mathrm{Re}_\lambda^{-1}\right) \tag{3.49}$$

with $a \simeq 12$.

Two-Way Coupling

We expect that these findings will hold, at least qualitatively, in the two-way coupling regime. However, since inertial particles tend to preferentially concentrate in the advected passive scalar fronts where temperature gradients are large, they act to smooth these gradients. Consequently, we expect that particle thermal feedback could potentially reduce the overall Nusselt number. To assess how the modulation of fluid temperature by thermal feedback from particles influences overall heat transfer, we have repeated the simulations considering two-way thermal coupling. We conducted two-way coupling simulations only for $\mathrm{St}_\vartheta/\mathrm{St} = 4.43$ and a fixed

volume fraction $\varphi = 4 \times 10^{-4}$, which also implies that the heat capacity ratio φ_ϑ is constant. Thus, the simulations are governed by only two free parameters—the Stokes number and the Reynolds number. As shown in Figure 3.8, in the two-way coupling regime, the temporal mixing layer thickness exhibits a $t^{1/2}$ growth, independent of the particle Stokes number. Higher particle inertia results in a slight increase in the mixing layer thickness, up to about 10% at $\mathrm{St} = 3$. This indicates that more massive particles can transport heat over longer distances, thereby reducing the mean temperature gradient of the carrier flow through their thermal feedback. While it has been observed that thermal feedback can reduce fluid temperature variance in homogeneous turbulence [32, 87], these results are not directly applicable to the present flow configuration. The presence of a large initial temperature inhomogeneity means that particles generate temperature fluctuations with their feedback when they cross the initial interface. Additionally, [87] considers particles with thermal inertia but no inertia, so they move as passive tracers, whereas inertial particles crossing temperature fronts significantly influence small-scale statistics [32], and this effect is expected to be more pronounced in a flow where the initial temperature difference between the two homogeneous regions drives the thermal exchange. Indeed, the effect of particle inertia is primarily observed in the second-order moments. Moreover, second-order moments evolve self-similarly once the $t^{1/2}$ growth is achieved.

Figure 3.10b illustrates the modulation of the maximum fluid temperature variance, i.e., the variance at the center of the thermal mixing layer, as a function of the Stokes number. This figure shows a reduction in fluid temperature variance with increasing particle inertia. Meanwhile, the variance of particle temperature increases with particle inertia because a longer thermal relaxation time allows particles to traverse through a larger temperature region while maintaining their original temperature. Furthermore, this effect is amplified by thermal feedback, which tends to reduce the temperature difference between the particle and the surrounding fluid, consequently it diminishes the particle temperature time derivative $\mathrm{d}\Theta_p/\mathrm{d}t = \dot{\Theta}_p = (T - \Theta_p)/\tau_\vartheta$. This is further highlighted when comparing the particle temperature variance with the fluid temperature variance (Figure 3.10a), or by examining the probability density function (pdf) of the rate of change of particle temperature, or particle temperature time derivative $\dot{\Theta}_p$. Figure 3.9 illustrates the pdf of $\mathrm{d}\Theta_p/\mathrm{d}t$ in the central part of the domain at the same dimensionless time for different Stokes numbers and Re_λ. As noted in [32], the primary effect of thermal feedback is to reduce the tails of the pdf due to the modulation of the carrier flow temperature,

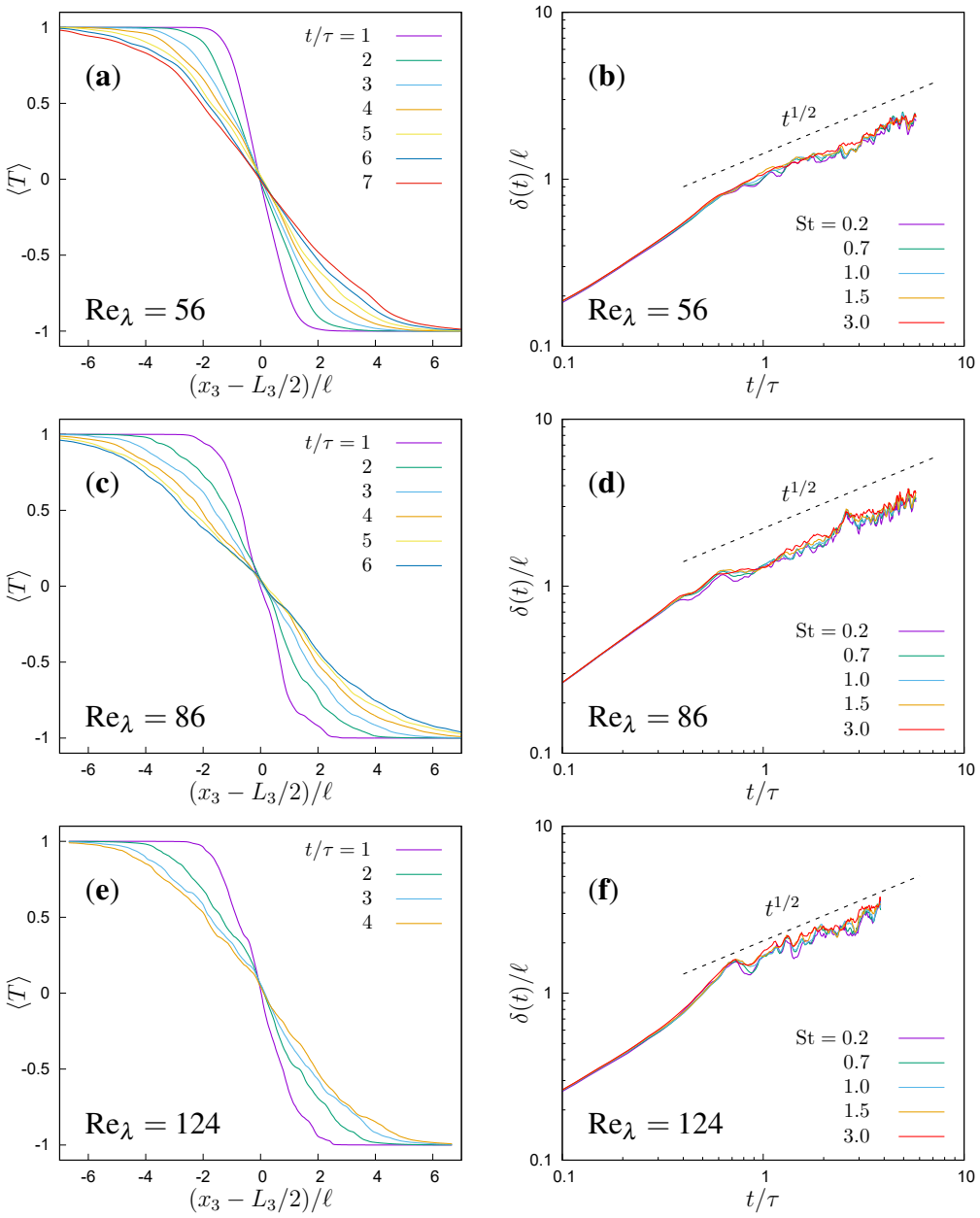

Fig. 3.8 Two-way coupling with $\mathrm{St}_\vartheta/\mathrm{St} = 4.43$: (**a**,**c**,**e**) time evolution of the dimensionless mean fluid temperature at $\mathrm{St} = 1$ and different Re_λ; (**b**,**d**,**f**) growth of the mixing layer thickness at different Stokes numbers and Taylor microscale Reynolds numbers.

which decreases the fluid-particle temperature difference and makes extreme variations in particle temperature less likely. The shape of the pdf is influenced by the particle inertia. As the Stokes number increases, the pdf narrows. This narrowing can be explained by the fact that particles with higher Stokes numbers respond more

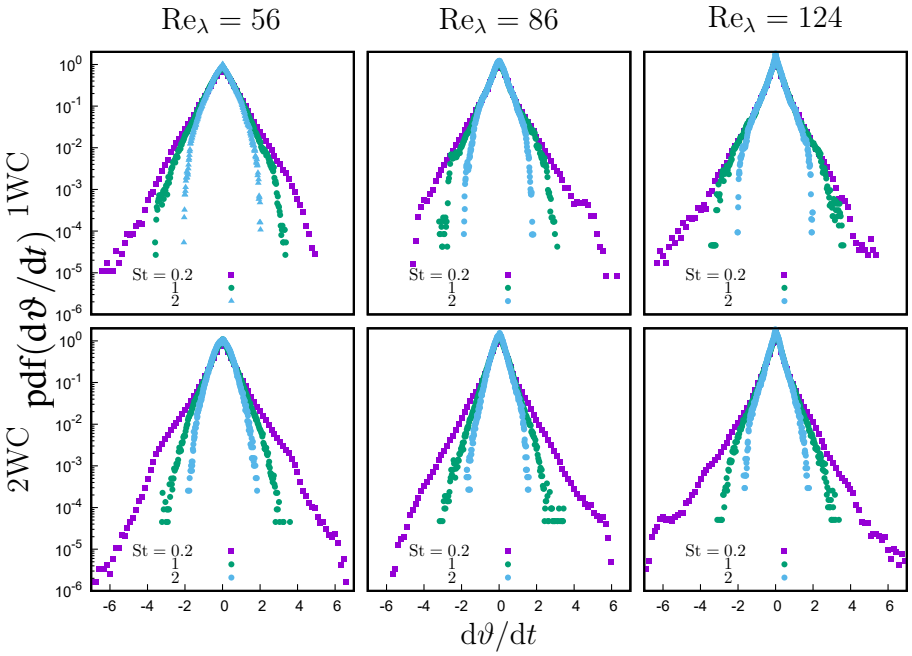

Fig. 3.9 Probability density function of the particle temperature derivative at $t/\tau = 4$ in one-way and two-way coupling simulations for different Taylor–Reynolds number (Re_λ) and three different Stokes numbers.

slowly to changes in the temperature field, producing an effect analogous to the observed inertial filtering of velocity due to particle inertia. This means that extreme derivatives of temperature are less likely to occur at higher inertia, even though the particle temperature may still differ significantly from the local temperature of the carrier flow. Consequently, the intermittency of particle temperature, as measured by the kurtosis, decreases with increasing Stokes number and with two-way thermal coupling effect.

Therefore, it is reasonable to anticipate that, in this case, particles contribute more to the heat flux compared to the fluid than in a one-way coupling regime. Figure 3.11 illustrates how the velocity-temperature correlation of both the fluid and particles evolves in time in a self-similar manner. Figure 3.12 compares the spatial distribution of velocity-temperature correlations of the fluid and particles at a fixed dimensionless time $t/\tau = 4$ (left panels) and depicts their $t^{-1/2}$ decay in time (right panels). It is evident that the particle temperature-velocity correlation consistently exceeds the fluid temperature-velocity correlation, resulting in a higher net heat flux per unit specific heat capacity, with a peak observed for a Stokes number close to unity. The overall effect can be quantified through the variation of the Nusselt

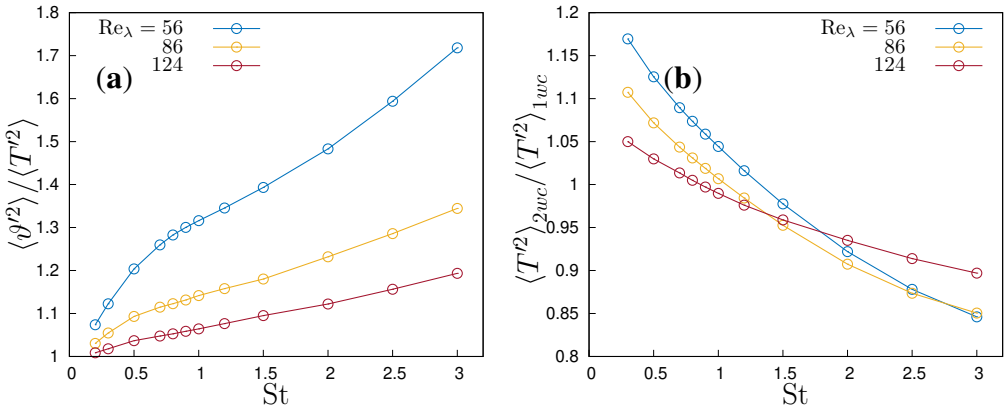

Fig. 3.10 (**a**) Particle temperature variance to fluid temperature variance ratio in two-way coupling simulations. (**b**) Two-way coupling fluid temperature variance to one-way coupling fluid temperature variance ratio in terms of the Stokes number for different Taylor microscale Reynolds numbers Re_λ.

number, which remains expressible as in (3.42)

$$\mathrm{Nu} = \mathrm{Nu}(\mathrm{Re}, \mathrm{Pr}, \varphi_\vartheta, \mathrm{St}, \mathrm{St}_\vartheta) = 1 + \mathrm{Nu}_c + \mathrm{Nu}_p \tag{3.50}$$

where Nu_p and Nu_c represent the particle and convective contributions to heat transfer, as defined in ((3.47)) and ((3.48)). In the two-way coupling regime, the temperature of the carrier flow is influenced not only by the flow conditions but also by the particles. Consequently, Nu_c is dependent on Stokes/thermal Stokes numbers and the thermal heat capacity ratio. Additionally, particle thermal feedback induces indirect particle-particle interactions mediated by the carrier flow, preventing φ_ϑ from being factored out in Nu_p. This results in a nonlinear dependence on φ_ϑ, meaning that a single simulation cannot capture the behavior across all heat capacity ratios. Thus, both Nu_c and Nu_p are functions of all the dimensionless governing parameters, i.e., $\mathrm{Nu}_c(\mathrm{Re}, \mathrm{Pr}, \varphi_\vartheta, \mathrm{St}, \mathrm{St}_\vartheta)$ and $\mathrm{Nu}_p(\mathrm{Re}, \mathrm{Pr}, \varphi_\vartheta, \mathrm{St}, \mathrm{St}_\vartheta)$. Figure 3.13 compares the particle and convective Nusselt numbers with their one-way coupling counterparts under the same parameters. The overall qualitative behavior is similar, with a peak in $\mathrm{Nu}_p/(\varphi_\vartheta \mathrm{Nu}_c)$ at $\mathrm{St} \sim \mathscr{O}(1)$. However, this ratio is consistently higher than in the one-way coupling regime, particularly showing a tendency to diverge when $\mathrm{St} \gtrsim 1$. Additionally, the ratio of particle heat transfer to convective heat transfer exhibits a trend similar to that observed with respect to Re_λ in the one-way thermal coupling regime.

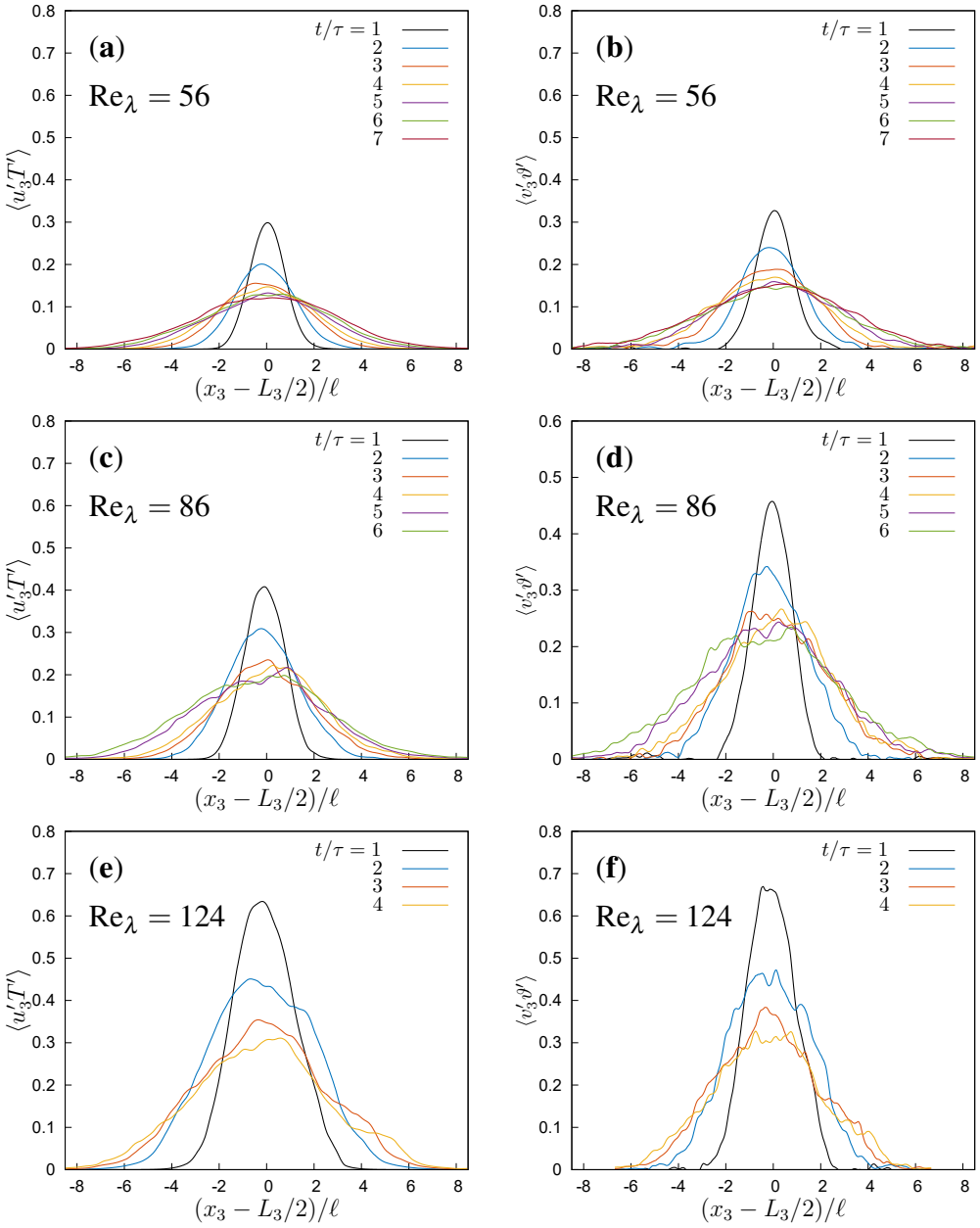

Fig. 3.11 Two-way coupling with St $= 1.0$: (**a**,**c**,**e**) time evolution of the fluid velocity and temperature correlation; (**b**,**d**,**f**) time evolution of the particle velocity and temperature correlation and different Re$_\lambda$.

The convective Nusselt number, Nu$_c$, increases with the Stokes number and approaches the value of the Nusselt number in a flow not influenced by particles (or in the one-way coupling case) when St $\gg 1$. The fluid temperature is influenced by heat exchange with the particles, and the thermal relaxation time of the fluid can be

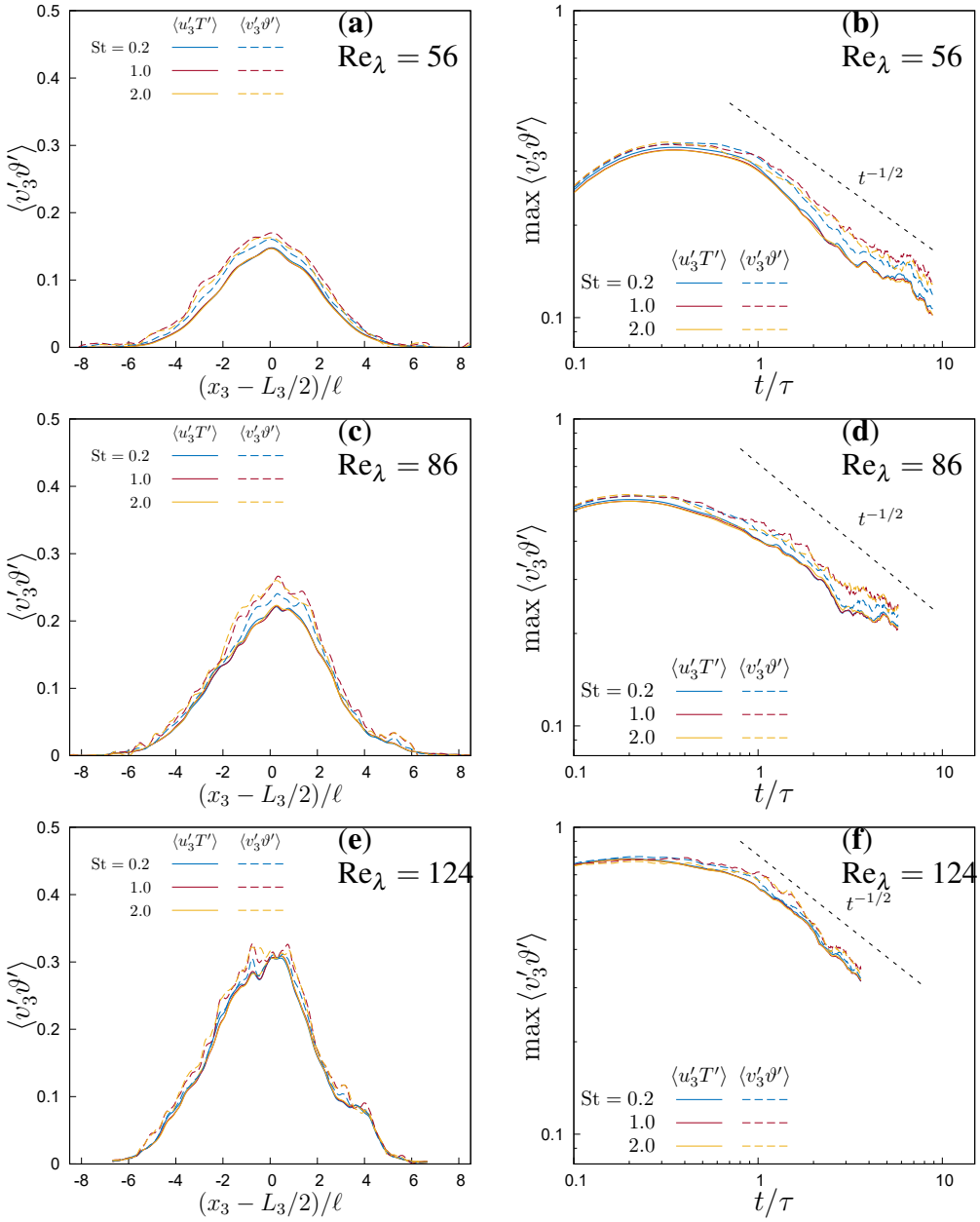

Fig. 3.12 Two-way coupling. (**a**,**c**,**e**) Spatial distribution of fluid and particle velocity-temperature correlations at $t/\tau = 4$; (**b**,**d**,**f**) maximum correlation at different Stokes number and different Taylor microscale Reynolds numbers.

estimated from Equation (3.3) as

$$\tau_T \sim \tau_\vartheta / \varphi_\vartheta .$$

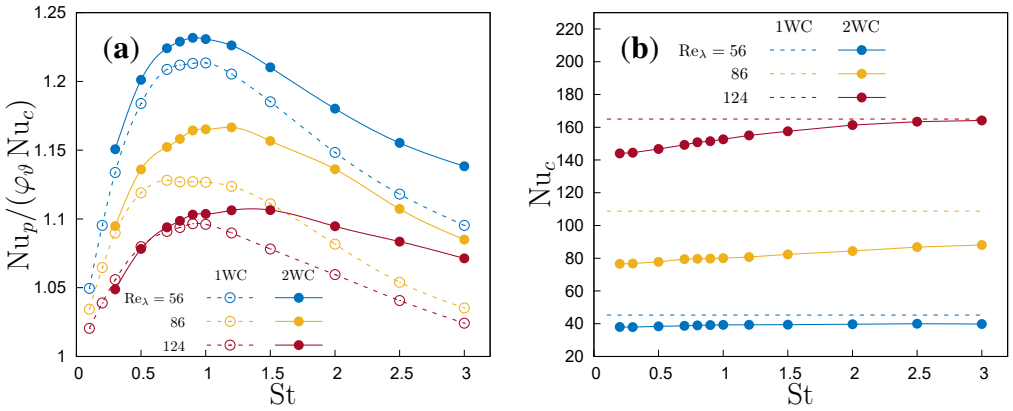

Fig. 3.13 (**a**) Particle contribution to the Nusselt number as a function of the Stokes number at different Taylor microscale Reynolds numbers. (**b**) Convective Nusselt number as a function of the Stokes number. In both panels, continuous lines indicate two-way coupling, and dashed lines indicate one-way coupling.

This expression provides the order of magnitude for the time required for particle feedback to alter the fluid temperature. Substituting the definition of τ_ϑ from Equation (2.93), this timescale matches the one derived by Pouransari and Mani [31], except for a numerical factor of 4π. Since temperature mixing is driven by the large scales of the flow, the timescale for this mixing evolution is the eddy turnover time, τ. Given that $\tau_\eta/\tau \sim \mathrm{Re}_\lambda^{-1}$ in homogeneous and isotropic turbulence [88], the ratio of these two timescales is given by

$$\frac{\tau_T}{\tau} \sim \frac{\tau_\vartheta}{\varphi_\vartheta \tau} = \frac{\mathrm{St}_\vartheta}{\varphi_\vartheta}\frac{\tau_\eta}{\tau} \sim \varphi_\vartheta^{-1}\mathrm{St}_\vartheta \mathrm{Re}_\lambda^{-1},$$

which, apart from an inconsequential numerical constant, aligns with the heat-mixing parameter introduced in [31] and the inverse of the Damköhler number used in [87]. This implies that for $\mathrm{St}_\vartheta \gg 1$, the effect of particles on the fluid temperature occurs on a timescale much longer than the timescale for thermal mixing layer evolution, making the influence of particles on overall heat transfer less significant. The dependence of τ_T/τ on Re_λ^{-1} means this effect becomes more pronounced at lower Reynolds numbers compared to higher Reynolds numbers.

The effect of inter-particle collisions

Numerical results indicate that the maximum particle contribution to the heat flux occurs during the self-similar stage of thermal interaction when the Stokes number is of order one. This corresponds to the point of maximum particle clustering, regardless of the particle thermal inertia, although the thermal inertia determines the peak contribution. However, particle feedback tends to attenuate temperature fluctuations, which reduces the transport caused by turbulent fluid flow fluctuations. It has been observed that collisions affect the flow primarily through the particle thermal back reaction on the fluid temperature field, rather than directly. Collisions increase the fluid-particle temperature difference by scattering particles, which in turn reduces the particle velocity-temperature correlation. Despite these effects, the overall impact on statistical measures remains minimal within the volume fraction range where the point-particle model is valid in both one- and two-way coupling regimes.

To better understand the impact of inter-particle collisions, we compare heat transfer in collisional and collisionless regimes where the fluid and particles are two-way thermally coupled. Simulations are conducted similarly to those in the collisionless regime, as described previously, with parameters listed in Table 3.1. We use a constant ratio of the thermal Stokes number to the Stokes number, set at 4.43, which is representative of water droplets suspended in air. Our focus is on single-point statistics for fluid and particle temperature and velocity. Since the velocity field is statistically homogeneous and the temperature field is homogeneous in the x_1 and x_2 directions, the statistics presented are averaged over planes normal to the inhomogeneous direction x_3 (i.e., in the (x_1, x_2) planes). Thus, all statistics are functions of (t, x_3). Due to the finite domain size and this plane-averaging method, all statistics are subject to some level of noise, which introduces uncertainty into the results. We estimate the uncertainty from the fluctuations in the fluid and particle velocity statistics in the one-way coupling regime, given that homogeneity implies uniform moments. The relative error in the mean temperature is less than 1%, while the error in the fluid second-order moments is about 6%. The error increases to around 8% in the particle's second-order moments for a single simulation. Conditional averages exhibit larger errors, up to 8-10% in the mean temperature difference during collisions, due to the more limited sample size. This error is reduced when additional realizations are considered. Figure 3.14 visualizes the

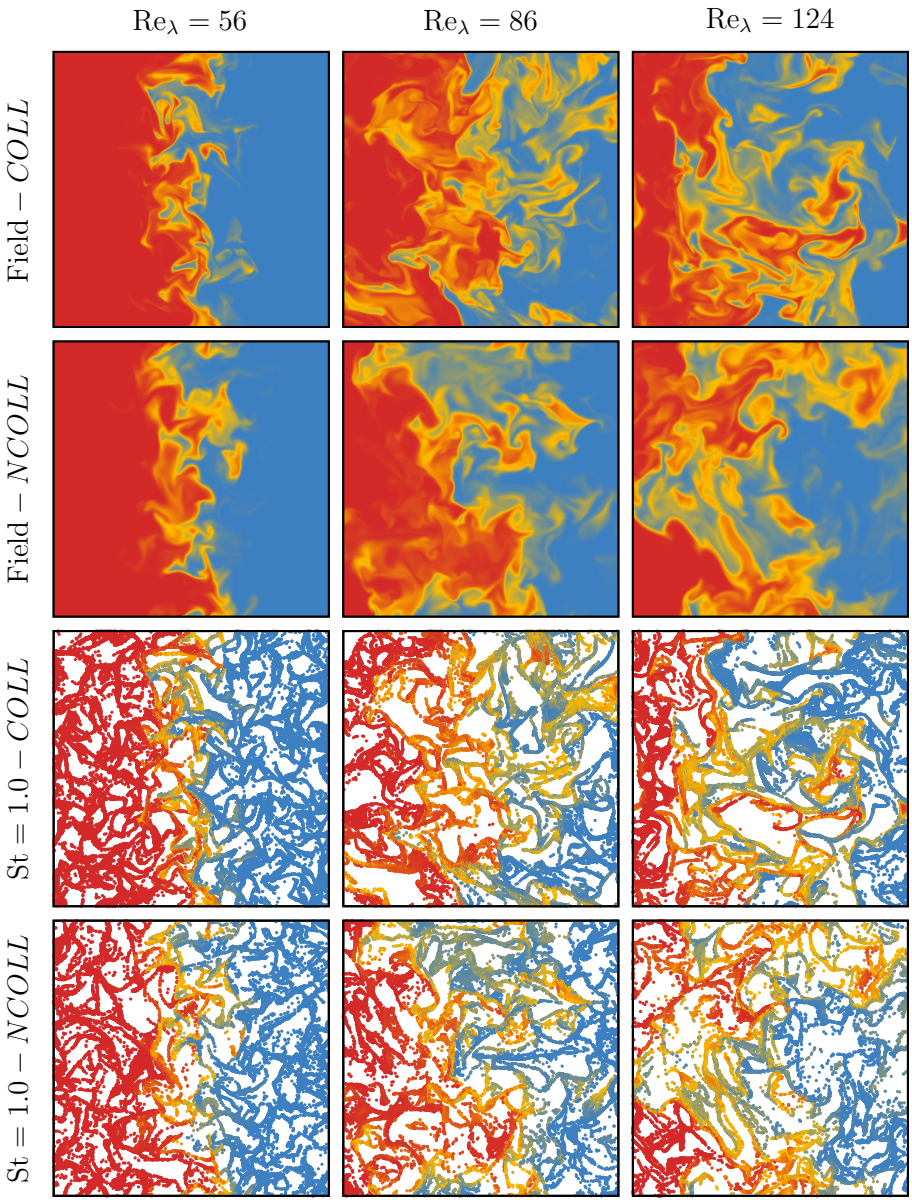

Fig. 3.14 Visualization of fluid fields and suspended particles at $\mathrm{St} = 1$ in a small slab around a (x_1, x_3) plane after three eddy turnover times ℓ/u' in collisional and collisionless regimes at different Re_λ. Particles, out of scale, are coloured according to their temperature, the red colour denotes the highest temperature in the domain, and the blue colour the lowest temperature.

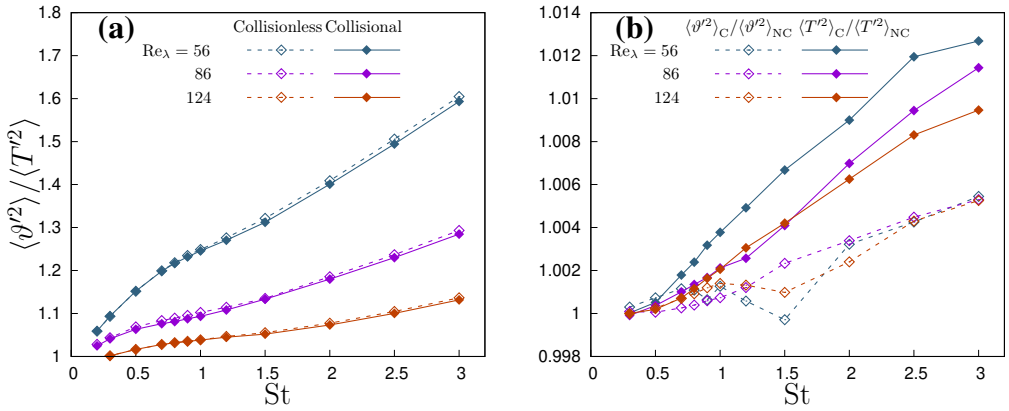

Fig. 3.15 (a) Ratio between particle temperature variance and fluid temperature variance (b) particle-to-particle and fluid-to-fluid temperature variance ratio in two-way coupling simulations with and without collisions. Variances are measure in the central part of the domain, where heat transfer takes place.

instantaneous temperature of the carrier flow and particles in a plane parallel to the mean temperature gradient after three eddy turnover times. It depicts the mixing of warmer and colder fluids by turbulent eddies and particles, which move across the plane initially separating regions at different temperatures, being heated or cooled by the fluid in the process. During this self-similar stage of evolution, the particle-to-fluid temperature variance ratio remains constant. Figure 3.15(a) shows that collisions slightly reduce the variance of particle temperature compared to the fluid temperature, especially at larger Stokes numbers. Due to particle thermal feedback, the fluid temperature variance increases more than the particle variance, particularly at high Stokes numbers, compared to the collisionless regime (see Figure 3.15(b)). However, this difference is minor and might only become significant at higher volume fractions.

Figure 3.18(a) illustrates a key result, the correlation between velocity and temperature fluctuations, which is proportional to the mean heat transfer across the layer separating the two homothermal regions. The mean heat transfer in the inhomogeneous direction x_3 is given by

$$\dot{q} = -\lambda \frac{\partial \langle T \rangle}{\partial x_3} + \rho_0 c_{p0} \langle u_3' T' \rangle + \varphi \rho_p c_{pp} \langle V_{p,3}' \Theta_p' \rangle, \tag{3.51}$$

where the first term represents diffusive heat transfer, the second term accounts for convection by the carrier flow, and the third term denotes the particle contribution.

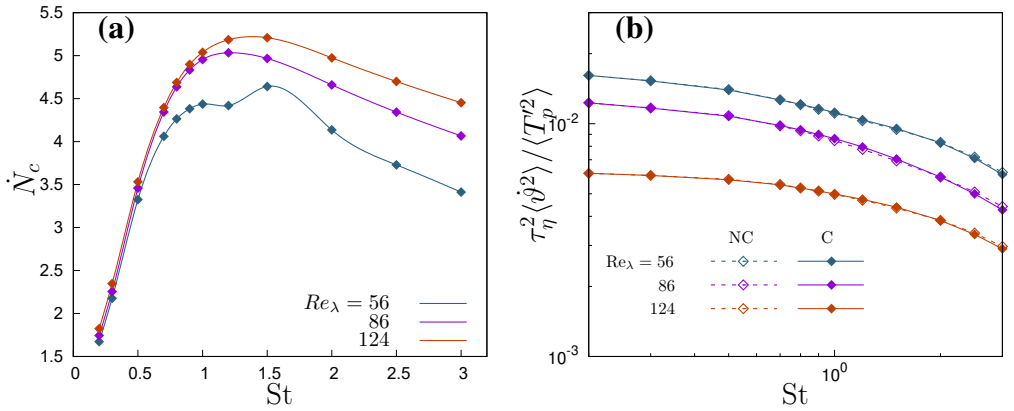

Fig. 3.16 (a) Mean collision rate, number of collisions per unit time and volume in terms of Stokes number at different Taylor microscale Reynolds numbers,(b) the normalized variance of particle temperature derivative as a function of St.

Similar to what we did in collisionless regime, in order to better understand the particle contribution in the mixing layer, the turbulent heat flux in the inhomogeneous direction x_3 can be normalized by the heat transfer in a static, non-moving system. This normalization is achieved using the mixing layer thickness δ, which is the relevant length scale in this flow, thus comparing it to heat transfer in a purely diffusive system. The ratio $\langle V'_{p,3}\Theta'\rangle/\langle u'_3T'\rangle$ measures the contribution of particles to heat transfer across the non-homothermal layer relative to the convective heat flux due to turbulent fluid motions. Figure 3.18(a) shows this ratio for three different Reynolds numbers as a function of the Stokes number. All quantities are computed at the center of the domain, where the correlations peak. During the self-similar stage of the thermal mixing layer, the ratio $\langle V'_{p,3}\Theta'\rangle/\langle u'_3T'\rangle$ remains constant over time, as all fluxes scale with the same $\delta(t)$. The ratio reaches a maximum when the Stokes number is around one, corresponding to the peak in particle clustering. In the limit of vanishing inertia (i.e., as the Stokes number approaches zero), particles behave like passive tracers. However, because the thermal inertia also diminishes in this limit (with $\mathrm{St}_\vartheta/\mathrm{St}$ held constant), $\langle V'_{p,3}\Theta'_p\rangle/\langle u'_3T'\rangle \to 1$ as $\mathrm{St}\to 0^+$. Conversely, at very large inertia (i.e., as $\mathrm{St}\to\infty$), particles' velocity and temperature tend to decorrelate from the fluid velocity and temperature, resulting in a gradual reduction of $\langle V'_{p,3}\Theta'\rangle/\langle u'_3T'\rangle$. This trend is consistent across all simulated Reynolds numbers. Particle inertia modulates the ratio $\langle V'_{p,3}\Theta'\rangle/\langle u'_3T'\rangle$, which increases with the Stokes number. Collisions scatter the particles, leading to a different modulation of fluid temperature fluctuations by particle thermal feedback in the two-way coupling

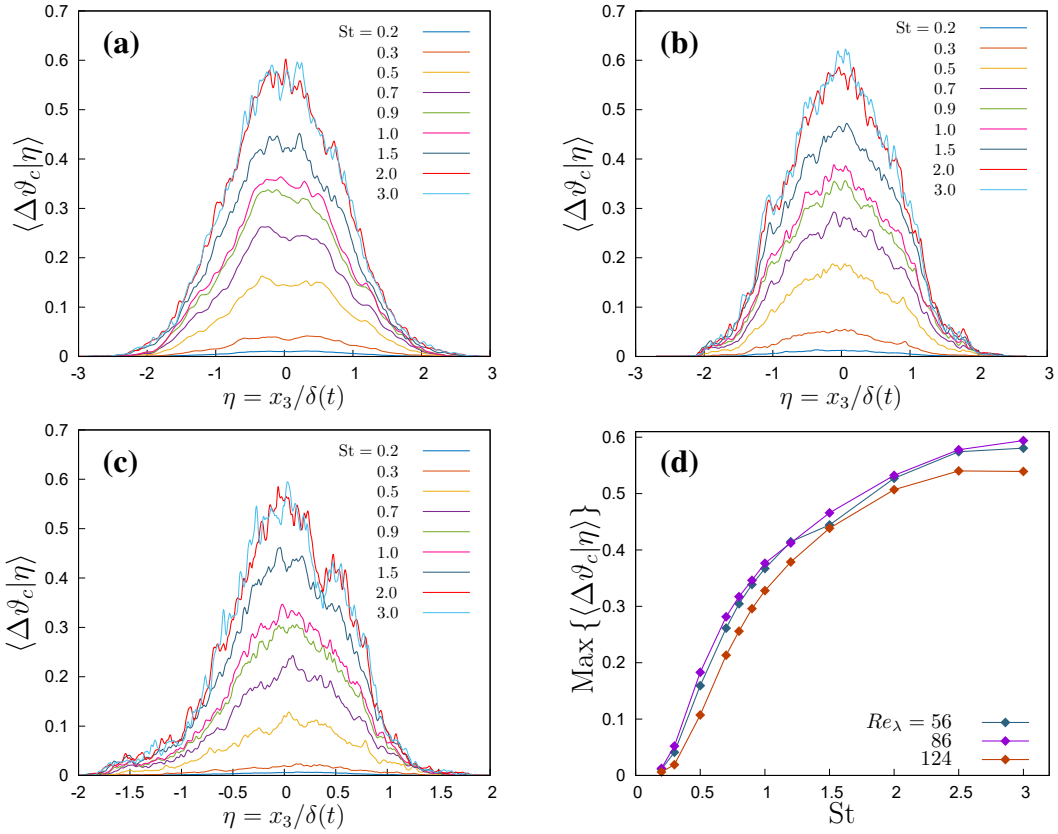

Fig. 3.17 Mean temperature difference between colliding particles $\Delta\vartheta_c = |\vartheta_a - \vartheta_b|$, where ϑ_a and ϑ_b are the temperatures of the colliding particles conditioned on the normalized position η in the x_3 direction at collision: (a) $\mathrm{Re}_\lambda = 56$, (b) $\mathrm{Re}_\lambda = 84$, (c) $\mathrm{Re}_\lambda = 124$. (d) Maximum of the mean temperature difference of colliding particles as a function of the Stokes number St.

regime. Specifically, collisions reduce the tendency of particles to concentrate in regions with large gradients of advected scalars [32].

As shown in Figure 3.16(b), the effect of particle collisions on the heat transfer is minor and, at the volume fractions considered here, negligible. Consequently, the variation in $\langle V'_{p,3}\Theta' \rangle / \langle u'_3 T' \rangle$ can be almost entirely attributed to the attenuation of the particle velocity-temperature correlation. The modification of particle trajectories leads to scattering, which decorrelates their velocity from their temperature, thereby reducing their capacity to transport heat over long distances. The collision rate in turbulent flows tends to be higher for larger particles due to their inertia, which decorrelates their velocity from the fluid velocity. This allows for significant relative velocities between particles even at small separations. Coupled with particle cluster-

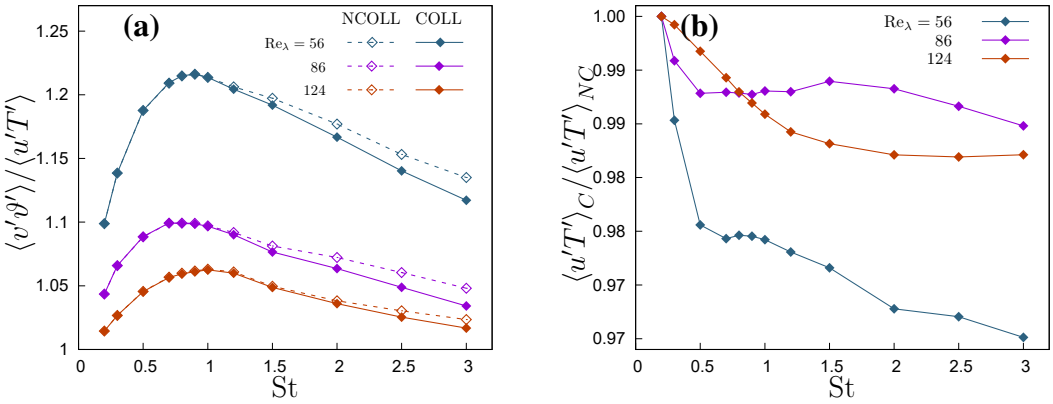

Fig. 3.18 (a) Particle to fluid velocity-temperature correlation ratio as a function of the Stokes number at different Taylor microscale Reynolds numbers. (Solid lines indicate the collisional regime, while dashed lines denote collisionless simulations.) (b) the ratio between fluid velocity-temperature correlation in collisional and collisionless regimes.

ing and preferential concentration, where local particle number densities increase in high strain regions (low vorticity), the collision rate reaches a maximum when the Stokes number is around one, as depicted in Figure 3.16(a). As the Stokes number increases, the collision rate gradually decreases, approaching the ballistic limit as $\mathrm{St} \to \infty$. Significant attenuation of the particle velocity-temperature correlation is observed only at high Stokes numbers, $\mathrm{St} \gtrsim 1.5$. Despite the reduction in collision rate, the variance of the fluid-particle temperature difference increases much faster with St. Figure 3.16(b) shows that $\tau_\eta^2 \langle \dot{\Theta}_p^2 \rangle$ becomes constant at low St and scales as St^α with $\alpha \approx -0.9$ at high St, so that

$$\langle (T - \Theta_p)^2 \rangle = \tau_\eta \langle \dot{\Theta}_p^2 \rangle \mathrm{St}_\vartheta^2 \sim \mathrm{St}^{\alpha+2}.$$

The behavior of the particle temperature time derivative $\dot{\Theta}_p$ in this inhomogeneous flow differs from that observed in homogeneous turbulence [11], due to the presence of a strong temperature gradient that dominates temperature variations over large scales. Large particles can travel further in the x_3 direction, thus entering regions with significantly different temperatures. Consequently, larger particles with higher thermal inertia experience larger temperature gradients on average than in homogeneous flow. This not only enhances local fluid-particle heat transfer but also contributes to a more pronounced reduction in the velocity-correlation correlation when collisions are considered. Collisions between particles with very different temperatures occur between particles from distant regions in the inhomogeneous

direction. This is feasible only for particles with large inertia and thermal inertia. However, collisions scatter particles velocities in the x_3 direction without affecting their temperatures, thereby reducing the $\langle V_p'\Theta'\rangle$ correlation. This effect is clearly visible in Figure 3.17(a,b,c), which displays the mean temperature difference between colliding particles as a function of the normalized position across the thermal mixing layer for different inertia values. Larger particles can more easily traverse temperature fronts [32] and, due to their greater heat capacity, retain their temperature better, leading to substantial temperature differences on collision.

3.4.2 Variable thermal Stokes to Stokes number ratio

In this section, we continue our investigations on the role of inertial particles in overall heat transport and temperature statistics under different conditions than the previous settings. Given the extensive parameter set, the focus is on the effects of particle inertia and thermal inertia, which can independently vary unlike the previous settings. Thus, in the new set of simulations presented here, particle Stokes numbers and paricle thermal Stokes number are not proportional. Other flow parameters, such as Taylor microscale Reynolds number, Prandtl number, particle-to-fluid density ratio and volume fraction, are kept constant and the same as previous simulations. All simulations in this section are conducted with a single Taylor microscale Reynolds number of $\mathrm{Re}_\lambda = 56$. Particle relaxation times are varied by adjusting the particle size and the specific heat ratio c_{pp}/c_{p0} between particles and fluid. Details of the simulation setup and flow parameters are provided in Table 3.3. Furthermore, inter-particle collisions are excluded from this analysis, based on results from Section 3.4.1, which demonstrated that collisions have a minor impact on the heat flux. This section focuses on how the ratio between the relaxation times (τ_ϑ/τ_v) can vary, unlike in the previous section where this ratio was fixed. Consequently, the numerical analysis examines particle thermal and dynamical relaxation times, with parameters chosen to explore Stokes numbers up to 6 and thermal Stokes numbers up to 10 in both one- and two-way coupling regimes. Unlike the previous simulations described in Section 3.4.1, this analysis treats particle inertia and thermal inertia as independent parameters, allowing St and St_ϑ to vary independently.

The interface that initially separates the two homothermal regions is disrupted by the turbulent velocity field and evolves into a thermal mixing layer characterized by high temperature variance and strong intermittency at its borders [77]. As

demonstrated in Section 3.4.1, the region where temperature is non-uniform and the two zones interact has a thickness that grows over time. After several eddy turnover times $\tau = \ell/u'$, where ℓ is the integral scale of the flow and u' is the root mean square of velocity fluctuations, the mean temperature of the fluid exhibits, within numerical uncertainty, a self-similar profile. As discussed earlier, δ, the thermal mixing layer thickness, serves as the relevant length scale of this self-similar evolution. Figure 3.19 illustrates the spatial distribution of the convective heat flux and particle temperature variance, normalized by the mixing layer thickness δ, for $\mathrm{St} = \mathrm{St}_\vartheta = 1$. Both the temperature variance and the temperature-velocity correlation reach their maximum at $x_3 = 0$, where the mean temperature gradient is the most pronounced. The temperature gradient across the mixing layer is approximately $(T_1 - T_2)/\delta$, so large-scale flow structures, with a scale of the order of the integral scale ℓ, experience a temperature difference of approximately $(T_1 - T_2)\ell/\delta$. This represents the expected scale of temperature fluctuations within the mixing layer. Consequently, if u' denotes the root mean square of the fluid velocity fluctuations, the correlation $\langle V_p'\Theta_p'\rangle$ can dimensionally scale as $u'(T_1 - T_2)\ell/\delta$, while the temperature variance should scale as $[(T_1 - T_2)\ell/\delta]^2$. For $t/\tau \gtrsim 3$, the curves of both moments are very close to each other, nearly collapsing within the noise limits associated with their computation. This indicates a self-similar or quasi self-similar behavior of particle second-order moments, a phenomenon also observed in section 3.4.1 for one- and two-way coupling regimes where $\mathrm{St}_\vartheta/\mathrm{St} = 4.43$. Therefore, even in these new simulations whre St and St_ϑ are not proportional and are variable, we are allowed rightfully average all rescaled moments over time thanks to this self-similarity. However, the more comprehensive analysis in this regard will be conducted in chapter 5. In this section, we will discuss the properties of the mixing layer based on these averaged moments at the center of the mixing layer. Given the quasi self-similar behavior, this central region can be assumed to be the legitimate representative of the entire layer.

This interaction, or more broadly, the thermal mixing layer (as described in [89, 77]), is also characterized by the onset of a significant velocity-temperature correlation. This correlation is primarily responsible for the transport of total enthalpy across the layer. By averaging the governing equation for fluid temperature (3.3),

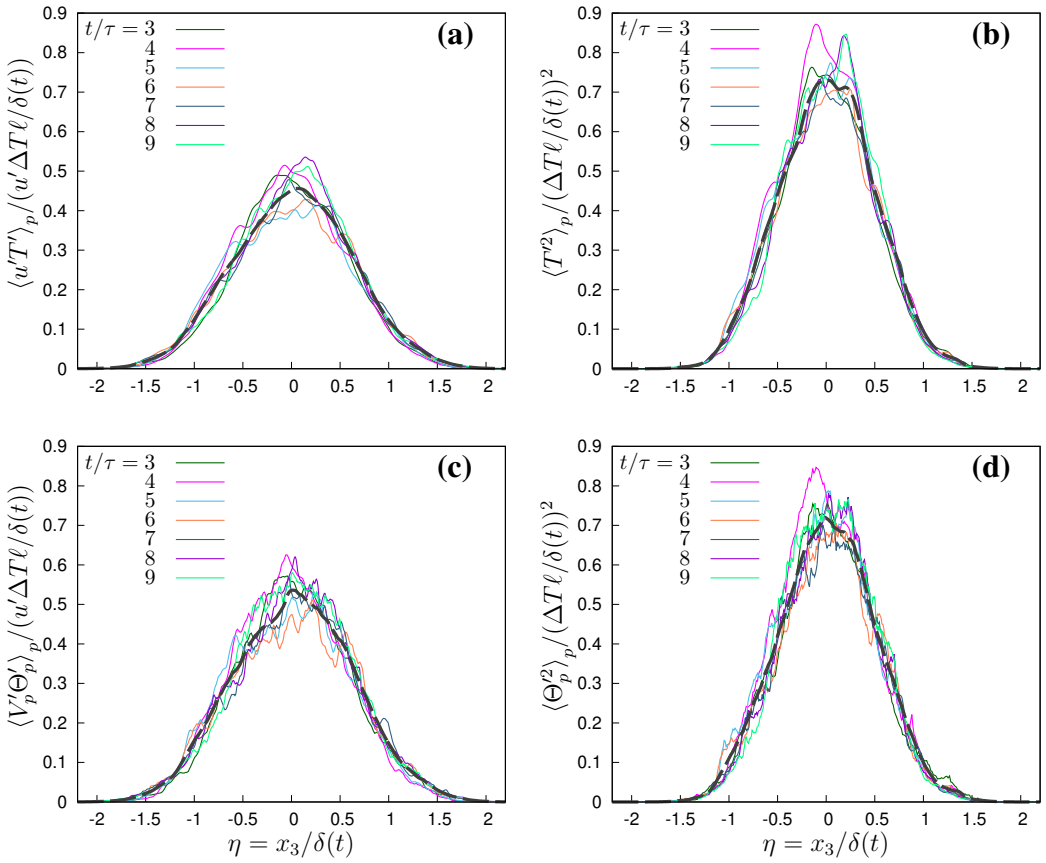

Fig. 3.19 (a), (c) Rescaled convective fluid and particle heat flux (temperature-velocity correlation) and (b), (d) rescaled fluid and particle temperature variance. Both the Stokes number and the thermal Stokes number are equal to 1 in this example. In all panels, $\Delta T = T_1 - T_2$ and the dashed lines indicate the time average of the rescaled variables for $t/\tau \geq 3$.

the mean total heat flux in the inhomogeneous direction x_3 can be expressed as

$$-\lambda \frac{\partial \langle T \rangle}{\partial x_3} + \rho_0 c_{p0} \langle u_3' T' \rangle + \varphi \rho_p c_{pp} \langle V_3' \Theta_p' \rangle_p, \tag{3.52}$$

or, in dimensionless form

$$-\frac{1}{\mathrm{Re}\,\mathrm{Pr}} \frac{\partial \langle T \rangle}{\partial x_3} + \langle u_3' T' \rangle + \varphi_\vartheta \langle V_{p,3}' \Theta_p' \rangle_p, \tag{3.53}$$

where the first term represents the mean temperature diffusion, the second term corresponds to the convective heat flux, and the third term accounts for the particle contribution to the mean heat transfer. Since $\delta(t)$ is the only relevant length scale in this problem, the quantity $\lambda(T_1 - T_2)/\delta(t)$ serves as the scale of the heat flux in static conditions. The Nusselt number, defined as the ratio of the actual heat flux to this static heat flux scale, can be expressed as

$$\mathrm{Nu} = 1 + \frac{\delta}{\kappa} \frac{\langle u_3' T' \rangle}{T_1 - T_2} + \varphi_\vartheta \frac{\delta}{\kappa} \frac{\langle V_3' \Theta_p' \rangle_p}{T_1 - T_2}. \tag{3.54}$$

Thus, the rescaled fluid and particle velocity-temperature correlations, as illustrated in figure 3.19(a), directly contribute to the Nusselt number for this flow configuration. Particles have a dual role in the interaction between the two regions, which globally manifests itself with a transport of heat from one to the other, a direct role, as their motion counteracts the enthalpy transfer, and an indirect role, due to the modulation of temperature and velocity fluctuations of the carrier fluid. However, indirect role acts only on the fluid temperature field, since the particle momentum feedback is not considered in this study. Therefore, both one-way and two-way thermally coupled regimes are considered, as their differences help to highlight the role of particle feedback in the flow, i.e., the indirect role of particles.

Temperature and velocity moments in terms of particle time derivatives

Given the flow inhomogeneity and unsteadiness of the fluid temperature field, in the following we consider conditional averages at a given time and position x_3 along the inhomogeneous direction, i.e., we define, for any function f of the state of the particle,

$$\langle f \rangle_p = \langle f | t, x_3 \rangle,$$

where $\langle\cdot\rangle$ is the statistical average, and define the fluctuation of f as $f' = f - \langle f \rangle_p$. We will now express the average temperature fluctuations and the heat flux in terms of the time derivatives of particle velocity (i.e., the acceleration) and temperature. By subtracting from (4.1) its conditional average, the particle temperature and velocity fluctuations can be expressed in terms of the fluctuations of the time derivatives, i.e.,

$$V'_{p,i} = u'_i - \tau_v \dot{V}'_{p,i}, \tag{3.55}$$

$$\Theta'_p = T' - \tau_\vartheta \dot{\Theta}'_p, \tag{3.56}$$

where fluid velocity and temperature are to be computed at particle position. In the following, we will skip the apex from all moments of second order or higher to keep notations simple. By multiplying the particle temperature fluctuation (3.56) by Θ'_p and T' and conditionally averaging, we have

$$\langle \Theta_p^2 \rangle_p = \langle T\Theta_p \rangle_p - \tau_\vartheta \langle \Theta_p \dot{\Theta}_p \rangle_p, \tag{3.57}$$

$$\langle T^2 \rangle_p = \langle T\Theta_p \rangle_p + \tau_\vartheta \langle T\dot{\Theta}_p \rangle_p. \tag{3.58}$$

Therefore, the ratio of particle temperature variance to fluid temperature variance at particle position is

$$\frac{\langle \Theta_p^2 \rangle_p}{\langle T^2 \rangle_p} = \frac{1 - \tau_\vartheta \left[\frac{\langle \Theta_p \dot{\Theta}_p \rangle_p}{\langle T\Theta_p \rangle_p} \right]}{1 + \tau_\vartheta \left[\frac{\langle T\dot{\Theta}_p \rangle_p}{\langle T\Theta_p \rangle_p} \right]}, \tag{3.59}$$

while, by multiplying (3.56) by the temperature derivative and conditionally averaging, we have instead a relation for the variance of the temperature derivative,

$$\langle \dot{\Theta}_p^2 \rangle_p = \frac{\langle T\dot{\Theta}_p \rangle_p - \langle \Theta_p \dot{\Theta}_p \rangle_p}{\tau_\vartheta}. \tag{3.60}$$

Equations ((3.59)-(3.60)) are general and can help to analyze the role of particle thermal inertia in the fluid and particle temperature statistics. Given the self-similarity of the flow, this ratio is independent of the position x_3 and time t. In the following, we will use it to discuss the behaviour of the flow in the central region of the mixing layer, in a thin region, of thickness much less than δ, where variance and heat flux have their maximum. All data presented in the figures refer to this zone, because the

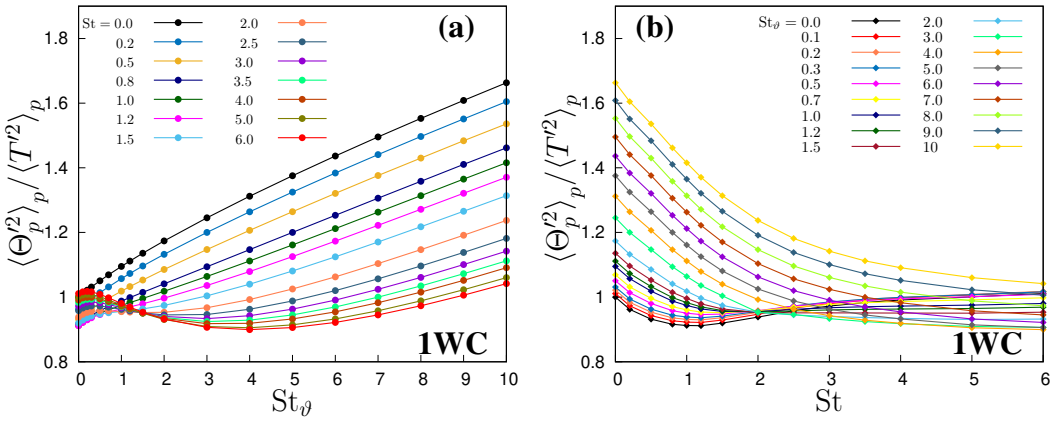

Fig. 3.20 Ratio between particle temperature variance to fluid temperature variance in one-way coupling simulations, (a) as a function of the thermal Stokes number and (b) as function of the Stokes number.

relative homogeneity of the flow in this zone [77] allows for the reduction of noise in the processing of numerical data.

Few information can be directly inferred from these equations, particularly regarding the limiting cases. In the zero-thermal inertia limit, $\mathrm{St}_\vartheta \to 0^+$, particle temperature variance and fluid temperature variance become the same, independent of the momentum relaxation time. On the other hand, in the opposite limit $\mathrm{St}_\vartheta \to +\infty$, the ratio equals $\langle \Theta_p \dot{\Theta}_p \rangle_p / \langle T \dot{\Theta}_p \rangle_p$. This highlights the importance of the particle temperature time derivative in determining particle temperature fluctuations. As discussed by Carbone et al. [32] and Bec et al. [11], particle thermal acceleration (or particle temperature time derivative) is responsible for fluid-particle small-scale thermal interaction. For instance, high thermal inertia particles act as thermal filters, smoothing out small-scale temperature fluctuations due to their slower thermal response. In two-way thermal coupling, particles can modulate not only the small-scale but also the large-scale structures of the thermal fields, depending on the level of coupling and particle concentration. However, high thermal inertia particles predominantly interact with large-scale temperature fluctuations, leading to a reduced local heat transfer with the surrounding fluid as their thermal response is less sensitive to small-scale variations. In particular, Carbone et al. in [32] analyzed the small-scale fluid-particle interaction based on the statistics of the particle temperature time derivative $\dot{\Theta}_p$ in both one-way and two-way coupling. They concluded that particle inertia generates a multifractal behavior, as indicated by Lagrangian temperature structure functions. This lack of smoothness in particle temperature difference,

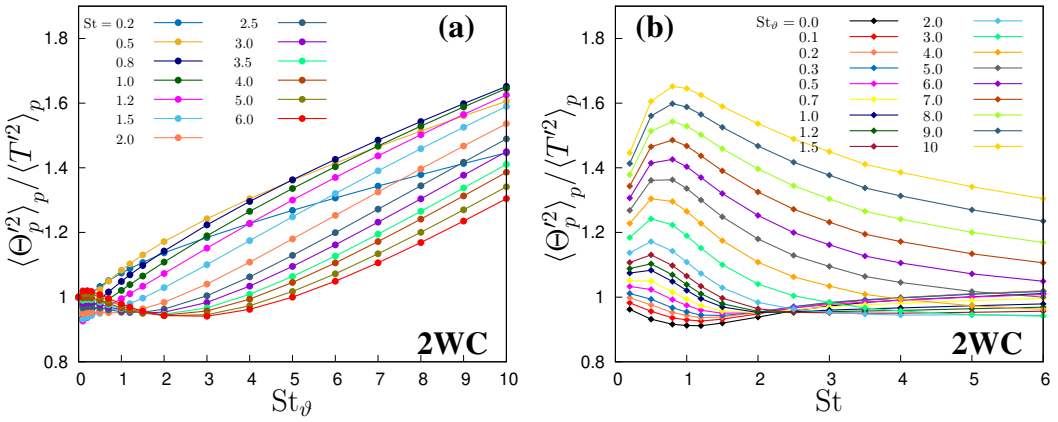

Fig. 3.21 Ratio between particle temperature variance to fluid temperature variance in two-way coupling simulations, (a) as a function of the thermal Stokes number and (b) as function of the Stokes number.

defined by [32] as thermal caustics, dominates at small scales, where the particle temperature difference at small separations rapidly increases as the Stokes number and the thermal Stokes number increase. We will also be back to this concept, the thermal caustics in the last chapter, 6. We will propose and discuss a novel theory to formulate the thermal caustics based on the particle temperature gradient and particle velocity gradient. Bec et al. [11] related the onset of fluid temperature fronts along particle Lagrangian paths to the dynamics of particle temperature time derivative, whose non-Gaussian statistics lead to a multifractal behavior. Note that at a fixed Stokes number, we can use (3.58) to understand the effect of particle thermal inertia at very high thermal Stokes numbers. Even though particle inertia does not explicitly appear in eqs. ((3.57)-(3.59)), it influences particle trajectories and, therefore, the fluid temperature at the particle position.

Figure 3.20(a) shows that the ratio of variances increases with St_ϑ for any Stokes number at large St_ϑ, i.e. at least when $\mathrm{St}_\vartheta \gtrsim \mathrm{St}$, but the slope reduces at higher inertia, so that at fixed St_ϑ, figure 3.20(b), it always reduces if $\mathrm{St} > 1$. On the contrary, at low thermal inertia, $\mathrm{St}_\vartheta < 1$, particle temperature variance remains always lower than fluid temperature variance and approaches it in the $\mathrm{St} \to \infty$ limit. In the one-way coupling regime, the denominator of (3.59) is a function of St only, and increases with St (figure 3.23(b)) so that the thermal inertia acts only on $\langle \Theta_p \dot{\Theta}_p \rangle_p$ in the numerator (figure 3.23(a)). In the two-way coupling case (figure 3.21), the growth with the thermal Stokes number is much faster, because particle enhance the dissipation of fluid temperature variance [32], and this effect grows monotonically

with their thermal inertia. This is essentially in agreement with our previous results [36], but in those works the ratio between particle thermal inertia and inertia is kept constant, so that an increase of inertia is associated to an increase of thermal inertia, and no independent limit with respect to each variable is possible. At very small St, when St_ϑ increases the particle variance deviates from fluid temperature variance. The effect of thermal inertia is dominant over the particle inertia in all range of Stokes number. Particle temperature variance is maximum for small particles with large thermal inertia (i.e. $\mathrm{St} \to 0$ and $\mathrm{St}_\vartheta \to \infty$), as the lag between T and Θ_p induced by a large St_ϑ allows for large particle temperatures deviations from the mean temperature of particles coming from the two homothermal regions. The minimum particle temperature variance occurs when particle relaxation time increases, $\mathrm{St} \to \infty$, for an intermediate thermal Stokes number, as $\mathrm{St}_\vartheta \to 0$ makes its variance equal to that one of the flow, and $\mathrm{St}_\vartheta \to \infty$ makes it increase.

It should be noted that in the two-way coupling regime, where the thermal feedback C_T is accounted for, the interaction described in equation (3.59) becomes significantly more complex. This is because the temperature T is no longer independent of the particle temperature Θ_p, leading to a coupling between the numerator and denominator of the ratio. The modulation of fluid temperature fluctuations implies that, even in the thermal ballistic limit ($\mathrm{St}_\vartheta \to \infty$), the ratio $\langle \Theta_p \dot{\Theta}_p \rangle_p / \langle T \dot{\Theta}_p \rangle_p$ does not approach a unique limit. The influence of particle modulation on fluid temperature fluctuations can be understood by comparing the fluid temperature variance in one-way and two-way coupling regimes, as shown in figure 3.22. This figure presents the ratio of variances in the two regimes as a function of St and St_ϑ. For small particles, where $\mathrm{St} \lesssim 1$ and $\mathrm{St}_\vartheta \lesssim 1.5$, the feedback effect results in an increase in the fluid temperature variance. Conversely, larger particles, with $\mathrm{St} > 1$ and $\mathrm{St}_\vartheta \gtrsim 1.5$, consistently reduce fluid temperature fluctuations. This damping effect becomes more pronounced at higher values of St_ϑ, while the modulation of fluid temperature variance by particles is almost negligible for $\mathrm{St}_\vartheta < 1$.

An equation for the ratio between particle and fluid temperature variance in a homogeneous and isotropic flow was proposed by [87] based on Langevin equations for fluid temperature fluctuations, and by [32] from the properties of the general solution of the quasi-linear equation for particle temperature and the statistics of temperature increments at very small and very large time separations. In both cases, an increase in thermal inertia consistently led to a reduction in the ratio $\langle \Theta_p'^2 \rangle_p / \langle T'^2 \rangle_p$, as larger inertia acts as a filter for the surrounding fluid fluctuations

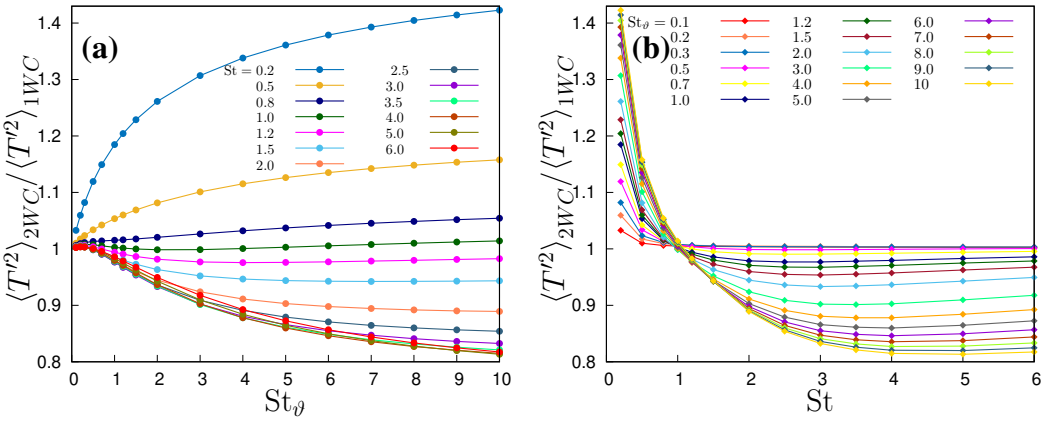

Fig. 3.22 Comparison between one- and two-way coupling: ratio between fluid temperature as function of (a) thermal Stokes number and (b) Stokes number.

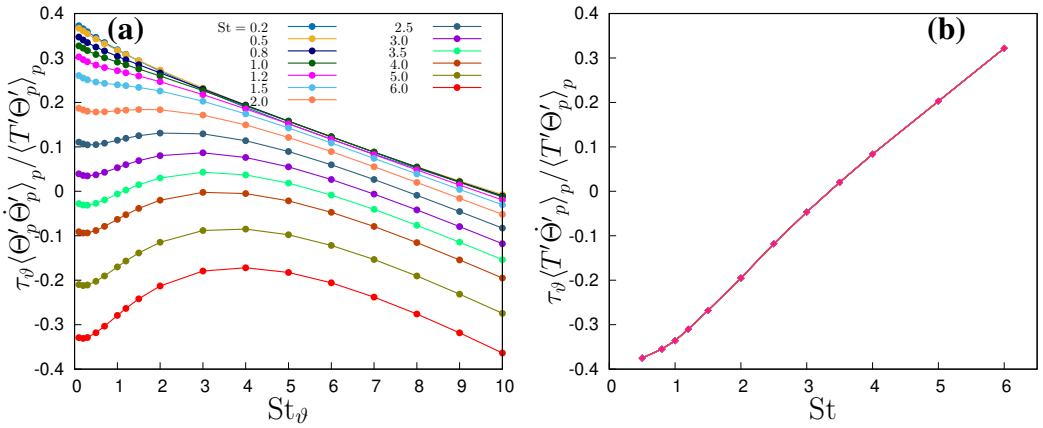

Fig. 3.23 Normalized particle temperature derivative correlation with (a) particle temperature and (b) fluid temperature.

of T sampled by the particle along its trajectory. Specifically,

$$\frac{\langle\Theta_p^2\rangle_p}{\langle T^2\rangle_p}=\frac{1}{1+\alpha\tau_\vartheta/\tau_T}, \tag{3.61}$$

where τ_T is the time-scale of fluid temperature fluctuations sampled by the particle, proportional to the large-scale eddy turnover time $\tau=\ell/u'$. The coefficient α is a dimensionless parameter; it is equal to 1 in [32], while in [87], it varies depending on the actual situation of the turbulence, serving as a fitting coefficient in the Langevin model to account for the effect of finite Reynolds number on the temporal scale experienced by an advected scalar. In contrast, in the present flow configuration,

increased thermal inertia allows particles originating from one of the two homogeneous regions to maintain their original temperature more effectively as they traverse the thermal mixing layer. This results in an enhanced temperature variance within the layer. Consequently, the large-scale temperature gradient imposed by the initial conditions, which induces a temperature modulation on the length scale δ, dominates over the small-scale effects of spatial clustering of particles at local temperature fronts. These local fronts are located in high-strain regions and influenced by velocity fluctuations.

Velocity-temperature correlation

The same argument applies to the role of particle inertia and thermal inertia in the velocity-temperature correlations, which are crucial for defining the heat transfer across the inhomogeneous layer. To analyze this, we can multiply equations (3.55) and (3.56) and take the conditional average, yielding

$$\langle V_{p,i}\Theta_p\rangle_p = \langle u_i T\rangle_p - \tau_v\langle T\dot{V}_{p,i}\rangle_p - \tau_\vartheta\langle u_i\dot{\Theta}_p\rangle_p + \tau_v\tau_\vartheta\langle\dot{\Theta}_p\dot{V}_{p,i}\rangle_p. \tag{3.62}$$

This can be divided by the fluid velocity-temperature correlation to obtain

$$\frac{\langle V_{p,i}\Theta_p\rangle_p}{\langle u_i T\rangle_p} = 1 - \tau_v\frac{\langle\dot{V}_{p,i}T\rangle_p}{\langle u_i T\rangle_p} - \tau_\vartheta\frac{\langle u_i\dot{\Theta}_p\rangle_p}{\langle u_i T\rangle_p} + \tau_v\tau_\vartheta\frac{\langle\dot{V}_{p,i}\dot{\Theta}_p\rangle_p}{\langle u_i T\rangle_p}. \tag{3.63}$$

Thus, the particle contribution to the heat flux can be decomposed in terms of the correlations between the particle derivatives and their interactions with fluid velocity and temperature fluctuations.

The ratio expressed in equation (3.63) is directly linked to the particle contribution to the heat flux across the thermal mixing layer, as detailed in equation (3.52) concerning the convective heat flux. This ratio, therefore, is a crucial aspect of any modeling efforts. The flux decomposition presented in equation (3.62) provides insight into how particle heat flux is influenced by both particle inertia and thermal inertia, as these parameters modulate particle velocity and temperature time derivatives. Figures 3.24, 3.25, and 3.26 offer an overview of the correlation ratio (3.63). Figure 3.24 presents an overall view of the ratio between particle velocity-temperature correlation and fluid velocity-temperature correlation, derived from 256 simulations in the one-way coupling regime and 221 simulations in the two-way

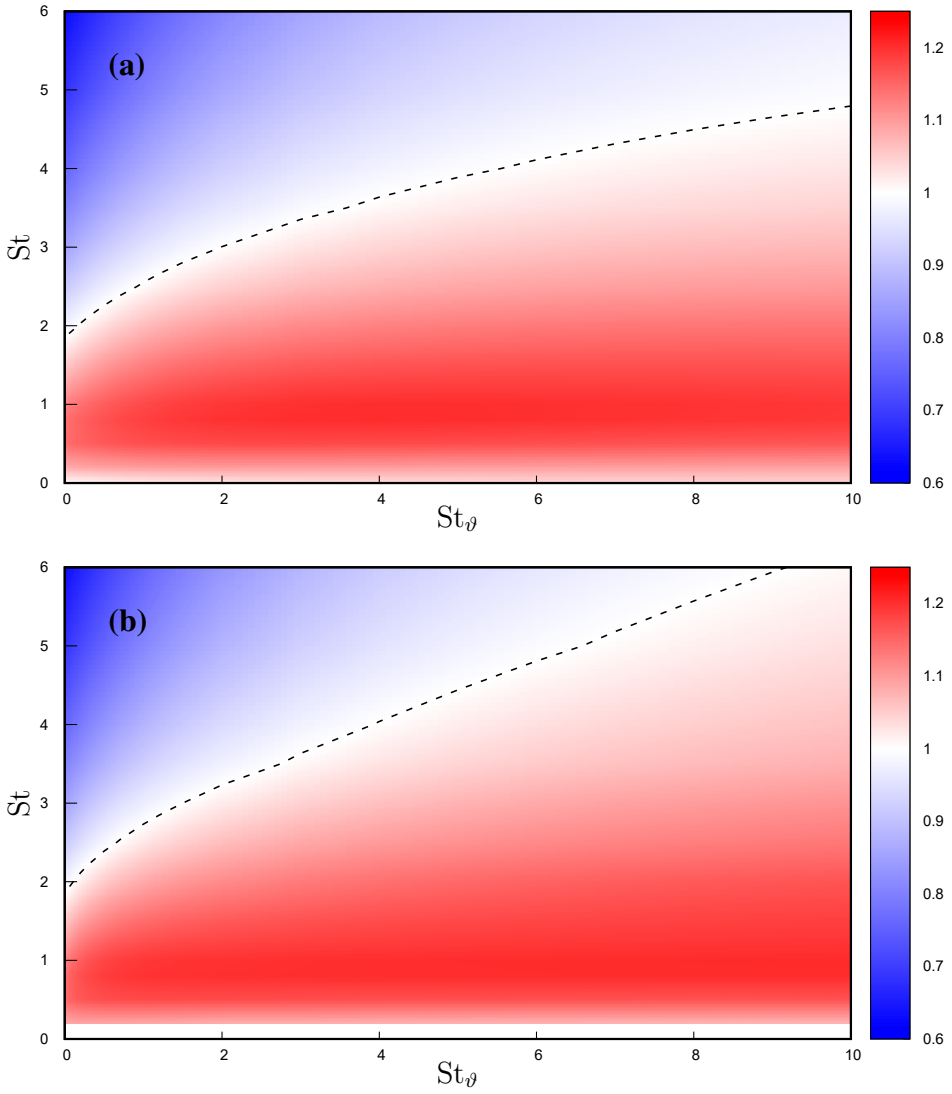

Fig. 3.24 Normalized particle velocity-temperature correlations $\langle V_p'\Theta_p'\rangle_p / \langle u'T'\rangle_p$ as function of the Stokes and thermal Stokes number: (a) one-way coupling regime, (b) two-way coupling regime. The dashed line indicates a value equal to one, where fluid and particle velocity-temperature correlations are equal.

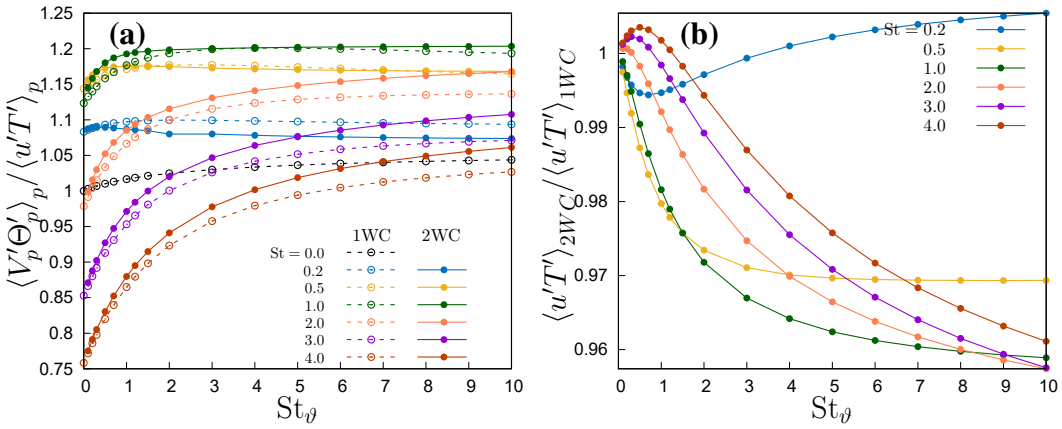

Fig. 3.25 (a) Normalized particle-to-fluid velocity-temperature correlation; (b) ratio between fluid velocity-temperature correlation in one- and two-way coupling regimes.

coupling regimes. This ratio consistently increases with thermal inertia (St_ϑ) at any given Stokes number, reaching an asymptotic limit that depends on the Stokes number. Particle inertia (St) causes this ratio to peak when the particle relaxation time is comparable to the Kolmogorov microscale (i.e., $\mathrm{St} \simeq 1$), a scenario where particles are expelled from the small-scale vortex cores. This effect is more clearly visible in figure 3.25(a), where each curve represents a specific Stokes number. For large Stokes numbers, the limit is always higher than one, meaning that when the thermal Stokes number is sufficiently large, the particle velocity-temperature correlation exceeds the fluid velocity-temperature correlation. The transition condition $\langle V_p'\Theta_p'\rangle_p = \langle u'T'\rangle_p$, shown by the dashed line in figure 3.24, can be fitted as

$$\mathrm{St} = a(1 + \mathrm{St}_\vartheta / b)^n, \tag{3.64}$$

with $a \simeq 1.85$, $b \simeq 0.62$, and $n \simeq 0.34$ in the one-way coupling regime, and $a \simeq 1.85$, $b \simeq 0.43$, and $n \simeq 0.32$ in the two-way coupling regime up to $\mathrm{St}_\vartheta \lesssim 2.5$. Beyond this threshold, the relationship tends to be linear for $\mathrm{St}_\vartheta \gg 1$, with $n \simeq 0.85$ for $\mathrm{St}_\vartheta > 2.5$. Stokes numbers below this threshold lead to an increase in the correlation ratio, while ratios for larger Stokes numbers fall below one. Given that $n < 1$, it is inferred that in the ballistic limit ($\mathrm{St} \to \infty$), particle velocity and temperature tend to decorrelate, regardless of particle thermal inertia. However, in the thermal ballistic limit ($\mathrm{St}_\vartheta \to \infty$), a significant correlation persists, often exceeding the fluid correlation, especially around a Stokes number of one. In the two-way coupling regime, this decorrelation process occurs more slowly due to the particle thermal

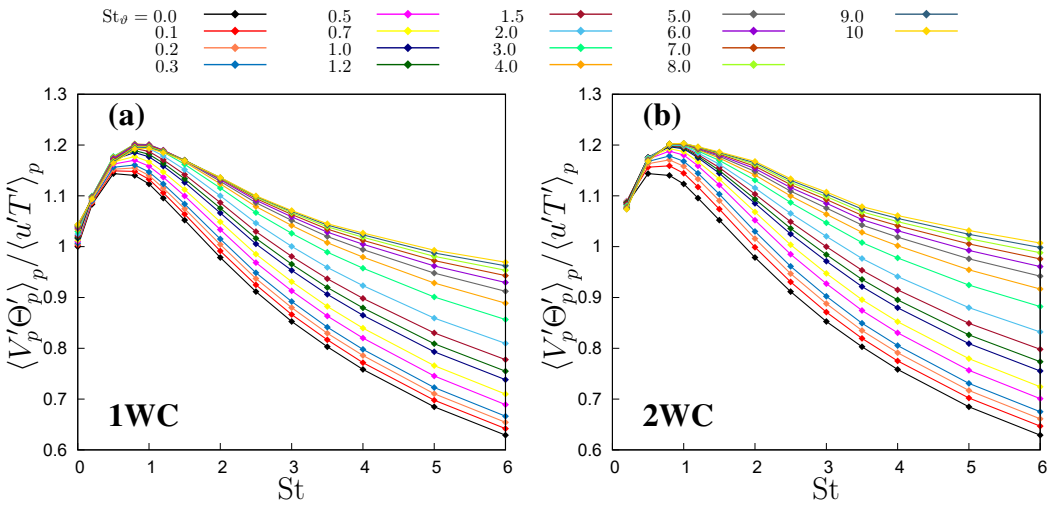

Fig. 3.26 Normalized particle velocity-temperature correlation as function of the Stokes number in: (a) one-way coupling, (b) two-way coupling.

feedback altering fluid temperature along its trajectory. This modulation of fluid temperature fluctuations by particles results in a reduction in the convective heat flux $\langle uT \rangle$, as observed in previous sections. Simulating $\mathrm{St} = 0$ is not feasible in the two-way coupling scenario because the number of particles N_p scales as $N_p \sim \varphi\,\mathrm{St}^{-3/2}$, diverging as $\mathrm{St} \to 0^+$. Thus, only $\mathrm{St} \geq 0.2$ is represented in figure 3.25. This limitation does not affect the one-way coupling regime, where particle interactions with the fluid phase are negligible, rendering their actual number irrelevant.

The data presented in section 3.4.1, where the ratio $\mathrm{St}_\vartheta/\mathrm{St}$ was kept fixed, corresponds to a diagonal cut in figure 3.24. This ratio is given by

$$\frac{\mathrm{St}_\vartheta}{\mathrm{St}} = \frac{3}{2}\frac{1}{\mathrm{Pr}}\frac{c_{pp}}{c_{p0}}, \tag{3.65}$$

where Pr is the Prandtl number, c_{pp} is the specific heat of the particle, and c_{p0} is the specific heat of the fluid. A higher ratio of particle to fluid specific heat results in higher overall correlation levels between particle temperature and velocity, as a smaller portion of the map in figure 3.24 is sampled. Maintaining a constant ratio between St_ϑ and St implies fixing the particle material while allowing the size to vary. For any type of particle, there exists a critical Stokes number beyond which the particle velocity-temperature correlation is lower than the fluid velocity-temperature correlation. At higher Stokes numbers, velocity and temperature consistently decorrelate. This behavior was not observed in section section 3.4.1 due to the maximum

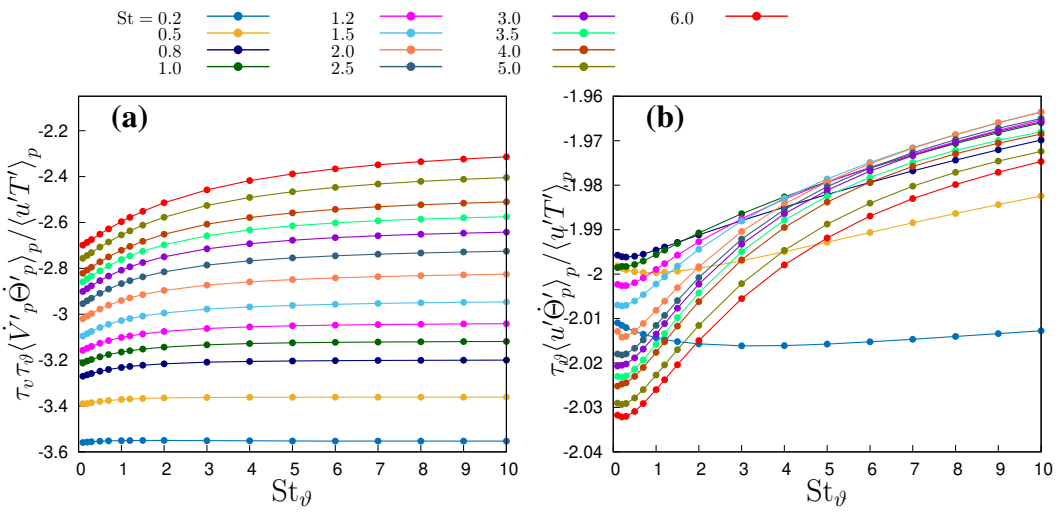

Fig. 3.27 (a) Normalized particle velocity and temperature derivatives correlation; (b) Normalized fluid velocity- particle temperature derivative correlation.

simulated Stokes number being limited to 3. In the two-way coupling regime, particle feedback generally increases the ratio (3.63), but most of the observed variations are attributed to the resulting damping of fluid correlations (see figure 3.25(b)), rather than an increase in particle correlations. This damping effect is due to particle preferential concentration near temperature fronts, as described by [11, 32] in homogeneous turbulence, which smooths fluid temperature gradients. Notably, only for Stokes numbers greater than one is there a small range of St_ϑ where particle modulation of fluid fluctuations produces a slight increase in the fluid velocity-temperature correlation. In all other cases, this correlation is reduced. This damping effect leads to an overall reduction in the fluid heat flux across the thermal mixing layer, except at low inertia.

To investigate the impact of particle inertia and thermal inertia on heat transfer, we analyze numerical simulation data by decomposing the velocity-temperature correlation $\langle V'_p \Theta'_p \rangle_p$ using the decomposition presented in equation (3.63). The contributions of the three terms in equation (3.63) are illustrated in figures 3.27 and 3.28(a) for the one-way coupling case. The first term, shown in figure 3.28(a), depends solely on St in the one-way coupling regime. Here, particle velocity and fluid temperature are independent of particle thermal inertia. This term decreases with increasing St and takes on negative values, similar to the second term depicted in figure 3.27(b). The second term, $\tau_\vartheta \langle u' \dot{\Theta}'_p \rangle_p$, exhibits a mild dependence on both St and St_ϑ, varying by no more than 2% within the studied parameter range. Both

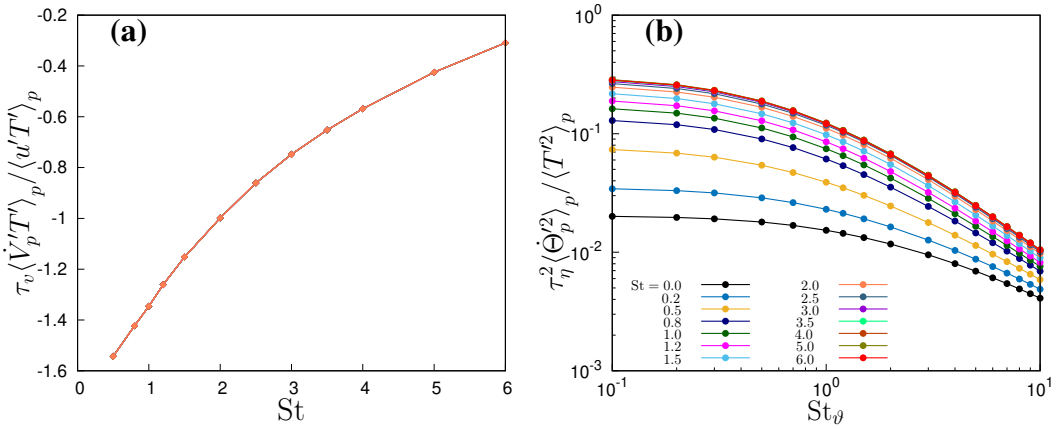

Fig. 3.28 (a) Normalized particle acceleration-temperature correlation; (b) normalized particle temperature derivative variance.

terms contribute to the particle temperature-velocity correlation and enhance heat transfer. Overall, the sum of these terms decreases with the Stokes number, with only a minor influence from the thermal Stokes number. Conversely, the third term in equation (3.63), which is proportional to the correlation between particle acceleration $\dot{V}_p$ and the temperature derivative $\dot{\Theta}_p$ (figure 3.27(a)), is negative due to the mean temperature gradient. This term reduces the $\langle V_p' \Theta_p' \rangle_p$ correlation, showing more significant effects at lower Stokes numbers and diminishing with increasing St and St_ϑ. The effect is more gradual compared to the first term, resulting in maximal correlation around $\mathrm{St} = 1$. However, it is responsible for decorrelation at large St, due to its strong dependence on St. The gradual reduction in correlation with St_ϑ is less pronounced compared to the reduction in temperature time derivative variance, as shown in figure 3.28(b). The variance of the temperature time derivative increases with the Stokes number but decreases with the thermal Stokes number. According to equation (3.60), this variance is proportional to the difference between the correlation of fluid temperature and its time derivative and the correlation between particle temperature and its time derivative. In homogeneous turbulence, a smooth temperature field results in a finite limit for the variance of Θ_p at small thermal Stokes numbers [32]. Conversely, in the limit of very high thermal inertia, the variance of the temperature time derivative tends to decrease as $\mathrm{St}_\vartheta^{-2}$ due to uncorrelated temperature increments [11, 32]. The data shown in figure 3.28(b) indicate a low thermal inertia limit at all simulated Stokes numbers, suggesting a smooth temperature field. In the self-similar stage with high thermal inertia, well-mixed regions within the thermal

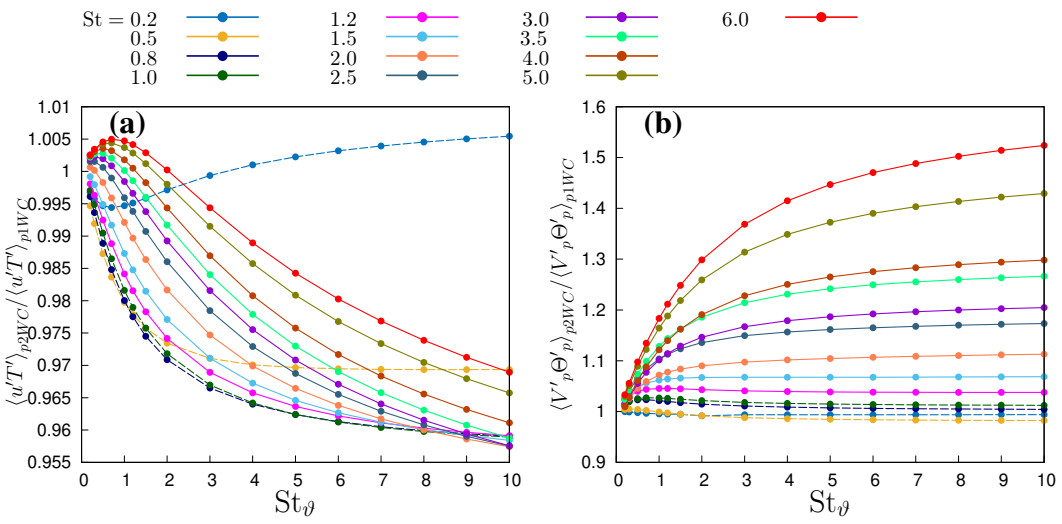

Fig. 3.29 Ratio between (a) fluid and (b) particle velocity-temperature correlation in one- and two-way coupling regimes.

mixing layer core exhibit an asymptotic scaling of $\mathrm{St}_\vartheta^{-2}$, similar to the behavior observed in homogeneous turbulence.

Decomposition in two-way coupling regime

In this section, we apply the decomposition from equation (3.62) to the two-way thermal coupling regime across a broad range of Stokes and thermal Stokes numbers. Our objective is to elucidate the role of particle thermal feedback by analyzing the flow at the same Reynolds number as in the previous section. To understand how particle feedback alters fluid temperature fluctuations and the fields encountered by the particles, we compare the ratios of the three terms in the decomposition (3.62) between the two-way and one-way coupling regimes, at the same Reynolds, thermal Stokes number and Stokes number. Figure 3.29(a) presents the particle and fluid velocity-temperature correlations. Given that particles tend to concentrate in regions with high temperature gradients [11, 32], the particle feedback generally reduces fluid temperature gradients. This reduction leads to a decrease in the fluid velocity-temperature correlation, which becomes more pronounced with increasing particle thermal inertia (i.e., with a higher thermal Stokes number). The effect is particularly notable when the Stokes number is around one, due to more intense particle clustering. For $\mathrm{St}_\vartheta \gg 1$, however, this relative reduction appears to be independent of St. At very high Stokes numbers, there is a slight increase in fluid

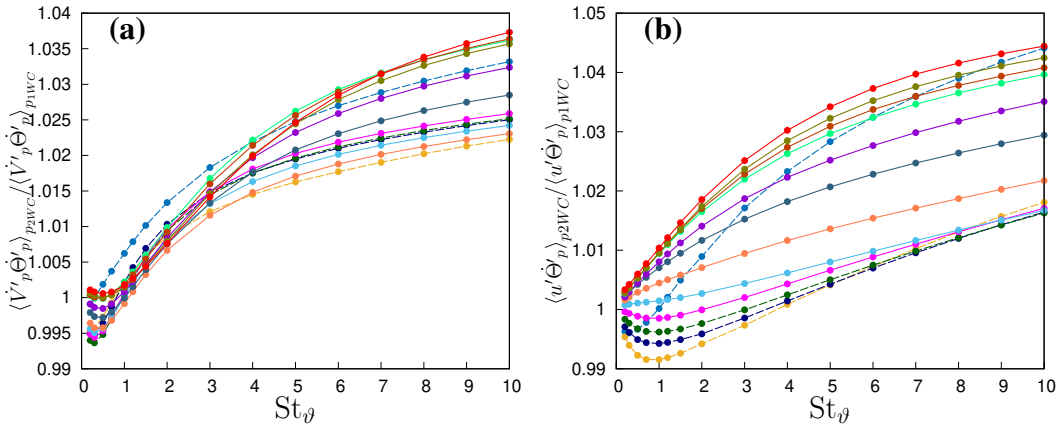

Fig. 3.30 (a) Ratio between normalized particle velocity and temperature derivative correlation and (b) normalized fluid velocity-particle temperature derivative correlation in one- and two-way coupling regimes. Legend as in Figure 3.29.

heat flux when $\mathrm{St}_\vartheta < 1$, peaking around $\mathrm{St}_\vartheta \simeq 0.5$. In these cases, particles may decorrelate from fluid motions, facilitating more frequent heat transfer between eddies at significantly different temperatures. Nonetheless, if the particle thermal inertia becomes exceedingly large, heat transfer slows down due to the particles crossing multiple fronts, whereas negligible particle thermal inertia results in minimal heat transfer, with optimal effects occurring at intermediate thermal inertia. Conversely, concerning particle heat flux, two-way coupling consistently enhances the particle velocity-temperature correlation. For small Stokes numbers, this effect is minimal and nearly independent of the thermal Stokes number. However, a substantial increase is observed when St exceeds a certain threshold. Feedback reduces the temperature difference between particles and the fluid, leading to slower variations in particle temperature. Consequently, particles are able to transport their enthalpy over longer distances across eddy borders in the inhomogeneous direction.

The impact of thermal feedback on the overall heat flux is influenced by the particle-to-fluid heat capacity ratio φ_ϑ. At the simulated volume fraction of 4×10^{-4}, the particle heat capacity exceeds that of the fluid, with $\varphi_\vartheta \simeq 1.664$, leading to an increase in the overall heat flux due to particle feedback. We now turn to analyze the three terms on the right-hand side of equation (3.62). It is important to note that all these terms are negative, indicating that the first two terms contribute to building the correlation, while the third term acts to dampen it. Intuitively, a positive velocity fluctuation correlates with a positive temperature fluctuation since the particle moves through a colder average region but experiences a negative temperature derivative.

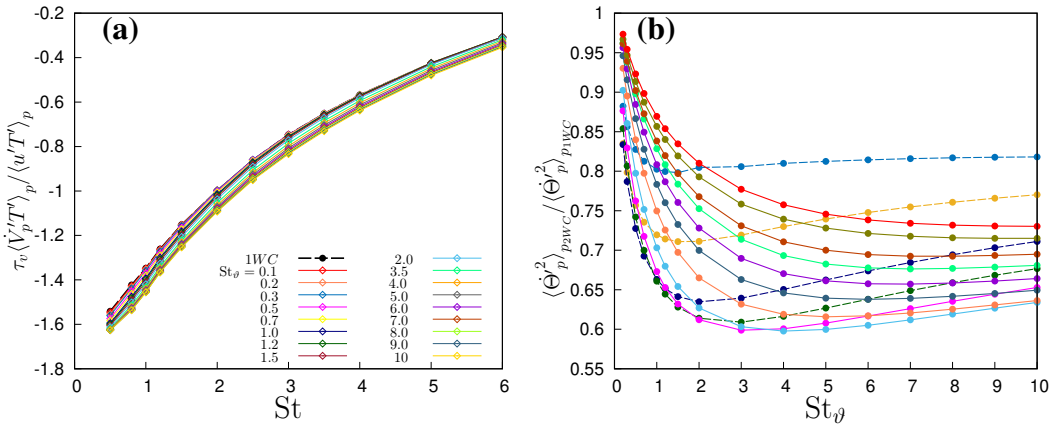

Fig. 3.31 (a) Particle acceleration-temperature correlation normalized with fluid velocity-temperature correlation, and (b) Ratio between particle temperature derivative variance in one- and two-way coupling regimes. Legend as in Figure 3.29.

However, this intuition will be confirmed by observation of the pdf of particle, which is presented and discussed in detail in chapter 4. The argument for the correlation involving particle acceleration is more complex. Higher particle accelerations are expected in regions of higher strain [90], though the velocity field is isotropic and lacks a preferential direction. However, we can use the results of the observation of particle pdf in phase space to explain the sign of $\dot{\Theta}_p$ and $\dot{V}_{p,i}$ in chapter 4. As we will show later, for particles that are being cooled, i.e. moving from warm region to cold region, we have, $\dot{\Theta}_p < 0$, $\Theta_p > 0$ and $V_P > 0$. Using the decomposition (3.62) we can deduce that the sign of acceleration should be positive since the correlation is positive. This assumption is in agreement with our observation here, resulting all three terms in the decomposition are negative. Figure 3.30(a) illustrates the correlation between particle acceleration and temperature time derivative, the last term in equation (3.62). This term increases with St_ϑ, showing a minor dependence on St. It contributes to reducing the particle heat flux, with its impact becoming more noticeable at high Stokes and thermal Stokes numbers. This term is multiplied by the product of the relaxation times, $\tau_v\tau_\vartheta$, making it significant and potentially dominant only at very high St and St_ϑ. However, for any given Stokes number, and thus a fixed τ_v, this term does not dominate the others up to $\mathrm{St} = 6$. If the ratio $\tau_\vartheta/\tau_v = \mathrm{St}_\vartheta/\mathrm{St}$ is kept constant, a reduction in the heat flux might be observed. This could explain the decrease in heat flux noted in certain flow configurations [30].

Figure 3.31(b) presents the first term in the decomposition, demonstrating that particle thermal feedback has a minimal impact on this correlation. Given that

particles are only one-way coupled in terms of momentum, fluid velocity and particle accelerations are unaffected by thermal effects, thus, thermal feedback primarily influences T'. The dominant effect is due to particle inertia, which leads to the gradual decoupling of particle motion from the fluid, thereby reducing the correlation $\langle \dot{V} T' \rangle_p$. Consequently, two-way coupling increases the contribution of the last two terms in equation (3.62), compensating for the observed reduction in $\langle u' T' \rangle_p$. Since their sum equals $-\tau_\vartheta \langle V \dot{\Theta} \rangle_p$, we can deduce that thermal feedback amplifies the magnitude of the correlation between particle velocity and the temperature time derivative. Simultaneously, the variance of the particle temperature time derivative is consistently reduced by thermal feedback. This reduction, attributed to the decreased temperature difference between particles and the surrounding fluid due to thermal feedback on the carrier fluid, is more pronounced at higher thermal Stokes numbers and around a Stokes number of unity. This suggests that the smoothing of fluid temperature gradients, where particles cluster, could be a contributing factor. Overall, thermal feedback results in an increased heat flux, driven by the enhanced particle velocity-temperature correlation, which offsets the reduction in the fluid correlation caused by the smoothing of fluid temperature gradients and variance. This effect is primarily due to the increased correlation between particle velocity and its time derivative, underscoring the significance of the particle temperature history. The role of τ_ϑ as a coefficient further amplifies this effect. For a more comprehensive understanding, further analysis of all terms in the enthalpy and velocity-temperature balance equations is needed.

3.5 Conclusion

In this chapter, we have explored the complex dynamics of heat transfer in non-isothermal particle-laden turbulent flows, utilizing a series of direct numerical simulations at different flow conditions. Our numerical simulations cover a wide range of flow conditions, to gain insights into the thermal and dynamical behavior of dispersed inertial particles in thermal mixing layers and their impact on overall heat transfer as well as the influence of inter-particle collisions on heat transfer process. The first part of the chapter presented an in-depth analysis of heat transfer enhancement in a turbulent mixing layer with dispersed particles neglecting the effect of inter-particle collisions and fixing the ratio of particle thermal-to-dynamic response times equal to

4.43. Moreover, the effect of turbulence on the heat transfer has been studied through changing Taylor microscale Reynolds number from 37 to 124. We demonstrated that the presence of particles alters the overall heat flux between two homothermal regions along with influencing on fluid and particles temperature statistics, while exhibiting a self-similar evolution of mixing dynamics at different flow conditions. The ratio of particle Nusselt number to the convective Nusselt number, a key metric for heat transfer enhancement compared to the unseeded flow, was found to remain constant during this self-similar evolution, indicating the persistent contribution of particles to the overall heat flux. Our findings highlight the significance of particle Stokes and thermal Stokes numbers, with maximum heat transfer efficiency occurring at intermediate Stokes numbers. However, we also observed that the influence of particles diminishes as the Reynolds number increases, suggesting a reduced role of particle-induced heat transfer at higher turbulence levels.

In the second section, we examined the impact of inter-particle particle collisions on heat transfer in the same flow configuration as the first part. Despite the potential for collisions to influence particle dynamics, our results indicate that their effect on overall heat transfer between two homothermal regions is minimal, particularly for Stokes numbers less than one. Even at higher Stokes numbers, where a slight reduction in relative particle-to-fluid velocity-temperature correlation was observed, the overall ability of particles to modulate large-scale fluid temperature fluctuations remained largely unaffected. These findings imply that, for dilute suspensions, particle-particle collisions do not necessitate inclusion in bulk heat transfer models, simplifying the modeling process without compromising accuracy.

The final section of the chapter focused on the thermal and dynamical performance in non-homothermal particle-laden turbulent flows, where the independent variation of Stokes and thermal Stokes numbers provided new insights into the heat transfer mechanisms between two homothermal layer. As a result of the previous section's finding, the inter-particle collision was not included in this set of numerical experiments. Our investigation revealed that particle inertia plays a dominant role over thermal inertia, particularly in determining the temperature variance and the ability of particles to contribute to the overall heat transfer. The absence of mean shear in the flow allowed us to isolate thermal effects, offering a clearer understanding of the particle thermal feedback in two-way thermal coupling regime. This section also introduced a novel decomposition of second-order moments, in terms of particle and fluid velocity and temperature and their derivatives facilitating a deeper

understanding of particle temperature fluctuations and their impact on the particle heat flux.

Together, these studies provide a comprehensive understanding of the thermal dynamics in non-isothermal particle-laden turbulent flows, contributing to the development of more accurate turbulence models and offering practical insights for engineering applications. The chapter establishes a strong foundation for future research, particularly in more complex and realistic flow configurations, where the interplay between particle and fluid phases can be further elucidated.

Chapter 4

Phase space analysis of the heat transfer in particle-laden turbulent flows

4.1 Introduction

The aim of this chapter is to employ the kinetic theory to derive the evolution equation for single-particle pdf of a discrete inertial particle dispersed by a turbulent field. In chapter 2.2, we have derived the governing equations for turbulent motion of continuous phase in Eulerian coordinate. Meanwhile, in 2.3 the Lagrangian equations of a spherical particles suspended in a turbulent flow has been provided to characterize the dynamics and thermodynamics of the particles. In this chapter, under the same assumptions we have used in the previous chapters, the transport equations for single-particle pdf is derived and discussed to further our knowledge about the performance of suspended particles in the turbulent flow. In fact, by utilizing the kinetic theory we aim at discovering the physics behind the behavior of particles that we already observed by DNS results in the previous chapters. Therefore, first we use the basic principal of statistical mechanics to derive the transport equation for pdf of a point-mass particle with a certain position, velocity and temperature and at a given time where it is interacting with random fluid velocity and temperature fields. Then, the statistical moments of such pdf will be visualized and discussed at different particle inertia and thermal inertia. It should be noted that the Taylor microscale

Reynolds number is fixed and equal to 56 throughout this chapter while a wide spectrum of Stokes number and thermal Stokes number is covered. Moreover, all the analysis in this chapter is done for the collisionless regimes since in chapter 3 we observed no significant influence of particle on the thermal field and heat transport process.

In order to start our phase space analysis, we need to recall the particle Lagrangian equations in 2.3. As we have seen, these equations describe the evolution of particle state variables. The evolution is indeed stochastic, due to the existence of forcing terms coming from the exerted force and convection by fluid. Since particles interact with the turbulent field, these terms in the equations are random and make the particle evolution random in phase space. Note that due to the dilute suspension particles are completely frictionless to be far away from granular flow condition. Similar to flow conditions in the numerical observations as presented in 3 it is assumed that there is no external field influencing particles, such as gravitational field or electric field, and only linear hydrodynamic force, modeled by Stokes drag acts on suspended particles. The same conditions also hold for the particle temperature field as in chapter 3, implying that there is no bulk heat source or sink exists and particles have finite thermal inertia with very low Biot number implying no heat diffusion within the particle is considered. Particle state variables, i.e. position $\boldsymbol{X}_p$, velocity $\boldsymbol{V}_p$ and temperature Θ_P form a 7 dimensional space in which the whole dynamics can be characterized. Following the typical procedure in statistical physics, the density of particle phase space can be defined as the fine-grained pdf of finding this particle at time t. By taking the time derivative of this fine-grained pdf and taking the ensemble average over the equations, the course-grained pdf transport equation can be obtained. Analogous to the Boltzmann treatment of a single molecule, and by neglecting inter-particle collisions, the transport equation for pdf includes some unclosed terms due to the interaction of particle state variable with fluid random fields. Thus, the particle Lagrangian evolution equations, which indeed characterize the stochastic evolution, are used to close such unclosed statistical moments. These unclosed terms are computed by direct numerical simulations and through the visualization of pdf in phase-space some new insights about the particle dynamical and thermal behaviors are obtained complementing our previous investigation for the same flow conditions. Moreover, by using the single point particle pdf the field-like macroscopic equations are derived to provide us with theoretical basis for two-fluid Eulerian-Eulerian description of the flow regime. However, in this present work we use the DNS data to

compute the statistical moment of the particle pdf, other studies in the literature like [24, 91, 92] usually develop the analysis by introducing closure models. They model fluid temperature and velocity field as Gaussian excitation in the particle Lagrangian equations, and then unclosed terms in the pdf equation by introducing appropriate closure problems. Nonetheless, in any case, we should note that the well-poseness of the problem can be only guaranteed if and only if the carrier flow field is known deterministically or stochastically. For instance, we solve directly the fluid turbulent equations by DNS while in other studies the reliable closure models are developed [92].

In last two decades one can find some enriched works like [25, 93, 26] in the literature which have developed kinetic method to derive the macroscopic conservation equations and the constitutive relations of an inertial particle interacting with turbulent fields. The pdf method applied in particle-laden turbulent flows has shown to successfully predict the dispersion statistics of particles suspended in non-isothermal homogeneous and isotropic turbulent flows [24, 91, 92]. However, for inhomogeneous systems like the wall-bounded flow the predictions are only, at best, in adequate agreement with equivalent simulation data [94–96]. The reason can be due to the incorporated a one-time one-particle pdf by most of kinetic-based studies on wall-bounded particle-laden flows which may lack the ability to capture all the details of the complex fluid-particle dynamical and thermal interaction. To the date of this publication, one of the big challenges of the pdf kinetic formalism used for modeling the particle-laden turbulent flows, is to close the phase space turbulent diffusion fluxes which appear in the pdf transport equation after ensemble averaging of the equation for conservation of phase space density [97].

Similar to the statistical physics, in addition to pdf-based method, trajectory-based method are used to study the particle-laden turbulent flow. In trajectory-based method stochastic evolution of particles are modeled by a set of discrete Langevine-like equations along particles' Lagrangian trajectories and individually solved. Due to the existence of a time correlation in the stochastic Lagrangian evolution equations,the full dynamics can be captured including the early actions of turbulence along particle trajectories. The results of this Lagrangian simulations can feed the pdf construction for pdf-based method like Direct Simulation Monte-Carlo. The lack of time correlation in one-point pdf used in the pdf-based method, results in missing the full statistical information as the discrete stochastic model. Pdf-based methods at best may contain only information of a single subset of

stochastic process, like Markov process. Two-time correlation can be considered to fix this issue, but the huge increase in the degrees of freedom, makes the problem computationally unfeasible. Especially in our physical problem, which deals with a turbulent flow regime containing of order of billions of suspended particles and scale-resolving nature of the DNS. In practice, one-time and single particle is the best choice considering the lack of information due to neglecting the temporal correlation [65]. Despite the powerful nature of such methodology, which has been successfully employed in other branches of physics turbulent flow interacting with particle requires more peculiar treatment. Turbulent flow leads to long-time correlations of particle dynamics to show strong features of non-Markovianity rather than Markovian processes driven by white noise, the methods developed in deriving the classical Fokker-Planck equation cannot be applied immediately [24]. For capturing non-Markovian effects of turbulence on particle diffusion in phase space, the well-known approaches include Kraichnan's Lagrangian history direct interaction (LHDI) theory,[24] functional method [26] and cumulant expansion method [25, 92] have been used. In Kraichnan's LHDI theory, random Galilean transformation (RGT) invariance can be imposed on the particle motion along its phase space trajectory to cancel the restriction on correlation time scales, [24] while in the functional method, the diffusion flux is expressed in terms of the functional derivative of the particle path with respect to a random impulse in phase space to allow for influences of long-time correlations on particle diffusion [98].

Pdf kinetic method can be also coupled with other numerical approaches like DNS, LES to simulate complex turbulent flows. For instance, the DNS/LES-pdf model obtains satisfactory results in modeling turbulence diffusion in particle-laden turbulent flows investigated by [25, 99, 100]. Similar to the other method in studying particle-laden turbulent flows, the kinetic pdf method needs to be improved. Yet, ad hoc assumptions in closing the turbulent flux in phase space, has been the main challenge and limitation for applying this method to the investigation of particle-laden turbulent flows comparing with other typical tools like DNS and LES. However, in case that the DNS data is present, like the case of this study, pdf method can be coupled with DNS to explore the phase space dynamics of the disperse particle in turbulent flows without any need of closure models. The DNS results obtained in chapter 3, can be used to compute the unclosed conditional averages in the pdf transport equation. Note that the pdf method results which are presented in this chapter, as a complementary part to the previous chapters, can contribute to those

study that are working on the closure problem for pdf methods and/or Eulerian-Eulerian modeling of non-isothermal particle laden turbulent flows. However, the complexity in derivation a suitable pdf equations still exists even in case of DNS-coupled kinetic method. This problem arises from the fundamental procedure of obtaining the kinetic evolution equation and develop the probabilistic description of disperse particle interacting with turbulent field.

4.2 Theoretical background

First we need to recall the particle Lagrangian equations from chapter 2 under the same assumptions we have used in the numerical experiments in chapter 3. This set of ordinary differential equations which characterize the particle dynamics and thermodynamics are given by

$$\frac{\mathrm{d}}{\mathrm{d}t}\begin{Bmatrix}\boldsymbol{X}_p(t)\\ \boldsymbol{V}_p(t)\\ \Theta_p(t)\end{Bmatrix} = \begin{bmatrix}0 & 1 & 0\\ 0 & -1/\tau_v & 0\\ 0 & 0 & -1/\tau_\vartheta\end{bmatrix}\begin{Bmatrix}\boldsymbol{X}_p(t)\\ \boldsymbol{V}_p(t)\\ \Theta_p(t)\end{Bmatrix} + \begin{bmatrix}0\\ (1/\tau_v)\boldsymbol{u}(t,\boldsymbol{X}_p(t))\\ (1/\tau_\vartheta)T(t,\boldsymbol{X}_p(t))\end{bmatrix} \tag{4.1}$$

The equation (4.1) describe the evolution of a system of N_p particles whose state variables are position vector $\boldsymbol{X}_p$, velocity vector $\boldsymbol{V}_p$ and temperature Θ_p. The dynamic matrix of this dynamical system is characterized by particle relaxation times, τ_v and τ_ϑ, i.e. the momentum and thermal response timescales to any random fields. Fluid random forces acting on the particles indicating the stochastic nature of the inter-phase exchange of momentum and energy. In other words, randomness enters into the particle equations only through the fluid velocity and temperature fields seen by particles. It is assumed that there is no other stochastic terms like Brownian effect due to the particle itself. The degrees of freedom of the each particle is 7, thus the corresponding 7-dimensional phase-space can be constructed in order to properly describe the system dynamics. However, for a system of particles with total number of particle N_p, the overall degrees of freedom is $7 \times N_p$. But in our case, since the particles are identical, we perform an analysis on a single particle and apply the formalism for the whole system. For any generic system of of N_p identical particles with state variables $Z = Z_1, Z_2, ..., Z_n$ while each state variable

has n components, the overall dimension of phase space is $n \times N_p$. Note that state variables can be vector or scalar depending of the problem of interest.

Kinetic theory has been used in studying many physical problem such as Brownian motion of a single particle in a quiescent fluid, single-phase and two-phase turbulent flows. In case of Brownian motion, the simplest assumption is to consider only the particle position as the only state variable. Accordingly, pdf of finding a single particle with state variable $\boldsymbol{X}_p$ can be defined by $f(t,\boldsymbol{x}_p)$, where $\boldsymbol{x}_p$ is the corresponding sampling variable of random variable $\boldsymbol{X}_p(t)$. The particle velocity $\boldsymbol{V}_p$ can be also considered as an additional state variable along with the particle position. Therefore, the pdf of finding the particle at time t is $f(t,\boldsymbol{x}_p,\boldsymbol{v}_p)$. In analysis of Brownian motion of a single particle in a fluid medium, Lagrangian equation of motion which has deterministic and stochastic terms is usually used. The equation is called Langevin equation and a Wiener process in time (zero-mean white noise) captures the randomness action on particles. Corresponding partial differential equation, i.e. the evolution equation for the particle, is called Fokker-Plank equation. The Brownian motion of particles in quiescent fluid has been extensively investigated since the genesis of modern physics. However, we do not consider the Brownian motion in our flow regime, but the fundamental of the kinetic theory analysis is used to develop the appropriate formalism for an inertial particle suspended in a turbulent non-isothermal flow.

Employing the kinetic theory for two-phase turbulent flow involves more complexity comparing to the Brownian motion in quiescent flows due to the existence of a turbulent flow and its interaction with suspended particles. The first step, is to define the suitable state variables of the system of fluid and particle. Discrete particle can be treated like any other similar particle in statistical physics, but with different scales. Meanwhile, fluid phase needs different treatment due to the turbulence nature. To model the fluid phase as a system of small particles, the Lagrangian turbulence consideration is needed. The required fluid particles is determined by characteristics Reynolds number Re to fully describe the fluid flow. Unlike the Hamiltonian system of particles or Brownian motion of a pollen grain in fluid, Lagrangian evolution of a fluid particle in turbulent regime, must have space correlation in addition to existing time correlation in particle momentum equation. In fact, to model fluid flow as an evolutionary system of N_f particles, we need to have the time history and space resolution of all the points in the flow domain. For Lagrangian description of suspension of N_p particles in a turbulent flow with N_f fluid particles the total num-

ber of particles becomes equal to $(N_p + N_f)$, that in most cases is computationally implausible. Therefore, we use statistical approach (moment approach) for fluid at continuum level, to solve all the spatio-temporal scales, then we use probabilistic description only for the discrete particles. However, for the single phase turbulent flow, Pope in [101] developed a pdf model by using one point pdf of fluid particle which has the scaling properties of an Eulerian turbulent field. An unclosed transport equation for $f(t, \boldsymbol{x}_f, \boldsymbol{v}_f)$ was derived from coarse-graining of flow domain and Lagrangian equation of a system of fluid particles. Such equation is unclosed and it needs some closure models like Generalized Langevin Model [101]. In two-phase turbulent flow there are two different approaches, one only considers particle state variables, and the other takes also the turbulent flow's state variables into account. For isothermal, non-isothermal and droplet-laden flow with phase change, the corresponding one-point particle pdfs are respectively $f(t, \boldsymbol{x}_p, \boldsymbol{v}_p)$, $f(t, \boldsymbol{x}_p, \boldsymbol{v}_p, \vartheta_p, t)$ and $f(t, \boldsymbol{x}_p, \boldsymbol{v}_p, \vartheta_p, a_p)$ where a_p is the droplet radius. If we want to model two-point fluid-particle pdf in these three cases we must add the corresponding turbulent fluid flow state variable in order to derive the transport equation for joint fluid-particle pdf. Such joints pdfs are respectively $f(t, \boldsymbol{x}_p, \boldsymbol{v}_p; \boldsymbol{x}_f, \boldsymbol{v}_f)$, $f(\boldsymbol{x}_p, \boldsymbol{v}_p, \vartheta_p; \boldsymbol{x}_f, \boldsymbol{v}_f, T_f)$ and $f(\boldsymbol{x}_p, \boldsymbol{v}_p, \vartheta_p, a_p; \boldsymbol{x}_f, \boldsymbol{v}_f, T_f, \rho_{v,f})$ where $\rho_{v,f}$ is the vapor density field in droplet-laden flow with phase change. Fluid particles are called seen-by-particle when they are sampled along particles Lagrangian trajectories while in the fluid pdf particles sampled when they are following fluid Lagrangian path lines. Note that fluid and particle Lagrangian trajectories are different due to the interaction between phases [92].

4.3 Single particle kinetic pdf model

In this section the kinetic theory is used for analysis of non-isothermal particle-laden turbulent flows. In this study, we only consider the suspended particle state variables and turbulent fields are solved by means of direct numerical simulation. Thus, any inter-phase exchange that may be included in the final pdf transport equation, will be computed by DNS. Accordingly, we do not need to use any closure problem and modeling. The Lagrangian stochastic equations of suspended particles are given by equation (4.1). We define the state vector of $p-th$ particle suspended in a turbulent fields as $\boldsymbol{Z} = (\boldsymbol{X}_p, \boldsymbol{V}_p, \Theta_p)$ and the pdf of finding such particle in sample space at time t, can be defined by $f(t, \boldsymbol{x}_p, \boldsymbol{v}_p, \vartheta_p)$. As mentioned before,

each individual particle has 7 degrees of freedom in the phase-space leading to an overall degrees of freedom of $7 \times N_p$ for the whole system of suspended particles. Since the particles are equal-sized and equal-shaped, the analysis is performed only for a single spherical particle in which subscript p denotes the number of particles in all following equations. The state vector $\boldsymbol{Z}(t,\omega)$ containing all relevant state variables evolves along particle Lagrangian path from initial condition $\boldsymbol{Z}_0(\omega)$ to the current time t. During the evolution, it is assumed that $\boldsymbol{Z}(t,\omega)$ is differentiable over time. For a specific realization ω from the set of all possible realizations, the state evolution from $\boldsymbol{Z}_0$ at time 0 to $\boldsymbol{Z}$ at time t is influenced by stochastic forces from fluid and is denoted as $\boldsymbol{Z}_t(\omega) = \boldsymbol{Z}(t,\omega)$. The fine-grained pdf at time t and phase space point $\boldsymbol{z}$ is given by

$$f_{f.g}(t,\boldsymbol{z},\omega) = \delta[\boldsymbol{z} - \boldsymbol{Z}(t,\omega)] \tag{4.2}$$

Here, $\boldsymbol{Z}(t,\omega)$ is the trajectory of the system in phase space given the initial condition ω, and $\delta[\boldsymbol{z} - \boldsymbol{Z}(t,\omega)]$ is the Dirac delta function, which is nonzero only when $\boldsymbol{z}$ equals $\boldsymbol{Z}(t,\omega)$. This fine-grained pdf describes the exact state of the system for each realization ω at time t. The fine-grained pdf represents also the phase space density of a system with state variable $\boldsymbol{z}$. Ensemble averaging of fine-grained pdf over all realization of the stochastic variables which appear in Lagrangian Stochastic equations gives us the coarse-grained average $f(t,\boldsymbol{z})$. By using this pdf we can define particle variables in terms of mean and fluctuating parts in an Eulerian partial differential equations indeed with some closure terms. In classical statistical mechanics, the fine-grained pdf is employed to characterize the microscopic state of a system within phase space. By averaging over an ensemble of such systems, ensemble averages are obtained for the system's properties.

The system under consideration has a sample space Ω, which is the set of all possible outcomes or realizations of the system, denoted by $\omega \in \Omega$. Each ω represents a particular state of the system. The distribution of these realizations in phase space is given by the function $f(\omega)$. This distribution function satisfies the normalization condition $\int \mathrm{d}\omega f(\omega) = 1$. This equation ensures that $f(\omega)$ is a probability density function (pdf), meaning that it describes the likelihood of the system being in a particular state ω. The coarse-grained pdf is obtained by averaging

the fine-grained pdf, i.e. $f_{f.g}(t,\boldsymbol{z},\omega) = \delta[\boldsymbol{z}-\boldsymbol{Z}(t,\omega)]$ over all possible realizations ω

$$f(t,\boldsymbol{z},\omega) = \langle f_{f.g}(t,\boldsymbol{z},\omega)\rangle = \int \mathrm{d}\omega\delta[\boldsymbol{z}-\boldsymbol{Z}(t,\omega)] = \langle\delta[\boldsymbol{z}-\boldsymbol{Z}(t,\omega)]\rangle \tag{4.3}$$

Equation (4.3) relates the transition from a fine-grained, detailed description of a system's state to a coarse-grained, statistical description by averaging over all possible realizations. This average gives us a broader statistical description of the system, smoothing out the fine details to focus on the overall distribution of the system's states in phase space. By using this relation, any generic observable $\tilde{o}$ is calculated by averaging over all possible realizations

$$\tilde{o}(t,\boldsymbol{z}) = \langle o(t,\boldsymbol{z})\rangle = \int \mathrm{d}\omega f(\omega)o(t,\boldsymbol{z}(\omega)) = \int \mathrm{d}o f(t,\boldsymbol{z})o \tag{4.4}$$

To compute this observable we can use two complementary approaches, pdf-base approach that tracks the evolution of pdf in phase space or trajectory-based approach that follows the system's individual trajectories. In pdf-based approach $f(t,z)$ is evolving in time since state variables depend on time through the trajectories $z_t(\omega)$ while in trajectory-based approach, individual trajectory of the system in phase-space $\boldsymbol{z}_\omega(t) = \boldsymbol{z}(t,\omega)$ evolve in time and $f(\omega)$ remains stationary while system's state evolves. Both methods ultimately allow for the computation of expected values for any generic observable, providing a complete statistical description of the system's behavior over time.

By recasting equation (4.1) and using the definition of particle state vector $\boldsymbol{Z}$, the Langevin-like Lagrangian stochastic equation can be expressed as

$$\frac{\mathrm{d}\boldsymbol{Z}(t)}{\mathrm{d}t} = \boldsymbol{F}[\boldsymbol{Z}(t)] + \boldsymbol{\zeta}(t) \tag{4.5}$$

where $\boldsymbol{F}[\boldsymbol{Z}(t)]$ is a linear function of particle state variables which has a deterministic nature and $\boldsymbol{\zeta}$ is the random force acting on particle from fluid turbulent fields. The stochastic force $\boldsymbol{\zeta}$ is a function of seen-by-particle velocity $\boldsymbol{u}(t,\boldsymbol{X}_p)$ and seen-

by-particle temperature $T(t,\boldsymbol{X}_p)$. In our analysis, these fluid seen-by-particle fields $\boldsymbol{u}(t,\boldsymbol{X}_p)$ and $T(t,\boldsymbol{X}_p)$ at the position of each particle is known from direct numerical simulation results. Therefore, pdf of finding a suspended particle with state variables $\boldsymbol{Z}=(\boldsymbol{X}_p,\boldsymbol{V}_p,\Theta_p)$ in turbulent flow at time t at phase-space point $(\boldsymbol{x}_p,\boldsymbol{v}_p,\vartheta_p)$ is denoted as $f_{f.g}(t,\boldsymbol{x}_p,\boldsymbol{v}_p,\vartheta_p)=\delta[\boldsymbol{x}_p-\boldsymbol{X}_p(t)]\delta[\boldsymbol{v}_p-\boldsymbol{V}_p(t)]\delta[\vartheta_p-\Theta_p(t)]$. The ensemble averaging over all possible realizations of particle's states gives the corresponding coarse-grained pdf as

$$f(t,\boldsymbol{x}_p,\boldsymbol{v}_p,\vartheta_p)=\langle f_{f.g}(t,\boldsymbol{x}_p,\boldsymbol{v}_p,\vartheta_p)\rangle= \int \mathrm{d}\boldsymbol{x}_p\mathrm{d}\boldsymbol{v}_p\mathrm{d}\vartheta_p\delta[\boldsymbol{x}_p-\boldsymbol{X}_p(t)]\delta[\boldsymbol{v}_p-\boldsymbol{V}_p(t)]\delta[\vartheta_p-\Theta_p(t)] \tag{4.6}$$

To derive the evolution equation for f, we first need to compute the time derivative of the fine-grained pdf. Subsequently, we will average this result to obtain the evolution equation for ff. We begin by differentiating $f_{f.g}$ with respect to time, utilizing the properties of the Dirac delta function to facilitate this differentiation.

$$\frac{\partial f(t,\boldsymbol{x}_p,\boldsymbol{v}_p,\vartheta_p)}{\partial t}=\langle\frac{\partial}{\partial t}f_{f.g}(t,\boldsymbol{x}_p,\boldsymbol{v}_p,\vartheta_p)\rangle=\frac{\partial}{\partial t}\langle f_{f.g}(t,\boldsymbol{x}_p,\boldsymbol{v}_p,\vartheta_p)\rangle= \frac{\partial}{\partial t}\int \mathrm{d}\boldsymbol{x}_p\mathrm{d}\boldsymbol{v}_p\mathrm{d}\vartheta_p\delta[\boldsymbol{x}_p-\boldsymbol{X}_p(t)]\delta[\boldsymbol{v}_p-\boldsymbol{V}_p(t)]\delta[\vartheta_p-\Theta_p(t)] \tag{4.7}$$

To derive the final form of the transport equation for f, we can move the partial derivative inside the integral. Consequently, the time derivatives of the three Dirac delta functions within the integral must be computed separately. Each time derivative is given by:

$$\begin{aligned}
\frac{\partial}{\partial t}\delta[\boldsymbol{x}_p-\boldsymbol{X}_p(t)]&=-\frac{\partial}{\partial \boldsymbol{x}_p}\frac{\mathrm{d}\boldsymbol{X}_p}{\mathrm{d}t}\delta[\boldsymbol{x}_p-\boldsymbol{X}_p(t)]=-\frac{\partial}{\partial x_p}\delta[\boldsymbol{x}_p-\boldsymbol{X}_p(t)]\boldsymbol{V}_p\\
\frac{\partial}{\partial t}\delta[\boldsymbol{v}_p-\boldsymbol{V}_p(t)]&=-\frac{\partial}{\partial \boldsymbol{v}_p}\frac{\mathrm{d}\boldsymbol{V}_p}{\mathrm{d}t}\delta[\boldsymbol{v}_p-\boldsymbol{V}_p(t)]=-\frac{\partial}{\partial v_p}\delta[\boldsymbol{v}_p-\boldsymbol{V}_p(t)]\boldsymbol{A}_p\\
\frac{\partial}{\partial t}\delta[\vartheta_p-\Theta_p(t)]&=-\frac{\partial}{\partial \vartheta_p}\frac{\mathrm{d}\Theta_p}{\mathrm{d}t}\delta[\vartheta_p-\Theta_p(t)]=-\frac{\partial}{\partial \vartheta_p}\delta[\vartheta_p-\Theta_p(t)]\dot{\Theta}_p
\end{aligned} \tag{4.8}$$

where $\boldsymbol{V}_p$, $\boldsymbol{A}_p$ and $\dot{\Theta}_p$ represent particle velocity, acceleration and temperature time derivative respectively. These quantities are determined from the Lagrangian particle stochastic equations which define the particle stochastic evolution as follows

$$\frac{\mathrm{d}\boldsymbol{X}_p(t)}{\mathrm{d}t} = \boldsymbol{V}_p(t) \tag{4.9}$$

$$\frac{\mathrm{d}\boldsymbol{V}_p(t)}{\mathrm{d}t} = \boldsymbol{A}_p(t) \tag{4.10}$$

$$\frac{\mathrm{d}\Theta_p(t)}{\mathrm{d}t} = \dot{\Theta}_p(t) \tag{4.11}$$

The final results for the time derivatives of each term, as obtained in Equation (4.8), can be substituted into Equation (4.7), yielding the following

$$\begin{aligned}
&\frac{\partial f(t,\boldsymbol{x}_p,\boldsymbol{v}_p,\vartheta_p)}{\partial t} = \frac{\partial}{\partial t}\langle f_{f.g}(t,\boldsymbol{x}_p,\boldsymbol{v}_p,\vartheta_p)\rangle \partial t = \\
&\frac{\partial}{\partial t}\int \mathrm{d}\boldsymbol{x}_p \mathrm{d}\boldsymbol{v}_p \mathrm{d}\vartheta_p \delta[\boldsymbol{x}_p - \boldsymbol{X}_p(t)]\delta[\boldsymbol{v}_p - \boldsymbol{V}_p(t)]\delta[\vartheta_p - \Theta_p(t)] = \\
&\int \mathrm{d}\boldsymbol{x}_p \mathrm{d}\boldsymbol{v}_p \mathrm{d}\vartheta_p \big(-\frac{\partial}{\partial \boldsymbol{x}_p}\delta[\boldsymbol{x}_p - \boldsymbol{X}_p(t)]\boldsymbol{V}_p\big)\delta[\boldsymbol{v}_p - \boldsymbol{V}_p(t)]\delta[\vartheta_p - \Theta_p(t)] \\
&+ \int \mathrm{d}\boldsymbol{x}_p \mathrm{d}\boldsymbol{v}_p \mathrm{d}\vartheta_p \big(-\frac{\partial}{\partial \boldsymbol{v}_p}\delta[\boldsymbol{v}_p - \boldsymbol{V}_p(t)]\boldsymbol{A}_p\big)\delta[\boldsymbol{x}_p - \boldsymbol{X}_p(t)]\delta[\vartheta_p - \Theta_p(t)] \\
&+ \int \mathrm{d}\boldsymbol{x}_p \mathrm{d}\boldsymbol{v}_p \mathrm{d}\vartheta_p \big(-\frac{\partial}{\partial \vartheta_p}\delta[\vartheta_p - \Theta_p(t)]\dot{\Theta}_p\big)\delta[\boldsymbol{x}_p - \boldsymbol{X}_p(t)]\delta[\boldsymbol{v}_p - \boldsymbol{V}_p(t)]
\end{aligned} \tag{4.12}$$

the partial derivatives in terms of particle position, velocity and temperature in the equation (4.13) can be taken out the integrals giving the following form

$$
\begin{aligned}
&\frac{\partial f(t,\boldsymbol{x}_p,\boldsymbol{v}_p,\vartheta_p)}{\partial t} = \\
&-\frac{\partial}{\partial \boldsymbol{x}_p}\int \mathrm{d}\boldsymbol{x}_p\mathrm{d}\boldsymbol{v}_p\mathrm{d}\vartheta_p\delta[\boldsymbol{x}_p-\boldsymbol{X}_p(t)]\delta[\boldsymbol{v}_p-\boldsymbol{V}_p(t)]\delta[\vartheta_p-\Theta_p(t)]\boldsymbol{V}_p(t) \\
&-\frac{\partial}{\partial \boldsymbol{v}_p}\int \mathrm{d}\boldsymbol{x}_p\mathrm{d}\boldsymbol{v}_p\mathrm{d}\vartheta_p\delta[\boldsymbol{x}_p-\boldsymbol{X}_p(t)]\delta[\boldsymbol{v}_p-\boldsymbol{V}_p(t)]\delta[\vartheta_p-\Theta_p(t)]\boldsymbol{A}_p(t) \\
&-\frac{\partial}{\partial \vartheta_p}\int \mathrm{d}\boldsymbol{x}_p\mathrm{d}\boldsymbol{v}_p\mathrm{d}\vartheta_p\delta[\boldsymbol{x}_p-\boldsymbol{X}_p(t)]\delta[\boldsymbol{v}_p-\boldsymbol{V}_p(t)]\delta[\vartheta_p-\Theta_p(t)]\dot{\Theta}_p(t) \\
&= \\
&-\frac{\partial}{\partial \boldsymbol{x}_p}\cdot\Big(f(t,\boldsymbol{x}_p,\boldsymbol{v}_p,\vartheta_p)\langle\boldsymbol{V}_p|\boldsymbol{x}_p,\boldsymbol{v}_p,\vartheta_p\rangle\Big) \\
&-\frac{\partial}{\partial \boldsymbol{v}_p}\cdot\Big(f(t,\boldsymbol{x}_p,\boldsymbol{v}_p,\vartheta_p)\langle\boldsymbol{A}_p|\boldsymbol{x}_p,\boldsymbol{v}_p,\vartheta_p\rangle\Big) \\
&-\frac{\partial}{\partial \vartheta_p}\cdot\Big(f(t,\boldsymbol{x}_p,\boldsymbol{v}_p,\vartheta_p)\langle\Theta_p|\boldsymbol{x}_p,\boldsymbol{v}_p,\vartheta_p\rangle\Big)
\end{aligned}
\tag{4.13}
$$

finally, the unclosed evolution equation for coarse-grained pdf of single particle suspended in a non-isothermal turbulent flow reads

$$
\begin{aligned}
&\frac{\partial f(t,\boldsymbol{x}_p,\boldsymbol{v}_p,\vartheta_p)}{\partial t}+\frac{\partial}{\partial \boldsymbol{x}_p}[f(t,\boldsymbol{x}_p,\boldsymbol{v}_p,\vartheta_p)\langle\boldsymbol{V}_p|\boldsymbol{x}_p,\boldsymbol{v}_p,\vartheta_p\rangle] \\
&+\frac{\partial}{\partial \boldsymbol{v}_p}[f(t,\boldsymbol{x}_p,\boldsymbol{v}_p,\vartheta_p)\langle\boldsymbol{A}_p|\boldsymbol{x}_p,\boldsymbol{v}_p,\vartheta_p\rangle] \\
&+\frac{\partial}{\partial \vartheta_p}[f(t,\boldsymbol{x}_p,\boldsymbol{v}_p,\vartheta_p)\langle\dot{\Theta}_p|\boldsymbol{x}_p,\boldsymbol{v}_p,\vartheta_p\rangle]=0
\end{aligned}
\tag{4.14}
$$

Typically, single-particle dynamical equations can be applied to many-particle systems while neglecting short-term particle-particle interactions (e.g., electrostatic or hydrodynamic effects). However, nearby particles remain correlated because they experience similar fluid velocities and temperatures. In general, this equation and stochastic process are formulated in a seven-dimensional phase space. In our specific case, the dimensionality is reduced to three because we only account for inhomogeneity in one direction. Since the particle velocity field is linear with the particle velocity field within the Stoksian regime, and we only have the inhomogene-

ity in temperature field in one direction, in which the thermal mixing takes place. To have the more appropriate equation for our study, We need to integrate the pdf transport equation (4.14) in two homogeneous direction over the remaining variables (x_1, x_2, v_1, v_2) to obtain the new pdf transport equation.

$$f^*(t, x_p, v_p, \vartheta_p) = \int_{\Sigma(x_p, v_p)} f(t, \boldsymbol{x}_p, \boldsymbol{v}_p, \vartheta_p) \mathrm{d}x_{p,1} \mathrm{d}x_{p,2} \mathrm{d}v_{p,1} \mathrm{d}v_{p,2} \tag{4.15}$$

where $\Sigma(x_p, v_p) = \left\{ (t, \boldsymbol{x}_p, \boldsymbol{v}_p, \vartheta) : x_{p,3} = x_p,\, v_{p,3} = v_p \right\}$.

Thus, the transport equation for the new probability density function f^* of for $p-th$ particle at time t, in the plane x with velocity v, which denotes the particle velocity in inhomogeneous direction x_3 and temperature ϑ is given by the following equation

$$\begin{aligned} &\frac{\partial f^*(t, x_p, v_p, \vartheta_p)}{\partial t} + \frac{\partial}{\partial x_p}[f^*(t, x_p, v_p, \vartheta_p) \langle V_p | x_p, v_p, \vartheta_p \rangle] \\ &+ \frac{\partial}{\partial v_p}[f^*(t, x_p, v_p, \vartheta_p) \langle A_p | x_p, v_p, \vartheta_p \rangle] \\ &+ \frac{\partial}{\partial \vartheta_p}[f^*(t, x_p, v_p, \vartheta_p) \langle \dot{\Theta}_p | x_p, v_p, \vartheta_p \rangle] = 0 \end{aligned} \tag{4.16}$$

4.4 Particle macroscopic field description

In section 4.3 kinetic theory has been used to derive the pdf transport equation of suspended particle in a non-isothermal particle-laden turbulent flow. The statistical moments of single-particle pdf transport equation (4.14), can reveal significant information about the particle dynamical and thermal performance. Nonetheless, the evolution equation of pdf, is not the only outcome of kinetic theory approach in the analysis of particle-laden turbulent flows. Another useful outcome of this formalism is to to derive the macroscopic field equations for suspended particle. The bridging from single particle stochastic Lagrangian evolution to statistical field description, posses similar basis to the classical statistical mechanics, in which the macroscopic description is achieved from the microscopic states of particles. But despite the similarities, there exist some differences. In statistical physics the particles of interest usually have the size of atoms or molecules of order of

nanometer while laden particles in the turbulent flows here have the larger size of order of microns. Moreover, the nature of system of particles in statistical physics, is Hamiltonian resulting in conservative dynamics in phase space, but the dynamics of suspended particles in turbulent flows is dissipate in phase-space. The phase-space in statistical physics is formed by particle positions and momenta while here we have another dimension in phase space which is the particle temperature. In addition to theses main differences, the most important one is the Eulerian-Lagrangian nature of particle-laden turbulent flows versus the Lagrangian dynamics of particles in statistical physics. On the other hand, the applications of kinetic method for single-phase turbulent flows, like the work done by Pope et al. in [101], uses the Eulerian stochatic evolution, i.e. Navier-Stokes equation, to close the statistical moments appear in the pdf transport equation. Instead, in particle-laden turbulent flows which is our case, not only fluid Eulerian stochastic equations should be used, but also particle Lagrangian stochastic evolution equations are present. Accordingly, a certain description is needed to avoid confusion between the position as Lagrangian variables or Eulerian parameters, through the relation between these quantities and the Lagrangian and Eulerian pdfs. This clarification is essential, since we aim to derive the field equations for particles in Eulerian reference frame.

The flow domain consists of N_p number of suspended particles, with state vector $\boldsymbol{Z} = (\boldsymbol{X}_p, \boldsymbol{V}_p, \Theta_p)$ at material coordinate. Each point in a generic 7 dimensional phase space of the system is given by $\boldsymbol{z} = (\boldsymbol{x}_p, \boldsymbol{v}_p, \vartheta_p)$ capturing the detailed state of the system for any realizations over particle Lagrangian path. Density of this multidimensional phase space can be described by the definition of fine-grained pdf and specify the exact state of the system. We have already derived the Lagrangian pdf transport equation $f(t, \boldsymbol{x}_p, \boldsymbol{v}_p, \vartheta_p)$ by ensemble averaging of fine-grained pdf over all possible states of the system. The Lagrangian pdf of the system is reported in equation (4.14) including some unclosed terms. Note that this pdf is derived under the assumption that the process is Markovian and initial states are equal to zero. To derive the corresponding Eulerian pdf for our particles, we need to integrate the Lagrangian pdf over all particles that pass through the fixed point $(\boldsymbol{x}, \boldsymbol{v}, \vartheta)$ in the Eulerian frame at time t. Therefore, $f^E(t, \boldsymbol{x}, \boldsymbol{v}, \vartheta)$ is defined as the Eulerian pdf of finding a particle with velocity $\boldsymbol{v}$ and temperature ϑ at Eulerian position $\boldsymbol{x}$ or spatial point at time t. In the Eulerian framework, we consider that phase-space density is concentrated at this fixed point in space with the given state variables. We can integrate Lagrangian pdf over all initial states of particles that could end up at point

$(\boldsymbol{x}, \boldsymbol{v}, \vartheta)$ at time t. Since we assume that initial states are zero we can obtain the following integral for the pdf. The transformation from Lagrangian state variables $\boldsymbol{x}_p$, $\boldsymbol{v}_p$ and ϑ_p to spatial point $\boldsymbol{x}$, $\boldsymbol{v}$, ϑ is given by

$$f^E(t,\boldsymbol{x},\boldsymbol{v},\vartheta) = \int \mathrm{d}\boldsymbol{x}_p \mathrm{d}\boldsymbol{v}_p \mathrm{d}\vartheta_p f(t,\boldsymbol{x}_p,\boldsymbol{v}_p,\vartheta_p)\delta[\boldsymbol{x}-\boldsymbol{x}_p(t)]\delta[\boldsymbol{v}-\boldsymbol{v}_p(t)]\delta[\vartheta-\vartheta_p(t)] \tag{4.17}$$

This integral effectively transforms the Lagrangian description into an Eulerian description by integrating over all particles and using Dirac delta functions to enforce the condition that the particle's phase space coordinates match the Eulerian coordinates. since the Lagrangian pdf, f, is already a function of state variable $(\boldsymbol{x}_p, \boldsymbol{v}_p, \vartheta_p)$, and delta function ensures we are evaluating at the point $(\boldsymbol{x}, \boldsymbol{v}, \vartheta)$ therefore, we get

$$f^E(t,\boldsymbol{x},\boldsymbol{v},\vartheta) = f(t,\boldsymbol{x}_p=\boldsymbol{x},\boldsymbol{v}_p=\boldsymbol{v},\vartheta_p=\vartheta) \tag{4.18}$$

Indeed, this relationship holds only in this specific case with zero initial states and Markovian property, which results in the Eulerian pdf f^E is directly given by the Lagrangian pdf evaluated at fixed point $(\boldsymbol{x}, \boldsymbol{v}, \vartheta)$ at time t. In other words, this equality holds under the assumption that the transformation from Lagrangian to Eulerian variables is straightforward and one-to-one. Moreover, the equation (4.18) means that the density function is the same, but the interpretation depends on whether we are looking at it from an Eulerian perspective (fixed spatial coordinates) or a Lagrangian perspective (following individual particles). From this relation we can define the fine-grained Eulerian pdf directly in state space as

$$f^E(t,\boldsymbol{x},\boldsymbol{v},\vartheta) = \langle \delta[\boldsymbol{x}-\boldsymbol{X}_p(t)]\delta[\boldsymbol{v}-\boldsymbol{V}_p(t)]\delta[\vartheta-\Theta_p(t)]\rangle \tag{4.19}$$

This expression provides a direct way to transform the Lagrangian description into the Eulerian description, capturing the probability density of finding particles with specific properties (e.g., velocity, temperature) at a given location and time. In the Eulerian framework, we are concerned with the density of particles at fixed spatial

coordinates, characterized by specific velocities and temperatures, and averaged over all particles in the system. In contrast, the Lagrangian description focuses on the instantaneous states of individual particles as they move along their trajectories, represented by the state variables $(\boldsymbol{X}_p(t), \boldsymbol{V}_p(t), \Theta_p(t))$. The Eulerian state variables $(\boldsymbol{x}, \boldsymbol{v}, \vartheta)$, on the other hand, describe the state of the system at fixed spatial points at a specific time t. The Lagrangian fine-grained pdf describes the probability density along the trajectories of individual particles, emphasizing their evolution over time. In contrast, the Eulerian fine-grained pdf represents the probability density at fixed spatial points, reflecting the distribution of particles in space at a given moment. To derive the coarse-grained pdf from the Lagrangian description, we average over the trajectories of individual particles, considering all possible realizations of their stochastic paths. For the Eulerian pdf, the averaging process is conducted at fixed spatial points, considering all particles that pass through these points at a given time. This results in a field description in the spatial reference frame, where the focus shifts from individual particle paths to the distribution of particle properties in space and time. From the equation (4.19) we can define the Eulerian instantaneous local particle number density $\tilde{n}(t,\boldsymbol{x})$, i.e. the local number of particles per unit volume at time t. by integrating the Eulerian pdf f^E over particle states, velocity v and temperature ϑ

$$\tilde{n}(t,\boldsymbol{x}) = \int \mathrm{d}\boldsymbol{v}\mathrm{d}\vartheta f^E(t,\boldsymbol{x},\boldsymbol{v},\vartheta) \tag{4.20}$$

where the Eulerian pdf f^E is related to the particle Lagrangian state variables $(\boldsymbol{X}_p, \boldsymbol{V}_p, \Theta_p)$ via the equation (4.19). By substituting this into the equation (4.20), we have:

$$\tilde{n}(t,\boldsymbol{x}) = \int \mathrm{d}\boldsymbol{v}\mathrm{d}\vartheta \langle \delta[\boldsymbol{x}-\boldsymbol{X}_p(t)]\delta[\boldsymbol{v}-\boldsymbol{V}_p(t)]\delta[\vartheta-\Theta_p(t)]\rangle \tag{4.21}$$

since the Dirac delta functions for $\boldsymbol{v}$ and ϑ are within the integral, they effectively integrate out the $\boldsymbol{v}$ and ϑ dependencies, leaving only the dependence on $\boldsymbol{x}$

$$\tilde{n}(t,\boldsymbol{x}) = \left\langle \delta[\boldsymbol{x}-\boldsymbol{X}_p(t)] \int \mathrm{d}\boldsymbol{v}\delta[\boldsymbol{v}-\boldsymbol{V}_p(t)] \int \mathrm{d}\vartheta\delta[\vartheta-\Theta_p(t)] \right\rangle \tag{4.22}$$

from the properties of Dirac delta function, we know that $\int \mathrm{d}\boldsymbol{v}\delta[\boldsymbol{v}-\boldsymbol{V}_p(t)] = 1$ and $\int \mathrm{d}\vartheta\delta[\vartheta-\Theta_p(t)] = 1$, therefore we are left with

$$\tilde{n}(t,\boldsymbol{x}) = \langle \delta[\boldsymbol{x}-\boldsymbol{X}_p(t)] \rangle \tag{4.23}$$

This shows that the instantaneous local particle number density at a fixed spatial position $\boldsymbol{x}$ and time t is given by the ensemble average of the Dirac delta function which indicates the presence of particles at the spatial location $\boldsymbol{x}$ at time t. Similarly, the momentum density or macroscopic particle velocity field and energy density or macroscopic particle temperature field can be defined by

$$\begin{aligned}
&\tilde{n}(t,\boldsymbol{x})\tilde{\boldsymbol{v}}(t,\boldsymbol{x}) = \\
&= \int \mathrm{d}\boldsymbol{v}\mathrm{d}\vartheta \langle \boldsymbol{V}_p(t)\delta[\boldsymbol{x}-\boldsymbol{X}_p(t)]\delta[\boldsymbol{v}-\boldsymbol{V}_p(t)]\delta[\vartheta-\Theta_p(t)]\rangle = \langle \boldsymbol{V}_p(t)\delta[\boldsymbol{x}-\boldsymbol{X}_p(t)]\rangle
\end{aligned} \tag{4.24}$$

$$\begin{aligned}
&\tilde{n}(t,\boldsymbol{x})\tilde{\vartheta}(t,\boldsymbol{x}) = \\
&= \int \mathrm{d}\boldsymbol{v}\mathrm{d}\vartheta \langle \Theta_p(t)\delta[\boldsymbol{x}-\boldsymbol{X}_p(t)]\delta[\boldsymbol{v}-\boldsymbol{V}_p(t)]\delta[\vartheta-\Theta_p(t)]\rangle = \langle \Theta_p(t)\delta[\boldsymbol{x}-\boldsymbol{X}_p(t)]\rangle
\end{aligned} \tag{4.25}$$

The time derivative of both sides of the equation (4.23) gives us the macroscopic field of the local number density of the particles

$$\begin{aligned}
\frac{\partial\tilde{n}(t,\boldsymbol{x})}{\partial t} &= \frac{\partial}{\partial t}\langle \delta[\boldsymbol{x}-\boldsymbol{X}_p(t)]\rangle = -\frac{\partial}{\partial \boldsymbol{x}} \int \mathrm{d}\boldsymbol{x}\delta[\boldsymbol{x}-\boldsymbol{X}_p(t)]\boldsymbol{V}_p(t) \\
&= -\frac{\partial}{\partial \boldsymbol{x}}\langle \boldsymbol{V}_p(t)\delta[\boldsymbol{x}-\boldsymbol{X}_p(t)]\rangle = -\frac{\partial}{\partial \boldsymbol{x}}[\tilde{n}(t,\boldsymbol{x})\tilde{\boldsymbol{v}}(t,\boldsymbol{x})]
\end{aligned} \tag{4.26}$$

If we calculate the temporal derivative, and use the property of the Dirac delta function, we can derive the local number density as

$$\frac{\partial \tilde{n}(t,\boldsymbol{x})}{\partial t}+\frac{\partial[\tilde{n}(t,\boldsymbol{x})\tilde{\boldsymbol{v}}(t,\boldsymbol{x})]}{\partial \boldsymbol{x}}=0 \tag{4.27}$$

If we use the same procedure as the local density field for derivation of the particle Eulerian field, we need to take time derivative of both sides of particle momentum density and energy fields

$$\begin{aligned}\frac{\partial \tilde{n}(t,\boldsymbol{x})\tilde{\boldsymbol{v}}(t,\boldsymbol{x})]}{\partial t}&=\frac{\partial}{\partial t}\langle \boldsymbol{V}_p(t)\delta[\boldsymbol{x}-\boldsymbol{X}_p(t)]\rangle=\frac{\partial}{\partial t}\int \mathrm{d}\boldsymbol{x}\delta[\boldsymbol{x}-\boldsymbol{X}_p(t)]\boldsymbol{V}_p(t)\\&=\int \mathrm{d}\boldsymbol{x}\frac{\partial \boldsymbol{V}_p(t)}{\partial t}\delta[\boldsymbol{x}-\boldsymbol{X}_p(t)]-\frac{\partial}{\partial \boldsymbol{x}}\int \mathrm{d}\boldsymbol{x}\boldsymbol{V}_p(t)\delta[\boldsymbol{x}-\boldsymbol{X}_p(t)]\boldsymbol{V}_p(t)\end{aligned} \tag{4.28}$$

$$\begin{aligned}\frac{\partial [\tilde{n}(t,\boldsymbol{x})\tilde{\vartheta}(t,\boldsymbol{x})]}{\partial t}&=\frac{\partial}{\partial t}\langle \Theta_p(t)\delta[\boldsymbol{x}-\boldsymbol{X}_p(t)]\rangle=\frac{\partial}{\partial t}\int \mathrm{d}\boldsymbol{x}\delta[\boldsymbol{x}-\boldsymbol{X}_p(t)]\Theta_p(t)\\&=\int \mathrm{d}\boldsymbol{x}\frac{\partial \Theta_p(t)}{\partial t}\delta[\boldsymbol{x}-\boldsymbol{X}_p(t)]-\frac{\partial}{\partial \boldsymbol{x}}\int \mathrm{d}\boldsymbol{x}\boldsymbol{V}_p(t)\delta[\boldsymbol{x}-\boldsymbol{X}_p(t)]\Theta_p(t)\end{aligned} \tag{4.29}$$

the particle velocity and temperature field equations after some manipulation can be rewritten in the following form

$$\frac{\partial(\tilde{n}\tilde{\boldsymbol{v}})}{\partial t}+\frac{\partial(n\tilde{\boldsymbol{v}}\otimes\tilde{\boldsymbol{v}})}{\partial \boldsymbol{x}}=\int \mathrm{d}\boldsymbol{x}\frac{\partial \boldsymbol{V}_p(t)}{\partial t}\delta[\boldsymbol{x}-\boldsymbol{X}_p(t)] \tag{4.30}$$

$$\frac{\partial(\tilde{n}\tilde{\vartheta})}{\partial t}+\frac{\partial(\tilde{n}\tilde{\boldsymbol{v}}\tilde{\vartheta})}{\partial \boldsymbol{x}}=\int \mathrm{d}\boldsymbol{x}\frac{\partial \Theta_p(t)}{\partial t}\delta[\boldsymbol{X}-\boldsymbol{X}_p(t)] \tag{4.31}$$

As it can be seen in the equations (4.30), and (4.31) the acceleration term and particle temperature time derivative terms within the integrals needs to be expanded by using the particle Lagrangian stochastic equations and the relation between the particle Eulerian and Lagrangian variables. To relate the particle Eulerian field variables we need to use particle Eulerian position $\boldsymbol{x}$, and its relation to the Lagrangian position in the material reference frame, $\boldsymbol{X}_p$. Any deformation rate with respect to

this Lagrangian position can be computed through $\boldsymbol{x} = \boldsymbol{x}(t, \boldsymbol{X}_p)$ which is a mapping from the Lagrangian position $\boldsymbol{X}_p$ in material frame to the current particle Eulerian position at time t. From the basic continuum mechanics we know that Eulerian velocity and temperature fields which indicate the current state is related to the Lagrangian variables by

$$\begin{aligned} \boldsymbol{u}(t,\boldsymbol{x}) &= \boldsymbol{u}(t,\boldsymbol{x}(t,\boldsymbol{X})) = \boldsymbol{u}(t,\boldsymbol{X}) \\ T(t,\boldsymbol{x}) &= T(t,\boldsymbol{x}(t,\boldsymbol{X})) = T(t,\boldsymbol{X}) \end{aligned} \tag{4.32}$$

where $\boldsymbol{x} = \boldsymbol{x}(t,\boldsymbol{X})$ is the fluid particle trajectory and is a mapping from initial position at time zero in material frame to the current position $\boldsymbol{x}$ at time t. Thus, $\boldsymbol{x}(0,\boldsymbol{X}) = \boldsymbol{X}$. For the fluid particle, trajectory $\boldsymbol{x} = \boldsymbol{x}(t,\boldsymbol{X})$ evolution equation is given by

$$\begin{aligned} &\frac{\partial x_i}{\partial t} = u_i(t,\boldsymbol{x}) = u_i(t,\boldsymbol{x}(t,\boldsymbol{X})) = u_i(t,\boldsymbol{X}) \\ &x_i(0,\boldsymbol{X}) = X_i \end{aligned} \tag{4.33}$$

The equation (4.33) defines the velocity field $\boldsymbol{u}$ evolving from an initial material point $\boldsymbol{X}$. The rate of change of the fluid velocity field at fixed material position $\boldsymbol{X}$ following the fluid particle reads

$$\begin{aligned} &\frac{\partial u_i(t,\boldsymbol{X})}{\partial t} = \frac{\partial u_i(t,\boldsymbol{x}(t,\boldsymbol{X}))}{\partial t} = \frac{\partial u_i}{\partial t} + \frac{\partial u_i}{\partial x_j}\frac{\partial x_j}{\partial t} = \frac{\mathrm{D}u_i(t,\boldsymbol{x})}{\mathrm{D}t} \\ &u_i(0,\boldsymbol{X}) = V_i \end{aligned} \tag{4.34}$$

From the equation (4.34), the material derivative can be defined to relate the time derivative in two reference frame

$$\begin{aligned} \frac{\mathrm{D}\boldsymbol{u}}{\mathrm{D}t} &= \frac{\partial \boldsymbol{u}}{\partial t} + \boldsymbol{u}\cdot\frac{\partial \boldsymbol{u}}{\partial \boldsymbol{x}} \\ \frac{\mathrm{D}T}{\mathrm{D}t} &= \frac{\partial T}{\partial t} + \boldsymbol{u}\cdot\frac{\partial T}{\partial \boldsymbol{x}} \end{aligned} \tag{4.35}$$

Similarly for the particle velocity and temperature fields we can define the material derivative as

$$\begin{aligned}\frac{\mathrm{D}_p\tilde{\boldsymbol{v}}}{\mathrm{D}t} &= \frac{\partial\tilde{\boldsymbol{v}}}{\partial t} + \tilde{\boldsymbol{v}}\cdot\frac{\partial\tilde{\boldsymbol{v}}}{\partial x}\\ \frac{\mathrm{D}_p\tilde{\vartheta}}{\mathrm{D}t} &= \frac{\partial\tilde{\vartheta}}{\partial t} + \tilde{\boldsymbol{v}}\cdot\frac{\partial\tilde{\vartheta}}{\partial x}\end{aligned} \tag{4.36}$$

where $\mathrm{D}_p(\cdot)/\mathrm{D}t$ compute the derivative in a frame that follows particle Lagrangian path line. This definitions enable us to relate the particle Lagrangian variables $\boldsymbol{V}_p$ and Θ_p to their corresponding Eulerian fields, $\tilde{\boldsymbol{v}}$ and $\tilde{\vartheta}$. These relations are given by

$$\begin{aligned}\tilde{\boldsymbol{v}}(t,\boldsymbol{x}) &= \tilde{\boldsymbol{v}}(t,\boldsymbol{x}(t,\boldsymbol{X}_p)) = \tilde{\boldsymbol{v}}(t,\boldsymbol{X}_p)\\ \tilde{\vartheta}(t,\boldsymbol{x}) &= \tilde{\vartheta}(t,\boldsymbol{x}(t,\boldsymbol{X}_p)) = \tilde{\vartheta}(t,\boldsymbol{X}_p)\end{aligned} \tag{4.37}$$

now we can define the trajectory of particle p which is moving by a synthetic velocity field $\boldsymbol{v}$ as

$$\begin{aligned}\frac{\partial\boldsymbol{x}}{\partial t} &= \tilde{\boldsymbol{v}}(t,\boldsymbol{x}) = \tilde{\boldsymbol{v}}(t,\boldsymbol{x}(t,\boldsymbol{X}_p)) = \tilde{\boldsymbol{v}}(t,\boldsymbol{X}_p)\\ \boldsymbol{x}(0,\boldsymbol{X}_p) &= \boldsymbol{X}_p\end{aligned} \tag{4.38}$$

consequently the rate of change of the particle velocity and temperature field following particle at fixed material position $\boldsymbol{X}_p$ are

$$\begin{aligned}\frac{\partial\boldsymbol{V}_p(t)}{\partial t} &= \frac{\partial\tilde{\boldsymbol{v}}(t,\boldsymbol{X}_p)}{\partial t} = \frac{\boldsymbol{u}(t,\boldsymbol{x}(t,\boldsymbol{X}_p)) - \tilde{\boldsymbol{v}}(t,\boldsymbol{x}(t,\boldsymbol{X}_p))}{\tau_v} = \frac{\boldsymbol{u}(t,\boldsymbol{x}) - \tilde{\boldsymbol{v}}(t,\boldsymbol{x})}{\tau_v} = \frac{\mathrm{D}_p\tilde{\boldsymbol{v}}(t,\boldsymbol{x})}{\mathrm{D}t}\\ \frac{\partial\Theta_p(t)}{\partial t} &= \frac{\partial\tilde{\vartheta}(t,\boldsymbol{X}_p)}{\partial t} = \frac{T(t,\boldsymbol{x}(t,\boldsymbol{X}_p)) - \tilde{\vartheta}(t,\boldsymbol{x}(t,\boldsymbol{X}_p))}{\tau_\vartheta} = \frac{T(t,\boldsymbol{x}) - \tilde{\vartheta}(t,\boldsymbol{x})}{\tau_\vartheta} = \frac{\mathrm{D}_p\tilde{\vartheta}(t,\boldsymbol{x})}{\mathrm{D}t}\end{aligned} \tag{4.39}$$

Note that fluid velocity and temperature fields in the equation (4.39) are computed at fixed particle material position $\boldsymbol{X}_p$ while we follow the fluid particle whose velocity is $\boldsymbol{u}$. Thanks to the equation (4.39) we can substitute the terms $\partial_t \boldsymbol{v}$ in (4.30) and $\partial_t \vartheta$ in (4.31). Now we are able to write the particle macroscopic equations in terms of Eulerian variables $\boldsymbol{x}$, $\boldsymbol{v}$ and ϑ like the fluid Navier-Stokes equations in the following form

$$\frac{\partial \tilde{n}}{\partial t} + \frac{\partial (\tilde{n}\tilde{\boldsymbol{v}})}{\partial \boldsymbol{x}} = 0 \tag{4.40}$$

$$\frac{\partial (\tilde{n}\tilde{\boldsymbol{v}})}{\partial t} + \frac{\partial [\tilde{n}\tilde{\boldsymbol{v}} \otimes \tilde{\boldsymbol{v}}]}{\partial \boldsymbol{x}} = \frac{\tilde{n}}{\tau_v}[\boldsymbol{u} - \tilde{\boldsymbol{v}}] \tag{4.41}$$

$$\frac{\partial (\tilde{n}\tilde{\vartheta})}{\partial t} + \frac{\partial (\tilde{n}\tilde{\boldsymbol{v}}\tilde{\vartheta})}{\partial \boldsymbol{x}} = \frac{\tilde{n}}{\tau_\vartheta}[T - \tilde{\vartheta}] \tag{4.42}$$

After derivation of particle Eulerian fields by using the statistical averaging over all possible states by using Eulerian pdf concentrated in a fixed point $(\boldsymbol{x}, \boldsymbol{v}, \vartheta)$ at time t, the next step is to take into account the turbulent flow effects. Due to the intrinsic nature of the turbulent two-phase flow, particle velocity and temperature field are turbulent and we can use the Reynolds decomposition as the fluid flow to write the fields equation in two parts, mean field and fluctuating field. The decomposition for particle number density, velocity and temperature fields are

$$\begin{aligned}
\tilde{n}(t,\boldsymbol{x}) &= \langle \tilde{n} \rangle (t,\boldsymbol{x}) + \tilde{n}'(t,\boldsymbol{x}) \\
\tilde{v}_i(t,\boldsymbol{x}) &= \langle \tilde{v}_i \rangle (t,\boldsymbol{x}) + \tilde{v}_i'(t,\boldsymbol{x}) \\
\tilde{\vartheta}(t,\boldsymbol{x}) &= \langle \tilde{\vartheta} \rangle (t,\boldsymbol{x}) + \tilde{\vartheta}'(t,\boldsymbol{x})
\end{aligned} \tag{4.43}$$

By employing these decomposition and taking the ensemble averaging similar to what we did for fluid turbulent fields in chapter 2, we can obtain the mean and fluctuating particle velocity and temperature fields. These mean values are introduced into the equation (4.40)-(4.42), then after ensemble averaging, the mean particle fields are obtained as

$$\frac{\partial\langle\tilde{n}\rangle}{\partial t}+\frac{\partial(\langle\tilde{n}\rangle\langle\tilde{\boldsymbol{v}}\rangle)}{\partial \boldsymbol{x}}=-\frac{\partial\langle\tilde{n}'\tilde{\boldsymbol{v}}'\rangle}{\partial \boldsymbol{x}} \tag{4.44}$$

$$\frac{\partial\langle\tilde{\boldsymbol{v}}\rangle}{\partial t}+\frac{\partial(\langle\tilde{\boldsymbol{v}}\rangle\otimes\langle\tilde{\boldsymbol{v}}\rangle)}{\partial \boldsymbol{x}}=\frac{1}{\tau_v}[\langle\boldsymbol{u}\rangle-\langle\tilde{\boldsymbol{v}}\rangle]-\frac{\partial\langle\tilde{\boldsymbol{v}}'\otimes\tilde{\boldsymbol{v}}'\rangle}{\partial \boldsymbol{x}} \tag{4.45}$$

$$\frac{\partial\langle\tilde{\vartheta}\rangle}{\partial t}+\frac{\partial(\langle\tilde{\boldsymbol{v}}\rangle\langle\tilde{\vartheta}\rangle)}{\partial \boldsymbol{x}}=\frac{1}{\tau_\vartheta}[\langle T\rangle-\langle\tilde{\vartheta}\rangle]-\frac{\partial\langle\tilde{\boldsymbol{v}}'\tilde{\vartheta}'\rangle}{\partial \boldsymbol{x}} \tag{4.46}$$

Due to the homogeneity in the fluid velocity field, particle velocity field is also homogeneous resulting in $\partial_j\langle\tilde{v}_i'\tilde{v}_j'\rangle=0$, i.e. the analogous particle Reynolds stress term in the particle macroscopic momentum equation (4.45). In addition, from the incompressibility of the mean particle number density field, we know that $\partial_j\langle\tilde{v}_j\rangle=0$, in our case where total number density of particles in the flow domain is constant ($N_p=Const.$). Therefore, the total mass of disperse particle in the whole flow domain should also remain constant ($M_p=N_p\times m_p=Const.$). This is equivalent to the equation (4.23). This constraint, causes that the macroscopic particle number density $\tilde{n}(t,\boldsymbol{x})$ to be conserved and satisfied the particle continuity equation (4.40). The implication is that the integral of pdf in phase-space which is equal to particle local number density (4.20) must also be conserved. Consequently, since the total number of particles in the flow domain is constant over time, the particle mean number density $\langle\tilde{n}\rangle(t,\boldsymbol{x})$ must satisfy a continuity equation that ensures the conservation of particles.

$$\frac{\mathrm{D}\langle\tilde{n}\rangle}{\mathrm{D}t}=-\langle\tilde{n}\rangle\frac{\partial\langle\tilde{v}_j\rangle}{\partial x_j}-\frac{\partial\langle\tilde{n}'\tilde{v}_j'\rangle}{\partial x_j}=0 \tag{4.47}$$

However, the particle instantaneous field is compressible, since fluctuation particle velocity field remains compressible even if in this case in which the flow is homogeneous and isotropic and total number of particles remains constant. From the definition of the particle material derivative, the instantaneous particle continuity equation (4.40) can be expanded and rewritten as

$$\frac{\mathrm{D}_p\tilde{n}}{\mathrm{D}t}=\frac{\partial\tilde{n}}{\partial t}+\tilde{v}_j\cdot\frac{\partial\tilde{n}}{\partial x_j}=-\tilde{n}\frac{\partial\tilde{v}_j}{\partial x_j} \tag{4.48}$$

In a generic case, the number density can include some additional terms, like condensational growth which is the case of droplet-laden flows. Because for compressible flow regimes, deformable particle, high volume fraction and in reactive flows that could lead to particle generation or destruction particle number density on average cannot be conserved. But, in our case, we do not lose or generate particles in the whole flow domain, thus $\mathrm{D}_p\langle\tilde{n}\rangle/\mathrm{D}t = 0$ in the computational domain, and in each computational cell of volume $\mathscr{V}$.

$$\int_{\mathscr{V}} \tilde{n}(t,\boldsymbol{x})\mathrm{d}\boldsymbol{x} = Const. \tag{4.49}$$

Meanwhile, due to the uniformity of the particle number density n, $\partial_j\langle\tilde{n}\rangle = 0$, and from $\partial_t\langle\tilde{n}\rangle = 0$ because of the nature of solid particles with no particle generation or loss, satisfying equation (4.47). On the other hand, $\partial_j\langle\tilde{v}_j\rangle = 0$ implies that the mean velocity field is uniform and incompressible. This is consistent with a scenario where there is no net flux or change in the mean particle number density over time. However, this condition holds only for mean particle number density, and fluctuating fields is compressible and subjected to a high level of non-uniformity due to the particle inertia and their inertia-induced clustering in certain regions that results in to preferential concentration in high strain-rate regions. If we employ Reynolds decomposition and introduce the decomposed particle fields (4.43) in the particle macroscopic instantaneous local fields (4.41) and (4.42), the particle fluctuating velocity and temperature fields are obtained as

$$\frac{\partial\tilde{v}_i'}{\partial t} + \frac{\partial(\tilde{v}_i'\tilde{v}_j')}{\partial x_j} = \frac{1}{\tau_v}[u_i' - \tilde{v}_i'] - \frac{\partial(\tilde{v}_i'\langle\tilde{v}_j\rangle)}{\partial x_j} - \frac{\partial(\tilde{v}_j'\langle v_i\rangle)}{\partial x_j} \tag{4.50}$$

$$\frac{\partial\tilde{\vartheta}'}{\partial t} + \frac{\partial(\tilde{v}_j'\tilde{\vartheta}')}{\partial x_j} = \frac{1}{\tau_\vartheta}[T' - \tilde{\vartheta}'] - \frac{\partial(\tilde{v}_j'\langle\tilde{\vartheta}\rangle)}{\partial x_j} - \frac{\partial(\langle\tilde{v}_j\rangle\tilde{\vartheta}')}{\partial x_j} \tag{4.51}$$

In order to derive the evolution equation for the particle temperature variance, we need to use the coarse-grained definition, and then by ensemble averaging we can derive the equations. We are also interested in particle heat flux transport equation, that can be obtained by following the same procedure as the particle temperature variance. First, these quantities are defined by

$$\tilde{n}(t,\boldsymbol{x})\tilde{\boldsymbol{v}}(t,\boldsymbol{x})\tilde{\vartheta}(t,\boldsymbol{x}) = \langle \boldsymbol{V}_p(t)\Theta_p(t)\delta[\boldsymbol{x}-\boldsymbol{X}_p(t)]\rangle \tag{4.52}$$

$$\tilde{n}(t,\boldsymbol{x})\tilde{\vartheta}(t,\boldsymbol{x})\tilde{\vartheta}(t,\boldsymbol{x}) = \langle \Theta_p(t)\Theta_p(t)\delta[\boldsymbol{x}-\boldsymbol{X}_p(t)]\rangle \tag{4.53}$$

similar to the steps we have taken for the particle temperature and velocity fields, by taking time derivative of both sides of the equations (4.52) and (4.53), we have

$$\begin{aligned}
&\frac{\partial[\tilde{n}(t,\boldsymbol{x})\tilde{\boldsymbol{v}}(t,\boldsymbol{x})\tilde{\vartheta}(t,\boldsymbol{x})]}{\partial t} = \frac{\partial}{\partial t}\langle \boldsymbol{V}_p(t)\Theta_p(t)\delta[\boldsymbol{x}-\boldsymbol{X}_p(t)]\rangle \\
&= \langle \frac{\partial \boldsymbol{V}_p}{\partial t}\Theta_p\delta[\boldsymbol{x}-\boldsymbol{X}_p(t)]\rangle \\
&+ \langle \frac{\partial \Theta_p}{\partial t}\delta[\boldsymbol{x}-\boldsymbol{X}_p(t)]\rangle \\
&- \frac{\partial}{\partial \boldsymbol{x}}\langle (\boldsymbol{V}_p \otimes \boldsymbol{V}_p\Theta_p)\delta[\boldsymbol{x}-\boldsymbol{X}_p(t)]\rangle
\end{aligned} \tag{4.54}$$

$$\begin{aligned}
&\frac{\partial[\tilde{n}(t,\boldsymbol{x})\vartheta(t,\boldsymbol{x})\tilde{\vartheta}(t,\boldsymbol{x})]}{\partial t} = \frac{\partial}{\partial t}\langle \Theta_p\Theta_p\delta[\boldsymbol{x}-\boldsymbol{X}_p(t)]\rangle \\
&= \langle \frac{\partial \Theta_p}{\partial t}\Theta_p\delta[\boldsymbol{x}-\boldsymbol{X}_p(t)]\rangle \\
&+ \langle \Theta_p\frac{\partial \Theta_p}{\partial t}\delta[\boldsymbol{x}-\boldsymbol{X}_p(t)]\rangle \\
&- \frac{\partial}{\partial \boldsymbol{x}}\langle (\boldsymbol{V}_p\Theta_P)\delta[\boldsymbol{x}-\boldsymbol{X}_p(t)]\rangle
\end{aligned} \tag{4.55}$$

after some manipulation, the final equations for particle instantaneous local temperature variance field and particle heat flux field can be expressed as

$$\begin{aligned}
&\frac{\partial(\tilde{n}\tilde{v}_i\tilde{\vartheta})}{\partial t} + \frac{\partial(n\tilde{v}_i\tilde{v}_j\vartheta)}{\partial x_j} = -\tilde{n}[\frac{1}{\tau_v}+\frac{1}{\tau_\vartheta}](\tilde{v}_i\tilde{\vartheta}) + \frac{\tilde{n}}{\tau_v}(u_i\tilde{\vartheta}) + \frac{\tilde{n}}{\tau_\vartheta}(\tilde{v}_iT) \\
&\frac{\partial(\tilde{n}\tilde{\vartheta}\tilde{\vartheta})}{\partial t} + \frac{\partial(\tilde{n}\tilde{v}_j\tilde{\vartheta}\tilde{\vartheta})}{\partial x_j} = \frac{2\tilde{n}}{\tau_\vartheta}[T\tilde{\vartheta} - (\tilde{\vartheta}\tilde{\vartheta})]
\end{aligned} \tag{4.56}$$

Now we can use the Reynolds decomposition to derive the particle temperature variance and particle heat flux transport equations which are given by

$$\frac{\partial\langle\tilde{v}_i'\tilde{\vartheta}'\rangle}{\partial t}+\frac{1}{\langle\tilde{n}\rangle}\frac{\partial\langle\tilde{n}'\tilde{v}_i'\tilde{v}_j'\tilde{\vartheta}'\rangle}{\partial x_j}=-\frac{\partial\langle\tilde{v}_i'\tilde{v}_j'\tilde{\vartheta}'\rangle}{\partial x_j}-[\frac{1}{\tau_v}+\frac{1}{\tau_\vartheta}]\langle\tilde{v}_i'\tilde{\vartheta}'\rangle$$
$$+\frac{1}{\tau_v}\langle u_i'\tilde{\vartheta}'\rangle+\frac{1}{\tau_\vartheta}\langle\tilde{v}_i'T'\rangle-\langle\tilde{v}_j'\tilde{\vartheta}'\rangle\frac{\partial\langle\tilde{v}_i\rangle}{\partial x_j}-\frac{\partial(\langle\tilde{v}_j\rangle\langle\tilde{v}_i'\tilde{\vartheta}'\rangle)}{\partial x_j}-\langle\tilde{v}_i'\tilde{v}_j'\rangle\frac{\partial\langle\tilde{\vartheta}\rangle}{\partial x_j} \tag{4.57}$$
$$\frac{\partial\langle\tilde{\vartheta}'^2\rangle}{\partial t}+\frac{1}{\langle\tilde{n}\rangle}\frac{\partial\langle\tilde{n}'\tilde{v}_j'\tilde{\vartheta}'^2\rangle}{\partial x_j}=-\frac{\partial\langle\tilde{v}_j'\tilde{\vartheta}'^2\rangle}{\partial x_j}+\frac{2}{\tau_\vartheta}[\langle T'\tilde{\vartheta}'\rangle-\langle\vartheta'^2\rangle]-2\langle\tilde{v}_j'\tilde{\vartheta}'\rangle\frac{\partial\langle\tilde{\vartheta}\rangle}{\partial x_j}$$
$$-\frac{\partial(\langle\tilde{v}_j\rangle\langle\tilde{\vartheta}'^2\rangle)}{\partial x_j} \tag{4.58}$$

Applying the incompressiblity condition of mean particle velocity field, along with the homogeneity and isotropy of particle velocity field impying $\langle\tilde{v}_j\rangle=0$, the particle heat flux and temperature variance can be reduced to the following form

$$\frac{\partial\langle\tilde{v}_i'\tilde{\vartheta}'\rangle}{\partial t}+\frac{1}{\langle\tilde{n}\rangle}\frac{\partial\langle\tilde{n}'\tilde{v}_i'\tilde{v}_j'\tilde{\vartheta}'\rangle}{\partial x_j}=-\frac{\partial\langle\tilde{v}_i'\tilde{v}_j'\tilde{\vartheta}'\rangle}{\partial x_j}-[\frac{1}{\tau_v}+\frac{1}{\tau_\vartheta}]\langle\tilde{v}_i'\tilde{\vartheta}'\rangle$$
$$+\frac{1}{\tau_v}\langle u_i'\tilde{\vartheta}'\rangle+\frac{1}{\tau_\vartheta}\langle\tilde{v}_i'T'\rangle-\langle\tilde{v}_i'\tilde{v}_j'\rangle\frac{\partial\langle\tilde{\vartheta}\rangle}{\partial x_j} \tag{4.59}$$
$$\frac{\partial\langle\tilde{\vartheta}'^2\rangle}{\partial t}+\frac{1}{\langle\tilde{n}\rangle}\frac{\partial\langle\tilde{n}'\tilde{v}_j'\tilde{\vartheta}'^2\rangle}{\partial x_j}=-\frac{\partial\langle\tilde{v}_j'\tilde{\vartheta}'^2\rangle}{\partial x_j}+\frac{2}{\tau_\vartheta}[\langle T'\tilde{\vartheta}'\rangle-\langle\tilde{\vartheta}'^2\rangle]-2\langle\tilde{v}_j'\tilde{\vartheta}'\rangle\frac{\partial\langle\tilde{\vartheta}\rangle}{\partial x_j} \tag{4.60}$$

Derivation of particle macroscopic fields from Eulerian pdf

Using this definition of Eulerian pdf, the instantaneous particle number density, velocity and temperature fields can be defined by

$$\tilde{n}(t,\boldsymbol{x}) = \int \mathrm{d}\boldsymbol{v}\mathrm{d}\vartheta f^E(t,\boldsymbol{x},\boldsymbol{v},\vartheta) \tag{4.61}$$

$$\tilde{n}(t,\boldsymbol{x})\tilde{\boldsymbol{v}}(t,\boldsymbol{x}) = \int \mathrm{d}\boldsymbol{v}\mathrm{d}\vartheta f^E(t,\boldsymbol{x},\boldsymbol{v},\vartheta)\boldsymbol{V}_p \tag{4.62}$$

$$\tilde{n}(t,\boldsymbol{x})\tilde{\vartheta}(t,\boldsymbol{x}) = \int \mathrm{d}\boldsymbol{v}\mathrm{d}\vartheta f^E(t,\boldsymbol{x},\boldsymbol{v},\vartheta)\Theta_p \tag{4.63}$$

In order to derive the transport equation for particle fields using the Eulerian pdf, we take the time derivative of the definition of particle number density, which is equation (4.61), and we get

$$\frac{\partial \tilde{n}(t,\boldsymbol{x})}{\partial t} = \frac{\partial}{\partial t}\Big[\int \mathrm{d}\boldsymbol{v}\mathrm{d}\vartheta f^E(t,\boldsymbol{x},\boldsymbol{v},\vartheta)\Big] = \int \mathrm{d}\boldsymbol{v}\mathrm{d}\vartheta \frac{\partial f^E(t,\boldsymbol{x},\boldsymbol{v},\vartheta)}{\partial t} \tag{4.64}$$

As we can see to continue with the derivation of mean particle number density field, we need to derive the transport equation or Boltzman-like equation for the particle Eulerian pdf f^E. To do this, we must take time derivative from the equation (4.19) which is integrated over particle velocity and temperature spaces leading to

$$
\begin{aligned}
&\int \mathrm{d}\boldsymbol{v}\mathrm{d}\vartheta \frac{\partial f^E(t,\boldsymbol{x},\boldsymbol{v},\vartheta)}{\partial t} = \\
&-\int \mathrm{d}\boldsymbol{v}\mathrm{d}\vartheta \Big(\frac{\partial}{\partial \boldsymbol{x}} \int \mathrm{d}\boldsymbol{x}\mathrm{d}\boldsymbol{v}\mathrm{d}\vartheta\, \delta[\boldsymbol{x}-\boldsymbol{X}_p(t)]\delta[\boldsymbol{v}-\boldsymbol{V}_p(t)]\delta[\vartheta-\Theta_p(t)]\boldsymbol{V}_p(t)\Big) \\
&-\int \mathrm{d}\boldsymbol{v}\mathrm{d}\vartheta \Big(\frac{\partial}{\partial \boldsymbol{v}} \int \mathrm{d}\boldsymbol{x}\mathrm{d}\boldsymbol{v}\mathrm{d}\vartheta\, \delta[\boldsymbol{x}-\boldsymbol{X}_p(t)]\delta[\boldsymbol{v}-\boldsymbol{V}_p(t)]\delta[\vartheta-\Theta_p(t)]\boldsymbol{A}_p(t)\Big) \\
&-\int \mathrm{d}\boldsymbol{v}\mathrm{d}\vartheta \Big(-\frac{\partial}{\partial \vartheta} \int \mathrm{d}\boldsymbol{x}\mathrm{d}\boldsymbol{v}\mathrm{d}\vartheta_\delta[\boldsymbol{x}-\boldsymbol{X}_p(t)]\delta[\boldsymbol{v}-\boldsymbol{V}_p(t)]\delta[\vartheta-\Theta_p(t)]\dot{\Theta}_p(t)\Big) \\
&= \\
&-\int \mathrm{d}\boldsymbol{v}\mathrm{d}\vartheta \Big[\frac{\partial}{\partial \boldsymbol{x}} \cdot \Big(f^E(t,\boldsymbol{x},\boldsymbol{v},\vartheta)\langle \boldsymbol{V}_p|\boldsymbol{x},\boldsymbol{v},\vartheta\rangle\Big)\Big] \\
&-\int \mathrm{d}\boldsymbol{v}\mathrm{d}\vartheta \Big[\frac{\partial}{\partial \boldsymbol{v}} \cdot \Big(f^E(t,\boldsymbol{x},\boldsymbol{v},\vartheta)\langle \boldsymbol{A}_p|\boldsymbol{x},\boldsymbol{v},\vartheta\rangle\Big)\Big] \\
&-\int \mathrm{d}\boldsymbol{v}\mathrm{d}\vartheta \Big[\frac{\partial}{\partial \vartheta} \cdot \Big(f^E(t,\boldsymbol{x},\boldsymbol{v},\vartheta)\langle \Theta_p|\boldsymbol{x},\boldsymbol{v},\vartheta\rangle\Big)\Big] \\
&= \\
&-\int \mathrm{d}\boldsymbol{v}\mathrm{d}\vartheta \Big[\nabla_{\boldsymbol{x}} \cdot (f^E(t,\boldsymbol{x},\boldsymbol{v},\vartheta)\langle \boldsymbol{V}_p|\boldsymbol{x},\boldsymbol{v},\vartheta\rangle)\Big] \\
&-\int \mathrm{d}\boldsymbol{v}\mathrm{d}\vartheta \Big[\nabla_{\boldsymbol{v}} \cdot (f^E(t,\boldsymbol{x},\boldsymbol{v},\vartheta)\langle \boldsymbol{A}_p|\boldsymbol{x},\boldsymbol{v},\vartheta\rangle)\Big] \\
&-\int \mathrm{d}\boldsymbol{v}\mathrm{d}\vartheta \Big[\nabla_{\vartheta} \cdot (f^E(t,\boldsymbol{x},\boldsymbol{v},\vartheta)\langle \Theta_p|\boldsymbol{x},\boldsymbol{v},\vartheta\rangle)\Big]
\end{aligned}
\tag{4.65}
$$

Since the integral is over $\boldsymbol{v}$ and ϑ, we can bring the gradient with respect to $\boldsymbol{x}$ outside the integral

$$
\begin{aligned}
&\int \mathrm{d}\boldsymbol{v}\mathrm{d}\vartheta \frac{\partial f^E(t,\boldsymbol{x},\boldsymbol{v},\vartheta)}{\partial t} = \\
&-\nabla_{\boldsymbol{x}} \cdot \Big[\int \mathrm{d}\boldsymbol{v}\mathrm{d}\vartheta (f^E(t,\boldsymbol{x},\boldsymbol{v},\vartheta)\langle \boldsymbol{V}_p|\boldsymbol{x},\boldsymbol{v},\vartheta\rangle)\Big] \\
&-\int \mathrm{d}\boldsymbol{v}\mathrm{d}\vartheta \Big[\nabla_{\boldsymbol{v}} \cdot (f^E(t,\boldsymbol{x},\boldsymbol{v},\vartheta)\langle \boldsymbol{A}_p|\boldsymbol{x},\boldsymbol{v},\vartheta\rangle)\Big] \\
&-\int \mathrm{d}\boldsymbol{v}\mathrm{d}\vartheta \Big[\nabla_{\vartheta} \cdot (f^E(t,\boldsymbol{x},\boldsymbol{v},\vartheta)\langle \Theta_p|\boldsymbol{x},\boldsymbol{v},\vartheta\rangle)\Big]
\end{aligned}
\tag{4.66}
$$

As it is seen in the equation (4.66), time rate of change of the pdf is balanced with three flux terms on the right hand side, position flux, velocity flux and temperature

flux. To obtain the final expression each flux must be explicit;y computed. Let us start with the position flux. In this term, the integration of pdf over particle velocity and temperature space resulting in $\int \mathrm{d}\boldsymbol{v}\mathrm{d}\vartheta f^E(t,\boldsymbol{x},\boldsymbol{v},\vartheta)$ which is the definition of particle number density fields $\tilde{n}(t,\boldsymbol{x})$. Moreover, the integration remove the conditional of particle velocity $\boldsymbol{V}_p$ on velocity itself and temperature, returning the velocity conditioned on position which is equal to macroscopic particle velocity field as it defined earlier, $\langle \boldsymbol{V}_p|\boldsymbol{x}\rangle = \boldsymbol{V}_p$. Moreover, the position flux can be computed from the definition of conditional average. The conditional particle velocity on particle position, velocity and tempera tut is given by

$$\langle \boldsymbol{V}_p|\boldsymbol{x},\boldsymbol{v},\vartheta\rangle = \frac{\int \mathrm{d}\boldsymbol{x}\mathrm{d}\boldsymbol{v}\mathrm{d}\vartheta \boldsymbol{V}_p \delta[\boldsymbol{x}-\boldsymbol{X}_p(t)]\delta[\boldsymbol{v}-\boldsymbol{V}_p(t)]\delta[\vartheta-\Theta_p(t)]}{f^E(t,\boldsymbol{x},\boldsymbol{v},\vartheta)} \tag{4.67}$$

On the other hand, the velocity and temperature flux terms are the integral of a divergence in velocity and temperature spaces over velocity and temperature. These terms must be zero because the integral of a divergence over all space is zero, if no flux exists at the boundaries of space. By applying the divergence theorem (Gauss's theorem) to these volume integrals, we can convert them into a surface integrals over the boundary of the velocity and temperature spaces which vanishes. For the velocity space we have

$$\int \mathrm{d}\vartheta\mathrm{d}\boldsymbol{v}\nabla_{\boldsymbol{v}}\cdot(f^E(t,\boldsymbol{x},\boldsymbol{v},\vartheta)\langle \boldsymbol{A}_p|\boldsymbol{x},\boldsymbol{v},\vartheta\rangle) = \oint_{\partial \boldsymbol{v}}(f^E(t,\boldsymbol{x},\boldsymbol{v},\vartheta)\langle \boldsymbol{A}_p|\boldsymbol{x},\boldsymbol{v},\vartheta\rangle)\cdot \boldsymbol{n}\mathrm{d}\boldsymbol{S}_{\boldsymbol{v}} \tag{4.68}$$

where $\partial \boldsymbol{v}$ represents the boundary of the velocity space, $\boldsymbol{n}$ is the outward normal vector on this boundary, and $\mathrm{d}\boldsymbol{S}_v$ is the surface element in velocity space. If we assume there are no particles entering or leaving the system through the boundaries of the velocity space (i.e., no particle flux at the boundary), the boundary term goes to zero:

$$\oint_{\partial \boldsymbol{v}}(f^E(t,\boldsymbol{x},\boldsymbol{v},\vartheta)\langle \boldsymbol{A}_p|\boldsymbol{x},\boldsymbol{v},\vartheta\rangle)\cdot \boldsymbol{n}\mathrm{d}\boldsymbol{S}_{\boldsymbol{v}} = 0 \tag{4.69}$$

The integral of the divergence in velocity space represents the net flux of the particle distribution function due to particle acceleration $\boldsymbol{A}_p$. If there is no net flux at the boundaries (no particles are entering or leaving the system), this term vanishes. It implies that the particle acceleration acting on particles does not create or destroy particles within the system, just redistributes their velocities internally. If there are particles entering or leaving through the boundaries in velocity space, the boundary term does not vanish. In this case, the term represents the net flux of particles due to particle acceleration at the boundaries. This would need to be accounted for explicitly in the transport equation by considering the boundary conditions of the system. Applying the Gauss's theorem to the volume integral in the temperature space, which is integral of divergence in the particle temperature space, gives

$$\int \mathrm{d}\vartheta \mathrm{d}\boldsymbol{v} \nabla_\vartheta \cdot (f^E(t,\boldsymbol{x},\boldsymbol{v},\vartheta)\langle\Theta_p|\boldsymbol{x},\boldsymbol{v},\vartheta\rangle) = \oint_{\partial\vartheta} (f^E(t,\boldsymbol{x},\boldsymbol{v},\vartheta)\langle\Theta_p|\boldsymbol{x},\boldsymbol{v},\vartheta\rangle) \cdot \boldsymbol{n}\mathrm{d}\boldsymbol{S}_\vartheta \tag{4.70}$$

where $\partial\vartheta$ represents the boundary of the temperature space, and $\mathrm{d}\boldsymbol{S}_\vartheta$ is the surface element in temperature space. The integral of the divergence in temperature space represents the net flux of the particle distribution function due to changes in temperature. If there is no net flux at the boundaries (no particles are entering or leaving the system), this term vanishes. If we assume there are no particles entering or leaving the system through the boundaries of the temperature space, the boundary term goes to zero. Then, the third term in the number density transport equation should also zero because the integral of a total derivative over all space is zero, assuming no flux at the boundaries in temperature space. It implies that temperature changes do not create or destroy particles within the system, just redistributes their temperatures internally. If there are particles entering or leaving through the boundaries in temperature space, the boundary term does not vanish. In this case, the term represents the net flux of particles due to temperature changes at the boundaries. This would need to be accounted for explicitly in the transport equation by considering the boundary conditions of the system.

$$\oint_{\partial\vartheta} (f^E(t,\boldsymbol{x},\boldsymbol{v},\vartheta)\langle\Theta_p|\boldsymbol{x},\boldsymbol{v},\vartheta\rangle) \cdot \boldsymbol{n}\mathrm{d}\boldsymbol{S}_\vartheta = 0 \tag{4.71}$$

The physical interpretation of these integrals is that they represent the net change in particle number density due to external influences (particle acceleration and temperature changes) at the boundaries of the velocity and temperature spaces. Consequently, in a generic case mean particle number density transport equation with non-Zero boundary fluxes can be written as

$$\frac{\partial \tilde{n}(t,\boldsymbol{x})}{\partial t} + \nabla_{\boldsymbol{x}} \cdot (\tilde{n}(t,\boldsymbol{x})\tilde{\boldsymbol{v}}(t,\boldsymbol{x})) = \oint_{\partial \boldsymbol{v}} (f^E(t,\boldsymbol{x},\boldsymbol{v},\vartheta)\langle \boldsymbol{A}_p|\boldsymbol{x},\boldsymbol{v},\vartheta\rangle) \cdot \boldsymbol{n}\mathrm{d}\boldsymbol{S}_{\boldsymbol{v}} + \oint_{\partial \vartheta} (f^E(t,\boldsymbol{x},\boldsymbol{v},\vartheta)\langle \Theta_p|\boldsymbol{x},\boldsymbol{v},\vartheta\rangle) \cdot \boldsymbol{n}\mathrm{d}\boldsymbol{S}_{\vartheta} \tag{4.72}$$

In practice, the boundary conditions would need to be specified to evaluate these terms accurately. These could represent physical boundaries where particles enter or exit the domain, such as walls, inlets, or outlets in a physical system. By assuming that all the boundary fluxes are zero in velocity and temperature spaces, and by introducing the derivative of f^E into the equation (4.73) we can obtain the transport equation for instantaneous local number density as:

$$\frac{\partial \tilde{n}(t,\boldsymbol{x})}{\partial t} + \nabla_{\boldsymbol{x}} \cdot (\tilde{n}(t,\boldsymbol{x})\boldsymbol{v}(\tilde{t,\boldsymbol{x}})) = 0 \tag{4.73}$$

The same procedure can be employed to derive the particle velocity and temperature fields from the definition provided in equations (4.62) and (4.63). If we perform the calculation starting from the field definitions, we can obtain the following equations

$$\frac{\partial \tilde{n}(t,\boldsymbol{x})\tilde{\boldsymbol{v}}(t,\boldsymbol{x})}{\partial t} + \nabla_{\boldsymbol{x}} \cdot \left(\tilde{n}(t,\boldsymbol{x})\tilde{\boldsymbol{v}}(t,\boldsymbol{x}) \otimes \tilde{\boldsymbol{v}}(t,\boldsymbol{x})\right) = \frac{\tilde{n}(t,\boldsymbol{x})}{\tau_v}[\boldsymbol{u}(t,\boldsymbol{x}) - \tilde{\boldsymbol{v}}(t,\boldsymbol{x})] - \boldsymbol{\Pi}_{\boldsymbol{v},\boldsymbol{a}}(t,\boldsymbol{x}) - \boldsymbol{\Pi}_{\boldsymbol{v},\dot{\vartheta}}(t,\boldsymbol{x}) \tag{4.74}$$

$$\frac{\partial \tilde{n}(t,\boldsymbol{x})\tilde{\vartheta}(t,\boldsymbol{x})}{\partial t} + \nabla_{\boldsymbol{x}} \cdot \left(\tilde{n}(t,\boldsymbol{x})\tilde{\boldsymbol{v}}(t,\boldsymbol{x}) \cdot \tilde{\vartheta}(t,\boldsymbol{x})\right) = \frac{\tilde{n}(t,\boldsymbol{x})}{\tau_\vartheta}[T(t,\boldsymbol{x}) - \tilde{\vartheta}(t,\boldsymbol{x})] - \boldsymbol{\Pi}_{\vartheta,\boldsymbol{a}}(t,\boldsymbol{x}) - \boldsymbol{\Pi}_{\vartheta,\dot{\vartheta}}(t,\boldsymbol{x}) \tag{4.75}$$

where $\mathbf{\Pi}_{\boldsymbol{v},\boldsymbol{a}}$ is the acceleration momentum flux representing the change of particle momentum due to the particle acceleration. It captures how variations in acceleration affect the distribution of momentum in the system. $\mathbf{\Pi}_{\boldsymbol{v},\dot{\vartheta}}$ is the particle temperature time derivative momentum flux representing the change of particle momentum due to the change in particle temperature derivative. It reflects how temperature changes influence the distribution of particle velocity. $\mathbf{\Pi}_{\vartheta,\boldsymbol{a}}$ is the particle acceleration heat flux due to the particle acceleration. This term represents the flux of thermal energy due to the acceleration of particles. It indicates how acceleration affects the thermal energy distribution. $\mathbf{\Pi}_{\vartheta,\dot{\vartheta}}$ represents the heat flux due to the particle temperature derivative. This term captures the flux of thermal energy due to changes in particle temperature. It shows how variations in temperature affect the thermal energy distribution. They are derived by considering how the phase-space distribution of particles (given by the pdf f^E) and their properties (velocity, acceleration, temperature) affect the overall fluxes. Understanding these fluxes helps in analyzing and modeling the behavior of particle-laden turbulent flows, especially in non-isothermal conditions. The explicit expressions for these kinetic fluxes are given by

$$\mathbf{\Pi}_{\boldsymbol{v},\boldsymbol{a}} = -\int \mathrm{d}\boldsymbol{v}\mathrm{d}\vartheta\, \nabla_{\boldsymbol{v}} \cdot \left(f^E(t,\boldsymbol{x},\boldsymbol{v},\vartheta)\, \boldsymbol{V}_p \otimes \boldsymbol{A}_p\right) \tag{4.76}$$

$$\mathbf{\Pi}_{\boldsymbol{v},\dot{\vartheta}} = -\int \mathrm{d}\boldsymbol{v}\mathrm{d}\vartheta\, \nabla_{\vartheta} \cdot \left(f^E(t,\boldsymbol{x},\boldsymbol{v},\vartheta)\, \boldsymbol{V}_p \cdot \dot{\Theta}_p\right) \tag{4.77}$$

$$\mathbf{\Pi}_{\vartheta,\boldsymbol{a}} = -\int \mathrm{d}\boldsymbol{v}\mathrm{d}\vartheta\, \nabla_{\boldsymbol{v}} \cdot \left(f^E(t,\boldsymbol{x},\boldsymbol{v},\vartheta)\, \Theta_p \otimes \boldsymbol{A}_p\right) \tag{4.78}$$

$$\mathbf{\Pi}_{\vartheta,\dot{\vartheta}} = -\int \mathrm{d}\boldsymbol{v}\mathrm{d}\vartheta\, \nabla_{\vartheta} \cdot \left(f^E(t,\boldsymbol{x},\boldsymbol{v},\vartheta)\, \Theta_p \cdot \dot{\Theta}_p\right) \tag{4.79}$$

In this study, we assume that all fluxes related to particle velocity and temperature fields are zero. However, this assumption may not always hold true depending on the boundary and flow conditions. In some cases, these fluxes may be non-zero and need to be computed to accurately derive the full particle field equations. Using Green's theorem and assuming that velocity and temperature fluxes vanish at the boundaries of the velocity and temperature spaces as $t \to \infty$. For example, in a periodic domain or in the absence of specific boundary effects, these fluxes can indeed average out to zero. In homogeneous and isotropic turbulent flow, the terms involving momentum and heat fluxes often average out to zero. However, if the temperature field exhibits inhomogeneity, the fluxes related to temperature gradients $\mathbf{\Pi}_{\vartheta,\boldsymbol{a}}$ and $\mathbf{\Pi}_{\vartheta,\dot{\vartheta}}$ will

generally be non-zero unless the boundary conditions are specifically designed to counteract these effects. In such cases, the impact of temperature inhomogeneity on fluxes must be carefully evaluated to ensure an accurate representation of the system.

4.5 Phase space structure analysis

In the section 4.3 the pdf transport equation (4.16) has been obtained. There are some mesoscopic information embedded in the unclosed terms, due to actions of the turbulent fluid velocity and temperature fields. The objective of this study is more concerned with the thermal behavior of particles and its impact on the heat transfer the heat transfer in the inhomogeneous direction x. Thus, the most significant term in the equation (4.16) is conditional average of particle temperature time derivative $\langle \dot{\Theta}_p | x_p, v_p, \vartheta_p \rangle$. In this section, we aim to further our analysis of the pdf behavior in phase space via three-dimensional and two-dimensional visual inspections of pdf which is obtained in section 4.3. As it is customary in other physical problem concerning with phase-space analysis e.g. astrophysics and accelerator physics [102], we employed the DNS data to visualize the pdf in a reduced ordered three-dimensional phase space, whose dimensions are determined by particle state variables $\boldsymbol{X}_p$, $\boldsymbol{V}_p$, and Θ_p. Due to the inhomogeneity of temperature field in direction x_3, and the homogeneity and linearity of the fluid velocity field, the phase space reduced from generic 7 dimensions to 3 dimensions. Instead of the full pdf in equation (4.14) we investigate equation (4.16) which corresponds to our physical problem and derived by integrating the full pdf equation (4.14) in directions x_1 and x_2 to remove the dependency on particle position and velocity in those directions. The pdf is computed at different section of the computational domain, different time and different particle inertia and thermal inertia ranges. The DNS data used for pdf computation, is for the case with fixed thermal Stokes to Stokes number equal to 4.43 and at fixed Taylor microscale Reynolds number equal to 56. The inter-particle collision effects are excluded throughout this chapter both in derivation of the equations and numerical simulations.

Figure 4.1 illustrates the pdf three-dimensional structure in particle three-dimensional phase space whose dimensions are particle position in inhomogeneous direction x_3, velocity and temperature at $\mathrm{St} = 1$ and dimensionless time t/tau equal to 4 (red/yellow), 7(blue/light blue), and 8 (green/light green). Two images indicate the

pdf distribution in particle phase space from different angle of views, in such a way that two isosurface of pdf at each instants is visible.

The PDF is computed on a plane located at the center of the domain, where thermal mixing is most intense. The bin count is carefully selected to strike a balance between adequate data sampling and minimizing statistical error. Note that for the sake of simplicity, since we excluded the other homogeneous directions. Thus, in visualization a variable X_p, and V_p are used which denote the particle position and velocity in direction of temperature inhomogeneity x_3. The particle position X_p, is also normalized by the mixing layer thickness, $\delta(t)$ for each instant. Additionally, the Z direction represents the particle velocity V_p, which is normalized by the root mean square (rms) of fluid velocity fluctuation, $u'_{rms} = 0.56$.

On the other hand, direction Y represents the particle temperature Θ_p normalized by the maximum standard deviation of the particle temperature ($\sigma_\vartheta(t)$), at the visualized dimensionless time t/τ. Note that $\sigma_\vartheta(t)$ is time-dependent and reduces with time unlike the u'_{rms} which is constant in time. As time progresses, in regions distant from the mixing zone, the normalized temperature increases, with the transition from the red to green isosurfaces corresponding to dimensionless times 4 to 8. Away from the mixing zone, particles are distributed near the maximum temperature in the left half-domain with higher temperature, while the same pattern can be seen for the right half-domain with lower temperature. In the central zone, where the mixing grows with time a self-similar structure is formed at each instant. Numerical observations has shown that the shape of this structure is independent of particle Stokes numbers and thermal Stokes number. However that we only reported one St number and one Re_λ, but we investigated different Stokes numbers from 0.2 to 3 at Taylor micro scale Reynolds number equal to 56, to confirm this self-similarity at different particle inertia and thermal inertia ranges. For each set of numerical simulation, the 3D structure persists self-similar evolution in time. Furthermore, the results show a similar 3D structure in phase-space for both one- and two-way thermal coupling regimes. Thus, we inferred that the turbulent flow dictates the evolution law implying that the self-similarity is rooted in the large-scale motion of turbulent flow.

Accordingly, we continue our investigation to develop a theoretical analysis for explanation of such self-similar behavior. At this point we aim to link this particular behavior in phase-space to the large-scale of turbulence. As it is customary in statistical physics and turbulence theory, we perform an theoretical analysis

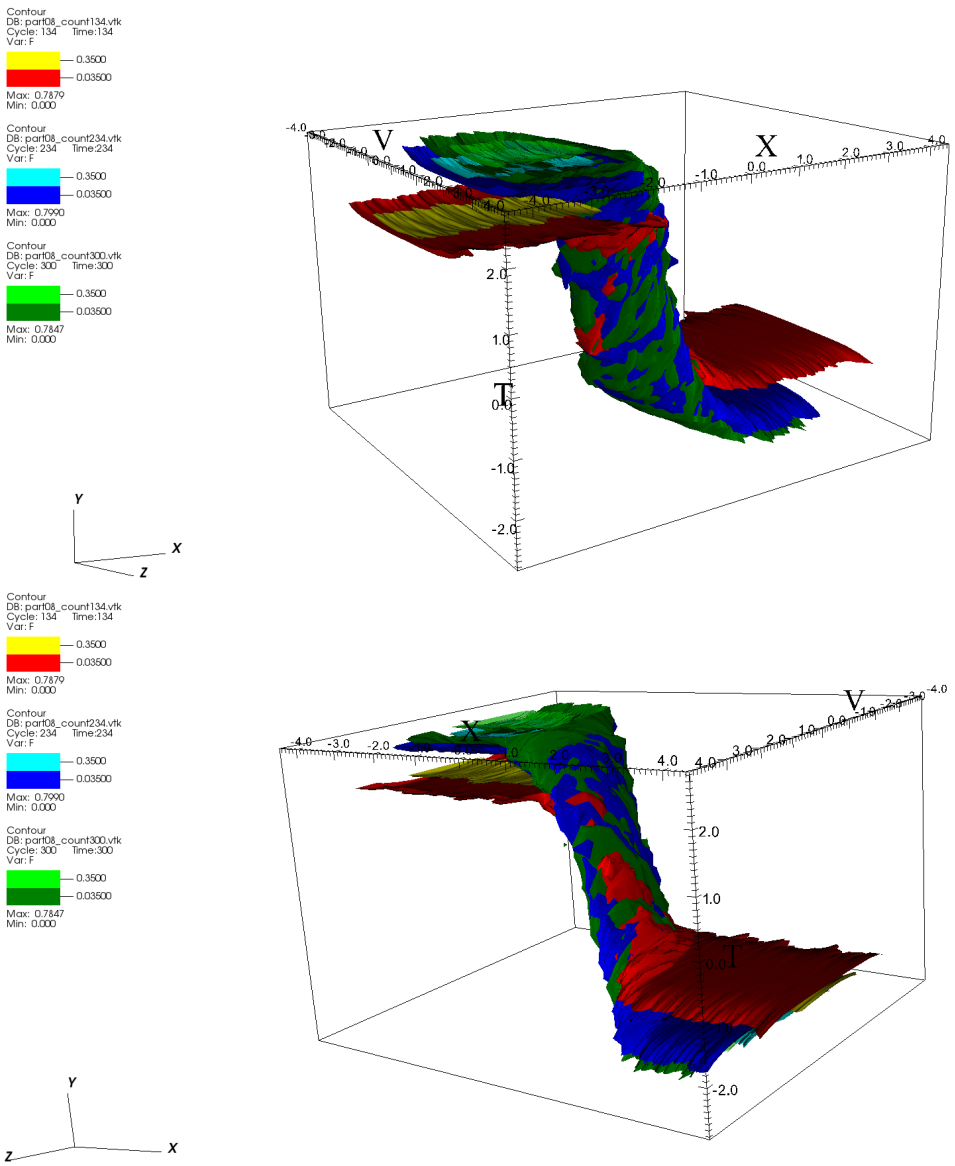

Fig. 4.1 Three-dimensional visualization of the single-particle pdf, f at St $= 1.0$ at $t/\tau = 4$ (red/yellow), 7 (blue/light blue), and 8 (green/light green). The two images plots show, from a different point of view, two isosurfaces of f at each instant. Position x, velocity v and temperature θ have been normalized with the mixing layer thickness δ, the velocity standard deviation and the temperature standard deviation in the middle section.

to find a power-law scaling for the pdf in phase-space. It should be noted that finding a purely power-law scaling for this complex physical problem is very hard to achieve analytically. 3D visualization indicates that despite the similar shape for each experiment, there is an overlap region at which is independent of time. More precisely, the perfect self-similar evolution of pdf in time only takes place only in a limited domain of phase-space, at which the thermal mixing evolves. This results can suggest to extract the potential power-law scaling in centeral zone of the phase-space. To better understand the pdf evolution, we also plotted an slice at $X_p = 0$ at which the mixing is maximum. This slice provides us a two-dimensional map of pdf on (V_p, Θ_p) plane.

Figures 4.2 and 4.3 depict the time evolution of a slice of the pdf at central plane, for different Stokes numbers at $\mathrm{Re}_\lambda = 56$ when $\mathrm{St}_\vartheta/\mathrm{St} = 4.43$. Dark colors on the maps indicate the lower value and brighter colors represent the higher values. Additionally, the continous white lines represent the states that mean particle temperature time derivative $\langle \dot{\Theta}_p | x_p, v_p, \vartheta_p \rangle$ is zero. In these 2D maps which are slices in direction x_3, an elliptical structure is formed such that its slop changes in time. The white slices on the maps, are the zones that $\langle \dot{\Theta}_p | x_p, v_p, \vartheta_p \rangle$ is equal to zero. By using the standard quadrant method, we can interpret the thermal mixing dynamics at this plane from the pdf behavior. In chapter 3 we discussed and quantified the contribution of particle to the transport of heat in inhomogenous direction. In physical space, due to the mean temperature gradient, thermal energy flows from the left half-domain with higher temperature T_1, to the right half-domain with the lower temperature T_2. This is the natural direction of the convective heat transfer and it is aligned with the fluid temperature gradient. Accordingly, particles moving in this direction, from left to right, have the positive velocity ($V_p > 0$) and acceleration ($A_p > 0$) and they are being cooled down. Consequently, the particle temperature time derivative is negative $(T - \Theta_p)/\tau_\vartheta = \dot{\Theta}_p < 0$ since particle temperature fluctuation is positive and fluid-particle temperature difference is negative ($\Theta_p > T$). The opposite scenario holds for the particles moving from colder region to the warmer region (from right to left) and being warmed up. This movement is also aligned with the natural direction of the flow since turbulent large-scale eddies sweep them from the right to the left. Considering the particle velocity-temperature correlation which quantify the particle heat flux in the inhomogeneous direction, for both cases the contributions are positive, thus we can conclude that particles enhance the heat transfer at mixing as numerical confirmed it in chapter 3. One can find the same information on the

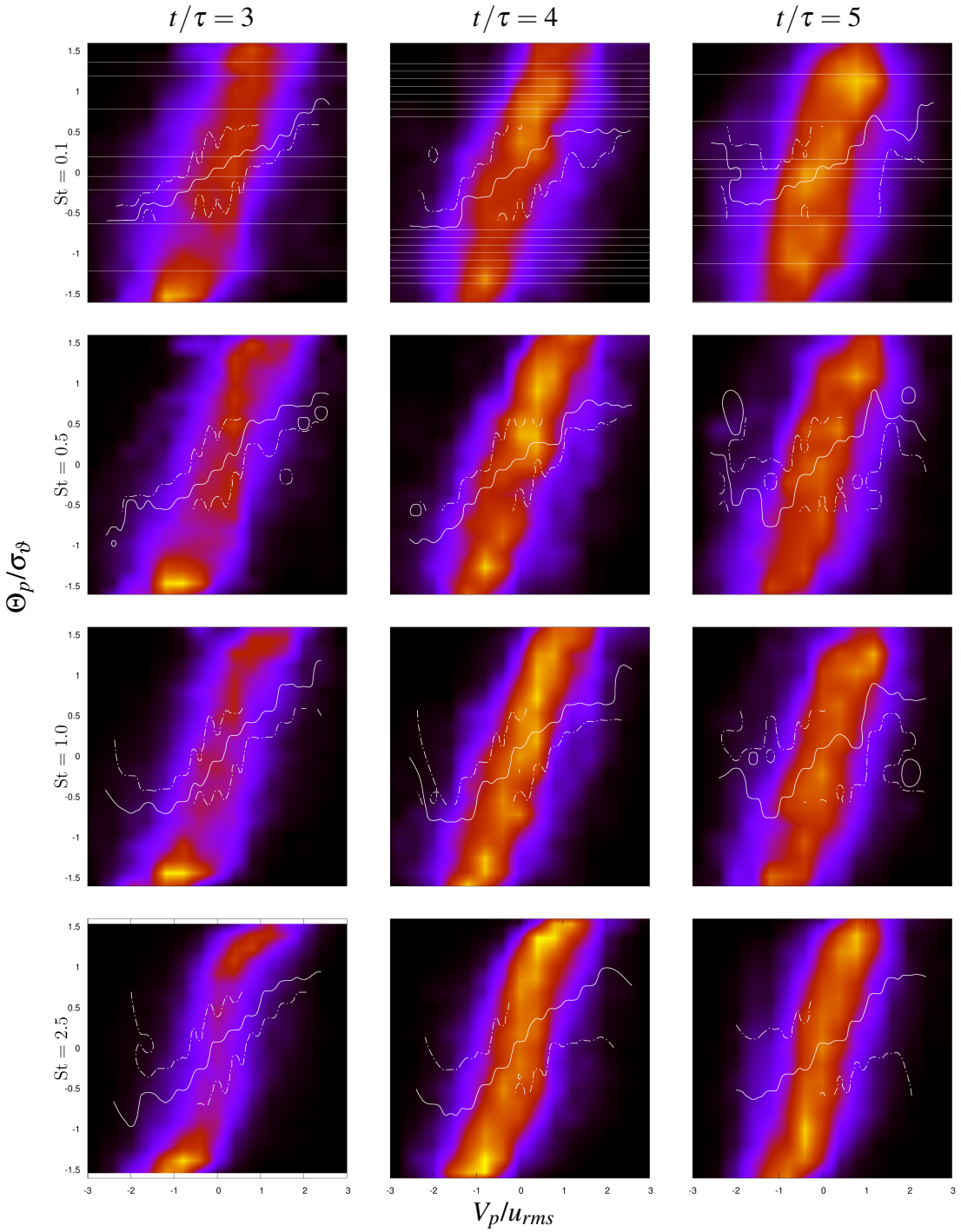

Fig. 4.2 Time evolution of a slice of single-particle pdf f in the central plane $x = 0$ for different St at $\mathrm{Re}_\lambda = 56$ and when $\mathrm{St}_\vartheta/\mathrm{St} = 4.43$. Dark color indicates lower values, brighter colors indicate higher values. Velocity and temperature have been normalized with their standard deviations. The continuous white line indicated the state where the mean particle temperature time derivative $\langle \dot{\Theta}_p | x_p, v_p, \vartheta_p \rangle$is zero, the dashed lines the states where the particle temperature time derivatives is equal to $\pm 0.2\sigma_\vartheta/\tau_\vartheta$.

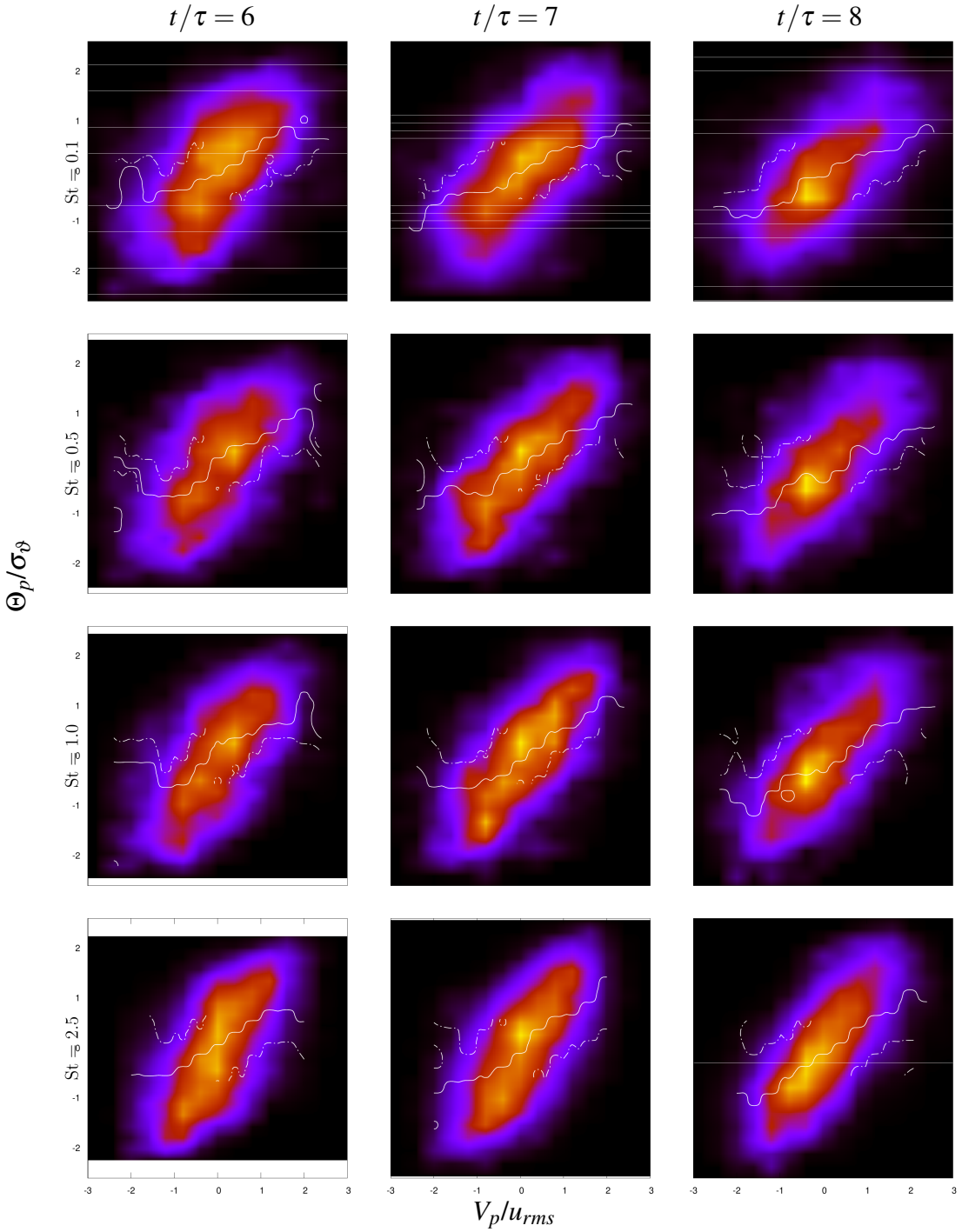

Fig. 4.3 Same data as previous figure, at later times, see its caption.

2D map of the pdf which is computed at the same plane as numerical results. In 4.2 and 4.3 we can see that most probable zones for all Stokes numbers and all instants are the first and third quadrants. First quadrant is associated with the particles that are cooled down with $V_p > 0$, $A_p > 0$, $\Theta_p > 0$ and $\dot{\Theta}_p < 0$ while the third quadrant is associated with particles that are warmed up with $V_p < 0$, $A_p < 0$, $\Theta_p < 0$ and $\dot{\Theta}_p > 0$. Particle temperature time derivative Θ_p is a measure of local inter-phase heat transfer and particle velocity-temperature correlation $\langle V_p \Theta_p \rangle$ is an indication of overall particle heat flux in the inhomogeneous direction. Although, the local heat transfer is negative and positive in first and third quadrants respectively, the overall particle heat flux is positive in both quadrants. In second quadrant where particles have positive temperature $\Theta_p > 0$ and negative velocity $V_p < 0$, negative acceleration $A_p < 0$ and positive particle temperature derivative $\dot{\Theta}_p$ repenting a case that particles with higher temperature are being warmed which is intuitively less probable. Numerical results also confirm that in this zone the probability distribution is low. Regardless of the Stokes number and time, in first quadrant near the central zone in which mixing takes place, some narrow particles exist. Due to the effects of turbulent mixing, these particles may be hindered from following the natural flow direction along the fluid temperature gradient. In this part, the overall particle heat flux must be negative $\langle V_p \Theta_p \rangle < 0$ but since the likelihood is quite low, the global particle heat flux is dominated by the positive heat flux from the most probable zones, i.e. quadrant 1 and 3. The quadrant 4 is the opposite of the quadrant 2 owning the same low probability to find particles that are cooled down in the low temperature part of the domain.

On all the 2D maps at all times and all Stokes numbers, we can see that pdf distributed along an inclined line on (V_p, Θ_p) plane. This inclined line is aligned with the white continuous line which represents the points where particle temperature time derivative is zero on average $\langle \dot{\Theta}_p \rangle = 0$. The alignment of the pdf with the inclined line corresponding to $\langle \dot{\Theta}_p \rangle = 0$ also ties into the overall positive heat flux in the system, confirming that the particles enhance heat transfer in the direction of the temperature gradient. This particular alignment likely corresponds to a balance between heating and cooling processes in the turbulent flow as explained earlier in different quadrants. This line likely represents a dynamic equilibrium in the turbulent mixing process. Identifying such features in the phase space can provide insights into the interplay between particle dynamics and the thermal field. At a fixed Stokes number, as time grows, the slope reduces toward the horizontal line,

and pdf compresses toward the center, moving away from the highest and lowest temperature areas and becomes narrower. We induce that the existing a strong fluid mean temperature gradient in our flow controls this slop since it is invariant of the particle inertia or thermal inertia. Accordingly, over a very long time, we expect the pdf to align completely horizontally with the $\Theta_p = 0$ line, reflecting thermal equilibrium between the two homogeneous regions as the fluid mean temperature gradient approaches zero.

Meanwhile, at this state, we expect that the pdf worm-shaped structure becomes more isotropic like a small circle around center, when temperature field becomes homogeneous given the eventual homogenization of the temperature field. As the mean temperature gradient diminishes, the pdf will reflect the increasingly uniform thermal environment, leading to a more isotropic distribution in the phase space. From the 2D visual inspection and from the physical condition of the flow, we can estimate the slope of the pdf by using the standard deviation of fluid temperature and velocity. However, in our configuration velocity field is homogenous and isotropic then the scaling remains constant in time. In chapter 3 DNS results showed that temperature standard deviation scaled with $\delta^{-1} = t^{-1/2}$, resulting in

$$slope = \frac{\sigma_\vartheta}{\sigma_v} = \frac{\delta(t)^{-1}}{1} = t^{-1/2} \tag{4.80}$$

From turbulence theory, we know that turbulence strongly influences particle dynamics, and the large-scale structures in turbulent flow are known to impose scaling laws on various quantities, including single-particle pdf. Our 3D and 2D observation of pdf self-similar structures in the phase space over time is consistent with the nature of turbulent mixing, where large-scale motions dominate the transport processes along with imposed mean temperature gradient. This scaling indicates that the strong mean temperature gradient between the two regions drives thermal mixing through the large-scale turbulent motions in the direction of temperature inhomogeneity, influencing the overall heat flux. Therefore, this analysis also suggest the same scaling for slope which can be obtained by $u'_{rms}(\Delta T/\delta)$, where $\Delta T = 2$ between two homothermal regions with $T_1 = 1 > T_2 = -1$. This indicates that the pdf slope's evolution which is observed on 2D maps, is governed by the same physical processes driving the thermal mixing.

The analysis of the pdf in phase space reveals a fundamental symmetry in its structure, which can be observed across the four quadrants. This symmetry is particularly evident when examining the central plane at $x = 0$. Assuming that this symmetry holds, we can express the pdf as follows

$$f(t,0,-v,-\vartheta) = f(t,0,v,\vartheta) \tag{4.81}$$

Furthermore, the symmetry can be extended to the spatial domain, implying that:

$$f(t,-x,-v,-\vartheta) = f(t,x,v,\vartheta) \tag{4.82}$$

This symmetry arises due to the odd nature of the mean temperature profile along the center of the domain. Given the pdf transport equation (4.16), it is invariant under the transformation of variables $(t,x,v,\vartheta) \rightarrow (t,-x,-v,-\vartheta)$, with f remaining unchanged. Because the mean temperature profile is odd, the system's dynamics are symmetrical when flipping both the spatial coordinates and the temperature (and velocity) signs. This results in the pdf being symmetric in phase-space. Additionally, under this transformation, the fluid velocity u and temperature T transform as $(u,T) \rightarrow (-u,-T)$. Utilizing these symmetry properties, the derivatives of the pdf with respect to position, velocity, and temperature can be related as follows:

$$\frac{\partial}{\partial x} f(t,-x,-v,-\vartheta) = -\frac{\partial}{\partial x} f(t,x,v,\vartheta) \tag{4.83}$$

$$\frac{\partial}{\partial v} f(t,-x,-v,-\vartheta) = -\frac{\partial}{\partial v} f(t,x,v,\vartheta) \tag{4.84}$$

$$\frac{\partial}{\partial \vartheta} f(t,-x,-v,-\vartheta) = -\frac{\partial}{\partial \vartheta} f(t,x,v,\vartheta) \tag{4.85}$$

These relations demonstrate the inherent symmetry in the pdf structure, which is consistent with the physical behavior of the system under the specified transformation. Moreover, self-similar solutions to the pdf transport equation (4.16) can be found by seeking solutions that are invariant with respect to certain homothetic transformations:

$$f(t,\lambda_1 x,\lambda_2 v,\lambda_3 \vartheta,\lambda_4) = \lambda_5 f(t,x,v,\vartheta) \tag{4.86}$$

The odd symmetry rooted in mean temperature field is essential for the self-similarity analysis because it dictates how the variables scale and evolve over time, maintaining the symmetry across the entire phase space. These self-similar solutions indicate that the pdf maintains its form under specific scaling transformations, reinforcing the concept of symmetry in the phase space. This symmetry plays a crucial role in the evolution of the pdf, particularly in understanding the thermal mixing and heat transfer dynamics in the system. y linking the symmetry properties of the pdf with its self-similar behavior, we gain deeper insights into the underlying mechanisms driving the evolution of the particle distribution in phase space. This understanding is essential for developing more accurate models of particle behavior in turbulent flows with thermal gradients. The observed symmetry in pdf is not just a mathematical curiosity but has profound implications for the physical behavior of the system, particularly in the context of self-similar solutions to the pdf transport equation. Specifically, the symmetry reduces the complexity of the problem by ensuring that the pdf must have a form that is consistent with the symmetrical properties of the system. Self-similar solutions are characterized by their invariance under certain homothetic transformations, where the variables of the pdf position, velocity, temperature, and time are scaled according to specific rules.

The symmetry of the pdf with respect to the phase-space transformation $(t,x,v,\vartheta) \rightarrow (t,-x,-v,-\vartheta)$ suggests that in the equation (4.86) the scaling factors λ_1, λ_2, and λ_3 must be chosen such that the symmetry is preserved in the self-similar solution. In other words, the self-similar scaling must respect the underlying symmetry of the PDF, which acts as a constraint on the form of the scaling laws. Moreover, the symmetry ensures that the pdf evolves in a manner that is consistent with the large-scale structure of the turbulent flow. The invariant properties under the transformation indicate that the mixing process, driven by the mean temperature gradient, leads to a self-similar evolution of the pdf. This is reflected in the alignment of the pdf along an inclined line on the (V_p,Θ_p) plane, as observed in the 2D maps. As time progresses, the slope of this line reduces, following a scaling law that is determined by the symmetry and the large-scale dynamics of the system. We can infer that the observed symmetry of the pdf in phase-space is directly linked to the self-similar behavior of

the system. The symmetry not only simplifies the form of the pdf but also dictates the scaling laws that govern its evolution. From the 2D and 3D visual inspections of pdf structure in phase-space, we deduced a scaling for the pdf which is assumed to be deriven by turbulent large scale as the standard deviation of fluid temperature field. This inference has been also applied to the moment of particle temperature derivative $\langle\dot{\Theta}_p\rangle$ resulting in $\delta^{-1} = t^{-1/2}$. Here, we aim to derive the scaling theoretically using the transport equation of the pdf. Therefore, as it conducted in previous section 4.4, we use the equation integrated over velocity and temperature paces which is

$$\int \mathrm{d}v\mathrm{d}\vartheta \frac{\partial f(t,x,v,\vartheta)}{\partial t} = -\nabla_x \cdot \Big[\int \mathrm{d}v\mathrm{d}\vartheta (f(t,x,v,\vartheta)\langle V_p|x,v,\vartheta\rangle)\Big]$$
$$-\int \mathrm{d}v\mathrm{d}\vartheta \Big[\nabla_v \cdot (f^E(t,x,v,\vartheta)\langle A_p|x,v,\vartheta\rangle)\Big] - \int \mathrm{d}v\mathrm{d}\vartheta \Big[\nabla_\vartheta \cdot (f(t,x,v,\vartheta)\langle \Theta_p|x,v,\vartheta\rangle)\Big] \tag{4.87}$$

by using the Green's theorem and assuming that the velocity and temperature fluxes at the boundaries of the velocity and temperature spaces vanish as $t \to \infty$. These conditions typically involve the decay of the pdf and its derivatives at infinity, which ensures that boundary terms vanish. Therefore, the integral equation reduces to

$$\int \mathrm{d}v\mathrm{d}\vartheta \frac{\partial f(t,x,v,\vartheta)}{\partial t} = -\nabla_x \cdot \Big[\int \mathrm{d}v\mathrm{d}\vartheta (f(t,x,v,\vartheta)\langle V_p|x,v,\vartheta\rangle)\Big] \tag{4.88}$$

Now, if we multiply both sides of the integral equations (4.88) by x and integrate over x from $x = -\infty$ to $x = +\infty$, the integral equation can be written as

$$\frac{\mathrm{d}}{\mathrm{d}t}\int x\tilde{n}(t,x)\mathrm{d}x - \int \tilde{n}(t,x)v\mathrm{d}x = 0 \tag{4.89}$$

Since $\int \mathrm{d}v\mathrm{d}\vartheta (f(t,x,v,\vartheta)\langle V_p|x,v,\vartheta\rangle) = \tilde{n}(t,x)v$ and $x\tilde{n}(t,x)v|_{-\infty}^{+\infty} = 0$. Vanishing fluxes at boundaries assumption in velocity and temperature space implies to look at the evolution of particle number density field as the integral representation of pdf including only the flux in position space. But we can do our self-similarity analysis

in a generic case in which all fluxes exists by introducing self-similarity scalings as follows:

$$f(t,x,v,\vartheta) = \frac{f}{\Delta}(\frac{x}{\delta},\frac{v}{\delta_v},\frac{\vartheta}{\delta_\vartheta}) = F(\eta,\tilde{v},\tilde{\vartheta}) \tag{4.90}$$

where the different scaling variables are $\eta = x/\delta(t)$, $\tilde{v} = v/\delta_v(t)$, $\tilde{\vartheta} = \vartheta/\delta_\vartheta(t)$, $F = f/\Delta(t)$. Let us first, look at the full integral equation without using the assumptions that remove the dependency of the pdf integral equation on the fluxes at the boundaries of velocity and temperature spaces. In this case, the full pdf integral equation is given by

$$\begin{aligned}&\frac{\mathrm{d}}{\mathrm{d}t}\delta^2\Delta\int \eta F \mathrm{d}\eta - \delta\delta_v\Delta\Delta_v\int F\tilde{v}\mathrm{d}\eta + \delta^2\delta_v\Delta\Delta_{A_p}\frac{\mathrm{d}}{\mathrm{d}\tilde{v}}\int \eta F\tilde{A}_p\mathrm{d}\eta \\ &+ \delta^2\delta_\vartheta\Delta\Delta_{\dot{\Theta}_p}\frac{\mathrm{d}}{\mathrm{d}\tilde{\vartheta}}\int \eta F\tilde{\dot{\Theta}}_p\mathrm{d}\eta = 0\end{aligned} \tag{4.91}$$

We also need to define three more scaling for the position, velocity and temperature fluxes due to the change in particle velocity, acceleration and particle temperature time derivative. These additional scaling are denoted as Δ_v, Δ_{A_p} and $\Delta_{\dot{\Theta}_p}$ respectively. Due to the homogeneity and isotropy of the velocity field, we can assume that particle velocity and acceleration have no scaling, leading to have $\delta_v = 1$. This hypothesis implies that the velocity field does not undergo a significant large-scale restructuring, which is well-justified by the isotropy and homogeneity of the turbulent flow. On the other hand, from the simulation results we have seen that particle temperature time derivative $\langle\dot{\Theta}_p\rangle$, scales with temperature standard deviation σ_ϑ, i.e. δ^{-1} in the central plane (x=0). In order to have the perfect self-similarity for f, the scaling for fluxes must be $\Delta_v = \delta$, $\Delta_{A_p} = \delta^0 = 1$ and $\Delta_{\dot{\Theta}_p} = \delta$. In fact, $\Delta_v = \delta$ suggests that the velocity flux scales with the same factor as the spatial scale, implying a linear relationship between spatial and velocity scales. This is a legitimate choice in our case, since the only existing force acting on particles is linear Stokes drag force. Meanwhile, $\Delta_{A_p} = \delta^0 = 1$ is an appropriate choice for the flux of particle acceleration in the velocity space. Because there is not any additional time-dependence in the acceleration flux term due to the assumed isotropy and homogeneity of the velocity field and the linear nature of Stokes drag. Moreover, $\Delta_{\dot{\Theta}_p} = \delta$ is justified by the need

to balance the inverse scaling of particle temperature time derivative $\dot{\Theta}_p$, ensuring that the flux term in the temperature space fits within the self-similar framework of the pdf evolution. Consequently all the time-dependent scaling terms vanish leading to

$$\frac{\mathrm{d}}{\mathrm{d}t}\int \eta F \mathrm{d}\eta - \int F\tilde{v}\mathrm{d}\eta + \frac{\mathrm{d}}{\mathrm{d}\tilde{v}}\int \eta F\tilde{A}_p \mathrm{d}\eta + \frac{\mathrm{d}}{\mathrm{d}\tilde{\vartheta}}\int \eta F\tilde{\dot{\Theta}}_p \mathrm{d}\eta = 0 \tag{4.92}$$

The absence of any scaling in the equation (4.93) signifies that the pdf evolves in a puerly self-similar manner. As we observed through our visual inspections, the form of the pdf remains consistent over time, indicating that any changes are purely scaling and do not alter the intrinsic shape of the distribution in phase space. Here we have proven the self-similarity by theoretical analysis which matches our numerical observations. For a more simplified case, when we assume vanishing fluxes at the boundaries of velocity and temperature space, we have

$$\frac{\mathrm{d}}{\mathrm{d}t}\int \eta F \mathrm{d}\eta = \int F\tilde{v}\mathrm{d}\eta \tag{4.93}$$

This integral equation suggests that the total number of particles (integral of the pdf) remains constant on average. Note, in this case we use the zero divergence constraint theat simplifies the analysis by assuming that the fluxes at the boundaries of the velocity and temperature spaces vanish as time progresses. Nonetheless, in a generic case, even with all fluxes in the position, velocity and temperature spaces, we can say that in our specific case the evolution of pdf should be purely self-similar. The reason of such behavior is that the total number of particles in our physical domain is constant. Accordingly, the integral of the pdf is equal to the number density field which in average should remain constant. The translation in phase-space is $\mathrm{d}/\mathrm{d}t(\int \mathrm{d}v\mathrm{d}\vartheta f(t,x,v,\vartheta)) = \mathrm{d}/\mathrm{d}t(\tilde{n}(t,x)) = 0$. This implies that the evolution of the pdf is balanced by the fluxes in the phase space, and the integral of the pdf over the entire phase space should be conserved. Even when considering all fluxes in the position, velocity, and temperature spaces, the evolution of the pdf in our specific case is expected to be purely self-similar. In a general case, changes in the moment integral of the pdf are balanced by fluxes in position, velocity, and temperature spaces. As we explained in the quadrant analysis in 2D map, the flux in

position space is related to how particles move through different regions of space in accordance with the natural direction of the flow and convection, and the flux in temperature space relates to the heat carried by particles in different part of the domain. The flux integrals describe how momentum and heat are transported by particles. For instance, if particles carry significant heat, the flux in temperature space will reflect how this heat is distributed and transported in the fluid. Self-similar evolution of pdf implies that the distribution of particles and their properties follows a scaling pattern which is related to the diffusive scale of the turbulent mixing. This formalism by analyzing the balance between the fluxes and the internal dynamics of the system, representing by pdf dynamic in phase-space, providing insight into how particles and heat are redistributed in the turbulent flow. Self-similarity analysis also helps to better understand how particles' dispersion and temperature variations scale with time.

4.6 Conclusion

This chapter has established a robust theoretical framework for applying kinetic theory to the study of non-isothermal particle-laden turbulent flows. The work bridges the gap between the detailed microscopic description of individual particles and the macroscopic statistical properties that emerge when considering the entire ensemble. Using a Lagrangian framework, we tracked the evolution of a particle state vector, leading to the derivation of the fine-grained pdf. By averaging this fine-grained pdf over all possible realizations, we derived the coarse-grained pdf, forming the basis for an Eulerian description of the system. This transition from a detailed Lagrangian to a statistically meaningful Eulerian description allows for modeling the macroscopic properties of the flow, smoothing out the complex details of individual particle trajectories.

Two main objectives were achieved in this chapter: the derivation of the single-particle pdf transport equation and the formulation of particle field-like macroscopic equations using the single-particle pdf under the general assumptions of this study. Moreover, the theoretical analysis was supported by DNS data to examine system dynamics and thermodynamics within phase space. The zero-divergence condition for fluxes at boundaries of particle velocity and temperature spaces was established,

ensuring the conservation of probability and the accurate representation of physical constraints, i.e. the constant total particle number in our case.

Through this rigorous analysis, we uncovered significant insights into the underlying physics of particle dispersion and thermalization. The 2D and 3D visualizations of the pdf in phase space offered compelling representations of particle distributions, revealing complex structures and patterns. Quadrant analysis was employed to categorize and interpret particle behavior in different regions, showing how particles are more likely moving from hot region to cold region to be cooled down or move from cold region to hot region to be warmed up. The probabilistic descriptions indicated that particles are more likely to move in directions aligned with the imposed mean temperature gradient which is in direction of temperature inhomogenity, resulting in an overall enhancement of the heat flux. Additionally, the time derivative of particle temperature provided information about local heat transfer, while the sign of particle temperature and velocity in different quadrants determined the overall contribution through the particle velocity-temperature correlation.

One of the key revelations of this chapter was the identification of self-similar behavior in the pdf structure, which is independent of particle inertia and thermal inertia. This finding implies that turbulent flow and the imposed mean temperature gradient primarily dictate the pdf evolution in phase space. Consequently, the symmetry properties and self-similarity of the pdf first-moment integral equation in phase space were examined, revealing important scaling laws and invariants that characterize the flow. The scaling of different terms in the pdf first-moment integral equation, including the moment integrals and flux integrals for position, velocity, and temperature, was meticulously analyzed. Self-similarity, a recurring theme throughout this chapter, suggests that the statistical properties of the system exhibit consistent behavior across different scales, a hallmark of turbulent flows The assumption of zero fluxes at the boundaries of velocity and temperature spaces, while simplifying the analysis, requires further investigation under more complex scenarios. The findings of this chapter lay a solid basis for understanding the complex interplay between particle-laden turbulent flows and thermal mixing dynamics. Future research could explore the impact of inter-particle collisions, the development of advanced closure models for the unclosed terms in the pdf transport equation, and the extension of the analysis to more complex geometries and flow conditions.

In conclusion, this chapter has laid the groundwork for a kinetic-based approach to modeling non-isothermal particle-laden turbulent flows. By transitioning from a detailed, fine-grained description to a coarse-grained, ensemble-averaged framework, we have established a comprehensive set of tools for analyzing and predicting the behavior of our fluid-particle systems. The exploration of quadrant analysis and pdf visualization, combined with the principles of self-similarity and scaling, provides a deep understanding of the complex interactions at play. These findings set the stage for further investigations into specific applications and the development of advanced numerical methods for simulating particle-laden turbulent flows in various engineering and environmental contexts.

Chapter 5

Self-similarity analysis

5.1 Introduction

Understanding the interplay between fluid turbulent fields and suspended inertial particles is essential for a wide range of environmental and industrial applications. This complex, multi-scale process involves various phenomena and mechanisms such as particle clustering, caustics, thermal caustics, inertia and thermal inertia filtering, and particle feedback. Unlike the single-phase non-isothermal turbulent flows, there are various inter-phase and inter-scale mechanisms that influence the heat transfer process. Ongoing research continues to further our understanding of the complex fluid-particle thermal interactions not only by numerical and experimental analyses, but also by developing novel theoretical methods. For instance, Saito et al. in [87] derived an analytical prediction for modulation of fluid temperature fluctuations by particles employing a Langevin model for fluid temperature fluctuations along the Lagrangian path of each individual particle . One of the powerful theoretical tools, which has been utilized in studying complex physical problems, is self-similarity analysis. Self-similarity analysis has long been a powerful tool in fluid dynamics and other scientific disciplines, offering a means to simplify and analyze complex phenomena by identifying invariant scaling laws. This chapter also plans to utilize a self-similarity analysis on the heat transfer within non-isothermal particle-laden turbulent flows. Therefore, in this analysis, we employ the insights gained from DNS presented in chapter 3 combined with particle field-like equations derived in chapter 4 from kinetic method. As observed and discussed in chapter 3 DNS results

revealed the formation of a time-evolving thermal mixing layer at the interface between two homothermal regions with different temperatures. As observed, this mixing layer thickness, δ, as defied in chapter 3, grows self-similarly with a scaling of $t^{1/2}$, providing a clear indication of the underlying evolution of thermal process within the flow domain. The observation of self-similar behavior in the mixing layer prompts a theoretical exploration to capture the thermal mixing dynamics in a more rigorous framework.

Accordingly, we will perform the self-similarity analysis both in integral and differential forms, on the fluid and particle mean temperature fields to explore the reason behind the observed self-similar behaviour of mixing considering the role of inertial particles. However, we have performed a wide range of different simulation to quantify the impact of particles on thermal mixing, here, we only consider use the data associated with a specific set of simulation to validate our theoretical analysis. In particular, we use the data obtained from the simulation at a single Taylor microscale Reynolds number equal to 56, when the inter-particle collisions are neglected and the ratio between the particle Stokes number to Stokes number is constant and equal to 4.43. Self-similarity provides a robust framework for better understanding the thermal interactions between particles and the fluid and their global effects on the thermal process. This analysis will not only validate the numerical observations but also contribute to a deeper theoretical understanding of the thermal mixing dynamics in such complex systems. By identifying self-similar structures and scaling laws, we can gain valuable insights into the fundamental mechanisms governing heat transfer, particle dynamical and thermal behaviors and their contribution to the mixing. Self-similar solutions allow not only for a simplifying framework for analyzing complex phenomena, but also to identify universal behaviors and study the scaling properties of a system, facilitating the development of general models and insights that can be applied across a wide range of scales.

Conceptually, this approach simplifies the study of transient and evolving systems, like our thermal mixing, by identifying scaling laws that remain invariant as the system evolves. It provides insights into the fundamental mechanisms driving the dynamics of turbulent flows and heat transfer, which are often obscured by the complexity of the inter-phase and inter-scale interactions involved. In the context of turbulent boundary layers, self-similarity has been instrumental in analyzing how velocity and temperature profiles develop and evolve. For instance, in boundary layer theory, self-similar solutions describe the scaling behavior of temperature and

velocity fields as the flow transitions from a laminar to a turbulent state. This is crucial for applications such as aerodynamic design, where understanding the growth and behavior of boundary layers directly impacts performance and efficiency. Similarly, in aerodynamic applications, self-similarity helps in understanding the transient behavior of flows over solid surfaces. For example, in unsteady aerodynamics, where the flow conditions change with time, self-similarity provides a framework to analyze how the flow adjusts and how heat transfer is influenced by evolving thermal fields. This is particularly important in scenarios such as aircraft takeoff and landing, where the aerodynamic and thermal conditions are transient and evolving. In our study, we apply self-similar analysis to a non-isothermal particle-laden turbulent flow, where the fluid temperature field is evolving and interacting with suspended inertial particles. The observed self-similar growth of the mixing layer thickness, characterized by a $t^{1/2}$ scaling, underscores the importance of self-similarity in understanding the dynamics of thermal mixing in such systems. This analysis allows us to capture how the thermal interactions between particles and the fluid lead to significant changes in the heat transfer characteristics over time with respect to the unseeded flow. Additionally, by leveraging self-similarity, theoretical models we can gain more insights into the role of thermal feedback from particles influences the overall heat transfer process.

By applying this approach to non-isothermal particle-laden turbulent flows, we gain a comprehensive understanding of the thermal interactions and their impact on heat transfer, contributing to both theoretical and practical advancements in the field. We show how in an unseeded turbulent flow without, temperature evolution can exhibit perfect self-similar behavior, meaning that the temperature profiles and mixing layers thickness grow in a predictable, scale-invariant manner. This self-similarity arises from the consistent scaling laws governing turbulent mixing and heat transfer. However, when particles are introduced, the system's behavior can deviate from perfect self-similarity. Particles introduce additional scales of time and length through their inertia and thermal inertia, which can lead to deviations from the ideal self-similar scaling. Specifically, the interaction between particles and the time evolving temperature field can result in quasi-self-similar behavior. This quasi-self-similar evolution is formulated by using the standard self-similarity analysis and Taylor expansion to capture the effect of particle thermal inertia which scales with τ_ϑ/t.

Furthermore, we use the integral form analysis based on the concept of moment integral in unsteady boundary layer flows. In boundary layer flows, first-moment integral equations are instrumental in deriving and understanding the mean profiles of velocity and temperature [103]. To quantify how suspended particles globally affect heat transfer throughout the entire flow domain, we introduce a new method called the Total Enthalpy Integral (TEI). This approach provides a comprehensive measure of heat transport by integrating the total enthalpy equation over space, capturing contributions from diffusion, convection, and particle thermal contents. The TEI has been effectively used in studying other turbulent flows, e.g. in [103], offering a precise way to measure how particles enhance global thermal mixing compared to turbulent flows without particles. This method enhances our understanding of how particles influence thermal mixing, which helps improve predictions for turbulent flows containing inertial particles in various applications.

The theory is confirmed by comparison with the statistics obtained from DNS. In the section 5.2 the self-similarity analysis for particle and fluid mean temperature fields in differential form is presented and discussed. In this part, we begin by analyzing the transport equations for the mean particle and fluid temperatures. We find that during the intermediate stage of the evolution of thermal mixing layer thickness, a quasi-self-similar solution can be achieved. This is characterized by particle thermal Stokes number, which influences how the solution approaches a self-similar form over time. Non-self-similar terms diminish as time progresses using the Taylor expansion around the τ_ϑ/t. In the section 5.3 the integral form of the mean temperature equations is provided and under the same assumptions, the self-similar analysis is provided. Subsequently, in section 5.4, similar analysis by introducing Total Enthalpy Integral (TEI) deduced from the self-similar behavior of pdf of inertial particle in phase-space which has been presented in the chapter 4 for two-way coupling regime is discussed. Finally, all the theoretical works are validated by the results of DNS for different flow conditions in 5.5.

5.2 Differential form

In this section, we're going to perform a self-similarity analysis for the particle and fluid mean temperature transport equations, considering cases where the two phases are either one-way or two-way thermally coupled. Essentially, this means we're

looking at how the unsteady fluid mean temperature evolution is influenced by the particles. Moreover, the same analysis is done on the particle mean temperature which is derived from kinetic method in chapter 4. In a general sense, when both one- and two-way thermal coupling regimes are considered, the fluid mean temperature field includes a source term that represents the thermal feedback from the particles on the fluid. We begin the differential form analysis with mean fluid temperature field in the most generic form, i.e. two-way thermal coupling regime, then the same will be conducted on the particle mean temperature field. To carry out our self-similarity analysis on the fluid mean temperature field, a self-similar ansatz solution for the partial differential equation (PDE) that governs the evolution for the fluid mean temperature must be introduced first. The ansatz is essentially a hypothesized form of the solution, often involving a combination of variables that reduces the number of independent variables in the PDE. This simplification can help identify self-similar solutions, which are solutions where the shape of the solution profile remains similar over time, even as the scale changes. Applying a self-similar ansatz to the fluid mean temperature field allows one to reduce the PDE to an ordinary differential equation (ODE) or a simpler PDE, which is easier to analyze. Therefore, such ansatz solution for the fluid mean temperature equation can be defined by

$$\langle T \rangle (t,x) = t^{-\alpha} f(\eta). \tag{5.1}$$

In this analysis, we're using the similarity variable $\eta = x/t^{\beta}$, where t^{α} and t^{β} are the time scaling factors, and α and β are the exponents derived from how the temperature fields evolve in our flow setup. The goal here is to understand how inertial particles affect heat transfer. Since there's no mean velocity field in our flow regime, the mean convection in the mean fluid temperature equation vanishes. As a result, the ansatz solution we've chosen is the most appropriate because it aligns well with the nature of our partial differential equation, which is similar to the simple unsteady heat conduction equation. However, unlike the basic static thermal diffusion equation, our situation involves two additional terms in the fluid mean temperature equation: the particle feedback term and the turbulent convective heat flux. These extra terms introduce significant complexity, making our problem more complex than a straightforward diffusion scenario under static conditions. From our simulation results, we have noticed that the physically relevant length scale, $\delta(t)$ which represents the time growing thickness of the mixing layer in the central zone—scales with $t^{1/2}$ over time. This scaling holds when we normalize it with the

large-scale flow, specifically the turbulent integral scale $\ell = u'/\tau$, as we discussed in Chapter 3. This finding justifies defining the similarity variable as $\eta = x/\delta(t)$, where $\delta(t) = 2\sqrt{\kappa t}$. Consequently, the self-similarity ansatz solution for our case can be formulated as follows

$$\langle T\rangle(t,x) = \delta(t)\phi_f(\eta), \tag{5.2}$$

where $\phi_f(\eta)$ is the dimensionless trial or shape function of the fluid mean temperature field. This function is assumed to have continuous first and second derivatives, be integrable, and meet the necessary boundary conditions. Given the definition of the self-similarity variable η and the time scaling factor, which corresponds to the mixing layer thickness $\delta(t)$, we find that the exponents in the ansatz solution are $\alpha = -\beta = -1/2$. With these exponents, the ansatz solution for the fluid mean temperature can be expressed as:

$$\langle T\rangle(t,x) = 2\sqrt{\kappa}t^{1/2} f(\frac{x}{2\sqrt{\kappa}t^{1/2}}). \tag{5.3}$$

This formulation highlights how the fluid mean temperature field as a dynamical variable evolves over time and space, where the factor $t^{-\frac{1}{2}}$ accounts for the time-dependent scaling, and the shape function $\phi_f(\eta)$ describes the spatial distribution in the self-similar form. This approach allows us to capture the key dynamics of the system, considering the physical complexity introduced by particle feedback and turbulent heat flux. In its most generic form, accounting for the two-way coupling regime, the original fluid mean temperature equation can be expressed as:

$$\frac{\partial\langle T\rangle}{\partial t} = \kappa\frac{\partial^2\langle T\rangle}{\partial x^2} - \frac{\partial\langle uT\rangle}{\partial x} + \frac{1}{\rho_0 c_{p0}}\langle C_T\rangle, \tag{5.4}$$

where the mean particle thermal back-reaction effect $\langle C_T\rangle$ on the fluid mean temperature is derived as

$$\begin{aligned}\langle C_T\rangle &= \frac{4}{3}\pi R^3\rho_p c_{pp}\sum_{p=1}^{N_p}\langle\frac{T-\vartheta}{\tau_\vartheta}\delta(\boldsymbol{x}-\boldsymbol{X}_p)\rangle \\ &= \frac{4}{3}\pi R^3\rho_p c_{pp}\frac{\langle T\rangle_p - \langle\vartheta\rangle}{\tau_\vartheta}\frac{N_p}{\mathscr{V}} \\ &= \varphi\rho_p c_{pp}\frac{\langle T\rangle_p - \langle\vartheta\rangle}{\tau_\vartheta}.\end{aligned} \tag{5.5}$$

The equation (5.5) indicates how the particles thermal back-reaction influences the fluid mean temperature field, integrating the effects of particle heating and cooling within the fluid flow. By substituting this feedback term $\langle C_T \rangle$ into the equation (5.4), and by using the definition of the thermal mass fraction or particle heat capacity ratio $\varphi_\vartheta = \varphi \rho_p c_{pp} / \rho_0 c_{p0}$, the fluid mean equation is rewritten as

$$\frac{\partial \langle T \rangle}{\partial t} = \kappa \frac{\partial^2 \langle T \rangle}{\partial x^2} - \frac{\partial \langle uT \rangle}{\partial x} - \varphi_\vartheta \frac{\langle T \rangle - \langle \vartheta \rangle}{\tau_\vartheta}. \tag{5.6}$$

The thermal mass fraction φ_ϑ, is a crucial parameter in analyzing heat transfer in multiphase flows, especially when particles are involved. It represents the ratio of the heat capacity of the dispersed phase (particles) to the heat capacity of the continuous phase (fluid). The parameter serves as a heat transfer enhancement factor in fluid-particle systems. Its role is twofold, heat storage capacity and thermal feedback mechanism. Generally, a higher φ_ϑ indicates that the particles have a greater ability to store heat compared to the fluid. This can lead to more efficient energy exchange between the particles and the fluid, especially in systems where rapid thermal equilibration is needed. As the particles absorb or release heat, they can significantly alter the temperature distribution within the fluid, enhancing the overall heat transfer process. On the other hand, as it can be seen in the equation (5.4), the source term due to the particle thermal feedback $(\varphi_\vartheta / \tau_\vartheta)[T - \vartheta]$ quantifies the impact of the particles on the fluid mean temperature. Accordingly, a higher φ_ϑ means that the particles have a more pronounced effect on the fluid mean temperature, either accelerating heating or cooling processes depending on the temperature difference and their range of inertia and thermal inertia. Note that there is a trade-off between the effects of the thermal mass fraction φ_ϑ on overall heat transfer. While a higher φ_ϑ can enhance overall heat transfer by increasing the thermal capacity of the system, it can also lead to increased thermal inertia, which might reduce the overall effectiveness of heat transfer under certain conditions. This creates a complex balance where an optimum value of φ_ϑ maximizes the overall heat transfer efficiency. The thermal mass fraction φ_ϑ is a key parameter for enhancing heat transfer, but it must be optimized to avoid the drawbacks of increased thermal inertia. The existence of an optimum φ_ϑ value highlights the importance of balancing heat capacity and thermal responsiveness to achieve the best overall heat transfer performance in multiphase systems. In our case study, this value is equal to 1.664, and we have observed an enhancement in overall heat transfer between two homothermal regions, for all set of simulations as

presented in chapter 3. Based on our investigation, we could expect a reduction in global heat transfer for very dense regime, in which $\varphi_\vartheta \gg 1$. From the definition of this parameter we know that, it can change through the alternation in particle volume fraction, heat capacity ratio and density ratio. In our study we density ratio and volume fraction have been fixed while the variation over the heat capacity have been observed. Based on our observation, the optimum value is for intermediate particle inertia and thermal inertia where the local heat transfer is high due to the enhanced and steeper temperature gradients and intermediate particle thermal response time which does not disrupt the heat transfer.

On the other hand, for particulate phase, the mean temperature field equation is given by

$$\frac{\partial\langle\vartheta\rangle}{\partial t}+\frac{\partial\langle v\vartheta\rangle}{\partial x}=\frac{1}{\tau_\vartheta}[\langle T\rangle-\langle\vartheta\rangle]. \tag{5.7}$$

To find the self-similar solution for our physical problem, specifically the mean temperature fields, we need to substitute the ansatz solution (5.2) into the fluid mean temperature equation (5.4) and particle mean temperature equation (5.7). Given the presence of derivatives in the original partial differential equation, all terms are expected to acquire a time-dependent factor in terms of α or β, or in terms of our defined time scaling variable $\delta(t)$ and self-similar variable η. Therefore, we anticipate that in the reduced-order equation, an ordinary differential equation in these variables and non-dimensional shape functions, all time-dependent exponents should cancel out, ensuring proper self-similar evolution. From a phenomenological perspective, we know that the proper self-similar evolution applies to the fluid mean temperature field in the one-way coupling scenario. However, in the two-way coupling regime, and in the particle mean temperature equation, self-similarity cannot be assumed a priori. In these cases, numerical observations and the behavior of the probability density function (pdf) in phase space, as discussed in Chapters 3 and 4, guide us towards a quasi-self-similarity analysis. It is evident that non-self-similar terms in the fluid mean temperature equation in two-way coupling regime arise from the presence of thermal feedback of inertial particles. Particles influence the main partial differential equation (5.6) through the particle thermal feedback term in two-way coupling, where $\varphi_\vartheta \neq 0$. We begin our differential self-similar analysis with the simplest case, which is fluid mean temperature equation in the

one-way coupling regime. In this case, $\varphi_\vartheta = 0$, and DNS results indicate that the ansatz solution should satisfy equation (5.6), with the mean temperature evolving in a proper self-similar manner. The mean temperature and turbulent flux in equation (5.6) can be non-dimensionalized by introducing dimensionless shape functions $\phi(\eta)$ and mean flux $\psi(eta)$ to ensure that the boundary conditions are satisfied. By definition, the dimensionless mean temperature $\phi(\eta)$ and the dimensionless mean flux $\psi(\eta)$ are functions of the dimensionless length scale, which is our self-similar variable η. These dimensionless shape functions are expressed in a generic form as follows

$$\langle T\rangle(t,x) = \frac{T_1+T_2}{2} - \frac{T_2-T_1}{2}\delta^0\phi_f(\eta), \tag{5.8}$$

$$\langle uT\rangle(t,x) = \kappa\frac{T1-T_2}{2}\delta^{\gamma_1}\psi_f(\eta). \tag{5.9}$$

Obviously, $\delta^0 = 1$ as it should be, due to satisfying the boundary conditions of the mean temperature field as $x \to \pm\infty$, which implies $\eta \to \pm\infty$. This is also consistent with dimensional analysis, which makes ϕ_f dimensionless. Regarding γ_1, when equation (5.9) is written in this form, γ_1 must be -1 based on dimensional considerations, provided that $\psi_f$is dimensionless, which it should be, as it represents the flux divided by its reference scale. The static diffusive scale of the flux is given by $\kappa\Delta T/\delta$, whereas a turbulent scale would be $u'\Delta T$, where u' is the root mean square (rms) of the velocity fluctuations. An even more refined scale would be $u'(\Delta T/\delta)\ell$, where ℓ is the integral scale. Here, $\Delta T/\delta$ represents the mean temperature gradient in the center of the domain, so $(\Delta T/\delta)\ell$ represents the temperature difference encountered and transported by large-scale turbulent eddies across the thermal mixing layer. All these scales are valid; they merely affect the coefficients in the resulting equations. Since velocity is statistically steady, u' and ℓ are constants, so the primary difference lies in whether the Peclet number is present in the equation. It is absent if the diffusive scale is used, but it appears in the last choice. When using the diffusive scale, the Nusselt number is simply given by ϕ_f without additional coefficients. We will continue our differential self-similar analysis using the diffusive scale.

We can now utilize the definitions of the dimensionless shape functions $\phi(\eta)$ and $\psi(\eta)$, and incorporate these ansatz solutions into the partial differential equation governing the fluid mean temperature field in the one-way coupling regime. In fact, by substituting these ansatz solutions into the original partial differential equation, we

transform it into a reduced ordinary differential equation expressed only in terms of η. From the boundary conditions, we know that $\phi_f(-\infty)$=1, $\phi_f(\infty)$=-1, and $\psi_f(\pm\infty) = 0$. The time and spatial derivatives in the original partial differential equation introduce terms involving the time scaling factor δ and the self-similar variable η. Self-similarity requires that all exponents of δ cancel each other out, resulting in a reduced equation that depends only on η and contains no time-dependent terms. This condition ensures that full self-similarity of the evolution is achieved. The time and space derivatives can be transformed into the reduced equation using the following relations

$$\frac{\partial \eta}{\partial t} = -\frac{x}{\delta^2}\delta' = -\eta\frac{\delta'}{\delta}, \tag{5.10}$$

$$\frac{\partial \eta}{\partial x} = \frac{1}{\delta}, \tag{5.11}$$

where $\delta' = \mathrm{d}\delta(t)/\mathrm{d}t$. Employing these transformation, and introducing all terms leads to the following reduced equation

$$\frac{T_2 - T_1}{2}\frac{\delta'}{\delta}\eta\phi_f'(\eta) = -\frac{T_2 - T_1}{2}\frac{\kappa}{\delta^2}\phi_f''(\eta) + \frac{T_2 - T_1}{2}\kappa\delta^{\gamma_1 - 1}\psi_f'(\eta), \tag{5.12}$$

where the sign $'$ in shape functions indicates the derivative with respect to η. Since $\delta'/\delta \propto 2\kappa/\delta^2$ the reduced equation can be rewritten as

$$2\eta\phi_f'(\eta)\delta^{-2} + \phi_f''(\eta)\delta^{-2} = \delta^{\gamma_1 - 1}\psi_f'(\eta). \tag{5.13}$$

To achieve a self-similar solution, the exponents must be consistent. Consequently, $\gamma_1 = -1$. This result is consistent with our earlier dimensional analysis, which indicated that $\gamma_1 = -1$ is necessary for the shape function of the flux in equation (5.9) to remain dimensionless. The reduced ordinary differential equation (5.13) enables us to express the convective heat flux as a function of the fluid mean temperature as

$$\psi_f'(\eta) = 2\eta\phi_f'(\eta) + \phi_f''(\eta). \tag{5.14}$$

Note that equation (5.14) is invariant under the transformation $\eta \to -\eta$, $\varphi_f \to -\varphi_f$, $\psi_f \to \psi_f$, so that φ_f is an odd function of η and ψ_f is an even function. The unknown value of $\psi_f(0)$ determines the convective heat flux between the two regions and,

thus, the convective Nusselt number of the flow, which, by using the definition in 3, can be expressed in terms of self-similar variables as $\mathrm{Nu}_c = \psi_f(0)/\left|\varphi_f'(0)\right|$.

As previously explained, the mean temperature equation for the particle phase, given by equation (5.7), cannot achieve proper self-similarity due to its inherent nature. Specifically, it lacks the diffusive term present in the fluid equation and includes a convection term from the fluid flow. These non-self-similar terms prevent us from deriving a reduced equation purely in terms of the self-similar variable η and eliminating all time-dependent terms. However, a similar analysis can still be performed, leading to a quasi self-similar solution for sufficiently large times, far from the initial conditions. To develop this quasi self-similar analysis, we express the self-similar ansatz solution as a Taylor expansion around the zeroth term, which is a function of η and corresponds to the fluid mean temperature solution in the one-way coupling case. As with the fluid analysis, we define the particle dimensionless mean temperature and heat flux in such a way that boundary conditions are satisfied. The same diffusive scale used for the fluid is applied here to define these functions, though they remain time-dependent unlike those in the one-way coupling fluid case. The particle dimensionless shape functions are given by

$$\langle\vartheta\rangle(t,x) = \frac{T_1+T_2}{2} - \frac{T_2-T_1}{2}\phi_p(t,\eta), \tag{5.15}$$

$$\langle v\vartheta\rangle(t,x) = \kappa\frac{T1-T_2}{2}\delta^{-1}\psi_p(t,\eta) \tag{5.16}$$

After introducing the particle dimensionless shape functions in the particle mean temperature equation, we have

$$\begin{aligned} &-\frac{T_2-T_1}{2}\left[\frac{\partial\phi_p(t,\eta)}{\partial t} - \frac{\delta'}{\delta}\eta\phi_p'(t,\eta)\right] = \frac{T_2-T_1}{2}\kappa\delta^{-1}\psi_p'(t,\eta) \\ &-\frac{T_2-T_1}{2}\frac{1}{\tau_\vartheta}[\phi_f(\eta)-\phi_p(t,\eta)]. \end{aligned} \tag{5.17}$$

The final form of the reduced mean particle temperature equation has the following form

$$\frac{\partial\phi_p(t,\eta)}{\partial t} + \frac{1}{4t}[-2\eta\phi_p'(t,\eta)+\psi_p'(t,\eta)] = \frac{1}{\tau_\vartheta}[\phi_f(\eta)-\phi_p(t,\eta)]. \tag{5.18}$$

Equation (5.18) allows us to determine the particle heat flux as a function of the particle mean temperature, which, in turn, depends on the carrier flow temperature.

In the tracer limit, where particle inertia vanishes $\tau_\vartheta \to 0^+$, the particle mean temperature matches the fluid mean temperature at the same position x and time t. Therefore, $\varphi_p(t,\eta) = \varphi_f(\eta)$, and the particle velocity-temperature correlation, as given by (5.18), becomes $\psi_p'(t,\eta) = 2\eta\varphi_f'(\eta)$. In this limit, the ratio between the particle and fluid velocity-temperature correlations is

$$\frac{\langle v\vartheta\rangle}{\langle uT\rangle} = \frac{\psi_p}{\psi_f} = \left[1 + \frac{1}{2}\phi_f'(\eta)/\int_{-\infty}^{\eta} s\phi_f'(s)\mathrm{d}s\right]^{-1}. \tag{5.19}$$

This equation shows how the particle heat flux compares to the fluid heat flux, adjusted for the fluid mean temperature gradient. As the temperature distribution changes, this ratio adjusts to reflect how the particle flux is influenced by the fluid mean temperature gradient. The correction factor $(1/2)\phi_f'(\eta)/\int_{-\infty}^{\eta} s\phi_f'(s)\mathrm{d}s$ accounts for the influence of the local gradient relative to the cumulative effect over the region of interest. As the Reynolds number increases, the difference between the particle and fluid velocity-temperature correlations diminishes. This is because the difference arises primarily from the diffusive term, which becomes less significant at higher Reynolds numbers. With finite particle inertia ($\tau_\vartheta > 0$) , there is a lag between the temperature of the carrier flow and the particle temperature, proportional to τ_ϑ. As time progresses, the characteristic timescale of the process, $\delta/\delta' \propto t$, increases. Consequently, the ratio τ_ϑ/t becomes smaller, reducing the influence of particle thermal inertia on particle thermal dynamics. Therefore, to analyze the particle dynamics in the quasi-steady regime, we can expand φ_p and ψ_p in a power series of τ_ϑ/t. Alternatively, we can express the particle shape functions using a Taylor expansion in terms of the inverse of time $(1/t)$, as follows

$$\phi_p(t,\eta) = \sum_{k=0}^{\infty} (t/\tau_\vartheta)^{-k}\varphi_k(\eta) = \phi_0(\eta) + (t/\tau_\vartheta)^{-1}\phi_1(\eta) + (t/\tau_\vartheta)^{-2}\phi_2(\eta) + \ldots, \tag{5.20}$$

$$\psi_p(t,\eta) = \sum_{k=0}^{\infty} (t/\tau_\vartheta)^{-k}\psi_k(\eta) = \psi_0(\eta) + (t/\tau_\vartheta)^{-1}\psi_1(\eta) + (t/\tau_\vartheta)^{-2}\psi_2(\eta) + \ldots, \tag{5.21}$$

where $\phi_0(\eta)$ and $\psi_0(\eta)$ denote the quasi-steady components, corresponding to the self-similar solution in the limit of $\tau_\vartheta \to 0^+$. The higher-order terms, $\phi_1(\eta)$ and $\psi_1(\eta)$, and so on, capture the deviations from the self-similar behavior due to the finite inertia. By introducing these expansions into (5.18) and by equating to zero

the coefficients of all powers of t one obtains the following equations,

$$\phi_0 - \phi_f = 0, \tag{5.22}$$

$$\frac{1}{2}\left(\psi_0' - 2\eta\phi_0'\right) = -\phi_1, \tag{5.23}$$

$$-(k-1)\phi_k + \frac{1}{2}\left(\psi_k' - 2\eta\phi_k'\right) = -\tau_\vartheta^{k-1}\varphi_{k+1} \quad \forall k \geq 1. \tag{5.24}$$

The zeroth order term equation (5.22) ensures that the leading term in the expansion of the particle mean temperature ϕ_p matches the fluid mean temperature ϕ_f in the limit of $\tau_\vartheta \to 0^+$. The first order term equation (5.23) elates the first-order correction in the expansion of ϕ_p to the first-order correction in ψ_p. It accounts for the deviations from the self-similar solution due to finite inertia. The higher order term equations (5.24) describe the relationship between the higher-order terms in the expansions of ϕ_p and ψ_p. Each term ϕ_k and ψ_k is influenced by the previous order terms and by the parameter τ_ϑ capturing the time-dependent corrections due to finite particle thermal inertia. This set of equations provides a framework for determining the non-self-similar components of the heat flux based on the deviations in the mean temperature distribution. However, since the system described by these equations is not fully closed, a complete solution cannot be obtained without introducing a parametrization for the velocity-temperature correlations. To resolve this, it is essential to introduce a parametrization that is consistent with both the reduced mean temperature equation (5.14) and the set of equations (5.22)-(5.24). This approach ensures that the additional terms introduced by the parametrization align with the existing equations and maintain the overall consistency of the model. An illustrative example of this approach is found in the work of Chamecki et al. in [104] where they employed a gradient-based parametrization to address the non-self-similar components of the particle concentration. By doing so, they were able to derive an analytical solution for the particle concentration in a self-similar form. This method effectively dealt with the additional complexities introduced by finite inertia and enabled a comprehensive analytical treatment of the problem. Thus, to apply a similar methodology in this context, one must develop a suitable parametrization for the velocity-temperature correlations that is consistent with the governing equations and the derived equations for the particle temperature and flux. This will allow for a closed system and facilitate the analytical or numerical solution of the problem.

We have derived the self-similar solution for the fluid mean temperature field in one-way thermal coupling regime ($\varphi_\vartheta = 0$) and the quasi-self-similar solution for the particle mean temperature field using a Taylor expansion in terms of the inverse time. Next, we will extend our analysis to the two-way thermal coupling regime ($\varphi_\vartheta \neq 0$), where both fields, the fluid and particle mean temperature fields, exhibit non-self-similar terms due to the influence of particles thermal inertia and their thermal feedback. In this case, the shape functions become time-dependent and can be represented as follows

$$\langle T \rangle(t,x) = \frac{T_1+T_2}{2} - \frac{T_2-T_1}{2}\phi_f(t,\eta), \tag{5.25}$$

$$\langle uT \rangle(t,x) = \kappa\frac{T_1-T_2}{2}\delta^{-1}\psi_f(t,\eta), \tag{5.26}$$

$$\langle \vartheta \rangle(t,x) = \frac{T_1+T_2}{2} - \frac{T_2-T_1}{2}\phi_p(t,\eta), \tag{5.27}$$

$$\langle v\vartheta \rangle(t,x) = \kappa\frac{T_1-T_2}{2}\delta^{-1}\psi_p(t,\eta). \tag{5.28}$$

In this case, we can substitute the dimensionless shape functions into the mean fluid temperature equation (5.6). After eliminating the temperature term, the equation simplifies to

$$\frac{\partial\phi_f(t,\eta)}{\partial t} - \frac{\delta'(t)}{\delta(t)}\eta\phi_f'(t,\eta) + \frac{\kappa}{\delta^2(t)}\psi_f'(t,\eta) = \frac{\kappa}{\delta^2(t)}\phi_f''(t,\eta) - \frac{\phi_\vartheta}{\tau_\vartheta}\left(\varphi_f(t,\eta) - \phi_p(t,\eta),\right) \tag{5.29}$$

and by using the scaling relation $\delta(t) = 2\sqrt{\kappa t}$, the reduced equation for fluid mean temperature in the two-way thermal coupling regime is

$$\frac{\partial\phi_f(t,\eta)}{\partial t} + \frac{1}{4t}\left(-2\eta\phi_f'(t,\eta) + \psi_f'(t,\eta) - \phi_f''(t,\eta)\right) = -\frac{1}{\tau_\vartheta}\left(\phi_f(t,\eta) - \phi_p(t,\eta)\right). \tag{5.30}$$

The dimensionless particle mean temperature equation for the two-way thermal coupling regime, expressed in terms of the introduced shape functions, takes the same form as the particle equation in the one-way coupling regime, as shown in Equation (5.18). At this stage, we can apply a similar expansion in inverse powers of t as was done for the quasi-self-similarity analysis of the particle mean temperature field in the one-way coupling regime. This allows us to expand all shape functions

in a series of inverse powers of time. Specifically, we can write

$$\phi_f(t,\eta) = \Phi_0(\eta) + \frac{\tau_\vartheta}{t}\Phi_1(\eta) + \left(\frac{\tau_\vartheta}{t}\right)^2 \Phi_2(\eta) + \ldots, \tag{5.31}$$

$$\psi_f(t,\eta) = \Psi_0(\eta) + \frac{\tau_\vartheta}{t}\Psi_1(\eta) + \left(\frac{\tau_\vartheta}{t}\right)^2 \Psi_2(\eta) + \ldots, \tag{5.32}$$

$$\phi_p(t,\eta) = \phi_0(\eta) + \frac{\tau_\vartheta}{t}\phi_1(\eta) + \left(\frac{\tau_\vartheta}{t}\right)^2 \phi_2(\eta) + \ldots, \tag{5.33}$$

$$\psi_p(t,\eta) = \psi_0(\eta) + \frac{\tau_\vartheta}{t}\psi_1(\eta) + \left(\frac{\tau_\vartheta}{t}\right)^2 \psi_2(\eta) + \ldots. \tag{5.34}$$

Substituting these expansions into Equation (5.30) and equating the coefficients of the powers of t^{-1}, we obtain equations for the various functions of η. The coefficient of t^0 yields

$$\Phi_0(\eta) - \phi_0(\eta) = 0. \tag{5.35}$$

At order t^{-1} from the two equations (using previous one) we get

$$-2\eta\Phi_0'(\eta) + \Psi_0'(\eta) - \Phi_0''(\eta) = -\varphi_\vartheta(\Phi_1(\eta) - \phi_1(\eta)) \tag{5.36}$$

and

$$-2\eta\Phi_0'(\eta) + \psi_0'(\eta) = \Phi_1(\eta) - \phi_1(\eta), \tag{5.37}$$

and so on for higher powers of t^{-1}. These equations show that at this order, we have two equations but four unknown functions, Φ_0, ϕ_0, Φ_1, and ϕ_1. This suggests that we can only determine two of the fluxes as functions of the temperatures. The complication arises because the fluxes with index 0 depend not only on temperatures with index 0 but also on temperatures with index 1 which makes the situation more complex compared to the one-way coupling case. To simplify the analysis, we subtract the two equations to isolate $(\Phi_1(\eta) - \phi_1(\eta))$. The correct subtraction is:

$$\Psi_0'(\eta) - \psi_0'(\eta) = \Phi_0''(\eta) - (1 + \varphi_\vartheta)(\Phi_1(\eta) - \phi_1(\eta)) \tag{5.38}$$

This subtraction helps isolate the contributions of $\Phi_1(\eta) - \phi_1(\eta)$ and provides a clearer view of how the fluxes are related to the temperatures at different orders,

which can be integrated in $(-\infty, \eta)$ (note that $\Phi_k(\pm\infty) = \psi_k(\pm\infty) = 0$) to give

$$\Psi_0 - \psi_0 = \Phi_0' - (1+\varphi_\vartheta)\int_{-\infty}^{\eta}(\Phi_1(s) - \phi_1(s))\mathrm{d}s. \tag{5.39}$$

This result shows how the difference in fluxes, $\Psi_0(\eta) - \psi_0(\eta)$, is related to the first derivatives of the temperature profiles and the integral of the difference between Φ_1 and ϕ_1, scaled by $(1+\varphi_\vartheta)$. This integration approach helps in understanding how the fluxes are adjusted by the non-self-similar parts of the temperature profiles. Dividing both sides of the equation (5.39) by $Psi_0(\eta)$, we obtain

$$\frac{\psi_0}{\Psi_0} = 1 - \frac{\Phi_0'}{\Psi_0} + \frac{1+\varphi_\vartheta}{\Psi_0}\int_{-\infty}^{\eta}(\Phi_1(s) - \phi_1(s))\mathrm{d}s. \tag{5.40}$$

This equation expresses the ratio of the particle heat flux ψ_0 to the fluid heat flux Ψ_0. The right-hand side of the equation shows how this ratio is adjusted by the derivative of the fluid mean temperature profile Φ_0' and an integral term that accounts for the difference between the non-self-similar parts of the temperature profiles Φ_1' and ϕ_1'. This helps in understanding how the fluxes are related and how deviations from self-similarity impact the heat flux ratio. If $\Phi_0' < 0$, this implies that the particle flux ψ_0 will be higher than the fluid flux Ψ_0 in the leading order. This result is consistent with the physical expectation that a steeper temperature gradient in the particle phase compared to the fluid phase leads to a higher particle heat flux. Since in this case, the term $-\Phi_0'/\Psi_0$ in the equation will be positive, effectively making ψ_0/Ψ_0 greater than 1, provided that the integral term $(1+\varphi_\vartheta/\Psi_0)\int_{-\infty}^{\eta}(\Phi_1(s) - \phi_1(s))\mathrm{d}s$ does not completely offset this increase. Therefore, if $\Phi_0' < 0$, the leading-order term of the particle flux ψ_0 is indeed greater than the leading-order term of the fluid flux Ψ_0, as ψ_0/Ψ_0 will be higher than 1. The negative value of $\Phi_0' < 0$ indicates the decrease in temperature with the spatial variable η, which is consistent with the physical behavior of mixing processes between two homothermal regions. Specifically, in our case, the fluid mean temperature gradient Φ_0' is maximum at the center of the flow domain, where the mixing layer is located. This gradient signifies the region where the temperature transitions most sharply, reflecting the active mixing between the two regions.

Meanwhile, summing equations (5.36) and (5.37) (with the latter multiplied by φ_ϑ), we can obtain an equation which represents the total enthalpy of the whole fluid-particle system in terms of the proper self-similar quantities indexed by 0. Such

total enthalpy of the system is derived as

$$-2(1+\varphi_\vartheta)\eta\Phi_0' + (\Psi_0' + \varphi_\vartheta\psi_0') = \Phi_0'' \tag{5.41}$$

which can allow to have particle heat flux ψ_0 as a function of fluid only quantities with index "0". We can also rewrite the equation as

$$\psi_0' = \frac{1}{\varphi_\vartheta}(\Phi_0'' - \Psi_0') + 2\frac{1+\varphi_\vartheta}{\varphi_\vartheta}\eta\Phi_0' \tag{5.42}$$

In other words, by adding the two flux-related equations, we isolate ψ_0' in terms of the fluid mean temperature and its first and second spatial derivatives, representing the convective and diffusive terms respectively. This equation also highlights that the particle heat flux is influenced by the mean temperature and its spatial derivatives, and it involves term related to fluid heat flux gradient Ψ_0'. This derivation is specific to the two-way thermal coupling regime. It shows that the non-self-similar term, due to the particles thermal feedback are canceled out by summing up process. By setting $\varphi_\vartheta \to 0^+$ in total enthalpy equation (5.41), we can also recover the one-way coupling self-similar equation as derived before for fluid mean temperature in equation (5.14). Since , Φ, Ψ, and all other variables depend on the parameter φ_ϑ and ultimately, the difference between the fluid and particle quantities in the total enthalpy equation goes to zero, which mitigates the singularity issue in the equation (5.42). The ratio between particle and fluid heat fluxes gradient, can be obtained as

$$\begin{aligned}\frac{\psi_0'}{\Psi_0'} &= \frac{\Phi_0''}{\varphi_\vartheta\Psi_0'} - \frac{1}{\varphi_\vartheta} + \frac{2(1+\varphi_\vartheta)\eta\Phi_0'}{\varphi_\vartheta\Psi_0'} \\ &= \frac{\Phi_0'' - \Psi_0' + [2(1+\varphi_\vartheta)\eta\Phi_0']}{\varphi_\vartheta\Psi_0'}\end{aligned} \tag{5.43}$$

The first term represents the contribution of the second derivative of the fluid mean temperature Φ_0'' to the fluid flux. It indicates how the spatial variation of the fluid mean temperature affects the particle flux, normalized by φ_ϑ and the fluid flux Ψ_0'. This term becomes significant when there are substantial gradients in the fluid temperature field. Sice this term is associated by the thermal diffusivity, the particles can reduce with increase in φ_ϑ. The second term is the turbulent convective heat flux which indicates the turbulent contribution to the overall heat transfer in the mixing layer. This term shows how particles modify the turbulent convective through their thermal feedback and their impact on φ_ϑ. Indeed, for a very large φ_ϑ this term shows

that overall heat transfer can be attenuated by the effect of particles. The third term accounts for the influence of the fluid mean temperature gradient ϕ_0' and the spatial variable η on the particle flux. The factor $2(1+\varphi_\vartheta)$ modifies how changes in the fluid mean temperature gradient impact the relative particle-to-fluid heat flux. This term highlights how the overall heat flux is adjusted due to the interaction between the particle temperature difference and the fluid. By analyzing this ratio, we can better understand the impact of particles on the overall heat transfer. The parameter φ_ϑ, which represents the thermal mass fraction of particles, plays a crucial role in determining this impact. The term $\Phi_0''/\varphi_\vartheta\Psi_0'$ reflects how the second derivative of the fluid temperature profile influences the particle flux through thermal diffusion. When φ_ϑ is at an optimal value, the particles can enhance the overall thermal diffusion compared to an unseeded flow. This enhancement occurs because the particles heat capacity contributes to smoothing out temperature gradients, leading to more efficient heat transfer through diffusion. However, molecular thermal diffusion is less effective in particle laden flows but particles can significantly enhance the turbulent diffusion process through the interaction with mixing. The term $(2(1+\varphi_\vartheta)\eta\Phi_0')/\varphi_\vartheta\Psi_0'$ represents the effect of the fluid temperature gradient and spatial position on the particle flux via turbulent convection. As φ_ϑ increases, the contribution of particles to turbulent convection also increases, potentially enhancing the overall convective heat transfer. However, this effect is optimized at a certain value of φ_ϑ. However, it is important to note that if φ_ϑ becomes too large, the enhancement in heat transfer due to particles may diminish. In such cases, the presence of an excessive number of particles might hinder the natural turbulent mixing processes, leading to a reduction in the overall heat transfer efficiency compared to unseeded turbulent flows. This behavior underscores the importance of optimizing φ_ϑ to achieve maximal heat transfer benefits from particle seeding.

The equation (5.43) indicates that at optimum value of φ_ϑ, the predominant terms in the particle heat flux is related to the fluid temperature mean gradient Φ_0'. It reflects that the temperature gradient is a key factor in determining the heat flux carried by the particles. For unseeded flow, which serves as baseline for perfect self-similar evolution corresponding to fluid mean temperature evolution in one-way coupling, equation (5.14) can be recovered from the equation (5.43). Therefore, by setting $\varphi_\vartheta = 0$, considering only the numerator of the equation (5.43), we will get

$$\Psi_0'(\eta) = 2\eta\Phi_0'(\eta) + \Phi_0''(\eta) \tag{5.44}$$

This is the same equation we already derived for one-way coupling, indicating that the variables with 0 index are associated with the fluid mean variable in perfect self-similar case.

5.3 Integral form

In this section the self-similarity analysis of the evolution of the fluid and particle mean temperature fields, is presented and discussed using an integral representation. In particular, we analyze the integral of the transport equation to derive the self-similar solution unlike the previous section in which the partial differential equations were used. The main advantages of this method over the previous method, is that the validation of the self-similarity (or lack of it) using integral quantities with numerical results of DNS data, is less subject to numerical noise and also can provide a global insights over the whole domain not only at a certain region like the central zone. From the differential form analysis, we also expect the proper self-similar solution holds for fluid mean temperature field in integral form. Similarly, as concluded from differential analysis, particle mean temperature field in integral analysis must deviate from the self-similar evolution. We also expect the deviation from the baseline, fluid integral in one-way coupling, for both particle and fluid mean integrals in two-way thermal coupling regimes. Similarly, for integral equations containing on-self similar terms, a quasi self-similarity analysis based on the inverse series of t will be developed to analytically demonstrate that this approach is also valid for integral equations. We can begin the self-similar analysis of the integral equations by applying the same ansatz solution, self-similar variables, time scaling factor, and shape functions for mean temperature and flux that were introduced and used for the differential analysis in Section 5.2. To proceed, we first multiply the original fluid mean temperature equation ((5.6)) by x and then integrate over x from $-\infty$ to $+\infty$. By following these steps, we derive the resulting integro-partial differential equation for the fluid mean temperature, which incorporates both one-way and two-way coupling effects in a generic form. The equation reads

$$\frac{\mathrm{d}}{\mathrm{d}t}\int_{-\infty}^{\infty} x\langle T\rangle \mathrm{d}x = \kappa \int_{-\infty}^{\infty} x\frac{\partial^2\langle T\rangle}{\partial x^2}\mathrm{d}x - \int_{-\infty}^{\infty} x\frac{\partial\langle uT\rangle}{\partial x}\mathrm{d}x - \frac{\varphi_\vartheta}{\tau_\vartheta}\int_{-\infty}^{\infty} x[\langle T\rangle - \langle\vartheta\rangle]\mathrm{d}x. \tag{5.45}$$

The equation (5.45) is indeed the first-moment integral of the fluid mean temperature in two-way thermal coupling regime. This is the first-moment of enthalpy which is carried by fluid mean temperature field in the fluid-particle system under the influence of particle thermal inertia catheterized by τ_ϑ, and thermal mass fraction φ_ϑ. The concept of first-moment of enthalpy equation integral has been successfully used in studying the heat transfer in boundary layer flows by Kianfar et al. in [103]. This integral equation includes three integrals, representing the diffusion, convection and particle thermal contributions to the fluid mean enthalpy in the domain. The next step is to compute each integral by computing each term in the right hand side of the equation. We start with the diffusion integral, and after integration by parts we can obtain two terms. The first term is zero because of boundary conditions, $\partial_x\langle T\rangle(-\infty) = \partial_x\langle T\rangle(\infty) = 0$, and $\langle T\rangle(\infty) = -1$ and $\langle T\rangle(-\infty) = 1$. Consequently, the diffusion integral is derived as

$$\int_{-\infty}^{\infty} x\frac{\partial^2\langle T\rangle}{\partial x^2}\mathrm{d}x = x\frac{\partial\langle T\rangle}{\partial x}\Big|_{-\infty}^{\infty} - \int_{-\infty}^{\infty}\frac{\partial\langle T\rangle}{\partial x}\mathrm{d}x = -(T_2 - T_1). \tag{5.46}$$

The same is done for computation of the heat flux integral and after integration by part we can get two terms. The first term is zero from the boundary conditions, zero flux at boundaries, $\langle uT\rangle(\infty) = \langle ut\rangle(-\infty) = 0$. This is true in our domain since the heat flux only exists in the central domain in which thermal mixing occurs. Therefore, the flux integral is given by

$$\int_{-\infty}^{\infty} x\frac{\partial\langle uT\rangle}{\partial x}\mathrm{d}x = x\langle uT\rangle\Big|_{-\infty}^{\infty} - \int_{-\infty}^{\infty}\langle uT\rangle\mathrm{d}x = -\int_{-\infty}^{\infty}\langle uT\rangle\mathrm{d}x \tag{5.47}$$

The results of the diffusion and flux integrals can be introduced in the first-moment of fluid enthalpy equation integral, equation (5.45) resulting in

$$\frac{\mathrm{d}}{\mathrm{d}t}\int_{-\infty}^{\infty} x\langle T\rangle\mathrm{d}x = -\kappa(T_2 - T1) + \int_{-\infty}^{\infty}\langle uT\rangle\mathrm{d}x - \frac{\varphi_\vartheta}{\tau_\vartheta}\Big[\int_{-\infty}^{\infty} x\langle T\rangle\mathrm{d}x - \int_{-\infty}^{\infty} x\langle\vartheta\rangle\mathrm{d}x\Big] \tag{5.48}$$

To determine the self-similar solution using the self-similar variable η, we adopt the same ansatz solution and exponents used in the differential form self-similarity analysis, along with the same exponents and dimensionless shape functions for both the fluid and particle mean temperatures and convective fluxes. Given the symmetry of the fluid mean temperature profile and to ensure convergence of the integral, it is

more appropriate to rewrite the dimensionless shape function $\phi_f(t,\eta)$ as

$$\langle T\rangle(t,x) - T_2 = \frac{T_1 - T_2}{2}(1+\phi_f(t,\eta)). \tag{5.49}$$

Here, instead of integrating over $(-\infty,+\infty)$, we integrate over $(0,+\infty)$. The dimensionless convective heat flux is given by

$$\langle uT\rangle(t,x) = \kappa\frac{T1 - T_2}{2}\delta^{-1}\psi_f(t,\eta). \tag{5.50}$$

On the other hand, for particles, the dimensionless mean temperature can be also written in a similar way to the fluid mean temperature in two-way thermal coupling regime,

$$\langle\vartheta\rangle(t,x) - T_2 = \frac{T_1 - T_2}{2}(1+\phi_p(t,\eta)). \tag{5.51}$$

By substituting all the dimensionless shape functions into the first-moment of entalphy equation integral, we obtain the dimensionless integral in terms of variable η and time t as

$$\begin{aligned}&\frac{T_1 - T_2}{2}\frac{\mathrm{d}}{\mathrm{d}t}\delta^2\int_0^\infty \eta(1+\phi_f)\mathrm{d}\eta = -\kappa(T_2 - T_1) + \kappa\frac{T_1 - T_2}{2}\int_0^\infty \psi_f \mathrm{d}\eta \\ &-\frac{\varphi_\vartheta}{\tau_\vartheta}\frac{T_1 - T_2}{2}\delta^2[\int_0^\infty \eta(\phi_f\mathrm{d}\eta - \phi_p(\eta))\mathrm{d}\eta].\end{aligned} \tag{5.52}$$

Note that Equation (5.52) has been derived for a general case, encompassing both one-way and two-way coupling regimes. In the one-way coupling scenario, the evolution is perfectly self-similar because there are no non-self-similar terms ($\varphi_\vartheta = 0$). Under these conditions, the integral equation allows us to determine the evolution of the self-similar length scale $\delta(t)^2$. However, in the more general case where two-way coupling is considered, Equation (5.52) can be expressed in terms of first-moment fluid mean temperature integral and flux integral. These integrals are defined by

$$\begin{aligned}\mathscr{I}_f &= \int_0^\infty x(\langle T\rangle - T_2)\mathrm{d}x = \frac{T_1 - T_2}{2}\delta^2\int_0^\infty \eta(1+\phi_f(t,\eta))\mathrm{d}\eta, \\ \mathscr{I}_p &= \int_0^\infty x(\langle\vartheta\rangle - T_2)\mathrm{d}x = \frac{T_1 - T_2}{2}\delta^2\int_0^\infty \eta(1+\phi_p(t,\eta))\mathrm{d}\eta, \\ \mathscr{J}_f &= \int_0^\infty x\langle uT\rangle\mathrm{d}x = \frac{T_1 - T_2}{2}\int_0^\infty \psi_f(t,\eta)\mathrm{d}\eta.\end{aligned} \tag{5.53}$$

These integrals can also be expressed in terms of normalized (or starred) integrals as follows

$$\begin{aligned}\mathscr{I}_f &= \frac{T_1 - T_2}{2}\delta^2 \mathscr{I}_f^*,\\ \mathscr{I}_p &= \frac{T_1 - T_2}{2}\delta^2 \mathscr{I}_p^*,\\ \mathscr{J}_f &= \frac{T_1 - T_2}{2}\mathscr{J}_f^*,\end{aligned} \tag{5.54}$$

where the starred integrals are given by

$$\begin{aligned}\mathscr{I}_f^* &= \int_0^\infty \eta(1+\phi_f(t,\eta))\mathrm{d}\eta,\\ \mathscr{I}_p^* &= \int_0^\infty \eta(1+\phi_p(t,\eta))\mathrm{d}\eta,\\ \mathscr{J}_f^* &= \int_0^\infty \psi_f(t,\eta)\mathrm{d}\eta.\end{aligned} \tag{5.55}$$

These definitions allow us to analyze the contributions of different terms in the integral equation and understand their roles in the evolution of the first-moment of fluid mean enthalpy integral within the fluid and particle system. In a perfect self-similar evolution, these starred integrals should remain constant in time. For instance, in one-way coupling regime, in which we have this condition, starred integrals that we have only first-moment of fluid mean temperature integral $\mathscr{I}_f^*$ and flux integral $\mathscr{J}_f^*$, and no particle integral is present. But in generic form in two-way coupling due to the effect of non self-similar term from the particle thermal feedback, the starred integrals can deviate from the one-way coupling case. Nonetheless, for the generic case, the first-moment integral equation reduced to an ordinary differential equation which gives the evolution of mixing layer thickness in terms of fluid and particle starred integrals. The reduced integral equations is given by

$$\frac{\mathrm{d}}{\mathrm{d}t}\delta^2(t) = -\frac{\varphi_\vartheta}{\tau_\vartheta}(1 - \frac{\mathscr{I}_p^*}{\mathscr{I}_f^*})\delta^2 + (2 + \mathscr{J}_f^*)\frac{\kappa}{\mathscr{I}_f^*} \tag{5.56}$$

This equation provides the rate of change of the mixing layer thickness $\delta^2(t)$. However, it is crucial to note that this equation cannot be used directly to find $\delta(t)$ in two-way thermal coupling regime due to the time-dependent nature of the starred

integrals caused by particle presence.

$$\left[\frac{\mathrm{d}}{\mathrm{d}t} - \frac{\varphi_\vartheta}{\tau_\vartheta}\right] \mathscr{I}_f = \kappa\left(2 + \mathscr{J}_f\right) - \frac{\varphi_\vartheta}{\tau_\vartheta}\mathscr{I}_p \tag{5.57}$$

This equation shows how the changes in the starred integrals influence the evolution of the mixing layer thickness. The presence of inertial particles affects the transport of the fluid mean enthalpy, and thus the first-moment integral $\mathscr{I}_f$ and fluid flux integral $\mathscr{J}_f$ do not remain constant over time, reflecting the non-conservative and perturbative nature of the fluid mean temperature in the two-way coupling regime. To better understand the mixing dynamics in this case, we can draw an analogy to boundary layer analysis in integral form. In boundary layer analysis, we often deal with the integral forms of equations to understand how mean enthalpy is transported across the boundary layer. Similarly, in this context, the integral equation helps us understand how the fluid mean enthalpy distribution changes over time in the presence of particles. In this , we can use the equation (5.57) to assess the deficit or excess of fluid mean enthalpy due to the particle effects. In our analysis, deficit refers to a situation where there is a reduction in the amount of enthalpy compared to what is expected in an idealized case,i.e. perfect self-similar evolution, while excess of enthalpy shows the situation when fluid mean enthalpy is higher than the expected value in the self-similar case. Unlike the boundary layer flow where the laminar flow is considered as the ideal case, our baseline here is associated with unseeded turbulent flow. Accordingly, the left hand side of the equation (5.57) represents the change in the fluid mean enthalpy over time, considering both the effects of particles and the turbulent flow. Meanwhile, the right hand side balances this change by turbulent convective heat flux, thermal diffusion and the particle thermal effect. Specifically, the term $(\varphi_\vartheta/\tau_\vartheta)\mathscr{I}_p$ accounts for the thermal influence of particles, which may either contribute to or reduce the fluid mean enthalpy content, depending on the φ_ϑ and τ_ϑ.

However, we can obtain the one-way thermal coupling fluid mean enthalpy by setting $\varphi_\vartheta = 0$. In this case, the self-similar solution for $\delta^2(t)$ can be found, since these starred integrals are not influenced by the particle thermal effects leading to a self-similar evolution for fluid mean enthalpy. Consequently, the fluid starred integrals remain time-independent during evolution and they only become functions

of spatial variable η. Starred integrals are given by

$$\begin{aligned}\mathscr{I}_f^* &= \int_0^\infty \eta(1+\phi_f(\eta))\mathrm{d}\eta,\\ \mathscr{J}_f^* &= \int_0^\infty \psi_f(\eta)\mathrm{d}\eta\end{aligned} \tag{5.58}$$

By using this integrals the equation (5.56) is reduced to the following equation, giving an ordinary differential equation for $\delta(t)^2$.

$$\frac{\mathrm{d}}{\mathrm{d}t}\delta^2(t) = \frac{(2+\mathscr{J}_f^*)\kappa}{\mathscr{I}_f^*} \tag{5.59}$$

In this case, we can solve the equation by assuming $\delta(0) = 0$, to get the solution of δ as follows

$$\delta^2(t) = \frac{(2+\mathscr{J}_f^*)\kappa}{\mathscr{I}_f^*}t. \tag{5.60}$$

This result is in agreement with the numerical observation presented in chapter 3, as we have seen that δ grows with time as $t^{1/2}$. Physical interpretation in this case, is that the fluid mean enthalpy is transported and balanced with thermal diffusion and turbulent heat flux with no perturbation from particles.

To gain further insight into the evolution of our particle-laden turbulent flow, we perform an integral analysis on particle mean temperature field similar to that used for the fluid mean temperature field. Specifically, we aim to derive the first-moment integral of the particle mean temperature equation, which will help us understand how the centroid or spatial variation of the particle mean temperature evolves over time. We begin by multiplying the particle mean temperature field equation (5.6) by the spatial coordinate x. This step is motivated by the desire to obtain a first-moment equation, which provides information on the average position weighted by temperature. After multiplying by x, we integrate over the entire spatial domain resulting in

$$\frac{\mathrm{d}}{\mathrm{d}t}\int_{-\infty}^{\infty} x\langle\vartheta\rangle\mathrm{d}x = -\int_{-\infty}^{\infty} x\frac{\partial\langle v\vartheta\rangle}{\partial x}\mathrm{d}x + \frac{1}{\tau_\vartheta}\int_{-\infty}^{\infty} x[\langle T\rangle - \langle\vartheta\rangle]\mathrm{d}x \tag{5.61}$$

This first-moment integral helps us understand the dynamics of thermal mixing between two homothermal region. It provides a global view of how the particle

temperature field evolves, influenced by both convective transport and the thermal interaction between the particles and the surrounding fluid. Following the integration process, where each term in equation (5.61) is integrated across the spatial domain, and applying integration by parts where necessary, we obtain the integral form of the particle equation. This process is parallel to the procedure used earlier for the fluid mean temperature, ensuring consistency in the treatment of both fields. Consequently, the first-moment integral of particle mean temperature equation is obtained as

$$\frac{\mathrm{d}}{\mathrm{d}t}\int_{-\infty}^{\infty} x\langle\vartheta\rangle \mathrm{d}x = \int_{-\infty}^{\infty}\langle v\vartheta\rangle \mathrm{d}x + \frac{1}{\tau_\vartheta}[\int_{-\infty}^{\infty} x\langle T\rangle \mathrm{d}x - \int_{-\infty}^{\infty} x\langle\vartheta\rangle \mathrm{d}x] \tag{5.62}$$

At this point, it is essential to define the dimensionless shape functions for both the fluid and particle mean temperature, as well as for the heat flux. These shape functions are determined using the boundary conditions and the scaling behavior of each term during their evolution. The expressions for these shape functions are as follows

$$\begin{aligned}
\langle T\rangle(t,x) - T_2 &= \frac{T_1 - T_2}{2}(1+\phi_f(t,\eta)),\\
\langle uT\rangle(t,x) &= \kappa\frac{T_1 - T_2}{2}\delta^{-1}\psi_f(t,\eta),\\
\langle\vartheta\rangle(t,x) - T_2 &= \frac{T_1 - T_2}{2}(1+\phi_p(t,\eta)),\\
\langle v\vartheta\rangle(t,x) &= \kappa\frac{T_1 - T_2}{2}\delta^{-1}\psi_p(t,\eta).
\end{aligned} \tag{5.63}$$

Now, after introducing the shape functions into the first-moment integral equation, it can be obtained as

$$\begin{aligned}
&\frac{T_1 - T_2}{2}\frac{\mathrm{d}}{\mathrm{d}t}\delta^2\int_0^{\infty}\eta(1+\phi_p)\mathrm{d}\eta = \kappa\frac{T_1 - T_2}{2}\int_0^{\infty}\psi_p\mathrm{d}\eta\\
&+\frac{1}{\tau_\vartheta}\frac{T_1 - T_2}{2}\delta^2[\int_0^{\infty}\eta(\phi_f\mathrm{d}\eta - \phi_p(\eta))\mathrm{d}\eta].
\end{aligned} \tag{5.64}$$

Similar to the fluid phase, the first-moment of mean temperature integrals and flux integrals can be expressed in terms of their starred values as follows

$$\begin{aligned}\mathscr{I}_f &= \frac{T_1 - T_2}{2}\delta^2 \mathscr{I}_f^*,\\ \mathscr{I}_p &= \frac{T_1 - T_2}{2}\delta^2 \mathscr{I}_p^*,\\ \mathscr{J}_p &= \frac{T_1 - T_2}{2}\mathscr{J}_p^*,\end{aligned} \tag{5.65}$$

where the starred integrals are given by

$$\begin{aligned}\mathscr{I}_f^* &= \int_0^\infty \eta(1+\phi_f(t,\eta))\mathrm{d}\eta, /nonumber\\ \mathscr{I}_p^* &= \int_0^\infty \eta(1+\phi_p(t,\eta))\mathrm{d}\eta,\\ \mathscr{J}_p^* &= \int_0^\infty \psi_p(t,\eta)\mathrm{d}\eta.\end{aligned}$$

As a result of these definitions, the equation for δ^2 in terms of the starred integrals is given by

$$\frac{\mathrm{d}}{\mathrm{d}t}\delta^2 = \frac{1}{\tau_\vartheta}\left(\frac{\mathscr{I}_f^*}{\mathscr{I}_p^*} - 1\right)\delta^2 + \kappa\frac{\mathscr{J}_p^*}{\mathscr{I}_p^*} \tag{5.66}$$

Equation (5.66) can be solved only *if* $\mathscr{I}_f^*$, $\mathscr{I}_p^*$ and $\mathscr{J}_p^*$. are constant in time. If they are not constant, the self-similar solution cannot be reached, because the equation would not have constant coefficient. Therefore, we need to use the quasi self-similar solution according to the Taylor expansion which has been provided in section 5.2. However, we can develop another way to be able to use the integral representation in two-way coupling based on the mean total enthalpy of the whole fluid-particle system. This argument is presented in the next section in detail.

$$\left[\frac{\mathrm{d}}{\mathrm{d}t} - \frac{1}{\tau_\vartheta}\right]\mathscr{I}_p = \kappa\mathscr{J}_p + \frac{1}{\tau_\vartheta}\mathscr{I}_f \tag{5.67}$$

5.4 Mean total enthalpy integral

In the previous section, we conducted a self-similarity analysis of the mean temperature equation for both phases separately. We demonstrated that the self-similar solution derived from the static heat diffusion model is applicable only to the fluid mean temperature in one-way thermal coupling regime in a consistent way with DNS results and differential analysis. Our analysis have shown that non-self-similar terms arise due to the presence of particles thermal feedback on the first-moment of fluid mean temperature integral. It also indicated that first-moment of particle mean temperature integral in both one-way and two-way coupling regimes, do not evolve self-similarly. However, it is possible to use perturbation theory, to develop the quasi self-similar integral analysis on particle and fluid first-moment integrals in two-way thermal coupling, but another approach based on the total entalphy of the system is used. In the differential analysis, we derived a set of quasi-self similar evolution to quantify the deviation due to particle thermal perturbation from the perfect self similar case by Taylor expansion of inverse time t. Here, we sum up two first-moment integrals, particle and fluid to obtain an integral equation for the whole system of fluid and particle in two-way coupling regime. This summation can cancel the non-self similar terms in the integral equations, which are present in each integral equation due to the mutual thermal effect between particles and fluid in two way thermal coupling regime. Accordingly, by summation of the first-moment integral of the fluid mean temperature (5.45) and the first moment integral of particle mean temperature (5.61), latter multiplied by φ_ϑ, the first-moment integral of mean total enthalpy of our system of fluid and particles can be written as

$$\frac{\mathrm{d}}{\mathrm{d}t}\int_{-\infty}^{\infty} x\langle T\rangle \mathrm{d}x + \varphi_\vartheta \frac{\mathrm{d}}{\mathrm{d}t}\int_{-\infty}^{\infty} x\langle \vartheta\rangle \mathrm{d}x = \kappa \int_{-\infty}^{\infty} x\frac{\partial^2\langle T\rangle}{\partial x^2}\mathrm{d}x - \int_{-\infty}^{\infty} x\frac{\partial\langle uT\rangle}{\partial x}\mathrm{d}x - \varphi_\vartheta \int_{-\infty}^{\infty} x\frac{\partial\langle v\vartheta\rangle}{\partial x}\mathrm{d}x. \tag{5.68}$$

Based on the results of the integrals computed in the previous section, we derive the weak form of the total enthalpy equation as follows

$$\frac{\mathrm{d}}{\mathrm{d}t}\int_{-\infty}^{\infty} x\langle T\rangle \mathrm{d}x + \varphi_\vartheta \frac{\mathrm{d}}{\mathrm{d}t}\int_{-\infty}^{\infty} x\langle \vartheta\rangle \mathrm{d}x = -\kappa(T_2 - T_1) - \int_{-\infty}^{\infty}\langle uT\rangle \mathrm{d}x - \varphi_\vartheta \int_{-\infty}^{\infty}\langle v\vartheta\rangle \mathrm{d}x. \tag{5.69}$$

The same dimensionless shape functions applied in the previous section is introduced into the weak form of the integral equation to obtain

$$\frac{T_1-T_2}{2}\frac{\mathrm{d}}{\mathrm{d}t}\delta^2[\int_0^\infty \eta(1+\phi_f)\mathrm{d}\eta+\varphi_\vartheta\int_0^\infty \eta(1+\phi_p)\mathrm{d}\eta]=-\kappa(T_2-T_1)$$
$$+\kappa\frac{T_1-T_2}{2}[\int_0^\infty \psi_f\mathrm{d}\eta+\varphi_\vartheta\int_0^\infty \psi_p\mathrm{d}\eta]. \tag{5.70}$$

At this point, we can use the definitions of the first moment mean temperature integrals, and first-moment flux integrals and their starred values to derive the evolution equation for $\delta(t)$ in terms of the starred values as

$$\frac{\mathrm{d}}{\mathrm{d}t}\delta^2(\mathscr{I}_f^*+\varphi_\vartheta\mathscr{I}_p^*)=\kappa(2+\mathscr{J}_f^*+\varphi_\vartheta\mathscr{J}_p^*). \tag{5.71}$$

By solving this ordinary differential equation and by setting the initial value as $\delta(0)=0$, the solution will be derived as

$$\delta^2(t)=\frac{\kappa(2+\mathscr{J}_f^*+\varphi_\vartheta\mathscr{J}_p^*)}{(\mathscr{I}_f^*+\varphi_\vartheta\mathscr{I}_p^*)}t. \tag{5.72}$$

Here, in accordance with the self-similar case in one-way coupling and the DNS results, we have derived an expression for $\delta(t)$ that confirms its growth with time as $t^{1/2}$. While the coefficients vary across different cases, the crucial point is that the scaling with time remains consistent. In DNS simulations, fluid temperature and velocity moments have been found to collapse when rescaled with the thickness of the thermal interaction layer δ_*, conventionally defined on the basis of the inverse temperature gradient as $\delta_*=(T_1-T_2)/\max|\partial T/\partial t|$. This thickness grows as $\delta_*/\ell\sim(t/\tau)^{1/2}$, where $\tau=\ell/u'$ is the large-scale eddy turnover time, ℓ is the integral scale of the turbulence and u' is the root mean square value of the velocity fluctuations. These results has been presented and discussed in chapter 3. Therefor, integral analysis proved that regardless of the particle thermal inertia and the thermal mass fraction, the mean total enthalphy should evolves in a quasi self similar way. However, its devation from the perfect self-similar evolution can be quantified by φ_ϑ. Moreover, Equation (5.72) quantifies the particle contribution to thermal mixing and interestingly expresses this contribution in terms of the particle thermal mass fraction φ_ϑ. While in Chapter 3 we quantified this contribution based on average values computed at the center, where the heat flux is maximal, the quantification through the mean total enthalpy analysis is in integral form over the entire flow

domain, which is potentially more comprehensive. The results from this theoretical analysis will be validated against DNS results in the following section. By setting $\varphi_\vartheta = 0$, the self-similar solution can be derived, i.e. (5.60). The equation can be also written in terms of total integrals, not the starred values as

$$\frac{\mathrm{d}}{\mathrm{d}t}(\mathscr{I}_f + \varphi_\vartheta \mathscr{I}_p) = \kappa(2 + \mathscr{J}_f + \varphi_\vartheta \mathscr{J}_p). \tag{5.73}$$

In this formulation, the equation demonstrates how the first-moment integral of the mean total enthalpy is transported in the two-way coupling regime. The time rate of change on the left-hand side is balanced by diffusion, turbulent convective flux, and particle flux on the right-hand side. This balance is analogous to the heat transfer analysis in boundary layers, where the excess or deficit of thermal energy is managed by various mechanisms.

Similar to the differential analysis, this equation suggests that there is an optimal value of φ_ϑ for maximizing the particle enhancement of the mean total enthalpy. This implies that, at this optimal value, the contribution of particles to thermal mixing is maximized. However, for very high values of φ_ϑ, the mean total enthalpy may actually decrease compared to the unseeded turbulent flow. This is because an excessive number of particles could disrupt the thermal distribution, leading to a reduction in overall enthalpy due to effects such as increased thermal resistance or changes in turbulence characteristics. Of course, when φ_ϑ is optimized, the particles contribute positively to the mean total enthalpy, and the system benefits from increased thermal mixing. Here, the contribution of $\varphi_\vartheta \mathscr{I}_p$ should ideally balance the heat fluxes and diffusion terms to maintain or increase the mean total enthalpy.

5.5 Validation

In this section, we utilize DNS data to rigorously validate our self-similarity analysis presented in previous sections. The validation process is carried out in two stages, each focusing on different aspects of the theoretical analysis. First, in Section 5.5.1, we concentrate on validating the differential form of the self-similarity analysis. This involves directly comparing the DNS data with the self-similar solutions obtained

from the differential equations governing the evolution of the system. However, direct comparison of local values in the differential form often encounters significant noise, which arises due to the inherent fluctuations in the DNS data at small scales. These fluctuations can obscure the underlying trends, making it challenging to directly validate the quasi-self-similar behavior of the system based on Taylor expansion of inverse of time to capture the perturbation of particle thermal inertia on the fluid self-similar evolution. Thuse, the fluid mean temperature evolution in one-way coupling is considered as the baseline for the differential analysis due to the intrinsic perfect self-similar evolution. Therefore, in order to mitigate the issues arise from using local DNS data in differential analysis, we extend the validation by considering the first-moment integrals of the mean temperature and flux to quantify the higher order values in the Taylor expansion. By integrating over space, we smooth out the local noise and obtain more stable quantities that still reflect the essential dynamics predicted by the self-similarity analysis. The first-order moment integrals in terms of τ_ϑ/t, capture the deviation of the self-similar solution in time at different particle inertia range. Moreover, they serve as a bridge between the noisy differential data and the global behavior of the system, providing a more reliable basis for validation.

Next, in Section 5.5.2, we extend our validation to the integral form of the self-similarity analysis. In this section, we compute the first-moment integrals of the mean temperature and flux for both the particle and fluid phases, as defined in the section 5.3. In this part, the particle mean temperature field in one-way coupling is validated by comparing the quasi-self-similar evolution with the fluid mean temperature field in integral form. Additionally, the quasi-self similar evolution of both fields in two-way thermal coupling regime will be validated. In particular, by analyzing the first-moment integrals, we validate the self-similarity analysis in its integral form in both cases. We assess how well the computed integral coefficients for both the fluid and particle phases align with the theoretical predictions in one- and two-way coupling regimes. The behaviour of thermal field in two cases is illustrated revealing the significance of particle thermal inertia, thermal feedback and thermal mass fraction on the global heat transfer in the whole domain. This step is crucial as it not only confirms the validity of the self-similar solutions but also ensures that the integral quantities, which represent global properties of the system, are consistent with the local behavior described by the differential form. Moreover, the mixing layer thickness δ is computed by solving the differential equation derived from the first-moment of mean total enthalphy equation integral. In this case, we can

quantify the particle thermal effects on the mean total enthalpy of the system and its effect on the evolution of thermal mixing layer through the thermal mass fraction φ_ϑ. However, the effect of particle inertia and thermal feedback are also embedded in the terms of the evolution equations of thermal mixing layer thickness.

Through this dual approach, by validating both the differential and integral forms, we provide a comprehensive validation of the self-similarity analysis, demonstrating its robustness in describing the dynamics of the fluid-particle system across different scales.

5.5.1 Differential form validation

The self-similarity analysis of fluid and particle mean temperature fields is compared with information extracted by DNS obtained in chapter 3, carried out within the point-particle Eulerian-Lagrangian approach in a parallelepiped domain with periodic boundary conditions. A direct comparison of the temperature moments is made difficult by the intrinsic uncertainty in data coming from numerical simulation, where the noise due to numerical constraints and the limited sample size prevents the computation of derivatives. Therefore, a better comparison can be obtained by deriving first-moment integrals which can describe globally the thermal mixing layer dynamics. In the validation of the differential form of our self-similarity analysis, we employ a Taylor series expansion in the inverse of time to capture the deviations of the particle mean temperature field from the baseline self-similar evolution observed in the fluid. Thus, the quasi-self-similar analysis is developed, as it allows us to account for the gradual deviations introduced by the presence of particles in the particle field even in one-way thermal coupling regime. These deviations can also act on the fluid mean temperature field along with the particles thermal feedback in two-way thermal coupling regime, leading to quasi-self similarity in both fields through these non-self-similar terms. Note that in this section, we only validate the theoretical analysis on the fluid and particle mean temperature fields in one-way coupling regime, and leave the two-way coupling analysis for the next section, integral analysis.

Consequently, in order to quantify particle perturbations on the particle mean temperature field, due to the particle thermal inertia in one-way thermal coupling regime, we analyze the first-order moment integrals of fluid and particle mean

temperature field, i.e. $\mathscr{I}_f$, $\mathscr{I}_p$, $\mathscr{J}_f$, and $\mathscr{J}_p$. These integrals serve as sensitive indicators of how the system deviates from the ideal self-similar state, i.e. the fluid mean temperature evolution in one-way thermal coupling regime. These integrals not only help in smoothing out the noise inherent in direct local comparisons but also highlight the cumulative effect of particle-induced perturbations by thermal inertia over time. By integrating such local deviations, the first-order integrals effectively capture the impact of particles on the overall thermal dynamics, thereby providing a clearer picture of the quasi-self-similar behavior that emerges due to the particle thermal inertia. This approach is specifically leveraged in the differential analysis validation to ensure that the influence of particle thermal inertia is accurately reflected in the evolving particle temperature field. We can observe that the first-moment integrals, which represent the spatial first-moment of the fluid and particle mean enthalpy, can be easily verified from the numerical simulations, because firs-moment integrals can be obtained directly by the flow statistics without the introduction of any hypothesis about the solution. First-order moment integrals for particle temperature fields in one-way coupling regime which evolution deviates from the perfect self-similar evolution, are given by

$$\mathscr{I}_f = \int_0^{+\infty} x(\langle T\rangle - T_2)\mathrm{d}x = \frac{T_1 - T_2}{2}\delta^2 \int_0^{+\infty} \eta(1+\phi_f(\eta))\mathrm{d}\eta, \tag{5.74}$$

$$\mathscr{I}_p = \int_0^{+\infty} x(\langle \vartheta\rangle - T_2)\mathrm{d}x = \frac{T_1 - T_2}{2}\delta^2 \int_0^{+\infty} \eta(1+\phi_p(t,\eta))\mathrm{d}\eta, \tag{5.75}$$

$$\mathscr{J}_f = \frac{1}{\kappa}\int_0^{+\infty} \langle uT\rangle \mathrm{d}x = \frac{T_1 - T_2}{2}\int_0^{+\infty} \psi_f(\eta)\mathrm{d}\eta, \tag{5.76}$$

$$\mathscr{J}_p = \frac{1}{\kappa}\int_0^{+\infty} \langle v\vartheta\rangle \mathrm{d}x = \frac{T_1 - T_2}{2}\int_0^{+\infty} \psi_p(t,\eta)\mathrm{d}\eta. \tag{5.77}$$

To perform the quasi self-similar analysis, we can use the Taylor expansion as it was employed in section 5.2. Accordingly, particle first-order moment of mean temperature and flux integrals $\mathscr{I}_p$, $\mathscr{J}_p$ must admit an expansion in series of the inverse time when the expansion of ϕ_p and ψ_p are introduced in the integrals. The first terms of such series, correspond to the integrals of ϕ_0 and ψ_0, which are the baseline of proper self-similar evolution in one-way thermal coupling regime with no particle thermal perturbation. These integrals can be obtained from the limits of $\mathscr{I}_p$ and $\mathscr{J}_p$ for large t. From the DNS results we know that, the time factor scaling, in our analysis, $\delta(t)$, scales as $t^{1/2}$, when the solution behaves in a perfect self-similar

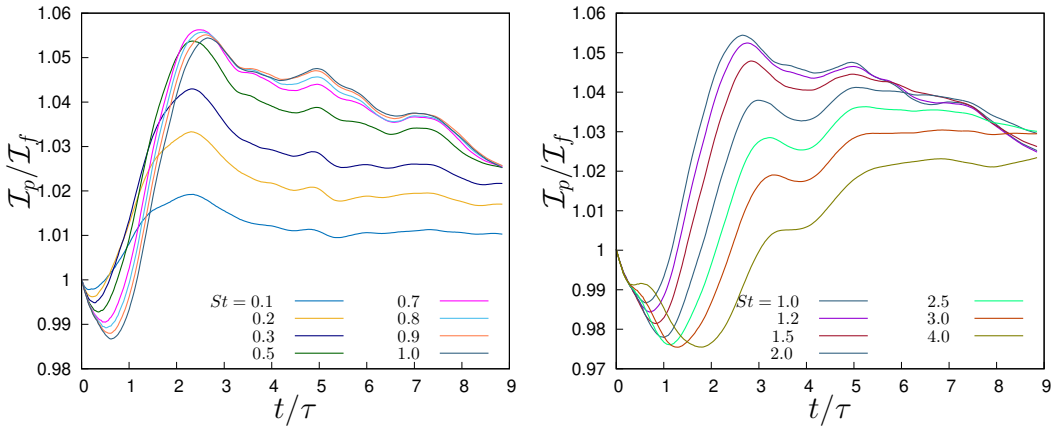

Fig. 5.1 Particle-to-fluid ratio of first-moment of mean temperature integrals $\mathscr{I}_p/\mathscr{I}_f$ for (a) particles with $St \leq 1$; (b) particles with St ≥ 1.

way in one-way thermal coupling regime. Therefore, by replacing the expansion of ϕ_p and using (5.22)-(5.24), we have

$$\begin{aligned}
\mathscr{I}_p &= \mathscr{I}_f + \frac{T_1 - T_2}{2}\delta^2 \left(\frac{\tau_\vartheta}{t} \int_0^{+\infty} \eta \varphi_1(\eta) \mathrm{d}\eta + \mathscr{O}\left(\frac{\tau_\vartheta}{t}\right) \right) \\
&= \mathscr{I}_f - \frac{T_1 - T_2}{2}\delta^2 \frac{\tau_\vartheta}{t} \left(\left(\frac{1}{2}\int_0^{+\infty} \psi_0 \mathrm{d}\eta - \int_0^{+\infty} \eta(1+\phi_0)\mathrm{d}\eta \right) + \mathscr{O}\left(\frac{\tau_\vartheta}{t}\right) \right) \\
&, = \mathscr{I}_f - \frac{T_1 - T_2}{2}\delta^2 \frac{\tau_\vartheta}{t} \left(\left(\frac{1}{2}\int_0^{+\infty} \psi_p \mathrm{d}\eta - \int_0^{+\infty} \eta(1+\phi_0)\mathrm{d}\eta \right) + \mathscr{O}\left(\frac{\tau_\vartheta}{t}\right) \right) \\
&= \mathscr{I}_f - \frac{\tau_\vartheta}{t}\left(\frac{\delta^2}{2}\mathscr{J}_p - \mathscr{I}_f \right) + \mathscr{O}\left(\frac{\tau_\vartheta}{t}\right). \qquad (5.78)
\end{aligned}$$

We can therefore derive the ratio between the first-moment integrals of both phases as

$$\frac{\mathscr{I}_p}{\mathscr{I}_f} = 1 + \frac{\tau_\vartheta}{t}\left(1 - \frac{\delta^2}{2}\frac{\mathscr{J}_p}{\mathscr{I}_f} \right) + \mathscr{O}\left(\frac{\tau_\vartheta}{t}\right). \qquad (5.79)$$

The equation (5.79) shows the quasi-self similar evolution of the particle mean temperature field in integral form, capturing the perturbation from the baseline due to the particle thermal inertia.

We utilize the results obtained from DNS at Taylor microscale Reynolds number of 56. In these simulations which are used to validate the self-similarity analysis, the ratio of the thermal relaxation time, τ_ϑ, to the Stokes relaxation time is set to 4.43, and the Prandtl number is kept constant at 0.71 and volume fraction is also fixed at

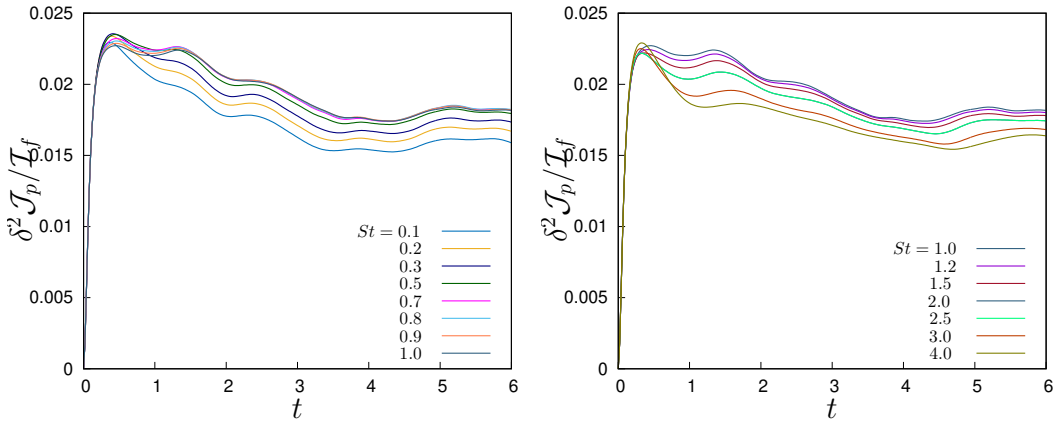

Fig. 5.2 The ratio of first-moment of particle flux integral to first-moment of fluid mean temperature, $\delta^2\mathscr{I}_p/\mathscr{I}_f$, for (a) particles with $St \leq 1$; (b) particles with St ≥ 1.

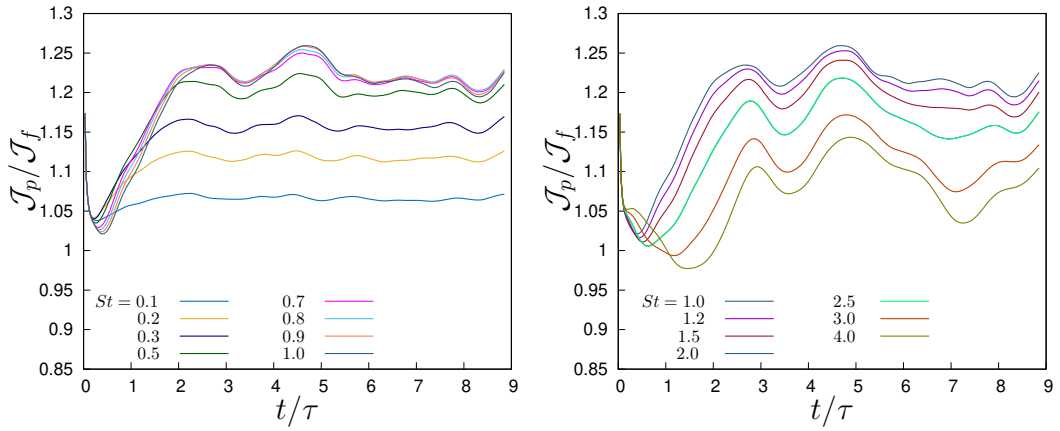

Fig. 5.3 Particle-to-fluid ratio of first-moment of flux integrals $\mathscr{I}_p/\mathscr{I}_f$ in one-way thermal coupling regime for (a) particles with $St \leq 1$; (b) particles with St ≥ 1.

4×10^{-4} (for further details on the simulated flow, refer to chapter 3). In Figure 5.1, the ratio of particle-to-fluid first-moment of mean temperature integrals $\mathscr{I}_p/\mathscr{I}_f$ is presented. Initially, during the first two eddy turnover times, τ, this ratio undergoes an initial transient phase. Following this initial transient, the ratio begins to show a gradual decay, eventually approaching a steady value, as predicted by equation (5.79). The fluid temperature evolution is primarily governed by the large-scale structures of the turbulent flow, leading to a time scaling proportional to large-eddy turnover timeτ. Consequently, t/τ_ϑ scales inversely with the large-scale Stokes number, $\mathrm{St}_\ell = \tau_\vartheta/\tau$. This inverse scaling implies that the corrections introduced by the particles thermal inertia are relatively small. As a result, the non-self-similar terms in the evolution tend to be influenced by statistical noise, which is an inherent

challenge in experimental data collection. This noise makes it difficult to accurately assess higher-order terms in the expansion described by equation (5.79), limiting our ability to validate these terms through the simulations.

The ratio of integrals increases as particle Stokes number increases, reaching a maximum when the Stokes number of the particles, $\mathrm{St} = \tau_v/\tau_\eta$, where τ_η is the Kolmogorov timescale, equals one. Beyond this point, the ratio decreases with further increases in particle inertia. This behavior arises because, while the correction is proportional to τ_ϑ, the coefficient of τ_ϑ/t is dependent on the particle flux, which diminishes when the thermal Stokes number exceeds one. We can verify this trend by examining the second term in the expansion (5.79), which represents the leading term of the non-self-similar correction, as illustrated in Figure 5.2. After the initial transient, the ratio $\delta^2 \mathscr{J}_p/\mathscr{I}_f$ exhibits a slow decay over time, consistent with the inverse power series expansion in time, and shows a similar non-monotonic dependence on particle inertia, peaking when the particle Stokes number is equal to one. However, the time-dependent variations are smaller, and the ratio stabilizes to a constant value after approximately five eddy turnover times. Moreover, when we examine the particle-to-fluid flux integrals ratio $\mathscr{J}_p/\mathscr{J}_f$ (see Figure 5.3), it is evident that this ratio remains almost constant over time. This observation suggests that the first term in the series expansion of $\psi_f(t,\eta)$ is zero. Consequently, this also implies that the higher-order terms in the expansion of $\phi_p(t,\eta)$ are independent of the particle heat flux. Simulations conducted at higher Stokes numbers exhibit more pronounced fluctuations, likely due to the reduced number of particles in the simulations, which were performed at a constant volume fraction.

5.5.2 Integral form validation

In this section, the DNS data is used to compute the first-moment of mean temperature integrals and the first-moment flux integrals for particle and fluid to validate the theoretical analysis performed in sections 5.3 and 5.4. The integral formalism based on first-moment integral equations enables us to measure the global heat transfer at the interface between two homothermal regions considering all fluid and particles effects on thermal mixing dynamics. Both one-way and two-way thermal coupling regimes are taken into account to validate the theoretical analysis in the most complex scenario in which particle thermal inertia as well as its thermal feedback affect the evolution of thermal field. DNS data are used from the simulation setup of

the collisionless regime at Taylor Reynolds number 56, and fixed ratio of particle thermal-to-momentum relaxation times equal to 4.43. In these simulations, a wide range of Stokes number from 0.1 to 4 is covered.

As seen in chapter 3, for such flow setup, we could quantify the role of particles in the overall heat transfer between two homothermal region. Our results were computed by using the correlation between maximum particle velocity and temperature fluctuating denoting the particle heat flux. Similarly, the same correlation was computed for the fluid fluctuating measuring the turbulent heat flux. Obviously, the maximum values for both phases correspond to the location at the central zone at which the thermal mixing is maximal. We have observed that the ratio of time-averaged particle-to-fluid velocity-temperature correlation shows a self-similar trend for different Taylor microscale Reynolds number and remains constant in time. Therefore, we used this ratio to indicate the particle contribution to the heat transfer at different inertia range. It has been revealed that the maximum contribution occurs in vicinity of Stokes number approaching unity, implying the non-local effect by clustering at this range of particle inertia. To validate the integral analysis, we time-averaged of the particle and fluid first-moment integrals, to be able to compute the ratio between them. Indeed, such ratio, is considered as the particle contribution according to its inertia to the overall heat flux. Unlike the numerical results, these flux integrals indicate the fluxes in the whole domain. Interestingly, we could observe the same pattern as the DNS results, but with some difference in magnitude, with the consistent maximum point nearby the Stokes number equal to one. This agreement observed for both one- and two-way thermal coupling regimes. Figure 5.4 shows both results, the one from the numerical results on the panel (a), and the ratio of computed flux integrals using the theoretical analysis. In agreement with the DNS results, we can see that the particle flux in two-way thermal coupling is higher than the one-way thermal coupling regime. This can be a considered as a validation for our self-similarity analysis in integral form. Figure 5.5 illustrates the time evolution of the ratio between the particle and fluid first moments of the flux integrals, $\mathscr{J}_p/\mathscr{J}_f$, for various particle Stokes numbers. The results demonstrate that, after an initial transient phase, this ratio gradually stabilizes to a constant value, consistent with our theoretical predictions from the integral form analysis. Although minor oscillations are observed, they remain within an expected range, confirming that the integral form analysis captures the quasi-steady-state behavior of the system. Importantly, the level of noise in this integral representation is significantly reduced

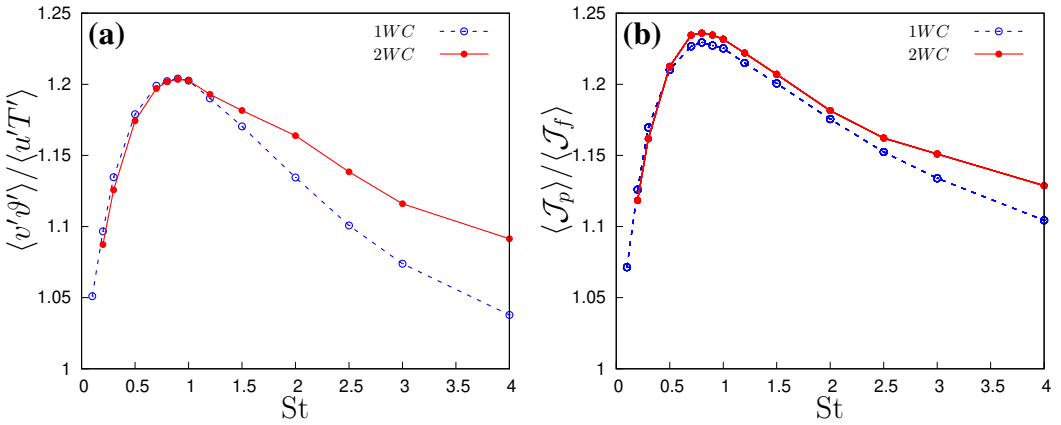

Fig. 5.4 The ratio of time-average particle-to-fluid (a) velocity-temperature correlation at $x = 0$ and (b) first-moment of flux integrals versus Stokes number in one and two-way coupling regimes.

compared to the differential representation. This reduction in noise is attributed to the smoothing effect of integration, which averages out local fluctuations and emphasizes the overall trends. As a result, the integral approach not only aligns with our expectations but also provides a more robust validation of the self-similar behavior, particularly in the presence of particle-induced perturbations due to particle thermal inertia and particle thermal feedback. The flow regime here is two-way thermal coupling, the case that both fluid and particles deviate from the perfect self-similar evolution, which is the fluid evolution in one-way thermal coupling regime. As we discussed in the section 5.3 the particle perturbation can be characterized by τ_ϑ and φ_ϑ. For the low inertia particles, the ratio indicates less oscillation compared to the high inertia particles, however, for larger time the ratio tends to relax on a certain value for each inertia range. For lower inertia particles with Stokes number less than one, the ratio of flux integrals increases with St, while after reaching the maximum value at $\mathrm{St} = 1$, the ratio reduces as St increases.

In figure 5.6 the time evolution of ratio of particle-to-fluid first-moment of mean temperature integrals is depicted. As predicted by the theoretical derivation, after an initial transient, as time progresses, the ratio relaxes self-similarly toward a certain value for all particle Stokes number in time. Similar to the flux integrals ratio, the increase with St up to Stokes number one is seen, and a reduction is observed as particle inertia increases. In accordance to the inverse of time in the Taylor expansion, for larger time, the asymptotic self-similar behavior can be achieved for all particle groups.

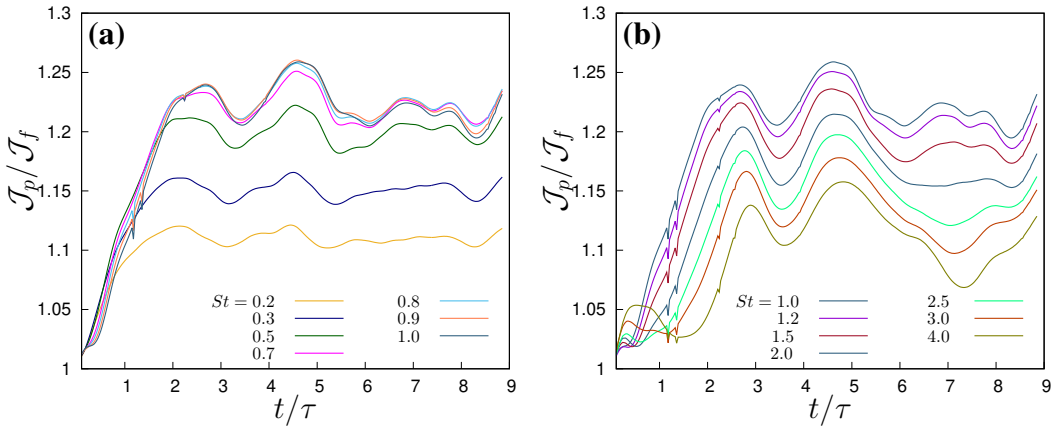

Fig. 5.5 Particle-to-fluid ratio of flux integrals $\mathcal{J}_p/\mathcal{J}_f$ in two-way coupling regime: (a) particles with $St \leq 1$; (b) particles with St ≥ 1.

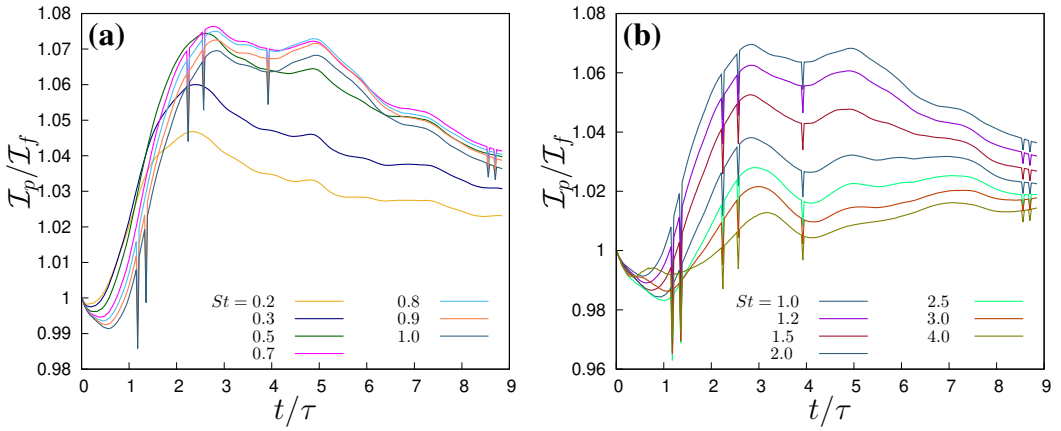

Fig. 5.6 Particle-to-fluid ratio of first-moment of mean temperature integrals $\mathscr{I}_p/\mathscr{I}_f$ in two-way coupling regime: (a) particles with $St \leq 1$; (b) particles with St ≥ 1.

Figure 5.7 shows the time evolution of particle first-moment of flux integrals for different particle Stokes numbers. As expected by the theoretical analysis, these integrals are zero at initial time, because there is no flux at initial instant. As time passes, the integrals for all particles relax on a constant value. The variations of flux integrals with St follows the same pattern as we have observed for the ratio of the particle to fluid integrals in figure 5.5.

Our objective is to formulate the impact of inertial particles on heat transfer using both numerical and theoretical approaches. Initially, we focused on the numerical aspect, where we also validated the self-similarity analysis under the assumption of mean total enthalpy of the fluid-particle system. Accordingly, in Section 5.4,

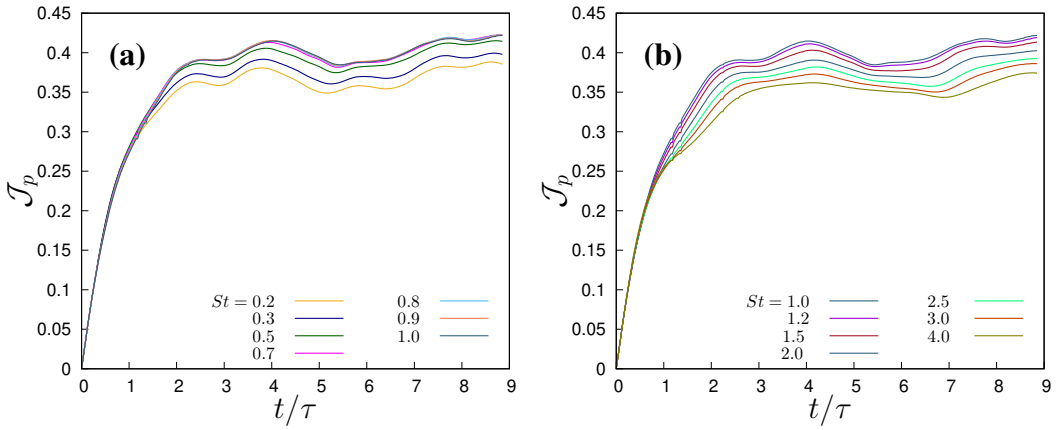

Fig. 5.7 Time variation of particle flux integrals, $\mathscr{J}_p$ in two-way coupling regime: (a) particles with $St \leq 1$; (b) particles with St ≥ 1.

we developed a theoretical framework to capture the effects of particle inertia and thermal feedback on the first-moment of the mean total enthalpy integral within a two-way coupling regime. A key strength of this formulation is that summing the first-moment mean enthalpy integrals for both fluid and particle leads to the cancellation of non-self-similar terms in the first moment of mean total enthalpy equation integral. This cancellation occurs because the mutual thermal interactions between the fluid and particles effectively neutralize each other. As a result, the combined integral provides a clear and simplified perspective on the mean total enthalpy evolution, isolated from the complexities of non-self-similar deviations. This approach allows us to quantify the influence of particles with thermal mass fraction φ_ϑ on the mean total enthalpy of the system. The integral equation derived from this formulation demonstrates how particles can enhance the mean total enthalpy, particularly at an optimal value of φ_ϑ. Furthermore, by setting $\varphi_\vartheta = 0$, we retrieve the baseline equation that describes the self-similar evolution of the fluid in a one-way thermal coupling regime. This baseline serves as a reference point against which the effects of particle thermal inertia can be measured. Thanks to this formulation, we gain valuable insights into the evolution of mean total enthalpy within the flow domain as a global measure. The rate of change in mean total enthalpy over time is balanced by diffusion, convection, and particle effects, providing a comprehensive understanding of the very complex thermal mixing dynamics at a global level. Additionally, the relevant length scale of the mixing dynamics, specifically the thickness of the mixing layer $\delta(t)$, can be accurately computed using these integrals. The correct scaling of $\delta(t)$ further confirms that the evolution of mean total enthalpy integral in the

two-way thermally coupled fluid-particle system is quasi-self-similar. An important advantage of this approach is that it does not need a Taylor series expansion, offering a more direct and practical method for quantification through the thermal mass fraction φ_ϑ. This is particularly beneficial in real-world applications where precise thermal management of fluid-particle systems is required. By relying on φ_ϑ, the formulation remains both theoretically robust and practically applicable, making it a powerful tool for understanding and optimizing heat transfer enhancement in complex fluid-particle systems.

Our physical problem, in its generic form, involves heat diffusion coupled with the effects of complex fluid flow. This general problem can be divided into four distinct cases, each representing different scenarios of thermal mixing, where the so-called mixing layer thickness, $\delta(t)$ evolves over time under varying dynamics imposed by the boundary conditions and flow regime. The simplest case is pure heat diffusion in a static condition, where there is no fluid flow ($u = 0$). In this scenario, δ^2 grows linearly with time, as predicted by the analytical solution to the well-known unsteady heat conduction problem. Here, the rate of thermal diffusion is solely governed by the thermal conductivity of the medium, resulting in a slow and steady thickening of the thermal mixing layer. When fluid flow is introduced, the situation changes. In the laminar flow regime, even though the flow is smooth and orderly, the presence of fluid motion enhances heat transfer compared to the static case. Consequently, δ^2 still evolves linearly with time but grows faster due to the additional convective transport of heat by the moving fluid. This scenario might represent cases like a laminar boundary layer developing over a flat plate. However, our specific case study does not involve laminar flow counterpart like the boundary layer flow. The next level of complexity arises when the flow regime becomes turbulent ($u' \neq 0$, $\varphi_\vartheta = 0$). In turbulent flows, the chaotic and random fluctuations of the fluid enhance the mixing process far more effectively than in laminar flows. As a result, δ evolves more rapidly over time compared to the laminar case, driven by the intense convective mixing characteristic of turbulence. This scenario aligns closely with our flow configuration without the presence of particles, where turbulence alone drives the rapid thickening of the thermal mixing layer.

Finally, we arrive at the most complex and complete picture, which is the primary focus of our study. In this case, we observe from our numerical experiments, and understand from the underlying physics, that thermal mixing is further enhanced when the turbulent flow carries inertial particles ($u' \neq 0$, $\varphi_\vartheta \neq 0$). In particular,

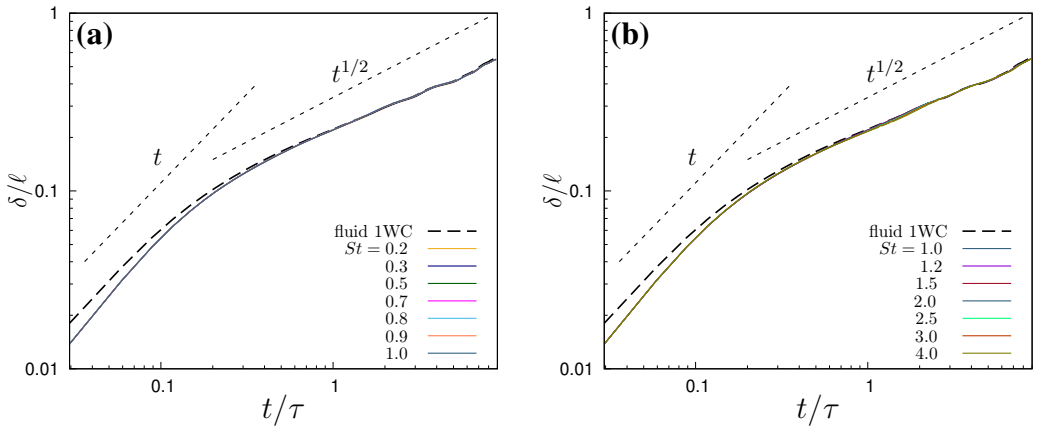

Fig. 5.8 Temporal growth of δ(t) normalized with integral scale ℓ at $\mathrm{Re}_\lambda = 56$, from the integral form self-similarity analysis of mean total enthalpy model in one and two-way coupling regime: (a) particles with $St \leq 1$; (b) particles with $\mathrm{St} \geq 1$.

the presence of inertia particles introduces additional mechanisms of heat transfer, including particle-induced thermal mixing, clustering, thermal caustics and thermal feedback, which mostly amplify the rate at which δ evolves under the optimum values of φ_ϑ. In this case, the interaction between turbulent eddies and particles results in a more vigorous mixing process, leading to a significantly faster growth of the mixing layer thickness than in any of the previous cases. This enhanced mixing is a key aspect of our study, highlighting the critical role that inertial particles play in modulating heat transfer in turbulent flows.

The equation (5.72) or its variant (5.73), can show us all the above-mentioned contributions in a single expression, and it can provide a simple differential relation (or algebraic relation after solving the differential equation) which contains the information about the molecular thermal diffusion, turbulent convection and particle contribution. In other words, this equation gives the solution to δ^2 at time t which can be interpreted as a measure of the mean total enthalpy of the fluid-particle system, as it reflects the overall energy contained within the thermal mixing layer, considering both the fluid and the particles. On the right-hand side, the numerator, represents the total heat flux, including contributions from molecular diffusion, turbulent convection, and particle heat flux. Meanwhile, denominator corresponds to the total mean temperature integral, accounting for both the fluid and the particle contributions. This equation encapsulates the balance between the energy contained in the system and the fluxes that contribute to its redistribution over time. If we assume $\delta(0) = 0$, the solution of δ from the mean tutal enthalpy integral equation

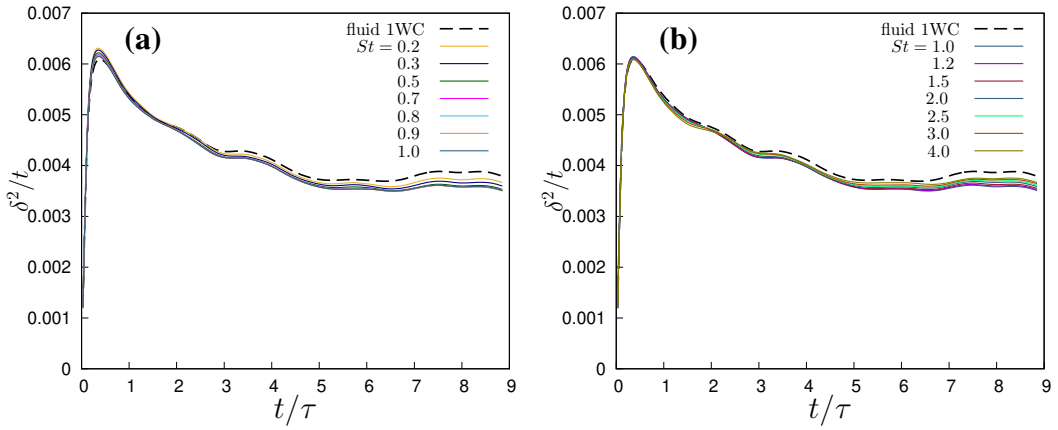

Fig. 5.9 Temporal variation of δ^2/t, for (a) particles with $St \leq 1$; (b) particles with St ≥ 1 in two-way coupling. In both panels, the dashed line represents the ratio in the one-way coupling regime ($\varphi_\vartheta = 0$). $\mathscr{J}_p$ and $\mathscr{I}_p$ ignored in the computation of δ, to allow comparison with one-way coupling.

can be computed. Figure 5.8 depicts the solution of the equation (5.72) at different Stokes numbers. Dashed line represents the baseline where $\varphi_\vartheta = 0$. As it can be seen all particle groups with different inertia collapse into one curve. Importantly, the same behavior is observed as the normalized δ with flow integral scale, ℓ computed and presented in chapter 3, scaling with t in initial transient and $t^{1/2}$ in larger time. However, there is an offset in magnitude which is related to the different approaches and coefficients in the equations. We can also use the equation (5.72) to plot the right hand side. The numerator is associated with the first-moment integral representation of the diffusion, convection and particle heat flux while denomenator shows thefirst moment of mean total enthalpy integral. Figure 5.9 shows that time variation of δ^2/t when $\varphi_\vartheta = 0$ with respect one-way coupling case. There is a small difference due to the particle thermal inertia, but the curve behaves very similar to the self-similar case and keeps the right-hand side constant in time.

Moreover, figure (5.72) shows the same quantity while $\varphi_\vartheta = 1.664$, the value of our investigation. According to the results, even in this case, we can observe the curve follows the pattern of the baseline indicating the quasi-self similar behavior in two-way coupling for mean total flux integral over mean total enthalphy integral at the mixing layer for all ranges of particle inertia. This results confirms that while particles modifies the magnitude of the thermal layer growth, through the feedback and its inertia influencing both mean total enthalpy and mean total flux, it does not fundamentally alter the self-similar nature of the evolution of the

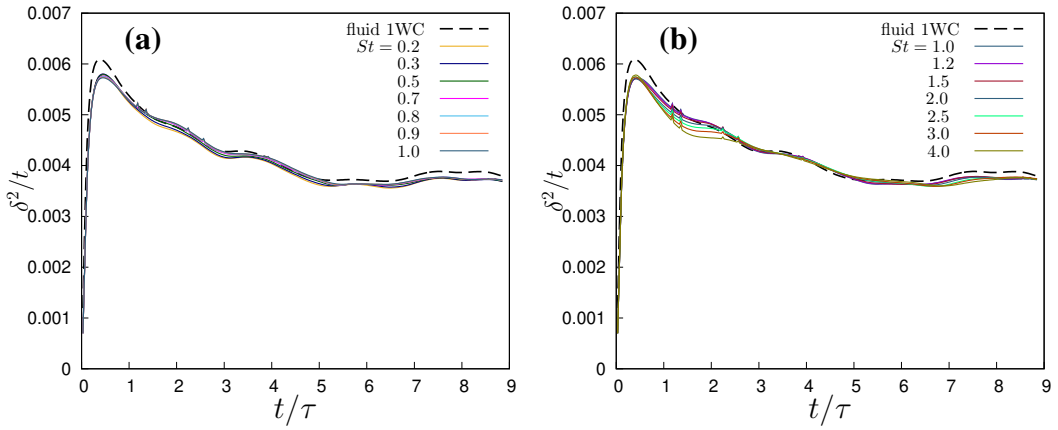

Fig. 5.10 Temporal variation of δ^2/t, for (a) particles with $St \leq 1$; (b) particles with St ≥ 1 in two-way coupling regime ($\varphi_\vartheta = 1.664$).

system. The particle-induced perturbations are captured effectively through the first-moment integrals, reinforcing the quasi-self-similar analysis in the differential form, especially under the influence of particle thermal feedback in two-way thermal coupling regime. For self-similar evolution to occur, both the numerator (total heat flux) and the denominator (total mean temperature integral) must scale in the same way over time. This is because self-similarity implies that the ratio between different physical quantities remains constant as the system evolves. If either the numerator or denominator scaled differently, this would indicate a breakdown of self-similarity, as the system would be evolving in a way that changes the relative importance of heat flux versus temperature distribution. In self-similar systems, it is expected that the magnitudes of the quantities involved in ratios like the one in the equation are of the same order. This ensures that the characteristic parameters of the system (like δ in our case) grow in a predictable, balanced way. If the magnitudes were not the same, it would suggest that one process (e.g., heat flux) is dominating or lagging behind the others (e.g., temperature distribution), which would disrupt the self-similar scaling. The fact that the numerator and denominator grow in the same way and have similar magnitudes is crucial for maintaining self-similar evolution. It means that the total heat flux and total enthalpy are evolving in a balanced manner, ensuring that the system remains self-similar over time. This is a key feature of systems where self-similarity is preserved, as it indicates that the fundamental scaling laws governing the evolution of the fluid-particle system are being followed.

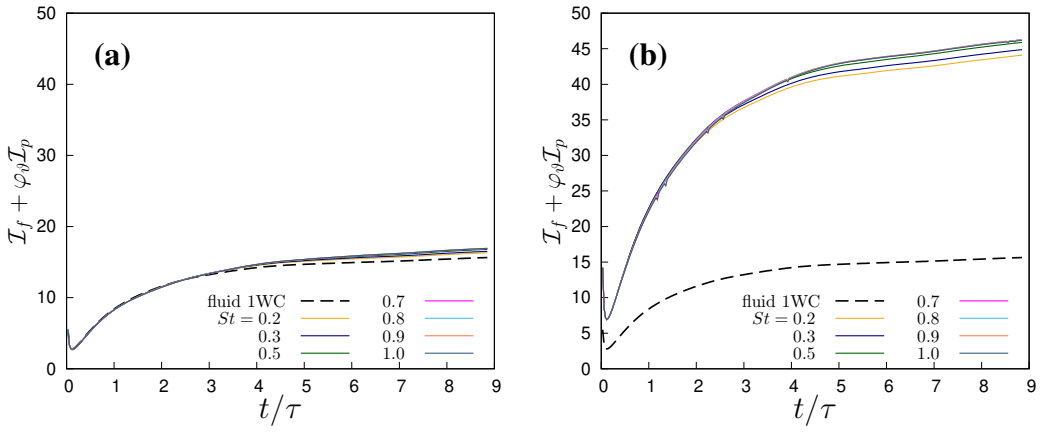

Fig. 5.11 First-order moment of mean total enthalpy integral, in two-way coupling regime relative to the first-order moment of fluid mean enthalpy integral in one-way coupling regime, particles with $St \leq 1$;: (a) only fluid mean enthalpy integral (one- and two-way coupling) $\varphi_\vartheta = 0$ (b) total enthalpy integral, (fluid and particle mean enthalpy integrals) $\varphi_\vartheta = 1.664$.

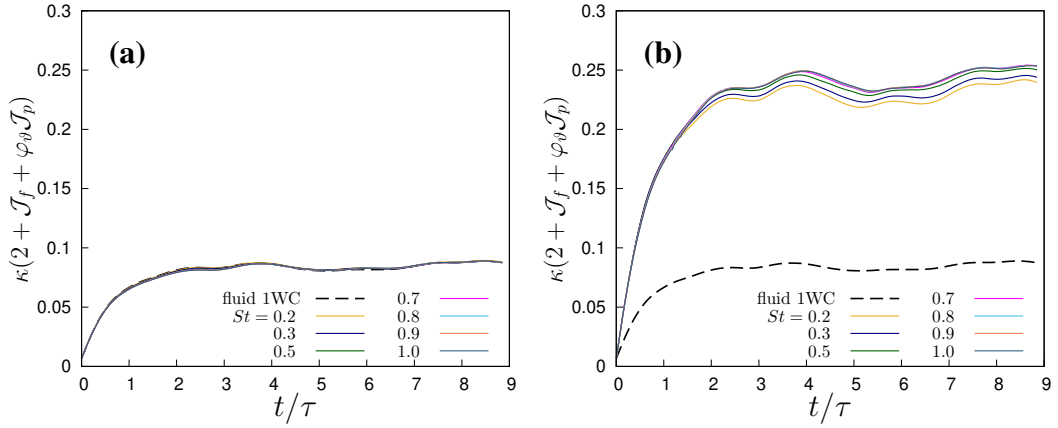

Fig. 5.12 Total heat flux integral, in two-way coupling regime relative to the fluid total heat flux integral unladen flow in one-way coupling, particles with $St \leq 1$;: (a) total heat flux integrals for unladen flow in one- and two -way coupling$\varphi_\vartheta = 0$ (b) total heat flux integral in two-way coupling relative to unladen flow in one-way coupling$\varphi_\vartheta = 1.664$.

Figure 5.11 illustrate the time evolution of the denominator of the equation (5.72) which represent the mean total enthalpy. Both cases, $\varphi_\vartheta = 0$ and $\varphi_\vartheta = 1.664$ are plotted to capture the perturbation of particles with respect to the baseline, the one-way thermal coupling. In case of zero thermal mass fraction, we observe a very tiny deviation from the baseline, and we could say they almost collapse to the perfect self-similar case. We can evidently see how particles increase the magnitude of the mean total enthalpy at $\varphi_\vartheta = 1.664$ but the evolution almost remains in the

same way as the one-way coupling. On the other hand, in figure 5.12 we can see the time evolution of the denominator of the equation (5.72), representing the mean total heat flux, including diffusion, convection and particle contribution. Similar to the numerator behavior, for $\varphi_\vartheta = 0$, all curve collapse to the baseline, while for $\varphi_\vartheta = 1.664$ we can see an enhancement in magnitude due to the particle contribution. However, due to the self-similar behavior of the system both magnitude in the presence of particle increases with the same magnitude keeping the ratio constant as time progresses, resulting in a scaling with $t^{1/2}$ for δ. Implication for turbulence modeling of two-phase flow could be that the particle contribution can be captured through the thermal mass fraction, φ_ϑ which is equal to 1.664 in our flow condition.

Note that while an optimal φ_ϑ value, e.g. in our case which is equal to 1.664, allows for effective heat transfer enhancement and the maintenance of self-similar evolution, a very large φ_ϑ could lead to a reduction in overall heat transfer and potentially disrupt the self-similar behavior of the fluid-particle system. This would occur because the particle-dominated dynamics could overwhelm the fluid thermal processes, leading to a breakdown in the coordinated scaling necessary for self-similarity. In such a case, the system might exhibit complex, non-self-similar behavior, where the evolution of the thermal mixing layer no longer follows a simple scaling law. This could manifest as irregular or non-uniform growth of the thermal layer, with different regions of the system evolving at different rates. At very large φ_ϑ the dynamics of thermal mixing becomes increasingly governed by particle behavior rather than a balanced interaction between the fluid and particles. This could result in different scaling laws for heat flux and temperature distribution, ultimately breaking the self-similarity. However, in some case when φ_ϑ can be larger than the value of this study, within a range where the particle effects are significant but not overwhelming, the system might still maintain self-similar behavior. In such cases, the particles still contribute to the overall thermal evolution without disrupting the coordinated scaling of heat flux and temperature distribution. This scenario corresponds to a situation where the particles have a much higher thermal capacity compared to the fluid. Thus, particles dominate the thermal mixing dynamics, possibly leading to phenomena like thermal choking, where the fluid ability to distribute heat is severely compromised. Physically, this means that the particles are absorbing or releasing heat at such a rate that it overwhelms the fluid ability to transfer heat effectively. Instead of enhancing the overall heat transfer, the particles could start to insulate portions of the fluid or create localized regions where heat transfer is less efficient, leading to a reduction

in the total heat transfer of the fluid-particle system. Thus, maintaining φ_ϑ within a suitable range is crucial for preserving the self-similar evolution of the fluid-particle system.

From the definition of the thermal mass fraction, there are three parameters that determine this quantity, particle volume fraction φ, particle-to-fluid density ratio ρ_p/ρ_0 and heat capacity ratio c_{pp}/c_{p0}. An increase in particle volume fraction can lead to move from two-way coupling regime and consequently lose the validity range of our mean total enthalpy analysis. Since we assumed that we are in two-way coupling range, then non-self similar terms due to the fluid-particle mutual thermal interaction cancel each other out. In denser regime, we might need to consider particle-to-particle interaction, resulting in potential disruption of the self-similarity. Moreover, in different flow configuration, other effects may be present and affect the thermal mixing dynamics. For instance, in wall-bounded flows, the particle-wall interaction can change the evolution of a particle-laden flows over a solid wall. Additionally, particle can be deposited over wall and add another mechanism to the heat transfer. But in general, in the unbounded flows like ours, we can expect that at higher volume fractions, particles can lead to a reduced fluid turbulent motion and, consequently, less effective thermal mixing. Moreover, higher particle volume fraction can generate significant disturbances in the fluid flow field, which can disrupt the scaling behavior needed for self-similarity. This might result in non-uniform temperature distributions and irregular growth of the thermal layer. Meanwhile, high particle-to-fluid density ratio can cause particles to settle or cluster, reducing their interaction with the fluid and thus their contribution to heat transfer. Conversely, a low density ratio may lead to particles being carried more easily by the fluid, potentially enhancing mixing but also possibly reducing their direct thermal impact. If the density ratio is too extreme (either very high or very low), it could lead to a decoupling of particle motion from the fluid flow, thereby disrupting the uniform distribution of heat and breaking the self-similarity. Moreover, particles with much higher heat capacity than the fluid, they can absorb or release significant amounts of heat without much change in their temperature, potentially dominating the thermal dynamics. This could reduce the fluid role in heat transfer and lead to less efficient thermal mixing. A very large heat capacity ratio could result in the particles either taking too long to heat up or cool down or absorbing or releasing too much heat too quickly, leading to localized thermal imbalances that disrupt the self-similar evolution of the system. If the thermal mass fraction is too high due to a combination

of high volume fraction, high density ratio, and high heat capacity ratio, the particles could dominate the heat transfer process. This might result in thermal choking, where the fluid's ability to transfer heat is compromised, leading to reduced overall heat transfer and potentially breaking self-similarity.

In conclusion, the parameters influencing thermal mass fraction φ_ϑ, i.e. volume fraction, density ratio, and heat capacity ratio, play crucial roles in determining the effectiveness of thermal mixing and the preservation of self-similarity in a particle-fluid system. If these parameters are not carefully balanced, the system may experience reduced heat transfer efficiency and disrupted self-similarity, leading to complex, non-uniform thermal dynamics that deviate from the expected self-similar evolution.

5.6 Conclusion

In this chapter, we explored the self-similar and quasi-self-similar evolution of thermal mixing dynamics in a non-isothermal particle-laden turbulent flow utilizing differential and integral representations of the fluid and particle mean temperature equations. The primary goal was to understand how particles influence the dynamics of the thermal mixing process within the flow domain in one- and two-way thermal coupling regimes. We began our analysis by deriving the self-similar solution for the fluid mean temperature field in one-way thermal coupling regime. In this flow regime, fluid mean temperature transport equation reduced to a time-independent ordinary differential equation indicating the perfect self-similarity in the evolution of thermal mixing layer thickness δ. However, particle mean temperature shows a deviation from proper self-similar evolution of fluid mean temperature scaling due to the particle thermal inertia. Accordingly, to formulate this perturbation arising from non-self-similar terms, a quasi-self-similar solution proposed by Taylor expansion around the fluid self-similar solution. This quasi-self similar solution incorporates the effects of a finite thermal relaxation time, τ_ϑ, relative to the evolving flow timescale t. This approach allowed us to capture the gradual divergence from strict self-similarity as the particle thermal inertia becomes significant. Meanwhile, in the two-way coupling regime, where particles and fluid mutually influence each other, both the fluid and particle mean temperature fields contain non-self-similar terms. The interaction between these fields complicates the thermal mixing dynamics, making it necessary

to expand the both fluid and particle mean temperature equations in a series of inverse powers of time. Through this expansion, we derived a set of differential equations that govern the relationship between particle and fluid mean temperatures at various orders of approximation. The analysis revealed that in the two-way coupling regime, the particle heat flux is influenced not only by the fluid mean temperature distribution but also by the temporal evolution of the mixing dynamics. Specifically, we identified how overall heat flux is modified by particles through both diffusive and convective mechanisms. Theoretical analysis, successfully formulate the modification in terms of particle thermal mass fraction, φ_ϑ in a consistent way with DNS results presented for the same flow configuration in chapter 3. The ratio of particle-to-fluid heat fluxes was found to depend on the fluid second spatial derivative and temperature gradient, highlighting the complex interplay between fluid and particle dynamics.

Additionally, the integral analysis and mean total enthalpy assumption in two-way thermal coupling provide a robust framework for understanding the thermal dynamics of our particle-laden turbulent flow. By integrating the fluid and particle mean temperature equations over the spatial domain in which the temperature field is inhomogeneous, we capture the cumulative effects of molecular diffusion, turbulent convection, and particle heat flux. The use of first-moment integrals allows for the validation of quasi-self-similar evolution, offering a clear way to quantify the deviations from baseline fluid behavior due to particle thermal mutual interactions. The mean total enthalpy integral assumption further simplifies the complex interplay between particles and the fluid by providing a global measure of energy distribution across the system. Thanks to this model, the non-self-similar term cancel each other out, simplifying the integral equation. This approach not only validates the self-similar scaling as observed in numerical experiments, but also highlights the critical role of particle thermal feedback in modulating the fluid mean temperature field. The integral analysis shows that while the fluid-particle system tends toward self-similarity, the introduction of particles introduces corrections that must be accounted for in therms of their thermal inertia.

Overall, the integral analysis and mean total enthalpy approach present a coherent methodology for dissecting the thermal behavior of complex, particle-laden turbulent flows, ensuring that both the global and local effects of particles on the thermal field are rigorously accounted for. This lays a strong foundation for further exploration and refinement of self-similarity concepts in multiphase flow systems. In conclusion, the chapter underscored the importance of considering both self-similar and non-self-

similar contributions when analyzing heat transfer in particle-laden turbulent flows. The findings suggest that while particles can enhance heat transfer through altering both thermal diffusion and turbulent convection, this enhancement is sensitive to the particle thermal mass fraction φ_ϑ and the particle inertia and thermal inertia. This analysis provides a framework for optimizing non-isothermal particle-laden flows in practical applications, where controlling the balance between fluid and particle contributions is key to achieving efficient thermal management.

Chapter 6

Thermal caustics

6.1 Introduction

The study of suspended inertial particles in turbulent flows is inherently complex due to the numerous complex phenomena involved. The influence of these phenomena on fluid-particle interactions varies with particle inertia, and particle thermal inertia in non-isothermal flows. Key phenomena include preferential concentration, turbophoresis, inter-particle collisions, path-history effects, sweep-stick mechanisms, caustics and thermal caustics. Preferential concentration, or the clustering of inertial particles in certain flow regions, depends mainly on particle inertia and how particles interact with different turbulent scales. The particle density is also crucial for characterizing clustering, and the range of turbulent scales affects clustering based on different turbulent structures. Large-scale coherent structures can induce different clustering behaviors compared to small-scale mechanisms. For example, in the low-inertia regime, particles cluster according to their interaction with local vortical structures, with centrifugal forces causing heavy particles to be expelled from vortices and light particles to be attracted to vortex centers. In the low-inertia regime, particles tend to be correlated with fluid motion, resulting in non-uniform particle distribution. Heavy particles often cluster in high-strain and low-vorticity regions, while light particles do the opposite [105–107]. Particle thermal inertia also changes the thermal behavior of particle in the flow, and in some cases make the particles cluster according to their thermal interactions with fluid turbulent temperature field, creating a sort of turbulence-induced thermophoresis. Due to this effect,

particles may tend to cluster in high fluid temperature gradient regions, as identified as temperature fronts by Bec et al. in [11]. Moreover, turbophoresis in homogeneous and isotropic turbulence, as studied by Bec et al. in [108], demonstrates that this effect is caused by the intrinsic instantaneous non-uniformities of turbulence, which are present throughout the inertial range. The findings indicated that inertial particles are ejected from highly active regions of the flow, leading to their concentration in less turbulent areas.

Goto et al. introduced sweep-stick mechanism which incorporate the multiscale cause of clustering especially in high Reynolds number flows. They argued that this mechanisms can better explain the reason of clustering in different turbulent range than the purely centrifugal mechanism which is considered more effective in short separation distances. Their results showed how inertial particles tend to stick to stagnation points of the fluid acceleration field and are thus swept along with them by the local fluid velocity to the region with high fluid acceleration [109]. In fact, sweep-stick mechanism is an extension of the centrifugal phenomenology to the particle response time within the turbulence inertial range to formulate the clustering in this turbulent range. As demonstrated by Chen et al. in [110] and Coleman et al. [111] there exist a strong correlation between the particle clustering and the location of fluid nearly zero-acceleration points especially at very high Reynolds number flows as confirmed by DNS results. Apart from these local effects, there is a non-local mechanism called path-history effect, that can effectively create a the non-uniform distribution of particles. This mechanism is more pronounced in higher particle inertia range ($\mathrm{St} \geq 1$), in which particles sample and respond to the history of the turbulent motions instead of the local fields along their trajectories [112].

Another important event that should be understood as well as the other mechanisms, is caustics in velocity field. This event, usually happen for larger inertial particles ($\mathrm{St} \geq 1$) causing that particles' trajectories cross and bringing two particle with different velocity very close together. As a result of such event, particle velocity field shows an explosive evolution creating a finite-time singularity in particle velocity, and consequently in particle velocity gradient and number density fields. Sling effect is identified as the cause of caustics in particle velocity field when particle inertia exceeds a certain threshold $\mathrm{St} \gg 1$, making their trajectories cross. In order to analyze the caustics, the particle velocity tensor dynamics is commonly investigated, to detect the event in which particle velocity develops blowup and becomes multivalued. Analyzing the collision rate of high inertia particles is also used to identified

the caustics events through the caustic-induced collision identifications. Moreover, the non-zero relative velocities of particles at small separations increase significantly as the Stokes number increases, in particular when it is above a threshold of the order of one Consequently, the relative velocity of inertial particle pairs in much larger than the fluid relative velocity at the same separation distance. Caustics forms as the phase-space manifold folds and, particle velocity at a given point becomes multi-valued, causing large velocity differences between nearby particles with very close trajectories. At the edge of a caustic the particle velocity gradient tensor, as an analogous measure to the fluid strain-rate rate tensor, shows finite-time singularity, having its trace diverge to minus infinity [113].

The caustics identification in particle-laden turbulent flows has been studied in last decades by using both Eulerian-Lagrangian and Eulerian-Eulerian simulations. For instance, Meneguz et al. in [114] used a full Lagrangian method to measure the rate of singularities in particle number density field using an Eulerian-Lagrangian DNS of homogeneous and isotropic turbulent flow. They assessed the particles' compressibility history and the buildup of high concentrations (singularities) within a region of caustics where particle trajectories cross. They identify a critical value of the particle Stokes number at which the overall compressibility of the particle concentration shifts from compression to expansion, and to determine the presence of singularities within the particle concentration field. The dynamics of rate of compressibility is computed by computing the divergence of particle velocity field along its trajectory. Then they computed all the spatially averaged moments of particle number density field by particle averaging of this compressibility tensor. Computed particle-averaged compressibility changes sign from negative to positive when the Stokes number increases and crosses a critical value. Boffetta et al. in [115] used an Eulerian-Eulerian model to investigate the regularity and compressibility of particle velocity field, in a one-way coupling regime neglecting the collision and gravity. The Eulerian model was based on assumption that particle velocity can be uniquely defined in every point in flow domain by a smooth field different from the fluid velocity field. However, the particle velocity field cannot be smooth in all times due to the presence of sling effect that generates shock-like structure or caustics in particle velocity and singularity in particle number density field for higher inertia particles. They used a Lagrangian model to capture the singularity in particle number density field, by using dynamical system tools, since the Eulerian model for higher Stokes number is incapable of capturing the caustic event an it is blow

up. Compressibility of particle velocity or particle number densty in Eulerian and Lagrangian form, has been commonly performed by using the-order-of-magnitude analysis, of the divergence of the particle velocity. An estimate usually used in numerical simulations to determine the caustic when the magnitude is significantly exceeds the assumed threshold.

Recently, Lee et al. in [116] develop an Eulerian approach to study the particle-laden turbulent flow with the presence of gravity. Particle Eulerian velocity field is assumed to be smooth in space and time, right before the caustic-induced collision makes it blowup. The effect of gravity on the occurrence of such event has been investigated in different flow conditions. A critical Stokes number has been introduced above which a collision starts occurring. They found that caustics is more likely to happen in regions with strongly compressive and weak stretching motion. For blowup identification they also studied the dynamics of particle velocity gradient tensor in terms of its eigenvalues. By analyzing the divergence of particle velocity field, the singularity in particle number density has been also identified.

On the other hand, while the concept of caustics in particle velocity fields has been well-established, the notion of thermal caustics has been introduced more recently by Carbone et al. [32] and Saito et al. [87]. Thermal caustics describe the behavior of fluid-particle thermal interactions where particles experience significant temperature differences, leading to non-smooth temperature profiles even at moderate thermal Stokes numbers. Current theoretical approaches to thermal caustics often focus on analyzing particle path history and its effect on temperature differences, drawing parallels with velocity caustics. In this approach, thermal caustics is assumed to occur when temperature difference between particle pairs is much larger than the fluid temperature difference at the same separation. The existing methodology in investigating thermal caustics is based on the similar analysis on caustics formation by studying the behaviour of velocity difference between particle pairs. These approaches generally involve examining how spatial clustering and preferential sampling of fluid temperature by particles contribute to thermal caustics. Although the concept of thermal caustics has been introduced and discussed in the literature, with contributions from Carbone et al. and Saito et al., there is still a lack of a comprehensive theoretical framework akin to the established theory for velocity caustics, which typically involves the dynamics of the particle velocity gradient tensor. Therefore, in this chapter, we propose a novel theory to characterize the formation of thermal caustics based on the dynamics of the particle temperature

gradient. This new theory aims to provide a more detailed analysis of thermal caustics compared to existing approaches, which primarily focus on particle path history effects. By developing this framework, we hope to advance the understanding of thermal caustics in non-isothermal particle-laden turbulent flows.

6.2 Thermal caustic formation theory

We start developing our new theory to characterize the thermal caustics, by recalling the Lagrangian equations of laden inertial particles in a non-isothermal turbulent flow under the assumptions in chapter 3. Accordingly, given the Lagrangian trajectory $\mathrm{d}\boldsymbol{X}_p/\mathrm{d}t = \boldsymbol{V}_p$, the particle acceleration and temperature time derivative evolution equations are given by

$$\frac{\mathrm{d}}{\mathrm{d}t}\boldsymbol{V}_p(t) = \frac{1}{\tau_v}\left(\boldsymbol{u}(t,\boldsymbol{X}_p) - \boldsymbol{V}_p\right) \tag{6.1}$$

$$\frac{\mathrm{d}}{\mathrm{d}t}\Theta_p(t) = \frac{1}{\tau_\vartheta}\left(T(t,\boldsymbol{X}_p) - \Theta_p\right) \tag{6.2}$$

As discussed in section 6.1 to formulate the caustics in particle-laden turbulent flows, it is customary to introduce a filed-like equations for suspended particles, and study the dynamics of the corresponding velocity gradient tensor [117–119]. The dynamics of the divergence of the particle velocity field can measure the compressiblity which is essential to identify the caustics. The finite time blowup in the velocity gradient tensor after a critical Stokes number causes the singularity in particle number density field. Since the thermal caustics is rooted in formation of caustics, we start our discussion with the caustics formation and subsequently we address the main objective, i.e. developing and proposing our theory for the formation of thermal caustics. In our case, we also use a field-like equations for the temperature field. Particle Eulerian number density, velocity field and temperature field has been already derived in chapter 4. Thus, particle velocity field $\boldsymbol{v}$ and temperature field ϑ which are assumed to be uniquely determined by the Eulerian position $\boldsymbol{x}$, are given by

$$\frac{\mathrm{D}_p}{\mathrm{D}t}\boldsymbol{v}(t,\boldsymbol{x}) = \frac{1}{\tau_v}\left(\boldsymbol{u}(t,\boldsymbol{x}) - \boldsymbol{v}(t,\boldsymbol{x})\right) \tag{6.3}$$

$$\frac{\mathrm{D}_p}{\mathrm{D}t}\vartheta(t,\boldsymbol{x}) = \frac{1}{\tau_\vartheta}\left(T(t,\boldsymbol{x}) - \vartheta(t,\boldsymbol{x})\right) \tag{6.4}$$

where $\mathrm{D}_p/\mathrm{D}t$ should be interpreted as particle material derivative, $\partial/\partial t + v_j\partial/\partial x_j$. For a generic flow the existence of $\boldsymbol{v}$ and ϑ is not guaranteed a priori, and it breaks when a caustic is formed. However, caustics are concentrated in small regions in space and have a lifetime of order τ_v [120, 121], so that these equations keep its validity before the formation, so that if these equations generate a smooth single-valued solution $(\boldsymbol{v},\vartheta)$ then the underlying assumption is valid and self-consistent, while in case of the formation of a caustic or thermal caustic, their spatial derivatives diverge at some time. The problem of the generation of caustics and thermal caustics leads to the conditions under which the gradient of $\boldsymbol{v}$ or the gradient ϑ have a finite time blow-up, so that equations (6.3) and (6.4) can still be used as a tool to analyze the path to caustics. As it discussed before, the identification of caustics and thermal caustics can be done both by analyzing the particle governing equations in Eulerian frame or Lagrangian frame. Thus, before deriving the complementary equations which are needed for our analysis, we provide the mapping from Eulerian and Lagrangian particle governing equations. However, in Eulerian-Lagrangian analysis of particle-laden turbulent flows, particle governing equations are naturally in a Lagrangian form if, alongside the Eulerian coordinates $(t,\boldsymbol{x})$, the Lagrangian coordinates of the particles $(t,\boldsymbol{X}_p)$, defined by

$$\frac{\partial}{\partial t}\boldsymbol{x}(t,\boldsymbol{X}_p) = \boldsymbol{v}(t,\boldsymbol{x}), \qquad \boldsymbol{x}(0,\boldsymbol{X}_p) = \boldsymbol{X}_p. \tag{6.5}$$

Equation (6.5) is the evolution equation of the Eulerian trajectory of the particle p, where $\boldsymbol{x} = \boldsymbol{x}(t,\boldsymbol{X}_p)$ is a mapping from a fixed material point $\boldsymbol{X}_p$, i.e. the position of the centre of the infinitesimally small volume surrounding each initial time $t = 0$, to the current Eulerian point $\boldsymbol{x}$ at particle trajectory at time t. From the continuum mechanics, we know that particle deformation-rate tensor, $\boldsymbol{F}$ acts as a linear map to generate a line element $\mathrm{d}\boldsymbol{x}$ by transforming the material line element $\mathrm{d}\boldsymbol{X}_p$ such that, $\mathrm{d}\boldsymbol{x} = \boldsymbol{F}\mathrm{d}\boldsymbol{X}_p$. Therefore, particle deformation-rate tensor is defined by

$$F_{ij} = \frac{\partial x_i(t, \boldsymbol{X}_p)}{\partial X_j} \tag{6.6}$$

Particle deformation-rate tensor evolves according to the following equation

$$\frac{\partial F_{ij}}{\partial t} = \sigma_{ik} F_{kj}, \qquad F_{ij}(0, \boldsymbol{X}_p) = \delta_{ij} \tag{6.7}$$

where $\sigma_{ik} = \partial v_i(t, \boldsymbol{X}_p)/\partial X_{p,k}$ denotes the material particle velocity gradient tensor. We also know that a scalar known as the Jacobian determinant J can be related to the deformation-rate tensor through $J(t, \boldsymbol{X}_p) = \det F_{ij}(t, \boldsymbol{X}_p)$ and can measure the change of volume from the reference frame. This quantity is very important in studying the caustics since it can quantify the compressibility of the particle velocity field, and its dynamics is influenced significantly by the occurrence of caustics. Formation of caustics, generate a discontinuity in this tensor leading to a finite-time blowup in particle velocity, velocity gradient tensor and number density field [116]. Corresponding Eulerian particle velocity gradient tensor $\boldsymbol{\sigma}$ and particle temperature gradient vector $\boldsymbol{\xi}$ can be defined by,

$$\sigma_{ij} = \frac{\partial v_i(t, \boldsymbol{x})}{\partial x_j} \qquad \xi_j = \frac{\partial \vartheta(t, \boldsymbol{x})}{\partial x_j}. \tag{6.8}$$

The studies have reported that the dynamics of σ_{ij} can explain the formation of velocity caustics through the sling effect for very large inertia particles in both collisional and non-collisional flows [118, 116]. In collisional regimes, indeed inter-particle collision increases the likelihood the caustics events. On the other hand, for low inertia particles, in which the particle velocity and its gradient are smooth in time and space, this quantity can describe the clustering of particles in high strain-rate regions. In some works carrier flow structure functions, has been used to find the multifractal dimension of particle clustering and spatial distribution in different particle inertia regimes [122, 123]. Ravichandran et al. [124] used the same notion of particle velocity gradient dynamics in low and intermediate Stokes number to investigate the heavy particles clustering in vortical flows. Recently, Esmaily et

al. [119] employed the idea of the particle velocity compressible field to analyze the clustering and dispersion of particles subject to a homogeneous and isotropic turbulent flow in different inertia range. Meibohm et al. 2023, in [125] studied the particle velocity gradient dynamics to find the caustics in the very low inertia range when $\mathrm{St} \ll 1$. They employed optimal fluctuation theory to model caustic formation in this low inertia range. Their finding showed caustics can even be formed in the low inertia range by a spatial instability in particles neighbourhoods. They showed the formation occurs when the fluid velocity gradients in the Q-R plane exceed a large threshold. Bec et al. in [126] discussed the recent statistical approach in quantification of particle clustering and identification of caustics in different range of particle Stokes numbers by analyzing the compressibility of the particle velocity field. They have shown how these mechanisms are characterized by the expansion and contraction of the particle volume in phase space.

By taking the gradient of the equations (6.3) and (6.4) the evolution equations for particle velocity gradient tensor σ_{ij} and particle temperature gradient vector ξ_j can be derived as

$$\frac{\mathrm{D}_p \sigma_{ij}(t)}{\mathrm{D}t} = \frac{A_{ij} - \sigma_{ij}}{\tau_v} - \sigma_{ik}\sigma_{kj}, \tag{6.9}$$

$$\frac{\mathrm{D}_p \xi_j}{\mathrm{D}t} = \frac{G_j - \xi_j}{\tau_\vartheta} - \xi_k \sigma_{kj} \tag{6.10}$$

where $A_{ij}(t,\boldsymbol{x})$ and $G_j(t,\boldsymbol{x})$ are the fluid velocity gradient tensor and temperature gradient vector at particle position respectively. Their evolution equations have been derived in chapter 2 and are given by

$$\frac{\mathrm{D}A_{ij}}{\mathrm{D}t} = -\frac{1}{\rho_0}\frac{\partial^2 p}{\partial x_i \partial x_j} + \nu \frac{\partial A_{ij}}{\partial x_k \partial x_k} - A_{ik}A_{kj} \tag{6.11}$$

$$\frac{\mathrm{D}G_j}{\mathrm{D}t} = \kappa \frac{\partial^2 G_j}{\partial x_k \partial x_k} - G_k A_{kj} \tag{6.12}$$

where $\mathrm{D}/\mathrm{D}t = \partial/\partial t + u_j \partial/\partial x_j$ is the fluid material derivative. As it has been discussed in chapter 2, the velocity gradient is enhanced by the non-linear and local term $-\boldsymbol{A}^2$ stretching-tilting term in (6.11) and is damped by both the diffusion term or

viscous Laplacian term and the non-local pressure Hessian term, which act in a way to reorientate the fluid velocity gradient tensor [42, 75, 43], while, on the contrary, the temperature gradient is only driven by the stretching due to the velocity gradient and the diffusion (e.g. [45]). Both equations are not closed from a Lagrangian point of view, because all the spatial derivative are unknown, and both the diffusive terms and the pressure Hessian require modelling, still they are they key for the understanding of small-scale phenomena, and stochastic models have been able to reproduce some important features, like the onset of a non Gaussian probability density function, intermittency, the average alignments of vorticity and strain-rate. Equations ((6.11)-(6.12) and equations ((6.9)-(6.10)) show a fundamental difference, due to the lack of stabilizing terms, like the diffusion and pressure Hessian, which prevent a finite time blow-up in the fluid equations. The properties of equations (6.9) have been studied by [120, 127, 118, 128, 116], which are dictated by the presence of the quadratic term on the right-hand side, which leads to a singularity. Since the particle dynamics in phase-space is dissipative [126], the volume in phase-space contracts and particle dynamics occurs on a multifractal attractor. Bec et al. in [126] depicts how the dynamics of particle which is dissipative and chaotic, stretches, folds, and contracts, and consequently making particle trajectories converge to a phase-space time-evolving attractor. In order to understand the physical properties of the suspended particles, we need to analyze this attractor by dynamical system theory [126]. Gustavsson et al. analyzed the dynamics of particle field gradient tensor and its relation to the particle compressibility sigularity due to caustics events by using DNS under the hypothesis of random uncorrelated motion (RUM) which is dominant in higher particle inertia range [118]. In flows with sufficiently intense turbulence, RUM which is based on a gas-kinetic model is used to analysis the particle clustering by non-local effects,e.g path-history clustering. In intense turbulence, particles are subjected to random, rapidly fluctuating forces due to the turbulent eddies. This randomness can lead to uncorrelated particle velocities, which is where the RUM model becomes applicable. These effects consider how the history of a particle's movement through different turbulent regions affects its tendency to cluster with other particles. [129, 118]. Furthermore, they characterized the effect of particle spatial distribution on collision rate. It has been found that the local particle number density is enhanced by this particle clustering effect, resulting in an enhancement in the collision rate especially for intermediate particles. On the other hand, at higher particle inertia range, where sling effect is dominant, the non-zero relative velocity

between two particles is increased. Sling effect brings particle arbitrarily close to each other, even when particles have very different velocities. This mechanisms is considered as caustics-induced collisions that occurs at high particle inertial range resulting from particles being slung by vertices [128]. This phenomenon can also be understood in terms of caustics in the phase space of the suspended particles [113], and has recently been investigated experimentally [128]. A particularly effective description of the collision-rate enhancement in terms of a stochastic model for the pdf of pairs of particles has been proposed by Zaichik et al. [105].

Specifically, we intend to apply the same theoretical framework that has been utilized for clustering characterization and caustics formation across low, intermediate, and high particle inertia ranges to the analysis of turbulence-induced turbophoresis and thermal caustics. Therefore, as we have done in chapter 3, we can express particle Lagrangian instantaneous velocity and temperature equations in terms of particle acceleration and particle temperature time derivative

$$V_{p,i} = u_i - \tau_v \frac{\mathrm{d}V_{p,i}}{\mathrm{d}t} \tag{6.13}$$

$$\Theta_p = T - \tau_\vartheta \frac{\mathrm{d}\Theta_p}{\mathrm{d}t} \tag{6.14}$$

Furthermore, by using the definition of particle material derivatives, we can expand the particle velocity and temperature field equations in terms of higher-order relaxation times as

$$\boldsymbol{v}(t,\boldsymbol{x}) = \boldsymbol{u}(t,\boldsymbol{x}) - \tau_v \frac{\mathrm{D}\boldsymbol{u}}{\mathrm{D}t} + \tau_v^2 \left[\frac{\mathrm{D}\boldsymbol{u}}{\mathrm{D}t} \cdot \boldsymbol{A} + \frac{\mathrm{D}_p}{\mathrm{D}t} \left(\frac{\mathrm{D}\boldsymbol{u}}{\mathrm{D}t} \right) \right] + \mathscr{O}(\tau_v^3) \tag{6.15}$$

$$\begin{aligned} \vartheta(t,\boldsymbol{x}) = T(t,\boldsymbol{x}) &- \tau_\vartheta \frac{\mathrm{D}T}{\mathrm{D}t} + \tau_v \tau_\vartheta \frac{\mathrm{D}\boldsymbol{u}}{\mathrm{D}t} \cdot \boldsymbol{G} - \tau_\vartheta \tau_v^2 \left[\frac{\mathrm{D}_p}{\mathrm{D}t} \left(\frac{\mathrm{D}\boldsymbol{u}}{\mathrm{D}t} \right) \cdot \boldsymbol{G} + \frac{\mathrm{D}\boldsymbol{u}}{\mathrm{D}t} \cdot (\boldsymbol{A} \cdot \boldsymbol{G}) \right] \\ &+ \tau_\vartheta^2 \left[\frac{\mathrm{D}_p}{\mathrm{D}t} \left(\frac{\mathrm{D}T}{\mathrm{D}t} \right) \right] - \tau_v \tau_\vartheta^2 \left[\frac{\mathrm{D}\boldsymbol{G}}{\mathrm{D}t} \frac{\mathrm{D}\boldsymbol{u}}{\mathrm{D}t} \right] - \tau_v^2 \tau_\vartheta^2 \left[\frac{\mathrm{D}\boldsymbol{u}}{\mathrm{D}t} \cdot \boldsymbol{A} \right] + \mathscr{O}(\tau_\vartheta^3 \tau_v, \tau_\vartheta \tau_v^3) \end{aligned} \tag{6.16}$$

The equations (6.15) and (6.16) captures both linear and nonlinear interactions between the particle's velocity and temperature fields, incorporating the effects of higher-order relaxation times. The τ_v^2 term in the velocity expansion includes the

effects of velocity gradients tensor on the particle's motion, capturing how the fluid's strain rate influences the particle's acceleration. The presence of cross-terms like $\tau_v\tau_\vartheta$ indicates interactions between the particle's dynamics and thermodynamics. These terms reflect how changes in the fluid's velocity field can influence the temperature evolution of the particle, and vice versa. These equations describe the coupling between the particle and the fluid, showing how the particle's state evolves due to the surrounding fluid's influence. The expansions highlight that this coupling is not only dependent on the instantaneous fluid conditions but also on the history of those conditions via higher-order terms. In turbulent flows, these equations are crucial because turbulence introduces rapid and complex changes in the fluid's velocity and temperature fields. The higher-order terms become significant in capturing how particles behave in such environments, including effects like clustering, preferential concentration, and caustic formation. The inclusion of higher-order terms improves the accuracy of models that predict particle behavior in fluid flows. This is particularly important in applications like aerosol dynamics, cloud formation, and industrial processes involving particle-laden flows. If we neglect the higher order terms in these equation, we can derive the particle velocity and temperature equations for low-inertia and low-thermal inertia particles which are highly correlated with fluid structures. Therefore, the equations (6.15) and (6.16) reduce to

$$\boldsymbol{v}(t,\boldsymbol{x}) = \boldsymbol{u}(t,\boldsymbol{x}) - \tau_v \frac{\mathrm{D}\boldsymbol{u}(t,\boldsymbol{x})}{\mathrm{D}t} \tag{6.17}$$

$$\vartheta(t,\boldsymbol{x}) = T(t,\boldsymbol{x}) - \tau_\vartheta \frac{\mathrm{D}T(t,\boldsymbol{x})}{\mathrm{D}t} \tag{6.18}$$

In this range of particle inertia and thermal inertia the dynamics of turbulent fluid flow is dominant over particle dynamics and thermodynamics. For tracers and thermal tracers with zero inertia and thermal inertia both particle velocity and temperature are equal to the fluid's fields. Meanwhile, for inertial and thermal inertial particles even with very small inertia and thermal inertia there is a difference between fluid particle trajectory and inertia particle path which is proportional to the particle relaxation times. Accordingly, in tracer limit, the particle acceleration and temperature derivative can be equal to the fluid acceleration and fluid temperature derivative computed at particle position along particle Lagrangian path. Therefore,

particle acceleration and temperature time derivative in terms of seen-by-particle quantities are given by

$$\frac{\mathrm{D}_p \boldsymbol{v}(t,\boldsymbol{x})}{\mathrm{d}t} \simeq \frac{\mathrm{D}\boldsymbol{u}(t,\boldsymbol{x})}{\mathrm{D}t} \tag{6.19}$$

$$\frac{\mathrm{D}_p \vartheta(t,\boldsymbol{x})}{\mathrm{d}t} \simeq \frac{\mathrm{D}T(t,\boldsymbol{x})}{\mathrm{D}t} \tag{6.20}$$

By using the field equations of particle velocity (6.3) and particle temperature (6.4), in this limit, the particle velocity and temperature in terms of fluid field variable seen by particle in an Eulerian description are given by

$$\boldsymbol{v}(t,\boldsymbol{x}) = \boldsymbol{u}(t,\boldsymbol{x}) - \tau_v[\partial_t \boldsymbol{u}(t,\boldsymbol{x}) + \boldsymbol{u}(t,\boldsymbol{x}) \cdot \boldsymbol{A}(t,\boldsymbol{x})] \tag{6.21}$$

$$\vartheta(t,\boldsymbol{x}) = T(t,\boldsymbol{x}) - \tau_\vartheta[\partial_t T(t,\boldsymbol{x}) + \boldsymbol{u}(t,\boldsymbol{x}) \cdot \boldsymbol{G}(t,\boldsymbol{x})] \tag{6.22}$$

where as it is given in equation (6.5), the Eulerian particle position is obtained through the mapping from material particle point $\boldsymbol{X}_p$ at initial time $t = 0$, to the position $\boldsymbol{x}$ at time t throgh $\boldsymbol{x}(t,\boldsymbol{X}_p)$. If we take divergence from equation (6.21), the trace of the equation is derived which can give us the evolution of particle volume in the tracer limit as

$$\nabla \cdot \boldsymbol{v}(t,\boldsymbol{x}) = -\tau_v \nabla \cdot [\boldsymbol{u}(t,\boldsymbol{x}) \cdot \boldsymbol{A}(t,\boldsymbol{x})] \tag{6.23}$$

The divergence of particle velocity field is connected to the particle number density field through

$$\frac{\mathrm{D}_p n}{\mathrm{D}t} = \frac{\partial n}{\partial t} + v_j \frac{\partial n}{\partial x_j} = -n\frac{\partial v_i}{\partial x_i} = -n\sigma_{ii}(t) = -n\mathrm{tr}(\sigma_{ij}) \tag{6.24}$$

Let us express equation (6.23) using the symmetric part of the fluid velocity gradient tensor, the strain-rate tensor $\boldsymbol{S}$ and its anti-symmetric part, the rotation-rate tensor $\boldsymbol{\Omega}$, and its second invariant Q introduced in Chapter 2.

$$\nabla \cdot \boldsymbol{v} = -\frac{\tau_v}{4}[\boldsymbol{S}^2 - \boldsymbol{\Omega}^2] = -\frac{\tau_v}{4}Q \tag{6.25}$$

This representation aids in characterizing the distribution of the particle field in cases of low particle inertia. Heavy particles are ejected from vortical structures when $\boldsymbol{\Omega} > \boldsymbol{S}$ and $Q > 0$, leading to clustering in regions of high strain where $\boldsymbol{S} > \boldsymbol{\Omega}$ and $Q < 0$. Haller et al. in [130] have shown, in a fixed frame of reference, that Q, cannot be negative in a region with closed streamlines. This can be inferred that that heavy particles are incapable of clustering near a vortical region. Furthermore, the sign of this divergence can determine the region where particles cluster (negative sign) or dispersed (positive sign). Despite the fluid velocity being incompressible and divergence-free ($\nabla \cdot \boldsymbol{u}(t,\boldsymbol{x}) = 0$), the particle velocity field can exhibit significant compressibility, even in the tracer limit. This arises because particles often cluster in areas of high number density, leading to a particle velocity field that is not divergence-free. Consequently, in regions where heavy particles are expelled, we observe $\nabla \cdot \boldsymbol{v} > 0$, whereas in regions where particles accumulate, $\nabla \cdot \boldsymbol{v} < 0$, indicating convergence in the particle velocity field. This equation also indicates that particles tend to cluster in regions of pressure maxima (often found outside vortices). The implication for the collision rate is that, in the limit of small Stokes number, particle inertia contributes to the compressibility of the particle velocity field. This increased compressibility leads to a higher probability of collisions, as particles become concentrated in localized regions. The equation (6.25) is valid only in the zero-inertia limit. For particles with larger Stokes numbers, which are ballistically decorrelated from the local fluid structures and experience trajectory crossing, due to sling effect, the particle velocity field $\boldsymbol{v}(t,\boldsymbol{x})$ is no longer a well-defined function of spatial coordinates. This non-local behavior in time can result in the particle velocity being multivalued and can lead to caustics in the fluid velocity field [117]. Note that in thermally driven flows,e.g. in buoyancy-driven flows, the clustering effect for particles with small Stokes numbers must be compared with the intensity of local temperature gradients. Preferential concentration is more pronounced in regions with strong negative thermal gradients, a condition frequently encountered in thermal boundary layers [131]. The equation (6.25) can be aslo expressed in terms of particle velocity gradient tensor σ_{ij} and fluid velocity gradient tensor A_{ij}. Indeed, this is the

trace equation of the vparticle velocity gradient tensor equation (6.9) in zero-inertia limit where St $\ll 1$.

$$\sigma_{ii} = \frac{\partial v_i}{\partial x_i} = -\tau_v[\frac{\partial u_j}{\partial x_i}\frac{\partial u_i}{\partial x_j} + u_j\frac{\partial^2 u_i}{\partial x_i \partial x_j}] = -\tau_v[A_{ij}A_{ji}] \tag{6.26}$$

In order to analyze the sling effect in this range of inertia, in addition to the compressibility of the particle velocity field, which is characterized by the trace of particle velocity field, we also need to assess the dynamics of particle velocity field. Therefore, we can easily take a gradient of the equation (6.21).

$$\boldsymbol{\sigma}(t,\boldsymbol{x}) = \boldsymbol{A}(t,\boldsymbol{x}) - \tau_v\nabla[\partial_t \boldsymbol{u}(t,\boldsymbol{x}) + \boldsymbol{u}(t,\boldsymbol{x})\cdot\boldsymbol{A}(t,\boldsymbol{x})] \tag{6.27}$$

The equation (6.27) can be also expressed in terms of fluid velocity gradient tensor as

$$\sigma_{ij} = A_{ij} - \tau_v[\frac{\mathrm{D}A_{ij}}{\mathrm{D}t} + A_{ik}A_{kj}] \tag{6.28}$$

In the tracer limit, equation (6.28) remain smooth in time and space since its dynamics is governed by the local fluid velocity gradient samples by particles along their Lagrangian path. The non-linear term $\boldsymbol{A}^2$ does not show any explosive evolution since it is damped by the pressure Hessian and diffusion terms. Consequently, the particle velocity gradient tensor never blow up in time and smoothly evolve avoiding the particle number density from discontinuity.

Analogously, a similar theoretical analysis can be applied to the particle temperature field to characterize the thermodynamics of particles in the zero-inertia and zero-thermal inertia limits. Thus, equation (6.22) is used to describe the thermal behavior of inertial particles in this regime. Given that the thermal behavior of inertial particles, even in the tracer limit, is significantly influenced by the fluid temperature gradient at the particle's position, we first take the gradient of equation (6.22) to obtain the particle temperature gradient field. The evolution of this gradient, coupled with the fluid velocity and temperature seen-by-particle fields, can then be used

to describe turbulence-induced clustering in the presence of the fluid temperature gradient at both the tracer and thermal tracer limits. Thus, particle temperature gradient fields in this limit reads

$$\boldsymbol{\xi}(t,\boldsymbol{x}) = \boldsymbol{G}(t,\boldsymbol{x}) - \tau_\vartheta \nabla[\partial_t T(t,\boldsymbol{x}) + \boldsymbol{u}(t,\boldsymbol{x}) \cdot \boldsymbol{G}(t,\boldsymbol{x})] \tag{6.29}$$

The equation (6.29) can be simplified and re-written in terms of fluid velocity gradient tensor and fluid temperature gradient vector as

$$\xi_j = G_j - \tau_\vartheta [\frac{\mathrm{D}G_j}{\mathrm{D}t} + G_k A_{kj}], \tag{6.30}$$

The equation (6.30) shows how particle temperature gradient is influenced by fluid velocity and temperature gradient according to their thermal inertia. Note that in the equation (6.30) the effect of particle inertia cannot be explicitly seen, however; it influences the dynamics of $\boldsymbol{\xi}$ through the coupling with $\boldsymbol{A}$. On the other hand, as explained earlier, the evolution of particle velocity tensor remain smooth in the low-inertia limit, obeying the equation (6.28). As expected, no caustics and thermal caustics occur in this range of particle inertia and thermal inertia. The equation (6.30) can also account for the turbulence-induced thermophoresis that makes particles cluster in a high fluid temperature gradient zones, or temperature fronts as observed in [11, 32]. Stretching-tilting the fluid temperature gradient by fluid velocity gradient tensor can determine and explain the preferential sampling of the fluid temperature field in low-inertial and low thermal inertia range. Furthermore, we can understand why maximum particle contribution to the heat flux in mixing layer, takes place for intermediate inertial particle, as seen in chapter 3, since the clustering and turbulence-induced clustering in high fluid temperature fronts are most active. Let's now examine the scenarios with higher particle inertia and thermal inertia, where caustics and thermal caustics are more likely to occur. As these inertial effects increase, particles become less correlated with the local fluid fields, and non-local influences become more significant. Consequently, the local effects can be neglected, allowing us to focus on the simplified forms of the equations provided in (6.9) and (6.10).

$$\frac{\mathrm{D}_p \sigma_{ij}(t)}{\mathrm{D}t} \simeq -\sigma_{ik}\sigma_{kj}, \tag{6.31}$$

$$\frac{\mathrm{D}_p \xi_j}{\mathrm{D}t} \simeq -\xi_k \sigma_{kj} \tag{6.32}$$

The presence of a quadratic term in equation (6.31) highlights the non-linearity of the dynamics of the particle velocity gradient tensor, which ultimately leads to a finite-time blowup. This implies that each occurrence of caustics results in a singularity within the particle velocity gradient, which in turn causes singularities in both the particle velocity and number density fields. These singularities are characterized by $\mathrm{tr}\boldsymbol{\sigma} \to -\infty$ and $||\boldsymbol{\sigma}|| \sim (t-t_*)^{-1}$, where τ_v is sufficiently large such that $\boldsymbol{\sigma}/\tau_v \ll \boldsymbol{\sigma}^2$. A similar behavior, where the gradient of the solution blows up, is observed in solutions to the inviscid Burgers equation during the formation of a shock. This equation provides an estimate for analyzing and identifying caustics, though it is important to note that the presence of quadratic non-linearity does not always result in caustics. The formation of caustics is a highly complex phenomenon, influenced by intricate and self-interacting dynamics among the components of $\boldsymbol{\sigma}$ [116]. The only way to accurately determine the behavior of the solution, including the potential for blowup, is to solve the particle velocity field equations (6.3). Unlike the particle velocity gradient tensor equation, the particle temperature gradient equation (6.32) is linear in this limit like the equation (6.12) due to the behaviour of fluid temperature as a passive scalar field. Using the formalism proposed in this study, the occurrence of thermal caustics can be identified through the dynamics of $\boldsymbol{\xi}$. In the high inertia range, every caustic is also a thermal caustic because the blowup in $\boldsymbol{\sigma}$ explodes the equation for $\boldsymbol{\xi}$ as well. However, in the high thermal inertia range, the occurrence of thermal caustics depends on the presence of caustics. If the particle inertia is low, we might still observe a significant amplification in $\boldsymbol{\xi}$ due to high thermal inertia, but since the particle inertia is not in the range where caustics are highly probable, no blowup will occur in equation (6.32).

In a generic case, the equations (6.9) and (6.10) can be used to characterize the caustic and thermal caustics in all range of inertia and thermal inertia. Along each particle Lagrangian path the linearity of (6.10) makes that no singularity can arise in finite time unless the coefficients, G and σ become singular. But we already know that $\boldsymbol{G}$ cannot explode due to the diffusion term in the fluid temperature gradient,

then the only source of singularity is $\boldsymbol{\sigma}$. In case of slowly varying $\boldsymbol{G}$ and $\boldsymbol{\sigma}$, it makes the particle temperature gradient tend to relax to an equilibrium gradient given by

$$\boldsymbol{\xi}_e = [\boldsymbol{I} + \tau_\vartheta \boldsymbol{\sigma}]^{-1} \boldsymbol{G}. \tag{6.33}$$

A unique equilibrium state exists, for any given temperature gradient $\boldsymbol{G}$, only if the operator

$$\boldsymbol{M} = \boldsymbol{I} + \tau_\vartheta \boldsymbol{\sigma} \tag{6.34}$$

can be inverted, i.e. if $-\tau_\vartheta$ is not an eigenvalue of $\boldsymbol{\sigma}$. Formally, equation (6.10) has an analytical solution provided that G and σ are known functions along particle Lagrangian paths: the general solution of (6.10) can be expressed as

$$\boldsymbol{\xi}(t) = \boldsymbol{\Phi}(t, t_0)\boldsymbol{\xi}(t_0) \tag{6.35}$$

where $\boldsymbol{\Phi}(t, t_0)$ is the transfer operator, given by the solution of

$$\dot{\boldsymbol{\Phi}}(t; t_0) = \boldsymbol{M}(t)\boldsymbol{\Phi}(t; t_0) \tag{6.36}$$

$$\boldsymbol{\Phi}(t_0, t_0) = \boldsymbol{I}. \tag{6.37}$$

The properties of operator $\boldsymbol{M} = \boldsymbol{I} + \tau_\vartheta \boldsymbol{\sigma}$ determine the possibility to generate a thermal caustics. Since $\boldsymbol{G}$ is a smooth field, even if strongly intermittent, it is $\boldsymbol{\sigma}$ which is responsible for the onset of any singularity. Let us call $\lambda_1 < \lambda_2 < \lambda_3$ the three eigenvalues of the symmetric part of particle velocity gradient tensor which is denoted by $\boldsymbol{\sigma_S}$. Analogously to the symmetric part of the fluid velocity gradient tensor, i.e. the fluid strain-rate tensor, theses three eigenvalues must be real. On the other hand, using the analogy to the fluid strain-rate tensor lets us assume that the first eigenvalue is positive, the last one is negative and the second one can be either positive or negative. since $\lambda_1 + \lambda_2 + \lambda_3 < 0$ [121], we know that at least the minimum eigenvalue λ_1 must be always negative. If we scalarly multiply equation (6.10) by $\boldsymbol{\xi}$ we have

$$\frac{\tau_\vartheta}{2} \frac{\mathrm{D}_p}{\mathrm{D}t} ||\boldsymbol{\xi}||^2 = -||\boldsymbol{\xi}||^2 - \tau_\vartheta \boldsymbol{\xi} \cdot \boldsymbol{\sigma}_S \boldsymbol{\xi} + \boldsymbol{\xi} \cdot \boldsymbol{G} \tag{6.38}$$

that is,

$$\frac{\tau_\vartheta}{2}\frac{\mathrm{D}_p}{\mathrm{D}t}\left|\left|\boldsymbol{\xi}\right|\right|^2 = -\boldsymbol{\xi}\cdot\left[\boldsymbol{I}+\tau_\vartheta\boldsymbol{\sigma}_S\right]\boldsymbol{\xi}+\boldsymbol{\xi}\cdot\boldsymbol{G} \tag{6.39}$$

Since the trace of $\boldsymbol{\sigma_S}$ is negative, so that $||\boldsymbol{\xi}||$ increases when

$$\frac{1}{\tau_\vartheta}-\mathrm{tr}\boldsymbol{\sigma}>0$$

i.e.

$$\tau_\vartheta > -\mathrm{tr}\boldsymbol{\sigma}>0$$

In the equation (6.39) the alignment of $\boldsymbol{\xi}$ with $\boldsymbol{\sigma_S}$ and $\boldsymbol{G}$ plays a crucial term in the evolution of $\boldsymbol{\xi}$. The alignment with $\boldsymbol{\sigma_S}$ can be computed by mustering the angel between $\boldsymbol{\xi}$ and the principal eigenvectors of $\boldsymbol{\sigma_S}$, similar the approach is used in order to capture the alignment between the fluid vorticity and the eigenvectors of fluid strain-rate tensor. Therefore, we can assume that for three eigenvalues λ_1, λ_2 and λ_3 which are ordered such that $\lambda_1 \leq \lambda_2 \leq \lambda_3$, $\boldsymbol{p}_1$ $\boldsymbol{p}_2$, and $\boldsymbol{p}_3$ denote the corresponding eigenvectors. Now, we are able to see the stretching or compressing of $||\boldsymbol{\xi}||$ in the principal eigenvectors of $\boldsymbol{\sigma_S}$. In the principal frame of $\boldsymbol{\sigma_S}$ first term in right-hand side of (6.38) captures this stretching/compressing through

$$-\left[\left(\frac{1}{\tau_\vartheta}+\lambda_1\right)\xi_1^2+\left(\frac{1}{\tau_\vartheta}+\lambda_2\right)\xi_2^2+\left(\frac{1}{\tau_\vartheta}+\lambda_3\right)\xi_3^2\right] \tag{6.40}$$

Since $\mathrm{tr}\sigma_S<0$, $\lambda_1<0$ and $\lambda_i \geq \lambda_1$ $\forall i$, we obtain the following estimate for the solution of the magnitude of $\boldsymbol{\xi}$ which is the solution of the equation (6.39),

$$-\left(1+\tau_\vartheta\lambda_3\right)\left|\left|\boldsymbol{\xi}\right|\right|^2+\boldsymbol{G}\cdot\boldsymbol{\xi} \lesssim \frac{\tau_\vartheta}{2}\frac{\mathrm{d}}{\mathrm{d}t}\left|\left|\boldsymbol{\xi}\right|\right|^2 \lesssim -\left(1+\tau_\vartheta\lambda_1\right)\left|\left|\boldsymbol{\xi}\right|\right|^2+\boldsymbol{G}\cdot\boldsymbol{\xi} \tag{6.41}$$

Consequently, we can say that when $\boldsymbol{\sigma}$ remains bounded, the smooth solution of the equation (6.39) exists implying that no caustics, and thermal caustics occur. In this case, there is an exponential growth in time if all eigenvalues are negative and satisfy $\lambda_3 < -1/\tau_\vartheta$, which makes the particle temperature gradient to become large in a time of order $1/|\lambda_3|$ but still finite without blowup. In the opposite case, $\lambda_1 > -1/\tau_\vartheta$, the gradient tends to approach an equilibrium state. In all other cases,

other case ($\lambda_3 > -1/\tau_\vartheta$) the gradient remains within those two bounds. As in [121], the dynamics of the trace of $\boldsymbol{\sigma}$ is dictated by the smallest eigenvalues of $\boldsymbol{A}$, which determines the behaviour of the smallest eigenvalue of $\boldsymbol{\sigma}$, making it diverge. In such a case, it is possible to reduce the problem into a one-dimensional problem. The first idea is that the timescale of variation of $\boldsymbol{A}$ and $\boldsymbol{G}$ is larger than the timescale of the variation of the particle gradients, dictated by the Stokes relaxation time, so that it is possible to consider a sort of "frozen" flow approximation. As it used in [121] and [116] for the caustics in particle velocity field, two stages are individuated: until $\sigma \ll 1/\tau_v$ the nonlinear terms in the equation for σ can be neglected and its growth can be approximated by the solution of the linearized equation, giving an exponential growth

$$\sigma \simeq \int_0^t A(t') \exp(-(t-t')/\tau) \mathrm{d}t'. \tag{6.42}$$

When $\sigma \sim 1/\tau_v$ nonlinear terms become significant and when $\sigma \gg 1/\tau_v$ they are the dominant term so that $\dot{\sigma} \simeq -\sigma^2$, which leads to finie-time blowup

$$\sigma \simeq \sigma_0 (t_* - t)^{-1} \tag{6.43}$$

(if we impose $\sigma(0) \simeq 1/\tau_v$ then $\sigma_0 = t_*/\tau_v$), leading to a caustics at time t_*. The same analysis, indeed for the first time, is performed here for the particle temperature gradient to characterize the thermal caustics. Accordingly, the one-dimensional version of the temperature gradient equation is

$$\dot{\xi} = \left[\frac{1}{\tau_\vartheta} + \sigma \right] + \frac{G}{\tau_\vartheta} \tag{6.44}$$

which could be obtained by projection onto the eigenvector of the smallest eigenvalue of σ_S. In the second stage of the caustic formation we have

$$\dot{\xi} \simeq -\left[\frac{1}{\tau_\vartheta} + \frac{\sigma_0}{t_* - t} \right] \xi + \frac{G}{\tau_\vartheta} \tag{6.45}$$

i.e., since $\sigma \gg \tau_\vartheta$, (and G i.e. $\sigma \gg \boldsymbol{G}/(\boldsymbol{\xi}\tau_\vartheta)$)

$$\dot{\xi} \simeq -\frac{\sigma_0}{t_* - t} \xi \tag{6.46}$$

. which leads to

$$\xi(t) \simeq \xi_0 \exp(-t/\tau_\vartheta)(1-t/t_*)^{-\sigma_0} = \xi_0 \exp(-t/\tau_\vartheta)(1-t/t_*)^{-t_*/\tau_v} \qquad (6.47)$$

Therefore any thermal inertia (whatever small) cannot prevent the formation of a thermal caustics. However, in the limit $\tau_\vartheta \to 0^+$ there is no caustic, as the solution if $\xi = G$ and G is a smooth, even if intermittent, field. The condition for a growth of ξ is that $\sigma < -1/\tau_\vartheta$, so that a small thermal inertia can delay the begin of the algebraic grows which brings to the blowup.

One should check [32] to see it s small St_ϑ lead to a reduced intermittency in the statistics of the gradient of temperature, which could be a signature of the fact that temperature caustics are much less frequent. In fact, it take a finite time before $\sigma < -1/\tau_\vartheta$, so that the parameter D in [121] (the duration of negative A) is important, because it could be too short to have the blow up for ξ. We have analyzed the possibility to form thermal caustics, which have been reported from the processing of direct numerical simulations to be a prominent feature of small-scale fluid-particle thermal interaction. In conclusion, a temperature caustics form whenever a caustic is formed, except in the limit for zero thermal inertia, because in such a case particle temperature becomes independent from particle velocity. This is a sort of singular limit in the sense of asymptotic perturbation.

6.3 Conclusion

In this chapter, we propose a novel theoretical framework to characterize the formation of thermal caustics, extending beyond the existing concepts of caustics in particle velocity fields. While previous studies have identified the occurrence of thermal caustics in non-isothermal particle-laden flows, by analyzing the path history effects and particle temperature differences, a comprehensive theoretical model analogous to the caustics framework based on the dynamics of velocity gradient tensor, has yet to be developed. Our new theory will be based on the dynamics of particle temperature gradients, aiming to provide a deeper understanding of thermal caustics. This framework will elucidate how the particle temperature gradient evolves across various ranges of particle inertia and thermal inertia, and under what conditions this evolution may lead to explosive behavior. The formalism provides a

detailed explanation of the conditions under which the particle temperature gradient undergoes rapid changes, resulting in the formation of thermal caustics. This framework aims to advance our understanding of thermal interactions within turbulent flows. It has been demonstrated that caustics inherently lead to the formation of thermal caustics through the interplay between the particle velocity gradient and the particle temperature gradient. In cases of high particle inertia, where caustics are observed, thermal caustics emerges, causing the particle temperature gradient to exhibit finite-time singularities, regardless of the of particle thermal inertia. The only scenario in which thermal caustics do not form in this high-inertia range is when the particle thermal inertia is zero. Conversely, in the low-inertia regime, even when particles possess high thermal inertia, the evolution of the particle temperature gradient remains smooth. While high thermal inertia may lead to some amplification, no caustics are anticipated in this regime, and consequently, thermal caustics do not form.

Concluding remarks and future work

Concluding remarks

This thesis has provided a comprehensive exploration of heat transfer in non-isothermal particle-laden turbulent flows, employing a combination of theoretical analysis, direct numerical simulations (DNS), and kinetic theory. By developing a robust theoretical framework and performing detailed simulations across various flow conditions, we have gained significant insights into the thermal and dynamical interplay between fluid and inertial particles, contributing to the understanding and modeling of these complex systems in practical applications. We began with establishing the theoretical foundations necessary for analyzing the behavior of both the continuous and discrete phases. Therefore, the governing equations for the fluid and particles were derived, and statistical analysis were performed by using turbulence theory to capture the multiscale effects of turbulence. Furthermore, the critical aspect of mutual fluid-particle thermal interaction was addressed, and particle thermal feedback on the fluid temperature field was formulated. The derivation of equations has conducted in a way applicable to the more generic turbulent flows laden with inertial particles, however, at the end of initial chapters, the relevant equations under the assumptions of this work were proposed for the numerical simulation in the subsequent chapters. In the subsequent chapters, we investigated in detail, the heat transfer mechanisms in turbulent thermal mixing layers evolving with inertial particles. We explored how particles, depending on their inertia and thermal inertia, influence the overall heat flux and temperature statistics. The impact of inter-particle collisions on the thermal field was also examined, revealing their effect on overall heat transfer and temperature statistics to be minimal in dilute suspension. Our findings also highlighted the significant role of particle inertia over thermal inertia in determining heat transfer efficiency, particularly emphasizing the importance of

intermediate Stokes numbers. At these intermediate values, maximum heat transfer enhancement occurs due to localized heat transfer processes. This is facilitated by particle clustering and the comparable scale separation between particle dynamics and small-scale turbulence. Moreover, the impact of the turbulence characteristics through altering the flow Taylor microscale Reynolds number was examined revealing that heat transfer reduces with this flow parameter. Particle thermal feedback was shown to lower the turbulent convective heat flux by smoothing the temperature gradient, which leads to an overall increase in overall heat flux in different ranges of particle inertia and thermal inertia and for all simulated Taylor microscale Reynolds numbers. When particle inertia and thermal inertia vary independently, DNS results indicated that the particle heat flux can be either lower or higher than the turbulent convective heat flux, depending on the ratio of particle thermal-to-dynamical relaxation times. A critical Stokes number was identified to characterize the threshold of this reduction or increase. We also showed how thermal mass fraction or particle heat capacity ratio can generally predict an enhancement or reduction in overall heat flux, based on the particle-to-fluid heat capacity ratio, particle-to-fluid density ratio, and particle volume fraction. Consequently, with a very high thermal mass fraction, particularly in a denser regime, the presence of particles is expected to diminish the overall heat flux. To better understand the particle heat flux, a novel decomposition in terms of fluid and particle correlations of velocity and temperature and their derivatives was proposed and discussed. It is found that the correlation between particle acceleration and temperature time derivative tends to reduce the particle heat flux, however, thermal feedback makes this reduction less effective, resulting in higher particle heat flux in two-way coupling regime.

Additionally, in the following chapter, the application of kinetic theory to our physical problem allowed us to bridge the gap between individual Lagrangian particles behavior and their macroscopic Eulerian field properties. Through the derivation of the single-particle probability density function (pdf) and the exploration of its self-similar behavior in phase space, we were able to identify scaling laws and invariants that can characterize the dynamics of our fluid-particle system. This approach not only deepened our understanding of the complex interactions between particles and the fluid but also provided valuable tools for predicting and analyzing the behavior of particle-laden turbulent flows in various engineering and environmental contexts. The particle continuum-like fields, derived in this chapter enabled us to develop our self-similarity analysis in the next chapter. Moreover, the pdf evolution in phase

space helped us to gain more insights about the self-similar behaviour of thermal mixing dynamics observed by direct numerical simulations. Moreover, the investigation into self-similar and quasi-self-similar thermal mixing dynamics offered new perspectives on how particles modify the thermal mixing process. The integral analysis and mean total enthalpy approach provided a coherent methodology for inspecting the thermal behavior of these flows, emphasizing the importance of considering both self-similar and non-self-similar contributions. The findings underscore the critical role of particle thermal feedback in modulating fluid temperature fields, for optimizing non-isothermal particle-laden flows in practical real-world applications. The final chapter introduced for the first time a novel theoretical framework for understanding the formation of thermal caustics, extending beyond the existing concepts in particle velocity fields. This framework provides a deeper insight into the conditions under which rapid changes in particle temperature gradients occur, leading to the formation of thermal caustics by introducing singularities in particle thermal field. The new theory shows how thermal caustics occur due to the explosive evolution in particle velocity gradient tensor at higher particle inertia resulting in finite time blowup in particle temperature gradient field. Moreover, the thermal behaviour of inertial particle can be better understood in different inertia and thermal inertia using this new formalism. The investigation of the dynamics of particle velocity gradient tensor and temperature gradient vector fields and their underlying coupled mechanisms represents a significant advancement in our understanding of thermal interactions within turbulent flows laden with inertial particles.

Future Work

The research presented in this thesis opens several avenues for future work. One promising direction is the extension of the current study to droplet-laden turbulent flows, where mass transfer, evaporation, and condensation processes are also considered along with the inter-phase exchange of momentum and sensible heat. Such an extension involves the modeling of phase change phenomena in droplets, adding further complexity to the dynamics and thermodynamics of fluid-particle interaction. Understanding the interplay between droplet dynamics, heat transfer, and phase change processes can lead to more accurate models and simulations, particularly in applications such as spray cooling, combustion, and cloud formation. Addition-

ally, the development of advanced numerical methods for simulating these complex processes in droplet-laden turbulent flows can enhance our ability to predict and control such systems in various engineering and environmental contexts. Exploring the effects of different flow configurations, including the influence of variable droplet size distributions and the interaction between droplets of varying properties, can further refine our understanding of two-phase flow systems when phase change also takes place. Moreover, the validation of the theory developed for thermal caustics in the last chapter will be another potential extension to this present work.

In summary, this thesis has made significant contributions to the field of non-isothermal particle-laden turbulent flows, providing a strong foundation for future research and practical applications. The insights gained and the methodologies developed here will undoubtedly inform and inspire continued exploration in this challenging and important area of heat transfer in two-phase turbulent flows.

References

[1] F. Doisneau, F. Laurent, A. Murrone, J. Dupays, and M. Massot. Eulerian multi-fluid models for the simulation of dynamics and coalescence of particles in solid propellant combustion. *Journal of Computational Physics*, 234:230–262, 2013.

[2] Hadi Pouransari and Ali Mani. Effects of Preferential Concentration on Heat Transfer in Particle-Based Solar Receivers. *Journal of Solar Energy Engineering*, 139(2):021008, 11 2016.

[3] Mona Rahmani, Akanksha Gupta, and Lluís Jofre. Aggregation of microplastic and biogenic particles in upper-ocean turbulence. *International Journal of Multiphase Flow*, 157:104253, 2022.

[4] Akim Lavrinenko, Alexandre Fabregat, Fernando Gisbert, and Jordi Pallares. Direct numerical simulation of pathogen-laden aerosol dispersion in buoyancy-driven turbulent flow within confined spaces. *International Communications in Heat and Mass Transfer*, 152:107272, 2024.

[5] Gaetano Sardina, Francesco Picano, Luca Brandt, and Rodrigo Caballero. Continuous growth of droplet size variance due to condensation in turbulent clouds. *Phys. Rev. Lett.*, 115:184501, Oct 2015.

[6] Bipin Kumar, Paul Götzfried, Neethi Suresh, Jörg Schumacher, and Raymond A. Shaw. Scale Dependence of Cloud Microphysical Response to Turbulent Entrainment and Mixing. *Journal of Advances in Modeling Earth Systems*, 10(11):2777–2785, November 2018.

[7] P Götzfried, B Kumar, R A Shaw, and J Schumacher. Droplet dynamics and fine-scale structure in a shearless turbulent mixing layer with phase changes. *J. Fluid Mech.*, 814:452–483, 2017.

[8] Taraprasad Bhowmick and Michele Iovieno. Direct numerical simulation of a warm cloud top model interface: Impact of the transient mixing on different droplet population. *Fluids*, 4(3):144, 2019.

[9] A. Celani, A. Lanotte, A. Mazzino, and M. Vergassola. Universality and saturation of intermittency in passive scalar turbulence. *Phys. Rev. Lett.*, 84:2385–2388, Mar 2000.

[10] Takeshi Watanabe and Toshiyuki Gotoh. Statistics of a passive scalar in homogeneous turbulence. *New Journal of Physics*, 6(1):40, apr 2004.

[11] J. Béc, H. Homann, and G. Krstulovic. Clustering, fronts, and heat transfer in turbulent suspensions of heavy particles. *Physical Review Letters*, 112:234503, 2014.

[12] G. I. Taylor. Diffusion by continuous movements. *Proceedings of the London Mathematical Society*, s2-20(1):196–212, 1922.

[13] Robert H. Kraichnan. Anomalous scaling of a randomly advected passive scalar. *Phys. Rev. Lett.*, 72:1016–1019, Feb 1994.

[14] Shankar Subramaniam and S. Balachandar. Computation and Analysis of Turbulent Flows. Academic Press, 2023.

[15] Luca Brandt and F Coletti. Particle-laden turbulence: Progress and perspectives. *Annu. Rev. Fluid Mech.*, 54:159–189, 2022.

[16] Guodong Gai, Abdellah Hadjadj, Sergey Kudriakov, and Olivier Thomine. Particles-induced turbulence: A critical review of physical concepts, numerical modelings and experimental investigations. *Theoretical and Applied Mechanics Letters*, 10(4):241–248, 2020.

[17] Varghese Mathai, Detlef Lohse, and Chao Sun. Bubbly and buoyant particle–laden turbulent flows. *Annual Review of Condensed Matter Physics*, 11(Volume 11, 2020):529–559, 2020.

[18] Said Elghobashi. Direct numerical simulation of turbulent flows laden with droplets or bubbles. *Annual Review of Fluid Mechanics*, 51(1):217–244, 2019.

[19] J.G.M. Kuerten. Point-particle dns and les of particle-laden turbulent flow-a state-of-the-art review. *Flow, Turbulence and Combustion*, 97:689–713, 2016.

[20] Xiaojing Zheng, Guohua Wang, and Wei Zhu. Experimental study on the effects of particle-wall interactions on vlsm in sand-laden flows. *Journal of Fluid Mechanics*, 914:A35, 2021.

[21] Hongyou Liu, Yuen Feng, and Xiaojing Zheng. Experimental investigation of the effects of particle near-wall motions on turbulence statistics in particle-laden flows. *Journal of Fluid Mechanics*, 943:A8, 2022.

[22] Elliott W. Lewis, Timothy C. W. Lau, Zhiwei Sun, Zeyad T. Alwahabi, and Graham J. Nathan. Insights from a new method providing single-shot, planar measurement of gas-phase temperature in particle-laden flows under high-flux radiation. *Experiments in Fluids*, 62, 2021.

[23] Andrew J. Banko, Laura VillafaÃ±e, Ji Hoon Kim, and John K. Eaton. Temperature statistics in a radiatively heated particle-laden turbulent square duct flow. *International Journal of Heat and Fluid Flow*, 84:108618, 2020.

[24] M. W. Reeks. On a kinetic equation for the transport of particles in turbulent flows. *Physics of Fluids A: Fluid Dynamics*, 3(3):446–456, 03 1991.

[25] R.V.R. Pandya and F. Mashayek. Non-isothermal dispersed phase of particles in turbulent flow. *J. Fluid Mech.*, 475:205 – 245, 2003.

[26] Leonid I. Zaichik, Vladimir M. Alipchenkov, and Artur R. Avetissian. A statistical model for predicting the heat transfer of solid particles in turbulent flows. *Flow Turbulence Combust*, 86:497 – 518, 2011.

[27] F Zonta, C Marchioli, and A Soldati. Direct numerical simulation of turbulent heat transfer modulation in micro-dispersed channel flow. *Acta Mechanica*, 195:305–326, 2008.

[28] J G M Kuerten, C W M van der Geld, and B J Geurts. Turbulence modification and heat transfer enhancement by inertial particles in turbulent channel flow. *Phys. Fluids*, 23(12):123301, 2011.

[29] M.H. Nakhaei and B. Lessani. Effects of solid inertial particles on the velocity and temperature statistics of wall bounded turbulent flow. *International Journal of Heat and Mass Transfer*, 106:1014–1024, 2017.

[30] B. Lessani and M.H. Nakhaei. Large-eddy simulation of particle-laden turbulent flow with heat transfer. *International Journal of Heat and Mass Transfer*, 67:974–983, 2013.

[31] Hadi Pouransari and Ali Mani. Particle-to-fluid heat transfer in particle-laden turbulence. *Phys. Rev. Fluids*, 3:074304, Jul 2018.

[32] Maurizio Carbone, Andrew D Bragg, and Michele Iovieno. Multiscale fluid-particle thermal interaction in isotropic turbulence. *J. Fluid Mech.*, 881:679–721, 2019.

[33] Izumi Saito, Takeshi Watanabe, and Toshiyuki Gotoh. A new time scale for turbulence modulation byÂ particles. *Journal of Fluid Mechanics*, 880:R6, 2019.

[34] Shuojin Li, Zhiwen Cui, Chunxiao Xu, and Lihao Zhao. Temperature statistics of settling particles in homogeneous isotropic turbulence. *International Journal of Heat and Mass Transfer*, 228:125555, 2024.

[35] Hamid Reza Zandi Pour and Michele Iovieno. Heat transfer enhancement by suspended particles in a turbulent shearless flow. *33rd Congress of the International Council of the Aeronautical Sciences, ICAS 2022*, 4:2452–2463, 2022.

[36] Hamid Reza Zandi Pour and Michele Iovieno. Heat transfer in a non-isothermal collisionless turbulent particle-laden flow. *Fluids*, 7(11):345, 2022.

[37] Hamid Reza Zandi Pour and Michele Iovieno. The effect of particle collisions on heat transfer in a non-isothermal dilute turbulent gas-particle flow. *8th World Congress on Momentum, Heat and Mass Transfer*, 03 2023.

[38] Hamid Reza Zandi Pour and Michele Iovieno. On the heat transfer in particle-laden turbulent flows: the effect of collision in an anisothermal regime. *9th World Congress on Mechanical, Chemical, and Material Engineering*, aug 2023.

[39] Hamid Reza Zandi Pour and Michele Iovieno. The impact of collisions on heat transfer in a particle-laden shearless turbulent flow. *Journal of Fluid Flow, Heat and Mass Transfer*, 10:140–149, 2023.

[40] Hamid Reza Zandi Pour and Michele Iovieno. Heat transport in a non-homothermal turbulent particle-laden flow in the collisional regime. *Journal of Physics: Conference Series*, 2685(1):012002, jan 2024.

[41] Hamid Reza Zandi Pour and Michele Iovieno. The role of particle inertia and thermal inertia in heat transfer in a non-isothermal particle-laden turbulent flow. *Fluids*, 9(1), 2024.

[42] Charles Meneveau. Lagrangian dynamics and models of the velocity gradient tensor in turbulent flows. *Annual Review of Fluid Mechanics*, 43(Volume 43, 2011):219–245, 2011.

[43] Perry L. Johnson and Michael Wilczek. Multiscale velocity gradients in turbulence. *Annual Review of Fluid Mechanics*, 56(Volume 56, 2024):463–490, 2024.

[44] Perry L. Johnson and Charles Meneveau. Turbulence intermittency in a multiple-time-scale navier-stokes-based reduced model. *Phys. Rev. Fluids*, 2:072601, Jul 2017.

[45] Xiaolong Zhang, Maurizio Carbone, and Andrew D. Bragg. Lagrangian model for passive scalar gradients in turbulence. *Journal of Fluid Mechanics*, 964, jun 2023.

[46] R. Gomes-Fernandes, B. Ganapathisubramani, and J.C. Vassilicos. Evolution of the velocity-gradient tensor in a spatially developing turbulent flow. *Journal of Fluid Mechanics*, 756:252–292, 2014.

[47] I. Paul, G. Papadakis, and J. C. Vassilicos. Evolution of passive scalar statistics in a spatially developing turbulence. *Phys. Rev. Fluids*, 3:014612, Jan 2018.

[48] G. G. Stokes. On the effect of the internal friction of fluids on the motion of pendulums. *Transactions of the Cambridge Philosophical Society*, 9:8–106, 1851.

[49] Joseph Boussinesq. *Théorie de l'Écoulement Tourbillonnant et Tumultueux des Liquides dans les Lits Rectilignes à Grande Section Transversale*. Gauthier-Villars, Paris, 1877.

[50] Alfred Barnard Basset. *A Treatise on Hydrodynamics: With Numerous Examples*. Deighton, Bell, and Company, Cambridge, UK, 1888.

[51] Carl Wilhelm Oseen. *Neuere Methoden und Ergebnisse in der Hydrodynamik*. Akademische Verlagsgesellschaft, Leipzig, Germany, 1927.

[52] M R Maxey and J J Riley. Equation of motion for a small rigid sphere in a nonuniform flow. *Phys. Fluids*, 26(4):883–889, 1983.

[53] R. Gatignol. Faxen formulae for a rigid particle in an unsteady non-uniform stokes flow. *Journal de mecanique theorique et appliquee*, 2(2):143–160, 1983.

[54] H. Homann and J. Béc. Finite-size effects in the dynamics of neutrally buoyant particles in turbulent flow. *Journal of Fluid Mechanics*, 651:81–91, 2010.

[55] L. Schiller and Naumann Z. A drag coefficient correlation. *Z.Ver.Deutsch.Ing*, 77:318–320, 1933.

[56] M. Boussinesq. Théorie de l'écoulement tourbillonnant et des mouvements périodiques dans un fluide visqueux. *Comptes Rendus de l'Académie des Sciences*, 101:558–560, 1885.

[57] Vincenzo Armenio and Virgilio Fiorotto. The importance of the forces acting on particles in turbulent flows. *Physics of Fluids*, 13(8):2437–2440, 08 2001.

[58] P. G. Saffman. The lift on a small sphere in a slow shear flow. *Journal of Fluid Mechanics*, 22:385 – 400, 1965.

[59] Dominique Legendre and Jacques Magnaudet. A note on the lift force on a spherical bubble or drop in a low-reynolds-number shear flow. *Physics of Fluids - PHYS FLUIDS*, 9:3572–3574, 11 1997.

[60] M. J. Lighthill. Drift. *Journal of Fluid Mechanics*, 1(1):31–53, 1956.

[61] T. R. Auton. The lift force on a spherical body in a rotational flow. *Journal of Fluid Mechanics*, 183:199–218, 1987.

[62] S. I. Rubinow and Joseph B. Keller. The transverse force on a spinning sphere moving in a viscous fluid. *Journal of Fluid Mechanics*, 11(3):447–459, 1961.

[63] W. E. Ranz and W. R. Marshall. Evaporation from drops - part 1. 1952.

[64] Neeraj S. Borker and Donald L. Koch. Slender body theory for particles with non-circular cross-sections with application to particle dynamics in shear flows. *Journal of Fluid Mechanics*, 877:1098–1133, 2019.

[65] Jean-Pierre Minier and Christophe Henry. The dynamics of discrete particles in turbulent flows: open issues and current challenges in statistical modeling, 2023.

[66] S. Elghobashi. On predicting particle-laden turbulent flows. *Applied Scientific Research*, 52(4):309–329, 1994.

[67] Alec J. Petersen, Lucia Baker, and Filippo Coletti. Experimental study of inertial particles clustering and settling in homogeneous turbulence. *Journal of Fluid Mechanics*, 864:925–970, February 2019.

[68] C. Poelma, J. Westerwee, and G. OOMS. Particle–fluid interactions in grid-generated turbulence. *Journal of Fluid Mechanics*, 589:315–351, 2007.

[69] Tim Berk and Filippo Coletti. Dynamics of small heavy particles in homogeneous turbulence: a lagrangian experimental study. *Journal of Fluid Mechanics*, 917, April 2021.

[70] Maurizio Carbone and Michele Iovieno. Application of the non-uniform Fast Fourier Transform to the Direct Numerical Simulation of two-way coupled turbulent flows. *WIT Trans. Eng. Sci.*, 120:237–248, 2018.

[71] M. A. T. van Hinsberg, J. H. M. ten Thije Boonkkamp, F. Toschi, and H. J. H. Clercx. Optimal interpolation schemes for particle tracking in turbulence. *Phys. Rev. E*, 87:043307, Apr 2013.

[72] Rémi Zamansky, Filippo Coletti, Marc Massot, and Ali Mani. Radiation induces turbulence in particle-laden fluids. *Physics of Fluids*, 26(7), July 2014. Publisher Copyright: © 2014 AIP Publishing LLC.

[73] Y. Pan and S. Banerjee. Numerical simulation of particle interactions with wall turbulence. *Physics of Fluids*, 8(10):2733–2755, 10 1996.

[74] P. Gualtieri, F. Picano, G. Sardina, and C.M. Casciola. Exact regularized point particle method for multiphase flows in the two-way coupling regime. *Journal of Fluid Mechanics*, 773:520–561, 2015.

[75] Maurizio Carbone and Michele Iovieno. Accurate direct numerical simulation of two-way coupled particle-laden flows through the nonuniform fast fourier transform. *Int. J. Safety and Sec. Eng.*, 10(2):191–200, 2020.

[76] Claudio Canuto, M. Yousuff Hussaini, Alfio Quarteroni, and Thomas A. ZangHawking. *Spectral Methods in Fluid Dynamics*. Springer, Heidelberg, 1988.

[77] Michele Iovieno, Silvio Di Savino, Luca Gallana, and Daniela Tordella. Mixing of a passive scalar across a thin shearless layer: concentration of intermittency on the sides of the turbulent interface. *J. Turbulence*, 15(5):311–334, 2014.

[78] Chong Shen Ng, Vamsi Spandan, Roberto Verzicco, and Detlef Lohse. Non-monotonic transport mechanisms in vertical natural convection with dispersed light droplets. *Journal of Fluid Mechanics*, 2020.

[79] Pedro Costa, Bendiks Jan Boersma, Jerry Westerweel, and Wim-Paul Breugem. Collision model for fully resolved simulations of flows laden with finite-size particles. *Phys. Rev. E*, 92:053012, Nov 2015.

[80] Peter A. Cundall and Otto D. L. Strack. A discrete numerical model for granular assemblies. *Geotechnique*, 29(1):47–65, 1979.

[81] Thorsten Poschel and Thomas Schwager. *Computational Granular Dynamics: Models and Algorithms*. Springer-Verlag Berlin Heidelberg, 2005.

[82] Michael P. Allen and Dominic J. Tildesley. *Computer Simulation of Liquids*. Oxford University Press, 2017.

[83] Loup Verlet. Computer "experiments" on classical fluids. i. thermodynamical properties of lennard-jones molecules. *Physical Review*, 159(1):98–103, 1967.

[84] R. Onishi, K. Takahashi, and J. C. Vassilicos. An efficient parallel simulation of interacting inertial particles in homogeneous isotropic turbulence. *Journal of Computational Physics*, 242:809–827, 2013.

[85] F.A. Jaberi. Temperature fluctuations in particle-laden homogeneous turbulent flows. *International Journal of Heat and Mass Transfer*, 41(24):4081–4093, 1998.

[86] H J Park, K O'Keefe, and D H Richter. Rayleigh-Bénard turbulence modified by two-way coupled inertial, nonisothermal particles. *Phys. Rev. Fluids*, 3:034307, 2018.

[87] I Saito, T Watanabe, and Toshiyuki Gotoh. Modulation of fluid temperature fluctuations by particles in turbulence. *J. Fluid Mech.*, 931:A6, 2022.

[88] A. S. Monin and A. M. Yaglom. *Statistical Fluid Mechanics*. MIT Press, Cambridge (MA), 1975.

[89] L. Mydlarski and Z. Warhaft. Passive scalar statistics in high Péclet number grid turbulence. *Journal of Fluid Mechanics*, 358:135–175, 1998.

[90] Rémi Zamansky. Acceleration scaling and stochastic dynamics of a fluid particle in turbulence. *Phys. Rev. Fluids*, 7:084608, Aug 2022.

[91] I. I. Zaichik and V. A. Pershukov. Modeling of particle motion in a turbulent flow with allowance for collisions. *Fluid Dynamics*, 30:49–63, 1995.

[92] Jean-Pierre Minier and Christophe Profeta. Kinetic and dynamic probability-density-function descriptions of disperse turbulent two-phase flows. *Phys. Rev. E*, 92:053020, Nov 2015.

[93] I.V. Derevich. Statistical modeling of particles relative motion in a turbulent gas flow. *International Journal of Heat and Mass Transfer*, 49(23):4290–4304, 2006.

[94] B. Arcen, A. Tanière, and M. Khalij. Heat transfer in a turbulent particle-laden channel flow. *International Journal of Heat and Mass Transfer*, 55(23):6519–6529, 2012.

[95] A. Bragg, D. C. Swailes, and R. Skartlien. Particle transport in a turbulent boundary layer: Non-local closures for particle dispersion tensors accounting for particle-wall interactions. *Physics of Fluids*, 24(10):103304, 10 2012.

[96] D. M. Shchadinskiy I. V. Derevich and Z. H. Tun. Probabilistic model of dispersed turbulent flow in channels with rough walls. *Aerosol Science and Technology*, 54(8):892–916, 2020.

[97] De-Yu Zhong, Guang-Qian Wang, Ming-Xi Zhang, and Tie-Jian Li. Kinetic equation for particle transport in turbulent flows. *Physics of Fluids*, 32(7):073301, 07 2020.

[98] K E Hyland, S McKee, and M W Reeks. Derivation of a pdf kinetic equation for the transport of particles in turbulent flows. *Journal of Physics A: Mathematical and General*, 32(34):6169, aug 1999.

[99] Rohit Dhariwal, Sarma L. Rani, and Donald L. Koch. Stochastic theory and direct numerical simulations of the relative motion of high-inertia particle pairs in isotropic turbulence. *Journal of Fluid Mechanics*, 813:205–249, 2017.

[100] Stephen B. Pope Hasret Turkeri and Metin Muradoglu. A les/pdf simulator on block-structured meshes. *Combustion Theory and Modelling*, 23(1):1–41, 2019.

[101] Stephen B. Pope. *Turbulent Flows*. Cambridge University Press, 2000.

[102] Anaelle Halle, Stéphane Colombi, and Sébastien Peirani. Phase-space structure analysis of self-gravitating collisionless spherical systems. *Astronomy & Astrophysics*, 2017.

[103] Armin Kianfar, Ahmed Elnahhas, and Perry L. Johnson. Quantifying How Turbulence Enhances Boundary Layer Skin Friction and Surface Heat Transfer. *AIAA Journal*, 61(9):3900–3909, September 2023.

[104] Marcelo Chamecki and Charles Meneveau. Particle boundary layer above and downstream of an area source: scaling, simulations, and pollen transport. *J. Fluid Mech.*, 683:1–26, 2011.

[105] Leonid I. Zaichik and Vladimir M. Alipchenkov. Pair dispersion and preferential concentration of particles in isotropic turbulence. *Physics of Fluids*, 15(6):1776–1787, 05 2003.

[106] Leonid I. Zaichik and Vladimir M. Alipchenkov. Statistical models for predicting pair dispersion and particle clustering in isotropic turbulence and their applications. *New Journal of Physics*, 11, 2009.

[107] Jaehun Chun, Donald L. Koch, Sarma L. Rani, Aruj Ahluwalia, and Lance R. Collins. Clustering of aerosol particles in isotropic turbulence. *Journal of Fluid Mechanics*, 536:219 – 251, 2005.

[108] Jérémie Bec and Robin Vallée. Homogeneous turbophoresis of heavy inertial particles in turbulent flow, 2024.

[109] Susumu Goto and J.C. Vassilicos. Sweep-stick mechanism of heavy particle clustering in fluid turbulence. *Physical Review Letters*, 100(5), 2008.

[110] L. CHEN, S. GOTO, and J. C. VASSILICOS. Turbulent clustering of stagnation points and inertial particles. *Journal of Fluid Mechanics*, 553:143–154, 2006.

[111] S. W. Coleman and J. C. Vassilicos. A unified sweep-stick mechanism to explain particle clustering in two- and three-dimensional homogeneous, isotropic turbulence. *Physics of Fluids*, 21(11):113301, 11 2009.

[112] Andrew D Bragg and Lance R Collins. New insights from comparing statistical theories for inertial particles in turbulence: I. spatial distribution of particles. *New Journal of Physics*, 16(5):055013, may 2014.

[113] M. Wilkinson and B. Mehlig. Caustics in turbulent aerosols. *Europhysics Letters*, 71(2):186, jun 2005.

[114] Elena Meneguz and Michael W. Reeks. Statistical properties of particle segregation in homogeneous isotropic turbulence. *Journal of Fluid Mechanics*, 686:338–351, 2011.

[115] G. Boffetta, A. Celani, F. De Lillo, and S. Musacchio. The eulerian description of dilute collisionless suspension. *Europhysics Letters*, 78(1):14001, mar 2007.

[116] Seulgi Lee and Changhoon Lee. Identification of a particle collision as a finite-time blowup in turbulence. *Scientific Reports*, 13, 2023.

[117] J. Bec. Fractal clustering of inertial particles in random flows. *Physics of Fluids*, 15(11):L81–L84, 09 2003.

[118] K Gustavsson, E Meneguz, M Reeks, and B Mehlig. Inertial-particle dynamics in turbulent flows: caustics, concentration fluctuations and random uncorrelated motion. *New Journal of Physics*, 14(11):115017, nov 2012.

[119] Mahdi Esmaily and Ali Mani. Modal analysis of the behavior of inertial particles in turbulence subjected to stokes drag. *Phys. Rev. Fluids*, 5:084303, Aug 2020.

[120] G. Falkovich, K. Gawędzki, and M. Vergassola. Particles and fields in fluid turbulence. *Rev. Mod. Phys.*, 73:913–975, Nov 2001.

[121] Tobias Bätge, Itzhak Fouxon, and Michael Wilczek. Quantitative prediction of sling events in turbulence at high reynolds numbers. *Phys. Rev. Lett.*, 131:054001, Aug 2023.

[122] L. Biferale, A.Â S. Lanotte, R. Scatamacchia, and F. Toschi. Intermittency in the relative separations of tracers and of heavy particles in turbulent flows. *Journal of Fluid Mechanics*, 757:550–572, 2014.

[123] J Bec, L Biferale, M Cencini, A S Lanotte, and F Toschi. Spatial and velocity statistics of inertial particles in turbulent flows. *Journal of Physics: Conference Series*, 333(1):012003, dec 2011.

[124] S. Ravichandran, P. Deepu, and Rama Govindarajan. Clustering of heavy particles in vortical flows: a selective review. *Sādhanā*, 42:597–605, 2017.

[125] Jan Meibohm, Kristian Gustavsson, and Bernhard Mehlig. Caustics in turbulent aerosols form along the vieillefosse line at weak particle inertia. *Phys. Rev. Fluids*, 8:024305, Feb 2023.

[126] J. Bec, K. Gustavsson, and B. Mehlig. Statistical models for the dynamics of heavy particles in turbulence. *Annual Review of Fluid Mechanics*, April 2023. Annu. Rev. Fluid Mech. 56: In press.

[127] M. Wilkinson and B. Mehlig. Caustics in turbulent aerosols. *Europhysics Letters*, 71:186–192, 2005.

[128] Gregory P Bewley, Ewe-Wei Saw, and Eberhard Bodenschatz. Observation of the sling effect. *New Journal of Physics*, 15(8):083051, aug 2013.

[129] J. Abrahamson. Collision rates of small particles in a vigorously turbulent fluid. *Chemical Engineering Science*, 30:1371–1379, 1975.

[130] George Haller and Themistoklis Sapsis. Where do inertial particles go in fluid flows? *Physica D: Nonlinear Phenomena*, 237(5):573–583, 2008.

[131] Vojtěch Patočka, Nicola Tosi, and Enrico Calzavarini. Residence time of inertial particles in 3d thermal convection: Implications for magma reservoirs. *Earth and Planetary Science Letters*, 591:117622, 2022.